

From the clouds to the ground
Effects of flow-precipitation interactions on snow
distribution in complex alpine terrain

THÈSE N° 8636 (2018)

PRÉSENTÉE LE 29 JUIN 2018

À LA FACULTÉ DE L'ENVIRONNEMENT NATUREL, ARCHITECTURAL ET CONSTRUIT
LABORATOIRE DES SCIENCES CRYOSPHÉRIQUES
PROGRAMME DOCTORAL EN GÉNIE CIVIL ET ENVIRONNEMENT

ÉCOLE POLYTECHNIQUE FÉDÉRALE DE LAUSANNE

POUR L'OBTENTION DU GRADE DE DOCTEUR ÈS SCIENCES

PAR

Franziska GERBER

acceptée sur proposition du jury:

Prof. D. Lignos, président du jury
Prof. M. Lehning, Dr R. Mott-Grünewald, directeurs de thèse
Prof. H. Wernli, rapporteur
Dr V. Vionnet, rapporteur
Prof. S. Takahama, rapporteur



ÉCOLE POLYTECHNIQUE
FÉDÉRALE DE LAUSANNE

Suisse
2018

Acknowledgments

I would like to thank a number of people who supported me during my PhD thesis.

First of all, I would like to thank my supervisor Michi. Without your support, sharing ideas and weekly fruitful discussions this thesis would not have been possible. Your guidance toward scientific thinking and writing was of particular importance. It was a great pleasure to work with you during the last four years – and I am looking forward to the next two years.

Furthermore, special thanks go to my co-supervisor Rebecca. Your knowledge about atmospheric processes in complex terrain and experience in very high-resolution modeling is irreplaceable. Additionally, I would like to thank you for running ARPS simulation, which were of great value for my analysis.

Many thanks to both of you, for introducing the Dischma-Experiment, supervising, discussing and encouraging me during the last four years!

As setting up WRF simulations reanalysis was a big challenge causing many frustrating hours, I would like to send big thanks to all the people who assisted me to get through the processes of numerous technical and numerical problems. Many thanks go to Mauro, who shared his knowledge to successfully apply for computational resources at the CSCS. A huge thank goes to Varun for the time he spent to properly configure WRF and for pre-processing of COSMO reanalysis. Further thanks go to Louis and Benoit for working on input data processing. Additionally, I would like to send special thanks to Megan who shared her WRF-experience, spent time to discuss the model setup and to identify errors. Furthermore, I would like to thank Changhai and the wrfhelp for helpful inputs concerning WRF. For advice about Alpine3D simulations and the use of MeteoIO, I would further like to thank Mathias (Bavay) and for his open ear and assistance with technical issues of any kind I would like to thank Mathias (Hauser).

For assisting with fieldwork and for adventures in the Dischma valley special thanks go to Sebastian (Schlögl). Additionally, I would like to thank Lisa, Urs, Prisco, Christian, Rebecca, Robert, Noah and Matthias (Heck) for supporting me in the field. Special thanks go to Sebastian (Hoch), who run and processed the Doppler wind lidar data and for introducing me to the installation and principles of wind lidar measurements. For our safety in the field and as a group leader and former supervisor during my internship at SLF special thanks go to Charles Fierz. *Im Zusammenhang mit der Feldarbeit möchte ich auch dem Team der Werkstatt des SLF ganz herzlich danken für die Unterstützung all unserer Feldkampagnen im Rahmen des Dischma-Experiments.*

For initializing the collaboration with MeteoSwiss I would like to send thanks to Urs (Germann). Additionally, special thanks go to Nikola for radar data processing and discussing and developing ideas and the whole team of MeteoSwiss in Locarno – it was a pleasure to visit you and work with you. Additionally, I would like to thank Alexis for his inputs about radar data analysis and concerning geostatistical methods.

For sharing the office, lunch breaks and leisure time, I would further like to thank my friends and colleagues at SLF. *Ein weiteres Dankeschön geht an den BC Chur – es war (und ist) ein grosses Vergnügen mit euch Badminton zu spielen. Zu guter Letzt möchte ich mich bei meiner Familie, bei Melanie und ganz besonders bei Mathias bedanken. Ihr habt mich durch alle Hochs und Tiefs dieser Arbeit begleitet, mich immer wieder aufgemuntert und wart auch sonst immer für mich da!*

Abstract

Knowledge about the spatial distribution of seasonal snow is essential e.g. to efficiently manage fresh water resources or for hydro-power companies. The large-scale gradient of snow accumulation over mountain ranges is mainly determined by lifting condensation and downstream drying. On the slope-scale, snow redistribution by wind and avalanches is the main source of variability. On a mountain-ridge to mountain-valley scale, small-scale orographic precipitation enhancement and preferential deposition interact and lead to asymmetric snow distribution across mountain ridges. However, their relative importance is barely known and the characteristics of preferential deposition are still under debate. Yet, especially in a changing climate, which may go along with modified dominant wind directions, it is important to understand precipitation processes shaping the snow cover.

Therefore, we investigate terrain-flow-precipitation interactions and their effect on mountain-ridge to mountain-valley scale snow precipitation and deposition in complex alpine terrain. To this end, the Weather Research and Forecasting (WRF) model is set up to downscale Consortium for Small-Scale Modeling (COSMO) analysis to a horizontal resolution of 50 m using a nesting approach. At 450 m resolution these simulations fairly represent large-scale precipitation variability with respect to high-resolution operational weather radar precipitation estimates, capturing the effect of large-scale orographic enhancement. Although, the model misses substantial small-scale precipitation variability even at a 50 m resolution, we demonstrate that the lee-side flow field and mountain-ridge scale precipitation processes start to be represented at this resolution. Thus, a model resolution of ≤ 50 m is required to represent mountain-ridge to mountain-valley scale precipitation patterns, which is far higher than model resolutions conventionally used to simulate snow water resources in alpine regions.

Small-scale orographic precipitation enhancement and mean advection are estimated to increase lee-side precipitation by up to 20 %, while a conservative estimate of (near-surface) preferential deposition reveals lee-side snow deposition enhancement on the order of 10 %. However, both processes strongly depend on atmospheric conditions such as atmospheric humidity or the strength of mean advection. The peculiarity of the lee-side flow field is of particular importance for the spatial distribution of snow accumulation, especially with regards to preferential deposition. This is further demonstrated by a very persistent eddy-like structure on the leeward side of the Sattelhorn ridge in the Dischma valley (Davos, CH), as reported based on Doppler wind lidar measurements and with corresponding flow field simulations at a resolution of 25 m by the Advanced Regional Prediction System (ARPS). Corresponding snow accumulation, assessed by the means of terrestrial laser scanning, confirms that snow distribution in very steep terrain is strongly influenced by post-depositional snow redistribution. Nevertheless, we can report a certain agreement of simulated pre-depositional precipitation patterns across mountain ridges with photogrammetrically determined snow distribution.

Overall, we demonstrate the necessity and value of high-resolution snow precipitation measurements and simulations, and we contribute to the understanding of the small-scale variability of snow distribution in alpine terrain.

Keywords

Terrain-flow-precipitation interactions • Snow precipitation and accumulation distribution • Lee-side flow field • Preferential deposition • Cloud dynamics • Spatial variability • Remote sensing • High-resolution numerical simulations

Zusammenfassung

Wissen über die räumliche Verteilung von saisonalem Schnee ist wichtig, zum Beispiel für effizientes Management von Frischwasser und Wasserenergie. Hebungs-Kondensation aufgrund der Strömung über einen Gebirgszug und das Austrocknen der Atmosphäre stromabwärts sind die wichtigsten Faktoren, die den grossskaligen Niederschlagsgradienten bestimmen. Auf der Hang-Skala wird die Schneeverteilung vor allem über die Umverteilung von Schnee durch Wind und Lawinen bestimmt. Auf der Bergrücken- zu Bergtal-Skala erfolgt eine starke Wechselwirkung zwischen orographischer Niederschlagsverstärkung und bevorzugter Ablagerung von Schnee, was zu einer asymmetrischen Schneeverteilung führt. Über die relative Wichtigkeit dieser Prozesse ist jedoch wenig bekannt und die Ausprägungen der bevorzugten Ablagerung von Schnee wird immer noch diskutiert. Vor allem in einem sich ändernden Klima, welches mit einer Veränderung der dominanten Windrichtung einhergehen kann, ist es wichtig Niederschlagsprozesse zu verstehen, welche die Schneedecke formen.

Deswegen untersuchen wir Gelände-Strömung-Niederschlagswechselwirkungen und deren Effekt auf die Niederschlags- und Schneeverteilung in gebirgigem Gelände auf einer Bergrücken- zu Bergtal-Skala. Wir konfigurieren das numerische Atmosphärenmodell “Weather Research and Forecasting model” (WRF) um Analysen des “Consortium for Small-Scale Modeling” (COSMO) Modells auf eine Auflösung von 50 m herunterzurechnen. Dazu benutzen wir verschachtelte Simulationen mit unterschiedlichen Auflösungen. Auf einer Auflösung von 450 m zeigt das Model eine angemessene Übereinstimmung mit operationellen Wetterradardaten und erfasst den Effekt der grossräumigen orographischen Niederschlagsverstärkung. Obschon das Model sogar auf einer Auflösung von 50 m einen Grossteil der Variabilität nicht auflöst, beginnt es das leeseitige Strömungsfeld und Niederschlagsprozesse auf der Bergrücken-Skala zu simulieren. Dies zeigt, dass eine Modellauflösung von ≤ 50 m wichtig ist um Niederschlagsprozesse auf der Bergrücken- zu Bergtal-Skala aufzulösen, was eine bei Weitem höhere Auflösung ist, als konventionell zur Schnee-Wasserressourcen Modellierung in alpinem Gelände benutzt wird.

Die kleinskalige orographische Niederschlagsverstärkung und die mittlere Advektion tragen bis zu 20 % zu erhöhtem Niederschlag im Lee bei, während eine konservative Schätzung der (bodennahen) bevorzugten Ablagerung von Schnee eine Zunahme der leeseitigen Schneeablagerung in der Grössenordnung von 10 % zeigt. Beide Prozesse sind jedoch stark von atmosphärischen Bedingungen, wie der Luftfeuchtigkeit oder der Stärke der mittleren Advektion, abhängig. Vorallem für die bevorzugte Ablagerung von Schnee, ist die Ausprägung des leeseitigen Strömungsfeldes von Wichtigkeit. Dies zeigen wir anhand von Doppler wind Lidar Messungen des Strömungsfeldes im Lee des Sattelhornes im Dischma-Tal (Davos, CH) und mit Strömungsfeldsimulationen mit einer Auflösung von 25 m mit dem Modell “Advanced Regional Prediction System” (ARPS). Dazugehörige Schneeablagerungsmessungen mit einem terrestrischen Laserscanner, bestätigen, dass die Schneeverteilung in sehr steilem Gelände stark durch Schneenumverteilung bestimmt ist. Dennoch können wir eine gewisse Übereinstimmung der simulierten Niederschlagsverteilung zu photogrammetrisch bestimmten Schneehöhenänderungen aufzeigen.

Insgesamt können wir die Nützlichkeit und Notwendigkeit von hochaufgelösten Schneemessungen und Simulationen demonstrieren. Ausserdem tragen wir zum Verständnis von kleinräumiger Schneeverteilungsvariabilität in alpinem Gelände bei.

Schlüsselwörter

Gelände-Strömung-Niederschlagswechselwirkungen • Schneefall- und Schneeablagerungsverteilung • Leeseitiges Strömungsfeld • Bevorzugte Ablagerung • Wolkendynamik • Räumliche Variabilität • Fernerkundung • Hochaufgelöste numerische Simulationen

Contents

Acknowledgments	i
Abstract	iii
Zusammenfassung	v
Nomenclature	xiii
1 Introduction	1
1.1 Motivation	2
1.2 Solid precipitation and snow accumulation in complex terrain	2
1.3 Numerical modeling of the atmosphere and snow processes	6
1.4 High-resolution remote sensing measurements	10
1.5 Objectives	14
2 A Close-Ridge Small-Scale Atmospheric Flow Field and its Influence on Snow Accumulation	15
2.1 Introduction	16
2.2 Data and Methods	17
2.3 Results and Discussion	22
2.4 Conclusion and Outlook	32
3 Spatial variability of snow precipitation and accumulation in COSMO–WRF simulations and radar estimations over complex terrain	35
3.1 Introduction	36
3.2 Data and Methods	38
3.3 Results and Discussion	43
3.4 Conclusions and Outlook	54
4 The importance of near-surface winter precipitation processes in complex alpine terrain	57
4.1 Introduction	58
4.2 Data and Methods	59
4.3 Results and Discussion	64
4.4 Conclusion and Outlook	73
5 Conclusions and outlook	75
5.1 Conclusions	75
5.2 Outlook	78

A	Supplementary Information for “A Close-Ridge Small-Scale Atmospheric Flow Field and its Influence on Snow Accumulation”	83
A.1	Meteorological stations	83
A.2	VAD-retrieved wind field and Backscatter	84
A.3	TLS measurement and post-processing	84
A.4	Technical information about ARPS and Alpine3D simulations	84
A.5	Alpine3D input	84
A.6	Flow conditions in the ARPS simulations	86
A.7	Alpine3D snow accumulation	86
B	Supplementary Information for “Spatial variability of snow precipitation and accumulation in COSMO–WRF simulations and radar estimations over complex terrain”	91
B.1	Morrison microphysics in WRF	91
B.2	Variability at the local domain	92
C	Supplementary Information for “The importance of near-surface winter precipitation processes in complex alpine terrain”	95
C.1	Model level dependency and precipitation growth	95
C.2	Stability analysis	95
D	Running COSMO-WRF on very high resolution over complex terrain	99
D.1	Introduction	99
D.2	Meteorological data	100
D.3	Geographical/static data	102
D.4	Installation of WRF and WPS	106
D.5	Running WPS	108
D.6	Running WRF	111
D.7	Post processing	115
D.8	Requirements	117
D.9	Vtable for COSMO-2 data	119
D.10	namelist.wps	120
D.11	namelist.input	121
	Bibliography	125
	Glossary	141
	Curriculum Vitae	143

List of Figures

1.1	Schematics of orographic precipitation processes	4
1.2	Remote sensing measurement devices	12
2.1	Field site in the upper Dischma valley, Davos, Switzerland	18
2.2	Overview of meteorological conditions and snow depth measurements	19
2.3	Hourly mean plane position indicator (PPI) radial velocity fields	24
2.4	Hourly mean range height indicator (RHI) radial velocity fields	25
2.5	Horizontal extent and temporal evolution of the eddy-like structure	26
2.6	Advanced Regional Prediction System (ARPS) flow fields over the Sattelhorn	27
2.7	Flow field classification and cross sections	28
2.8	Snow depth changes – TLS measurements versus Alpine3D simulations	30
3.1	Overview over the study area and the simulation domains	39
3.2	Station comparison for WRF simulations – Station <i>Dischma Moraine</i>	44
3.3	Station comparison for WRF simulations – Station <i>FLU2</i>	45
3.4	Snow precipitation maps for radar estimates and WRF simulations	47
3.5	Domain-wide 24 h precipitation statistics - 450 m	48
3.6	Normalized variograms of detrended snow precipitation – Radar versus WRF (450 m) . .	51
3.7	Normalized log-log variograms of snow precipitation – Radar versus WRF (450 m) . . .	52
3.8	Spatial 2D-autocorrelation maps	54
3.9	Normalized variograms of detrended snow precipitation – Resolution comparison	55
4.1	Overview of the study area, cross-sections and simulation domains	60
4.2	Illustration of precipitation processes	63
4.3	Cross-sections across Bocktenhorn for model resolution comparison	66
4.4	Cross-sections for the precipitation event on 31 January 2016	67
4.5	Cross-sections for the precipitation event on 5 March 2016	68
4.6	COSMO–WRF precipitation patterns vs. airborne photogrammetric snow depth changes	72
A.1	Lidar backscatter and vertical profile of horizontal wind – 28 October 2015	87
A.2	Lidar backscatter and vertical profile of horizontal wind – 29 October 2015	88
A.3	Snow depth changes – TLS measurements versus Alpine3D simulations (incl. snow drift)	89
B.1	Domain-wide 24 h precipitation statistics - 300 m	92
B.2	Normalized variograms of detrended snow precipitation – Radar versus WRF (300 m) . .	93
B.3	Normalized log-log variograms of snow precipitation – Radar versus WRF (300 m) . . .	93
C.1	Level dependency of snow precipitation – 31 January 2016	96
C.2	Level dependency of snow precipitation – 5 March 2016	97
C.3	Time-cross-section diagrams for 31 January 2016	98
C.4	Time-cross section diagrams for 5 March 2016	98
D.1	Illustration of boundary smoothing	104

List of Tables

2.1	ARPS simulation characteristics	21
3.1	Simulation setup COSMO–WRF	40
3.2	Large-scale linear trends of entirely-filtered radar and WRF precipitation patterns – regional domain	50
4.1	Characteristics of the wind conditions and peak snow precipitation distances	62
A.1	Overview over the meteorological stations	83
A.2	Technical details about the initial conditions in the ARPS simulations	85
A.3	ARPS wind fields used as input for Alpine3D	85
B.1	Large-scale linear trends of entirely-filtered radar and WRF precipitation patterns – local domain	93
C.1	Cross-section mean precipitation rate change – 31 January 2016	96
C.2	Cross-section mean precipitation rate change – 5 March 2016	97
D.1	Transformation of soil levels from COSMO to WRF	102
D.2	Description and suggestions for WRF pre-processing options	109
D.3	Constants for precipitation rate calculation	116

Nomenclature

Abbreviations

1D	one-dimensional
2D	two-dimensional
3D	three-dimensional
Alpine3D	Alpine surface processes model
ALS	Airborne laser scan
AO	Arctic Oscillation
ARPS	Advanced Regional Prediction System
COSMO	Consortium for Small-Scale Modeling
COSMO-2	COSMO simulations with a resolution of 2.2 km
COSMO-WRF	WRF simulations (see: WRF) driven by boundary conditions from COSMO
d01-d04	Nested simulation domains in COSMO-WRF
DAV2	Automatic weather measurement station near Davos
Dischma Moraine	Automatic weather measurement station near Davos
Dischma Ridge	Automatic weather measurement station near Davos
DISCHMEX	Dischma Experiment
DNS	Direct numerical simulations
ENSO	El Niño/Southern Oscillation
FLU2	Automatic weather measurement station near Davos
IBM	Immersed Boundary Method
ICAR	Intermediate Complexity Atmospheric Research Model
IMIS	Intercantonal Measurement and Information System
IQR	Interquartile range
LES	Large eddy simulation
lidar	Doppler wind Light Detection and Ranging
m ag	meter above ground
m asl	meter above sea level
Meso-NH	Mesoscale non-hydrostatic model
MeteoSwiss	Swiss Federal office of Meteorology and Climatology
METI	Ministry of Economy, Trade, and Industry
NAO	North-Atlantic Oscillation

NASA	National Aeronautics and Space Administration
Noah-MP	Noah land surface model with multi-parameterization options
PBL	Planetary boundary layer
PPI	Plane position indicator
radar	Radio Detection And Ranging
RANS	Reynolds-Averaged Navier-Stokes equations
RHI	Range height indicator
RWS	Ridge wind speed
SWE	Snow water equivalent
TLS	Terrestrial laser scan
USGS	United States Geological Survey
UTC	Coordinated Universal Time
VAD	Velocity azimuth display
VPR	Vertical Profile of Reflectivity
WD	Wind direction
WFJ2	Automatic weather measurement station near Davos
WRF-LES	The WRF model (see: WRF) in LES mode
WRF	Weather Research and Forecasting model
YSU PBL	Yonsei University PBL parameterization

Symbols and Definitions

N	Brunt-Väisälä frequency
N_{stat}	Brunt-Väisälä frequency based on station measurements
Nh_m/U	Froude Number
I_d/h_m	slope characteristic
h_m	maximum height of the obstacle
I_d	downstream half length of the obstacle
U	wind speed
Z	radar reflectivity
S	snow water equivalent estimate of precipitation from radar data
γ	semivariance
α_i, β_i and l_i	slope, intercept, and scale breaks of the log-linear models
r	Pearson's correlation coefficient
dt	time step

Introduction

Snow is an important source of water. In some regions of the world such as the Alps, the Californian Sierra Nevada or the Atlas mountains, it even is the predominant source of fresh water. Snow provides drinking water and is essential for hydro-power and winter tourism (Schmucki et al., 2017). On the other hand, it poses a risk in form of avalanches or flood events during spring melt. Furthermore, snow distribution has an influence on the local alpine ecology (Wipf et al., 2009) and on permafrost (Haberkorn et al., 2015). To efficiently manage snow water resources as well as for avalanche warning knowledge about the seasonal snow cover and its spatial distribution are crucial. Therefore, it is of paramount importance to investigate processes shaping the snow cover, especially in a changing climate (Bavay et al., 2009, Section 1.1). Furthermore, knowledge about snow distribution is important to validate the precipitation estimate of operational weather forecasts and to improve the understanding of the feedback of snow to the atmosphere.

The spatial distribution of snow is modulated on many different levels – from initial precipitation formation by ice nucleation in clouds down to the redistribution of snow by wind and avalanches. On large scales, synoptic weather systems determine the development of precipitation events. Especially in complex terrain many additional processes act on the snow distribution, such as cloud dynamics, which may regionally or locally enhance precipitation, and pre- and post-depositional particle-flow interactions (i.e. the influence of the local flow field on the pathways of snow particles and the particle distribution in the air), which lead to strong local differences in snow accumulation in the vicinity of mountain ridges. On small scales (10's of meters) and on large scales (several 10's of kilometers) the processes of precipitation formation and snow redistribution are relatively well known. On intermediate scales (few hundred meters to few kilometers), however, the proposed processes are still under debate and their relative importance is hardly known (Section 1.2).

To improve the knowledge about the processes acting at a mountain-ridge to mountain-valley scale and to assess their relative importance, very high-resolution models are needed (Section 1.3). To investigate and verify processes in reality and to validate models, high-resolution measurements of snow precipitation, snow accumulation and wind fields are essential (Section 1.4). Both, very high-resolution modeling and retrieving spatial high-resolution measurements of flow fields, snow precipitation and snow accumulation, is challenging given the chaotic behavior of the atmosphere. Recent improvements in computing resources as well as in measurement techniques, however, make it possible to perform very high-resolution atmospheric simulations and to take spatial high-resolution measurements of flow fields, snow precipitation and snow accumulation.

1.1 Motivation

Snow distribution in alpine catchments has manifold impact on human life. As a freshwater resource snow contributes to the most essential livelihood of humankind. In addition, it is an important resource of energy in the form of hydropower and the basis of winter tourism. Especially in complex alpine terrain, the spatial snow distribution determines the river catchment runoff. Runoff rates are strongly enhanced by snow melt during spring (López-Moreno and García-Ruiz, 2004) and particularly during rain-on-snow events, which may even lead to flash floods (McCabe et al., 2007; Freudiger et al., 2014). Elevation and terrain aspect and there respective snow loading were found to have a strong influence on the runoff contribution (Garvelmann et al., 2015). Therefore, knowledge about the spatial snow distribution is relevant for runoff estimates and flood prevention. Except from floods snow is a danger in form of avalanches, which are e.g. dependent on snow amounts or drifting and blowing snow (e.g. Schweizer et al., 2003).

Given its sensitivity to temperature, the availability of snow is strongly affected by climate change. Since the end of the 19th century, the sustained emission of greenhouse gases resulted in an increase of global temperatures of about 1 °C. The alpine regions form no exception: temperature even rose by about 2 °C between the end of the 19th century and the end of the 20th century (Gobiet et al., 2014). Despite this warming tendency, several exceptionally cold winters were recorded in Europe at the beginning of the 21st century. Beside atmospheric modes, such as the North-Atlantic Oscillation (NAO) or the Arctic Oscillation (AO), different reasons causing circulation changes, which lead to these cold winters are discussed (e.g. Croci-Maspoli and Davies, 2009; Petoukhov and Semenov, 2010; Gerber et al., 2014). Nevertheless, temperature projections are quite consistent between different models, and rising temperatures are expected to result in a shortening of the snow cover duration (Brown and Mote, 2009) and hence a shift to earlier peak river runoff in spring (Nohara et al., 2006).

However, temperature evolution is only one aspect influencing snow water resources. Especially in mountain regions interactions between changes in temperature and precipitation are expected to influence the snow cover duration and accumulation rates (Brown and Mote, 2009). Precipitation projections, however, were for a long time rather uncertain (e.g. Barnett et al., 2005). For Europe, models suggest an increase of precipitation in the North and a decrease in the South (Hartmann et al., 2013; Gobiet et al., 2014). Based on a recent study by Frei et al. (2018) snow precipitation in the Alps was found to be significantly decreasing, with a robust signal among different models. However, a strong elevation dependency is found with even a slight increase in snow precipitation at highest levels, most likely due to a shift of the temperature regime, which allows for stronger snowfall events (Frei et al., 2018).

Perennial snow and glaciers are very sensitive to changes in temperature and are known to be good climate indicators (Vaughan et al., 2013), confirming the increasing temperatures. Seasonal snow, however, shows a much stronger temporal variability and changes may strongly be affected by inter-annual phenomena such as the El Niño/Southern Oscillation (ENSO), the NAO and other phenomena such as persistent blocking systems, which were found to potentially have impacts on precipitation from seasonal to decadal variations (Beniston, 2003). A climate-induced shift in atmospheric patterns might therefore strongly affect seasonal snow amounts. The climate-driven glacier retreat makes seasonal snow water resources even more important in future. Furthermore, changes in snow distribution affect river runoff and may cause changes in permafrost, which may potentially lead to rock fall (Haberkorn et al., 2015). Improved understanding about processes driving snow distribution patterns on a mountain-ridge to mountain-valley scale and the ability to model them, is thus crucial for future prediction of water resources and natural hazard management, especially in a changing climate.

1.2 Solid precipitation and snow accumulation in complex terrain

Snow accumulation patterns are determined by many processes – from ice nucleation in clouds down to post-depositional snow redistribution by wind and avalanches. In complex terrain precipitation production and deposition are additionally altered by the interaction of atmospheric flow and topography.

1.2.1 Microphysical processes

Solid precipitation is formed by microphysical processes at subzero temperatures. To initiate the formation of solid precipitation, ice nucleation is needed. This either happens by homogeneous freezing at $<-40^{\circ}\text{C}$ or at higher temperatures by heterogeneous freezing at ice nuclei (Stoelinga et al., 2013). Once ice crystals are initiated, many processes can contribute to precipitation growth. Ice particles may grow by deposition from the gas phase. This process is especially efficient if the air is supersaturated with respect to ice but undersaturated with respect to liquid water, allowing for growth of ice particles on the expense of cloud droplets (e.g. Korolev, 2007), the so called (Wegener-)Bergeron-Findeisen process. Further microphysical processes are aggregation, the collection of falling solid particles, and riming, the collection of supercooled droplets onto falling ice particles (Stoelinga et al., 2013). Riming at snowflakes leads to rimed snow particles or even graupel-like particles. Pure graupel particles, however, are usually formed by riming at an initial ice kernel (Reinking, 1975). In addition to these processes of precipitation growth, there are few mechanisms, which may lead to the multiplication of ice precipitation particles. Rime-splintering and droplet shattering are processes where liquid droplets freeze from the outside and explode when the built-up pressure in the particle becomes too large (Hallet and Mossop, 1974; Hobbs and Alkezweeny, 1968). Fragmentation can occur when fragile ice particles collide and break up into several parts (Brewer and Palmer, 1949). In orographic precipitation events with intermediate upward motion in winter, vapor is approximately equally lost to deposition and growth of cloud droplets, which can then be collected by falling ice particles. Thus, these precipitation growth processes were found to be equally important for winter orographic precipitation (Stoelinga et al., 2013).

1.2.2 Pre-depositional terrain-flow-precipitation interactions

Large-scale orographic enhancement Mountain ranges generally lead to an increase in precipitation. There are several factors that determine strength and efficiency of this “large-scale orographic enhancement”. For a simple terrain-flow interaction on a mountain-range scale, the flow is forced over the mountain range, air masses cool as they are lifted and consequently water vapor condensates (Figure 1.1a). Falling ice particles therefore additionally grow by riming or deposition due to a region enriched with cloud liquid water on the windward side of the mountain range (e.g. Bader and Roach, 1977; Smith, 1979; Stoelinga et al., 2013). The strength and efficiency of this mechanism depend on the inflow speed, mountain-range width and height. Precipitation increases about linearly with mountain height (Colle, 2004), while the mountain width may shift microphysical processes toward more (less) vigorous condensation and therefore riming (deposition) dominated precipitation for narrower (wider) barriers (Choularton and Perry, 1986; Colle and Zeng, 2004). The strength of the advection, determines the amount of precipitation that is transported over the barrier and is depleted by sublimation or evaporation due to descending air flow on the leeward side of the barrier (Sinclair et al., 1997; Colle, 2004; Roe and Baker, 2006). This effect is stronger for narrower barriers. When air is blocked on the windward side of the barrier, an effective widening of the barrier may occur leading to enhanced precipitation further upstream on the windward side of the barrier, as particles have more time to develop (e.g. Peterson et al., 1991; Doyle, 1997; Sinclair et al., 1997; Houze et al., 2001; Colle, 2004; Colle et al., 2005).

While processes described above explain the influence of pure terrain-flow interactions on precipitation formation for flow over a mountain range, especially in winter months this flow usually goes along with a baroclinic atmosphere or a frontal system, with an associated (non-orographic) large-scale atmospheric circulation (Stoelinga et al., 2013). When a dynamically-induced atmospheric system passes over an orographic barrier the two systems likely interact. Precipitation particles from high-level “seeder” clouds, which develop by the dynamic large-scale circulation may fall through low-level orographically-induced “feeder” clouds. By collecting cloud condensate of the “feeder” cloud they can effectively grow and thereby produce enhanced precipitation. This process was first proposed by Bergeron (1965), who called it seeder-feeder mechanism.

Small-scale orographic enhancement The seeder-feeder mechanism may act on different scales. It was previously reported for small mountain ranges on a regional scale (e.g. Purdy et al., 2005) but also

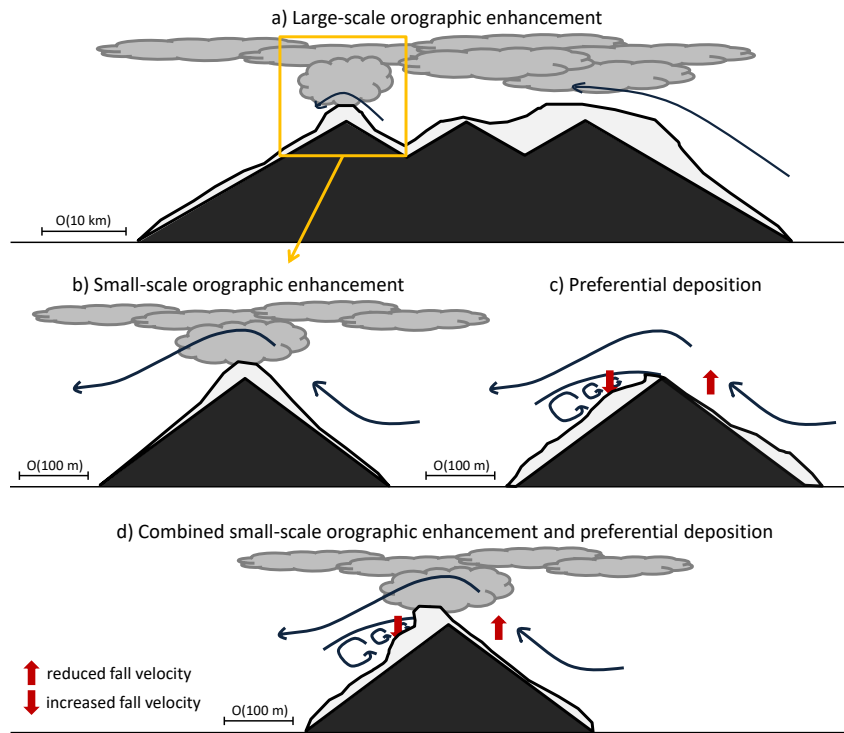


Figure 1.1: Schematics of orographic precipitation processes which are most relevant for this thesis. a) Large-scale orographic enhancement, b) small-scale orographic enhancement (e.g. seeder-feeder mechanism), c) preferential deposition and d) the expected effect of combined small-scale orographic enhancement and preferential deposition.

at a mountain-ridge scale (e.g. Dore et al., 1992; Mott et al., 2014). Hence, the driving mechanism of small-scale orographic enhancement is the same as for large-scale orographic enhancement (i.e. lifting condensation) but refers to its local occurrence. While large-scale orographic enhancement leads to enhanced snow accumulation at the windward side of a mountain range and reduced precipitation on the leeward side due to drying of the atmosphere (Stoelinga et al., 2013; Houze, 2012), enhanced precipitation due to orographic precipitation enhancement on a mountain-ridge scale by a low-level cloud is mainly expected over the mountain peak (e.g. Hill et al., 1981, Figure 1.1b). Furthermore, it can be modulated by advection, which may even reverse the pattern of the large-scale orographic enhancement, leading to enhanced precipitation downwind of the ridge, as the downwind transport of precipitation may be more efficient than the sublimation of precipitation on the leeward side (Zängl, 2008; Mott et al., 2014).

Preferential deposition Particle-flow interactions may further strengthen the pattern of enhanced snow accumulation on the leeward side of the ridge by the process of preferential deposition (Lehning et al., 2008, Figure 1.1c). Snow accumulation on the windward side of the ridge may be reduced due to updrafts interacting with the terminal fall velocity of snow particles, resulting in an enhanced transport of particles over the ridge to the leeward side, where they will be preferentially deposited in the area of flow separation. Small-scale flow blocking on the windward side of the ridge (Carruthers and Hunt, 1990) or post-depositional snow transport (Mott and Lehning, 2010, Section 1.2.3) may be a reason for considerable snow accumulation upstream of the ridge (Lehning and Mott, 2016). Different studies found evidence for enhanced snow loading of leeward slopes likely due to preferential deposition both in model simulations and measurements (Lehning et al., 2008; Dadic et al., 2010b; Mott et al., 2010; Mott and Lehning, 2010; Mott et al., 2011).

1.2.3 Post-depositional processes

The final snow distribution is strongly dependent on post-depositional processes and is subject to continuous changes. On the one hand, snow may be redistributed by avalanches (e.g. Bernhardt and Schulz, 2010). On the other hand, wind-induced snow redistribution strongly affects the snow cover (e.g. Mott et al., 2010). The efficiency of snow redistribution by wind is strongly dependent on the type of snow and wind speeds (Doorschot et al., 2004). There are different mechanisms of wind redistribution. Creeping particles are particles rolling on the ground. Saltation describes the process of particles travelling on ballistic paths. When hitting the ground they may rebound or eject other particles. Finally, suspension describes particles that are fully decoupled from the ground.

Wind redistribution of snow has a strong influence on snow accumulation patterns (e.g. Scipi3n et al., 2013; Vionnet et al., 2017). In addition to its influence on snow distribution, blowing snow sublimation may locally reduce deposited snow mass (Bernhardt et al., 2012; Groot Zwaaftink et al., 2013; Vionnet et al., 2014). The estimated amount of blowing snow sublimation strongly varies between case studies and is dependent on the meteorological conditions, grid resolution and the modeling approach (MacDonald et al., 2010; Vionnet et al., 2014). Vionnet et al. (2014) report a reduction of snow mass by 5.3 % for a single blowing snow event, while estimates of up to 17 % to 19 % were presented for a crest in the Canadian Rocky mountains (MacDonald et al., 2010). However, for the Alps the effect of blowing snow during a whole winter season was shown to be small but with strong spatial variability (Groot Zwaaftink et al., 2013).

1.2.4 Process interactions and snow accumulation

Measurement evidence The heterogeneity of snow accumulation has long been recognized and widely investigated (e.g. Bl3schl, 1999; Sturm and Benson, 2004). Snow accumulation variability has been linked to terrain factors based on point measurements of snow depth (e.g. Winstral and Marks, 2002) and by applying remote sensing techniques (e.g. Schirmer et al., 2011; Lehning et al., 2011; Deems et al., 2013, Section 1.4.3). However, snow distribution measurements always include the effect of both, pre-depositional precipitation processes (i.e. cloud dynamics and particle-flow interactions) and post-depositional snow redistribution. Based on radar precipitation measurements (Section 1.4.2) and airborne terrestrial laser scans (Section 1.4.3), Scipi3n et al. (2013) could show that the very small-scale variability of snow distribution is strongly dependent on post-depositional processes, stating that near-surface precipitation processes as well as snow redistribution strongly increase the spatial variability of snow accumulation patterns compared to snow precipitation patterns. The importance of near-surface processes for snow accumulation is confirmed by Mott et al. (2014) and Grazioli et al. (2015). However, especially in complex terrain, near-surface processes are difficult to measure, which makes it extremely challenging to address the importance of the different processes for snow distribution.

Modeling evidence To avoid measurement uncertainties and to retrieve a complete picture of processes, mountain-ridge scale snow precipitation and accumulation are often addressed based on numerical simulations. Different snow models have been developed to simulate snow accumulation and redistribution based on physical principles (e.g. Lehning et al., 2008; Vionnet et al., 2014). Physical model based studies confirm and highlight the strong influence of preferential deposition and post-depositional snow redistribution for snow accumulation variability (Mott et al., 2010; Vionnet et al., 2014). However, to capture important processes, very high-resolution simulations are needed. Mott and Lehning (2010) addressed the impact of the grid resolution in semi-idealized simulations and could show that the snow loading on the leeward side of a mountain ridge is fairly represented at horizontal model resolution of ≤ 50 m. However, windward slopes only gain a substantial amount of snow for simulations with resolutions as high as 5 m to 10 m. Beside the model resolution, models always go along with simplifications of physical processes (Section 1.3).

Given these simplifications, especially characteristics of preferential deposition are still strongly discussed. In a recent study, Wang and Huang (2017) hypothesize that the interaction of particles with the flow may change the flow field and thereby influence snow deposition patterns. Additionally, they claim that

stability and advection have a strong influence on preferential deposition, with a shift of peak accumulation from windward to leeward slopes with increasing strength of advection. In a systematic study based on an idealistic setup of large-eddy simulations (LESs) over a hill, Comola et al. (2018) hypothesize that preferential deposition depends on the flow regime, but also on the particle type with different behaviour for rounded and dendritic particles. They further show that the assumption of inertialess particles, which is made by most models, may give appropriate results for dendritic snow crystals. However, precipitation patterns for rounded particles strongly differ in their idealized simulations.

Model studies mentioned above, however, do not include the effect of precipitation dynamics but focus only on particle-flow interactions. In contrast a recent study by Vionnet et al. (2017) includes cloud-dynamical effects together with preferential deposition and post-depositional snow redistribution. In their model simulations spatial variability of precipitation, especially at high altitudes, is mainly determined by the formation of graupel. The importance of graupel and rimed particles was reported earlier and was found to be one of the most efficient processes of snowfall enhancement (Grazioli et al., 2015). It is often linked to strong updrafts and turbulence, which promote the occurrence of super-cooled cloud droplets (Grazioli et al., 2015). This is further consistent with results by Mott et al. (2014), who analyzed local radar measurements over a mountain peak, in which they found evidence for local precipitation enhancement, potentially due to a seeder-feeder effect. Temporal variation of the location of peak precipitation in their analysis was partly interpreted as a sign of preferential deposition.

Importance of processes On a mountain-range scale it is well known that snow accumulation is strongly affected by large-scale orographic enhancement introducing a large-scale gradient of enhanced snow accumulation on the windward side of the orographic barrier and reduced snow accumulation downstream due to drying of the atmosphere (e.g. Houze, 2012; Stoelinga et al., 2013). Compared to the effect of pre-depositional processes, drifting and blowing snow were found to produce much smaller scale structures such as cornices and dunes (e.g. Mott et al., 2010). Small-scale structures due to drifting and blowing snow are strongly affected by local topographic features and may change during the winter season due to changes in the surface topography by the snow cover (Mott et al., 2010; Schirmer et al., 2011). In a recent study, Vionnet et al. (2017) present, based on large-eddy simulations at 50 m horizontal resolution coupled to a snow model, that final snow accumulation patterns are even mainly determined by post-depositional snow redistribution. However, pre-depositional precipitation processes at a mountain-ridge scale were, so far, only discussed qualitatively (Mott et al., 2014). The relative importance of the different processes acting at a mountain-ridge scale (Figure 1.1) is still barely known (Mott et al., 2014; Vionnet et al., 2017). A quantification of these processes is challenging as small-scale orographic enhancement of precipitation and preferential deposition occur simultaneously at about the same scales.

1.3 Numerical modeling of the atmosphere and snow processes

Numeric weather prediction models are designed to simulate weather or climate either as forecast or reanalysis. They are widely used for weather predictions but also for climate projections as well as to understand atmospheric processes in the past, present and future. Numerical weather prediction models can be setup at many different resolutions from hundreds of kilometres down to a few meters. Depending on their purpose they can be run globally, regionally or locally. In a numeric weather prediction model the full set of equations describing atmospheric motions is solved. Given the non-linearity of these equations they have to be solved numerically, usually by the use of finite differences. Therefore, the atmosphere has to be divided into a 3-dimensional grid. Depending on the grid resolutions atmospheric models need to be supplemented with sub-grid scale parametrizations of processes such as e.g. radiation, cloud microphysics and dynamics, land-surface interactions and turbulence. Such models are e.g. the Advanced Regional Prediction System (ARPS, Xue et al., 2001), the Consortium for Small-Scale Modeling (COSMO) model (further developed from the Lokal Modell, Steppeler et al., 2003) or the mesoscale non-hydrostatic model (Meso-NH, Lafore et al., 1998). Another widely used atmospheric model is the Weather Research and Forecasting (WRF) model (Skamarock et al., 2008). To run atmospheric simulations at a regional scale, initial and boundary conditions need to be provided to the simulation. Usually initial and boundary

conditions for regional atmospheric simulations are taken from global or regional numerical simulations that cover a larger domain.

1.3.1 Precipitation processes in numerical simulations

Precipitation processes are very complex and happen on many different scales (Section 1.2). This makes it extremely difficult to properly parameterize them for an accurate representation in numerical models. Different approaches to parameterize microphysics have been developed. An explicit representation, describing the size distribution of precipitation particles based on a set of size bins for each hydrometeor species, is too computationally expensive for most applications (Stoelinga et al., 2013). However, bulk microphysics parameterizations are widely used. They describe each hydrometeor species based on their bulk properties using a distribution function. Most common forms of particle size distribution functions for solid precipitation are exponential or gamma distributions (Stoelinga et al., 2013). Generally, two types of bulk microphysics parameterizations are distinguished. One-moment schemes only predict the mixing ratio of hydrometeors, while prescribing the number concentration. On the other hand, two-moment schemes include prognostic equations for the mixing ratio and number concentration, allowing for a shift to either more small or large particles (Stoelinga et al., 2013). Snow was found to be well approximated by an exponential particle size distribution (Gunn and Marshall, 1958). Anyhow, evidence was found for size distributions towards even further enhanced appearance of small particles and less large particles (Field et al., 2005). Moreover, assumptions concerning the relationship between particle size and fall speed are required. Particle fall speed was found to be well represented by power-law functions. However, they show a strong dependence on the particle shape (Mitchell, 1996). The diversity of particle shapes is often disregarded in microphysics parameterizations, and particles are assumed to be spherical and described by a constant density. Additionally, most popular microphysics schemes do not distinguish more than five classes of precipitation particles, usually including rain, snow, graupel or hail, cloud ice and cloud droplets. Along with all above mentioned assumptions, ice initiation, particle growth and the transition between different species need to be described, introducing additional uncertainties. Moreover, effects of the interaction of precipitation with other processes, from simple advection (Hahn and Mass, 2009) to more complex interactions with turbulence in the planetary boundary layer (Jankov et al., 2007) or land-surface processes and radiation (Stoelinga et al., 2013), are not to be underestimated. Given the diverse nature of solid precipitation particles and the complex interactions with other processes, makes it exceedingly difficult to identify the reason for inaccurately simulated precipitation in numerical simulations.

1.3.2 High-resolution modeling of the atmosphere in complex terrain

Besides highly complex numerical weather prediction models, a wide range of modeling approaches has been proposed to downscale precipitation processes over complex terrain. Most simple models are based on a downscaling of variables of interest by making use of statistical approaches (Maurer et al., 2010; Bárdossy and Pegram, 2011; Stoner et al., 2012). More sophisticated models include physical principles such as the linear theory model to capture the effect of orographic precipitation enhancement (Smith and Barstad, 2004). Although still based on many assumptions, it has been shown to reasonably represent large-scale orographic precipitation enhancement over complex terrain (e.g. Roth et al., 2018). The Intermediate Complexity Atmospheric Research Model (ICAR), a recently developed model, which is based on mountain wave theory, shows a good agreement of precipitation patterns with respect to numerical weather prediction simulations (Gutmann et al., 2016). However, traditionally these models as well as mesoscale numerical weather prediction models are applied at resolutions ≥ 1 km. Yet, at this resolution topography and land characteristics are poorly resolved. Small mountain valleys and peaks may even be missing. Due to the missing resolution of static parameters and given the poor resolution of the grid, even in numerical weather prediction models numerous atmospheric processes cannot be resolved. Therefore, these processes still need to be parametrized. Parametrization of processes, however, always goes along with simplifications (Buzzi, 2008), which results in a loss of accuracy of the model output. To explicitly resolve terrain-flow interactions and snow precipitation processes at a mountain-ridge to mountain-valley scale very high-resolution models are needed. Thus, to include small-scale atmospheric

processes like lee-side flow separation, applying large-eddy simulations (LES) is a reasonable approach. However, numerical modeling of atmospheric processes in complex alpine terrain is challenging due to numerous reasons.

Large-eddy simulations Given the degree of resolved turbulence, simulations may be divided into three categories: direct numerical simulations (DNS), large-eddy simulations (LES) and simulations solving the Reynolds-Averaged Navier-Stokes equations (RANS, Zhong and Chow, 2013). In DNS the full spectrum of length scales, and thus all turbulent motions, are resolved, which implicates the need of extremely high resolutions in both, space and time. Thus, they are limited to very small domains given the high computational costs. On the other end of the spectrum, in RANS all the turbulent motions are averaged out. Vertical turbulent motions in the planetary boundary layer (PBL) are considered based on a PBL parameterization. In between, LES resolve large energy-containing eddies, while sub-grid scale turbulent motions are still parameterized (Lilly, 1962; Deardorff, 1970). The size of resolved eddies, depends on the resolution of the numerical simulation. Subgrid-scale turbulence is modeled by a turbulent closure, usually by the Smagorinsky scheme (Smagorinsky, 1963) or the 1.5-order turbulent kinetic energy closure (Deardorff, 1980; Moeng, 1984), which uses a prognostic equation for turbulent kinetic energy.

Challenges Going toward very high-resolution simulations allows to resolve additional processes, however, it also implies numerous challenges. To perform very high-resolution simulations the so called *terra incognita* or *gray zone* (Wyngaard, 2004) between mesoscale simulations, for which all boundary-layer processes need to be parametrized, and large-eddy simulations, where most large-scale eddies are resolved, needs to be bridged. Simulations with grid resolutions within the *terra incognita*, however, may lead to unrealistic flow characteristics and often suffer from numerical instabilities over steep slopes (e.g. Klemp et al., 2003). Although the representation of topography and land characteristics in very high-resolution simulations is improved, the availability of high-resolution static data becomes a limiting factor, especially in complex terrain, which is poorly sampled due to bad accessibility. The choice of the vertical coordinate becomes more challenging (although usually prescribed by the chosen model) in rough compared to flat terrain (Zhong and Chow, 2013). Pressure coordinates are intersecting with topography and do not allow to easily refine the vertical resolution close to the surface. Terrain-following (sigma) coordinates, on the other hand, enable to easily refine the lowest atmospheric levels. However, required coordinate transformations lead to numerical dispersion and instabilities (Lundquist et al., 2010). Especially, steep slopes in complex topography introduce problems when calculating the pressure gradient, as the height difference between neighboring grid points may be up to an order of magnitude larger than the vertical grid spacing (Doyle et al., 2013). Thus, too steep slopes in simulations using terrain-following coordinates are critical and should commonly be limited to maximum terrain slope angles of $\sim 30^\circ$ to 45° based on a rule of thumb by De Wekker (2002). In complex alpine terrain this is a strongly limiting factor. Slope, aspect and topographic shading further have a strong impact on radiation and need to be taken into account for simulations over complex terrain (Zhong and Chow, 2013). Moreover, turbulence closure becomes more challenging in complex terrain, as assumptions made by the traditional Smagorinsky and the 1.5-order turbulent kinetic energy closure may be no more valid (Weigel and Rotach, 2004; Mirocha et al., 2010). For example, advection of turbulent kinetic energy may become significant in complex terrain making the assumption of equal production and dissipation inappropriate (Lundquist and Chan, 2007). Besides, backward energy transport from small to large scales, so-called backscatter, becomes important in regions of strong shear, instabilities or close to solid boundaries (Mason and Thompson, 1992; Kosović, 1997). The difficulty to measure flow fields in mountainous terrain reduces the availability of good evidence to validate high-resolution simulations in complex terrain. Furthermore, high resolutions imply a high number of grid cells and require the use of a very small time step. This makes simulations extremely computationally demanding.

Recent improvement and applications Owing to improvements in computational capabilities, high-resolution simulations became more widely applicable in recent years. Challenges in LES simulations are actively investigated and many recent improvements were possible. More sophisticated turbulence closure

models are tested (e.g. Mirocha et al., 2010; Mirocha et al., 2014). Further improvement to achieve an adequate representation of turbulence has been made by applying perturbations to the input flow (Faure, 2008; Mirocha et al., 2014; Muñoz-Esparza et al., 2017). Promising results could also be achieved by applying the immersed boundary method (as proposed by Peskin, 1972), which allows to represent the atmosphere in Cartesian coordinates, to avoid coordinate transformations (e.g. Lundquist et al., 2010; Lundquist et al., 2012; Ma and Liu, 2017). Nesting of simulations from mesoscale down to microscale (LES) simulation has been widely investigated and step-wise refinement of the resolution was found to be beneficial (e.g. Talbot et al., 2012; Mirocha et al., 2014; Mazzaro et al., 2017). Moreover, it could be shown that LES simulations being fed with unrealistic input from a parent domain with grid resolution in the *terra incognita* may recover given an appropriate fetch distance (Mazzaro et al., 2017). To allow for additional refinement of the turbulent flow near the surface in nested LES domains but to avoid large grid aspect ratios in the parent domain, vertical nesting was implemented in the WRF model (Daniels et al., 2016). Most of these studies are, however, still based on either idealistic simulations or over moderate and simple topography. Nevertheless, LES have been successfully applied to simulate atmospheric processes over complex terrain for quite some time. Semi-idealized very high-resolution simulations of wind fields were extensively used to analyze flow fields over complex terrain (Raderschall et al., 2008; Mott et al., 2010; Mott et al., 2014). Mott et al. (2010) use Advanced Regional Prediction System (ARPS) simulations to downscale the flow field over complex terrain to extremely high resolutions (up to 5 m horizontal grid spacing) based on a semi-idealized approach with constant atmospheric boundary conditions but real terrain. Semi-idealized simulations with constant atmospheric conditions over complex terrain have the advantage that they may be run for a very short time period, preferably until they reach an equilibrium. This offers a possibility for very high-resolution simulations on relatively low computational cost and numerical instabilities, which may likely occur for very high resolutions do not harm these simulations if they occur after the onset of an equilibrium. Real-case simulations were applied to address boundary layer flow over complex terrain (e.g. Chen et al., 2004; Chow et al., 2006; Weigel et al., 2006) or to investigate cloud seeding (Xue et al., 2013; Chu et al., 2014). A recent study has also investigated winter precipitation over complex topography (Vionnet et al., 2017).

1.3.3 Modeling alpine surface processes

To address the effect of terrain-flow-precipitation interactions on the snow distribution on the ground, a link between the atmosphere and the snow cover is needed. Current atmospheric models, however, have a quite simple snow model and e.g. do not include post-depositional snow redistribution. Thus, more specific snow models are needed to link the atmospheric flow field to snow deposition on the ground.

Model approaches Snow models, which physically describe the energy balance of snow, have originally been developed for avalanche warning (e.g. Lehning et al., 1999; Vionnet et al., 2012). While still mainly used for avalanche warning, they have been applied to other fields such as e.g. to assess climate change (Bavay et al., 2009). Augmenting a one-dimensional snow model with an atmospheric forcing, lateral transport and a radiation scheme, allows to simulate snow processes at each grid point over a certain area (e.g. Lehning et al., 2006).

To consider the effect of drifting and blowing snow, snow models need to be augmented with a wind field and a snow transport module including the processes of saltation, suspension and preferential deposition. For both components – input flow and the description of snow transport – a wide variety of approaches has been proposed (e.g. Nemoto and Nishimura, 2004; Liston et al., 2007; Lehning et al., 2008; Schneiderbauer and Prokop, 2011). Descriptions of saltation ranges from semi-empirical relationships and local momentum balance models to Lagrangian approaches. While simpler models neglect the advection effect of suspension, more sophisticated approaches solve transport equations including the effect of turbulence. However, retrieving appropriate wind fields to drive these models is a big challenge. A simple extrapolation from station measurements is often inappropriate in complex terrain (Bernhardt et al., 2009). Thus, computational fluid dynamics (e.g. Gauer, 2001; Schneiderbauer and Prokop, 2011) or large-eddy simulations from numerical weather models have been applied (e.g. Raderschall et al., 2008; Lehning et al., 2008; Bernhardt et al., 2009; Mott et al., 2010; Vionnet et al., 2014).

It has been shown, that the small-scale flow field and turbulence are very important for snow drift patterns (Mott and Lehning, 2010). Thus, to address small-scale snow drift patterns in complex terrain, it is essential to drive the surface processes model with high-resolution atmospheric simulations. One approach is to generate a set of flow fields based on LESs using semi-idealized very high-resolution simulations (Section 1.3). To drive the alpine surface processes model for each initialization time step the most appropriate flow field may then be chosen (e.g. Alpine3D, Raderschall et al., 2008; Lehning et al., 2008; Mott et al., 2014). This setup has been successfully applied to evaluate flow fields and investigate corresponding preferential deposition as well as snow distribution patterns due to post-depositional processes (Mott et al., 2010, Section 1.2.4). Very high-resolution simulations with a horizontal grid spacing of 5 m may be achieved (Mott et al., 2010). Another approach is to couple a snow model to an atmospheric model, which is run in LES mode by introducing transport equations for snow (Meso-NH/Crocus, Vionnet et al., 2014; Vionnet et al., 2017).

Terrain-flow-precipitation interactions in numerical models So far, dynamical precipitation processes and particle-flow interactions are mainly addressed separately. Knowledge about particle-flow interactions is widely based on idealized or semi-idealized numerical simulations and uncoupled snow distribution modeling (e.g. Mott et al., 2010; Mott et al., 2014; Wang and Huang, 2017; Comola et al., 2018). Only recently, Vionnet et al. (2014) and Vionnet et al. (2017) run a coupled atmosphere-snow model, using constant snowfall or real conditions, respectively (Section 1.2.4). Advantages of a fully coupled atmosphere-snow model are that it may be run based on real-case mesoscale boundary conditions, which are downscaled using a nesting approach (Vionnet et al., 2014) and the possibility to address the relative importance of snow drift and precipitation processes. However, these advantages go along with a lower model resolution given the high computational costs. To the best of the knowledge of the author, real-case high-resolution LESs over complex terrain investigating terrain-flow-precipitation interactions and snow accumulation patterns are still rare. Thus, to gain a better understanding of precipitation processes and to include the influence of a highly variable atmosphere, there is a need for real-case high-resolution simulations and corresponding field measurements.

1.4 High-resolution remote sensing measurements

Although today's numerical models are sophisticated and able to reproduce atmospheric phenomena quite accurately, measurements are still highly important. On the one hand, high-resolution measurements are required to validate high-resolution numerical simulations. On the other hand, measurements may add to process understanding. Given the chaotic behavior of the atmosphere, measuring atmospheric phenomena is challenging. As for numerical models the measured properties always depend on the resolution of the measurements, both in time and space and will never be able to capture the full variability. While for a long time measurements of wind, precipitation and the snow cover were mainly based on point measurements the introduction of remote sensing techniques brought the possibility to achieve spatial measurements.

Principle of remote sensing This introduction to the principle of remote sensing techniques of the atmosphere is based on Banta et al. (2013). Details about different instruments will be given in the respective sections. Remote sensing techniques introduced in this study are all based on active sensors, i.e. instruments, which are sending out an electromagnetic wave and record the return signal. When using a *pulsed* signal the distance of the back-scattering target is a function of the travel time of the signal. The signal may be split into different *range gates* by recording it in discrete time intervals, determining the resolution of the sampling volume in the beam direction. The sampling resolution in the azimuth is determined by the beam width and increases with distance from the instrument. Atmospheric targets are ranging from hail, rain and solid precipitation particles over cloud droplets to aerosols and molecules. The wavelength of the instrument has to be chosen such that the targets are backscattering the signal in the Rayleigh regime, i.e. the wavelength needs to be larger than the targets. As longer wave lengths go along with a stronger signal the maximum range of measurements decreases with decreasing wavelength. The signal emitted is strongly dependent on the characteristics of the antenna. There are two main antenna

characteristics, the antenna *gain* and the *side lobes*. The *gain* determines how well the signal may be bundled. For a well bundled signal the *main lobe* is narrower pointing into the main beam direction. The *side lobes* refer to the portion of the signal, which is emitted in different directions than the main beam direction. All these characteristics of the emitted signal are important to interpret the signal.

1.4.1 Spatial and high-resolution wind measurements

The wind field in complex terrain strongly influences processes of precipitation generation as well as pre- and post-depositional processes forming the final snow cover (Section 1.2.2). To understand the complex nature of flow fields, high-resolution spatial wind measurements are essential.

Commonly, wind speed and direction are measured by meteorological stations at an elevation of 10 m above ground. High-frequency turbulence measurements may be achieved by sonic anemometers. They are based on the travel time of sound waves between three transmitters and receivers. They are widely applied to characterize the turbulent behavior of the atmospheric boundary layer and are applied, e.g. to study the threshold of blowing snow (Doorschot et al., 2004) or to address the sensible heat flux over snow covered terrain (Schlögl et al., 2017). However, these measurements are restricted to point measurements.

To achieve information about the 3-dimensional flow field Doppler wind light detection and ranging (lidar, Figure 1.2a) measurements may be used. As given by their name (“light”), they operate at wave lengths in the visible and infrared between about 500 nm and 10 μ m detecting molecules and/or aerosols (Banta et al., 2013). Doppler wind lidar measurements are based on the principle of a frequency shift of an emitted laser beam when interacting with moving aerosols or molecules (Werner, 2005). Based on the Doppler principle, the velocity in beam direction may be determined, which is also referred to as radial velocity. The only requirement for successful velocity measurements using the Doppler principle is a strong enough signal allowing to estimate the frequency shift (Banta et al., 2013). Doppler wind lidars have three different modes of operation. Velocity azimuth display (VAD) scans may be used to retrieve three dimensional wind vectors in the vertical above the lidar (Werner, 2005). This is based on a conical scan in clock-wise direction from North. Additionally, scans in vertical slices, which are also known as range height indicator (RHI) scans and in horizontal cones, known as plane position indicator (PPI) scans may be achieved by Doppler wind lidars. For PPI and RHI, the flow field in the direction of the beam (i.e. radial velocity) can be determined, and allows to obtain 2-dimensional flow patterns. Algorithms to determine the 3-dimensional wind components from one Doppler wind lidar are available (e.g. Choukulkar et al., 2012). However, given the complex wind fields and clutter due to the surrounding topography, they cannot be easily applied in complex terrain. Therefore, the installation of at least two Doppler wind lidars would be necessary to retrieve the wind components (Hill et al., 2010). Power supply needed to run a Doppler wind lidar, however, is strongly restricting the installation of devices in remote regions.

1.4.2 High-resolution precipitation measurements

The Radio Detection And Ranging (Radar) technology was originally developed for military purposes and development started before the second world war. However, weather radar technology established quickly after and has undergone strong development since (Banta et al., 2013). It is widely applied for precipitation forecasting as well as for research. Radar technology is based on the emission and reception of electromagnetic waves in the frequency range of radio waves. Typical wave lengths for radar operation are between 1 mm and 100 m, with wave lengths of ~ 10 cm being best suited for hydrometeors (Banta et al., 2013).

Weather radars operating at different wavelengths and frequencies are classified by letters. X-band and C-band radars are operating at wave length of 2.5 cm to 4 cm and 4 cm to 8 cm, respectively (Graf et al., 2013). Compared to S-band radars, which operate at wave length of 8 cm to 15 cm, X- and C-band radars have the advantage that they need smaller antennas but are still able to operate with a reasonable narrow beam and lower *side lobes* (Germann et al., 2015). Compared to X-band radars C-band radars may detect particles up to larger sizes. All this makes them well suited for the operation in complex terrain. X-band radars, on the other hand, given the even shorter wavelengths, may operate with yet smaller antennas and hence are cheaper and prone to the use for non-stationary field experiments.

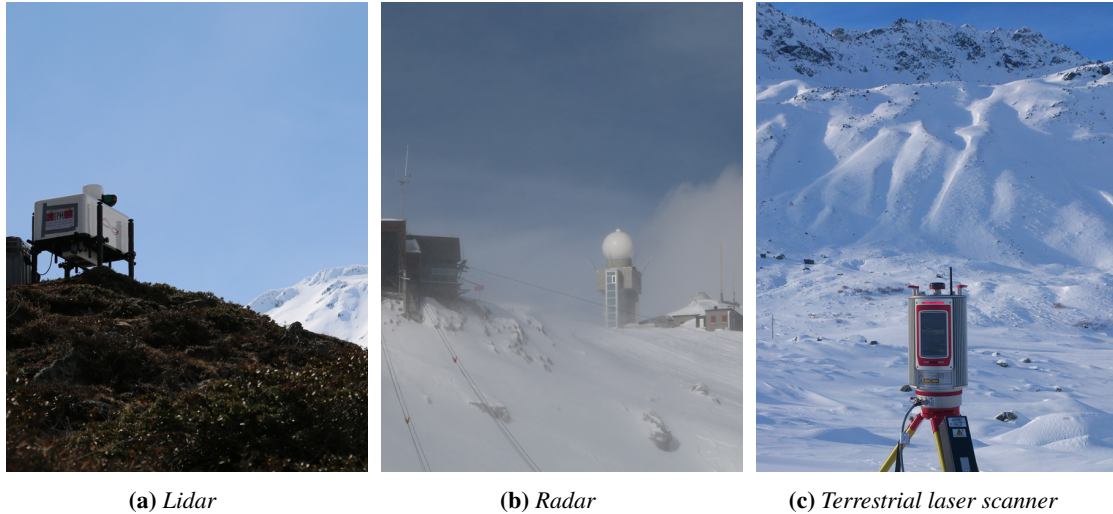


Figure 1.2: Remote sensing measurement devices. *a) A Doppler wind light detection and ranging (lidar), b) a C-band dual-polarized Doppler radio detection and ranging (Radar) and c) a terrestrial laser scanner to retrieve high-resolution wind, precipitation and snow distribution measurements, respectively.*

The most commonly derived product from precipitation radar signals is reflectivity (Z), which gives information about the intensity of precipitation. The radar reflectivity is obtained from the so-called “radar equation”, which describes the received power as a function of the radar characteristics, the distance from the instrument, the averaged cross section of all scattering particles in the sampling volume and the signal loss by attenuation (i.e. the reduction of the signal by interactions with atmospheric constituents, Banta et al., 2013). Therefore, reflectivity is a measure of the intensity of precipitation, resulting in a strong signal for either large particles or a large number of small particles. As explained for lidar measurements (Section 1.4.1) precipitation radars may also make use of Doppler frequency shifts to obtain information about the particle motion (Banta et al., 2013). Additionally, dual-polarization – the emission of electromagnetic waves with a horizontal (vertical) orientation of the electric (magnetic) field and vice versa – of the signal may be used to detect the shape of precipitation particles (Banta et al., 2013). Spherical particles are expected to return equal signal in the horizontal and vertical direction. Needles and plates would be expected to show a stronger signal in the horizontal direction as they tend to fall with a horizontal orientation (Banta et al., 2013).

Field experiments using a mobile dual-polarized Doppler X-band radar were previously performed in the region of Davos to study precipitation structures and small-scale orographic enhancement (e.g. Mott et al., 2014). In this thesis, radar precipitation estimates from the operational weather radar network of the Swiss Federal Office of Meteorology and Climatology (MeteoSwiss) are used. The advantage of operational weather radar measurements is that they are continuously operating, as they are used for weather prediction. The operational radar network of MeteoSwiss in its fourth generation consists of 5 dual-polarized Doppler C-band radars (Germann et al., 2015). The most recent addition was the installation of the radar on Weissfluhgipfel (near Davos in the Canton Grison, Figure 1.2b).

Precipitation measurements in complex terrain are especially challenging due to partial beam shielding, ground clutter and the harsh conditions on one side (Joss and Waldvogel, 1990) and small-scale precipitation patterns due to orographic effects on the other side. The MeteoSwiss radar network has been designed such that large overlap of the five radars is achieved, which improves correction of beam shielding and is a backup in case one of the radars has a problem (Germann et al., 2015). To achieve reliable precipitation estimates, complex algorithms to eliminate clutter and to correct for beam shielding have been designed (Germann et al., 2006). In addition to a good post-processing to eliminate effects of topography, high-resolution measurements are essential to capture the small-scale variability of precipitation in complex terrain. MeteoSwiss radars achieve a resolution of 83 m in range with a beam width of 1° . For operational

use measurements are averaged over 500 m in range. A scan procedure scanning 20 elevations (between -0.2° and 40°) every 5 min, is run to capture the high temporal variability of precipitation (Germann et al., 2015).

1.4.3 Spatial snow depth measurements

In complex terrain snow accumulation strongly varies in space (Section 1.2.2), which makes snow distribution measurements challenging. For a long time, snow depth measurements were mainly based on point measurements. Point measurements of snow depth or snow water equivalent, however, are not spatially representative, as they are strongly influenced by the slope, aspect and elevation (Grünwald and Lehning, 2015) as well as by the local influence of wind on snow deposition and redistribution (e.g. Lehning et al., 2008; Lehning and Fierz, 2008; Mott et al., 2010, Section 1.2.2). Transect measurements of snow depth are possible by the use of portable rulers. However, they are invasive and destructive, preventing repetitive measurements at the same locations (Kinar and Pomeroy, 2015). Especially in complex alpine terrain avalanche danger and difficult access further restrict in situ measurements.

Recent improvements in remote sensing technology, however, make it possible to achieve high-resolution spatial snow depth measurements at different resolutions, accuracy and coverage. Precise but spatially restricted snow depth measurements may be achieved using terrestrial laser scan (TLS) measurements (Prokop, 2008; Grünwald et al., 2010, Figure 1.2c). They usually cover a domain of few hundred square meters to few square kilometers. The resolution strongly depends on the distance to the target, the chosen beam width and the sampling interval (Lichti and Jamtsho, 2006). TLS measurements are the most simple remote sensing measurements introduced in this thesis and are only based on the travel time of the emitted laser beam, which is reflected at the surface. A point cloud of distances is retrieved by vertically and horizontally scanning the desired surface. To obtain snow depth or snow depth changes two TLS measurements are subtracted in a post-processing procedure (e.g. Prokop, 2008; Wirz et al., 2011; Sommer et al., 2015). To precisely match two laser scans it is important to scan a set of reference points in the measurement domain. Matching of scans introduces additional uncertainty and the selection of reference points is essential for good results. Georeferencing of snow surface scans in rough terrain may be further improved by adjusting bare-ground areas, which are assumed to be constant between two TLS measurements (Sommer et al., 2015). For proper TLS measurements it is further essential to have clear conditions as precipitation (snow or rain as well as cloud droplets) reflect the laser beam and result in biased measurements.

To investigate larger areas analogously to TLS measurements airborne laser scan (ALS) measurements may be performed (Wehra and Lohrb, 1999). ALS are based on the same principle as TLS but with the laser mounted on an airplane or helicopter. As well as for TLS clear sky conditions are essential for successful ALS measurements. Furthermore, ALS measurements are very expensive. Except from laser scanning, airborne photogrammetry either by airplanes, helicopters and recently drones, is applied to obtain digital elevation models of snow covered terrain (e.g. Bühler et al., 2015). As drones are quite easy to handle and cheap compared to other options they are heavily used recently (e.g. Bühler et al., 2016; De Michele et al., 2016).

To gain information about the change in snow depth due to a snowfall event ideally a scan right before and a scan right after the snowfall event are taken. However, often this requirement cannot be fulfilled due to different reasons. For both terrestrial and airborne laser scanning as well as for photogrammetry cloud free conditions are essential. For terrestrial laser scanning additionally, the accessibility of the scanning position may be restricted by avalanche danger.

1.5 Objectives

The relative importance of mountain-ridge scale winter precipitation processes in complex alpine terrain is still barely known, due to strong terrain-flow-precipitation interactions. On the one hand, cloud-dynamical processes may lead to orographic precipitation enhancement. On the other hand, near-surface particle-flow interactions have an impact on precipitation distribution across mountain ridges. To improve our understanding of these processes and their contribution to snow accumulation distribution, high-resolution numerical and experimental models are essential. Additionally, high-resolution spatial measurements of snow accumulation as well as precipitation and the local wind field are important to prove theoretical concepts, to improve the process understanding and are needed to validate model simulations.

In this thesis terrain-flow-precipitation interactions in complex terrain are addressed, focusing on:

- How does the small-scale lee-side flow field affect preferential deposition in very steep terrain?
- Can real-case high-resolution large-eddy simulations represent the spatial variability of precipitation in complex terrain?
- At which resolution do the small-scale flow field and mountain-ridge scale precipitation processes start to be resolved?
- What is the relative importance of mountain-ridge scale processes on snow distribution?

Chapter 2 The small-scale flow field on the leeward side of a mountain ridge and its influence on snow accumulation is investigated. Analyses are based on a unique data set of Doppler wind lidar measurements over a mountain ridge for a snowfall event in October 2015 with corresponding snow accumulation measurements, performed by terrestrial laser scanning. To interpret radial flow fields resolved by Doppler wind lidar measurements, semi-idealized Advanced Regional Prediction System (ARPS) large-eddy simulations (25 m horizontal grid spacing) for different initial conditions, as observed during the snowfall event in October 2015, complete the data set. Results are interpreted based on a flow regime classification. To assess snow distribution, ARPS simulations are further used to perform simulations with the alpine surface processes model (Alpine3D), which are compared to reference snow accumulation measurements by terrestrial laser scanning.

Chapter 3 To address small-scale precipitation patterns over complex terrain, Weather Research and Forecasting (WRF) simulations, initialized by Consortium for Small Scale Forecasting (COSMO) analysis (COSMO-WRF), have been introduced (Appendix D). The COSMO-WRF setup is validated against automatic weather stations. COSMO-WRF simulations together with high-resolution operational weather radar data are used to address the horizontal spatial variability of snowfall over alpine terrain and to address the question if COSMO-WRF is able to represent precipitation patterns based on three precipitation events in winter 2016. To analyze spatial precipitation patterns a variability analysis, based on general trends, empirical variograms and two-dimensional autocorrelation maps, is performed. Using the results of this analysis, dominant processes are addressed. Additionally, the dependency of the spatial variability on different model resolutions is determined.

Chapter 4 Finally, terrain-flow-precipitation interactions in very high-resolution (50 m horizontal grid spacing) COSMO-WRF simulations are analyzed. The importance of high-resolution simulations to resolve different precipitation processes is assessed based on precipitation distribution across mountain ridges, including the effect of terrain smoothing in the model. To address the importance of cloud-dynamical and particle-flow interactions in the model, we attempt to separate the two processes by assuming that near-surface precipitation patterns are dominated by particle-flow interactions, while farther above ground cloud dynamical processes and mean advection are dominant. Precipitation patterns are analyzed with respect to theoretical concepts. Finally, we make a rough estimate of the importance of different mountain-ridge scale processes, based on the assumption that they predominantly act at different levels. This analysis is further supported by a comparison of modeled precipitation patterns versus photogrammetrically determined snow depth measurements.

A Close-Ridge Small-Scale Atmospheric Flow Field and its Influence on Snow Accumulation

postprint version of the article published in *Journal of Geophysical Research – Atmospheres*, 122, 7737–7754, 2017, doi:[10.1002/2016JD026258](https://doi.org/10.1002/2016JD026258)^{*}, Franziska Gerber^{1,2}, Michael Lehning^{1,2}, Sebastian W. Hoch³, Rebecca Mott²

Candidates contribution: *Terrestrial laser scans (TLS) have been taken by the candidate. Post-processing of TLS data and simulations with the Alpine surface processes model Alpine3D have been performed by the candidate. Furthermore, she performed the analysis and wrote the manuscript together with all co-authors.*

Abstract The rough, steep and complex terrain in the alpine environment causes a variety of flow patterns such as blocking, speed-up, or flow separation, which influence precipitation, snow deposition and ultimately snow distribution on the ground. Cloud-terrain interactions, flow-particle interactions, and snow transport affect snow accumulation patterns, but the relative importance of these processes is not fully understood, in particular in complex mountainous terrain. A unique combination of measurements and model simulations is used in a local case study during a two-day snowfall event to demonstrate the current understanding of snow accumulation in very steep alpine terrain. Doppler wind lidar measurements show an eddy-like structure on the leeward side of the Sattelhorn ridge (in the Dischma valley near Davos, Switzerland), which could partly be replicated by Advanced Regional Prediction System (ARPS) flow simulations. Snow deposition measurements with a terrestrial laser scanner (TLS) show a complex deposition pattern, which is only partially captured by Alpine3D deposition simulations driven by the ARPS flow fields. This shows that additional processes such as avalanches may play a role or that a more

^{*}Slight changes to the submitted version are applied to assure consistency throughout the thesis.

¹Laboratory of Cryospheric Sciences, School of Architecture and Civil Engineering, École Polytechnique Fédérale de Lausanne, Lausanne, Switzerland.

²WSL Institute for Snow and Avalanche Research SLF, Davos, Switzerland.

³Department of Atmospheric Sciences, University of Utah, Salt Lake City, Utah.

refined simulation of flow or flow-particle interactions is required to fully understand snow distribution in very steep mountainous terrain.

2.1 Introduction

Over complex terrain snow cover exhibits a high spatial heterogeneity and a strong temporal (seasonal and interannual) variability, both on large mountain range scales (e.g. Beniston, 1997; Blanchet et al., 2009; Marty and Blanchet, 2012) and on river catchment scales (e.g. Jost et al., 2007; Grünwald and Lehning, 2011). Catchment-scale variability plays an important role, especially in regions where snow is the major source of water. Additionally, catchment-scale and local-scale variability of the snow cover influence local ecology (Wipf et al., 2009) and can affect the snow cover stability with respect to avalanches (Schirmer et al., 2010). To assess and predict seasonal water storage and resources, a better understanding of processes responsible for catchment- and local-scale snow distribution variability are fundamental.

On a large scale, variability in snow accumulation is mainly determined by interaction of mountain ranges with the large-scale atmospheric circulation causing orographic precipitation (Stoelinga et al., 2013). Increased snow deposition is expected on the windward side of mountain ranges by the process of blocking and lifting (Houze, 2012). Spatial snow accumulation structures on the catchment scale are strongly affected by precipitation-altitude effects (e.g. Wastl and Zängl, 2008) and by the interaction of local topography with the flow field. Wind-induced processes influence cloud dynamics (Choularton and Perry, 1986; Dore et al., 1992; Zängl, 2008; Zängl et al., 2008; Mott et al., 2014) and close-ground pure particle-flow interactions have a strong influence on snow distribution in complex terrain (Choularton and Perry, 1986; Colle, 2004; Zängl, 2008; Lehning et al., 2008; Dadic et al., 2010b; Mott et al., 2010; Winstral et al., 2013) such as preferential deposition (Lehning et al., 2008). Preferential deposition may lead to enhanced snow accumulation on the leeward side of the mountain. Strong upslope flow on the windward side of a mountain ridge reduces the local snow deposition due to reduced fall velocities, while enhanced snow deposition may occur on the foot of the windward side, where wind speeds are weak and on the leeward side of the ridge due to flow separation, weak winds, and higher concentration of snow. On the smallest scale snow accumulation patterns are formed by drifting and blowing snow due to strong local wind gusts and depending on the small-scale terrain (Mott et al., 2010; Lehning and Fierz, 2008).

Furthermore, snow accumulation in complex terrain strongly depends on elevation but also on the slope angle (Farinotti et al., 2010; Kerr et al., 2013). Farinotti et al. (2010) found slopes steeper than 55° to be barely snow covered. Despite the importance of avalanches, snow slides, and wind for snow depletion in steep terrain, Wirz et al. (2011) and Sommer et al. (2015) can still show significant snow accumulation in very steep rock walls. The steepness and size of a mountain ridge with respect to atmospheric stability, as typically expressed through the Froude number, further strongly influence the flow patterns that impact preferential snow deposition. Following Baines (1995), for idealized conditions three flow regimes based on slope steepness, wind speed, and atmospheric stability may be distinguished: (i) “lee-side bluff body boundary-layer separation”, (ii) “complete attachment”, and (iii) “post-wave separation”. “Lee-side bluff body boundary-layer separation” occurs over steep slopes, especially for weakly stably stratified atmospheres. For less steep obstacles under the same stability regime, flow separation may be completely suppressed, while for stronger stability a separation may occur further away from the ridge, the so-called “post-wave separation”.

Previous studies found strong indications of preferential deposition in radar data and snow deposition patterns (Mott et al., 2010; Mott et al., 2014). Moreover, model simulations show reliable results supporting the mechanism of preferential deposition (e.g. Dadic et al., 2010a; Mott et al., 2014). Recent results by Wang and Huang (2017) show that enhanced deposition may be on windward or leeward slopes depending on surrounding topography, wind speed and atmospheric stability. However, a systematic investigation of these effects is missing. Furthermore, these advances in the process understanding are still mainly based on model simulations and the modeling of snow accumulation remains challenging.

To further investigate the processes driving snow deposition across a mountain ridge, we present a case study of a precipitation event at the Sattelhorn ridge in the Dischma valley near Davos, Switzerland. Highly resolved radial wind velocity measurements with a pulsed Doppler wind Light Detection and

Ranging (lidar) system are combined with Advanced Regional Prediction System (ARPS) flow simulations to better understand the complex flow field over the Sattelhorn ridge. Snow accumulation measurements by terrestrial laser scans (TLS) and simulated snow accumulation distribution driven by ARPS wind fields complete this unique collection of measured and simulated data. This set of data is in agreement with differences found between modeled and measured snow accumulation on steeper slopes (Mott et al., 2010; Mott et al., 2014), but overall enables us to reveal a more complex picture of preferential deposition in very steep terrain than previously found for more gentle terrain.

2.2 Data and Methods

Since 2013, the Dischma Experiment (DISCHMEX), has mainly been concerned with processes controlling snow accumulation and ablation in the Dischma valley near Davos, Switzerland, to improve the prediction of seasonal snow water resources in alpine valleys. Snow accumulation and ablation patterns are monitored using terrestrial laser scans (TLSs, Section 2.2.3), and two meteorological stations (Section 2.2.1) have been installed to record the near-surface meteorological conditions. The experiment was augmented with Doppler wind lidar observations (Section 2.2.2) between 20–30 October 2015 to resolve the fine-scale flow features in the wind field, especially in the vicinity of one main ridgeline during a precipitation event. This setup is used to highlight the complex interaction of wind and snow accumulation on a very steep rock wall.

During the lidar campaign, high pressure dominated the region from 20–28 October 2015 (MeteoSchweiz, 2015). On 28 October 2015, Foehn conditions set in, followed by a cold front that reached the study area on the night of 28–29 October 2015 from the west and produced measurable snowfall (referred to as snowfall event, hereafter). TLSs were performed on 28 and 30 October 2015, i.e. prior and after the snowfall event on the 29 October 2015 between 01:50 and 10:00 UTC+1 (Section 2.2.3). Numerical simulations with ARPS were conducted for different atmospheric conditions (Section 2.2.4) to analyze the detailed flow structure in the vicinity of the Sattelhorn ridge during the event and to force simulations with the Alpine surface processes model Alpine3D (Lehning et al., 2008).

2.2.1 Meteorological stations

Measurements from two meteorological stations in the upper Dischma valley are used in this study: station *Dischma Moraine*, located on a moraine of the Scaletta glacier at 2532 m above sea level (m asl) and station *Dischma Ridge* at 3034 m asl on the ridge between Piz Grialetsch and Scalettahorn. Station *Dischma Moraine* is used as reference for snow depth measurements, while station *Dischma Ridge* provides information about wind speed and direction of the airmass entering the Dischma valley from the south (Figure 2.1a and Appendix A.1).

To evaluate the near-surface atmospheric stability, surface temperature data from the Intercantonal Measurement and Information System (IMIS) station *IMIS DAV2*, located at 2561 m asl about 8 km west of the Dischma valley, and from the Weissfluhjoch research site *WFJ2* (WSL Institute for Snow and Avalanche Research SLF, 2015) at 2540 m asl located 13 km to the north-west of the Dischma valley, were used. *WFJ2* further provides precipitation measurements. Bulk atmospheric stability estimates during the snowfall event were derived from potential temperature differences between station *Dischma Ridge* and stations *IMIS DAV1* and *IMIS FLU2* which are located at the Chrachenhorn at 2871 m asl and at the Flüelapass at 2404 m asl, respectively. Details for all the stations are given in Appendix A.1.

2.2.2 Doppler wind lidar

A Halo Photonics Streamline scanning Doppler wind lidar was deployed on a small terrain knoll near Dürrboden in the upper Dischma catchment (Figure 2.1). A scan pattern consisting of 6 different scans was repeated every 10 min. The scans included a vertical stare, 3 plane position indicator (PPI) scans at elevation angles of 5°, 25° (later 28°) and 75°, and 2 range height indicator (RHI) scans with azimuth angles of 330° and 227° representing the main valley axis and a plane intersecting the north slope of the

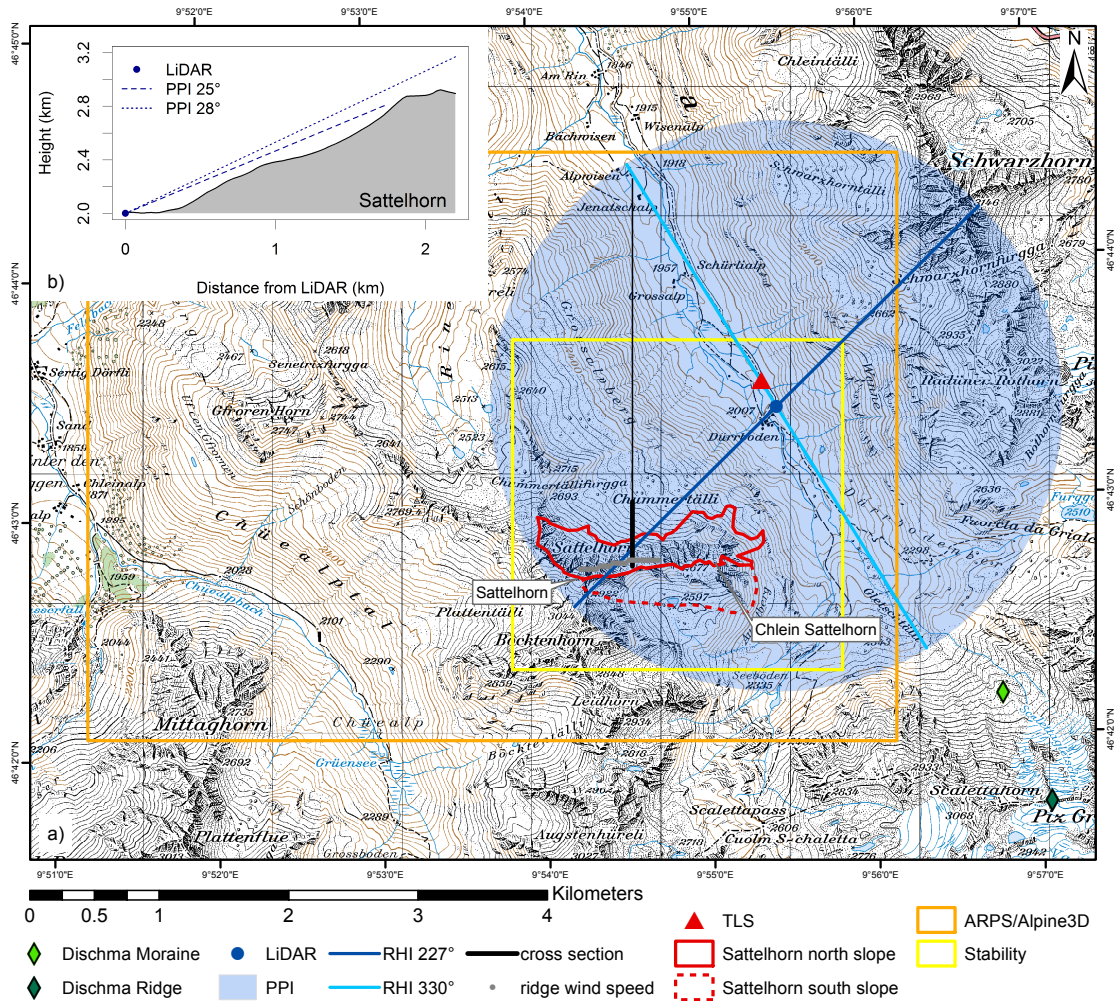


Figure 2.1: a) Field site in the upper Dischma valley, Davos, Switzerland. Diamonds: meteorological stations Dischma Moraine (light green) and Dischma Ridge (dark green). The Doppler wind lidar (blue dot) was deployed close to Dürnboden. The maximum extent sampled by the lidar scans is shaded in blue. Plane position indicator (PPI) angles of 25° and 28° intersect with the north slope and clear the main ridge line of the Sattelhorn, respectively (shown in inset b). The blue lines indicate the along-valley (330°, light blue) and cross-valley (227°, dark blue) azimuthal directions of the range height indicator (RHI) scans. Red triangle: Approximate position of the terrestrial laser scanner (TLS), from which the northern slopes of the Sattelhorn are scanned (solid red). The dashed red line marks the southern slopes of the Sattelhorn. The north-south profile (black line) is used to visualize the flow field over the ridge in the Advanced Regional Prediction System (ARPS) simulations (see Figure 2.6). Gray dots: Grid points of ARPS simulations used to calculate maximum ridge wind speed. Orange area: Area covered by ARPS and Alpine3D simulations. Yellow area: Domain used to estimate the atmospheric stability in the simulations. Basemap: pixmaps © 2018 swisstopo (5704 000 000).

Sattelhorn (Figure 2.1). The range gate length was 24 m and radial velocities were retrieved from up to 2.2 km distance under ideal conditions. The elevation angle of the intermediate PPI scan was changed from 25° to 28° on 28 October 2015 around 16:00 UTC+1. At 25° elevation, the scan intersected with the north slope of the Sattelhorn, while at 28° the scan cleared the main ridge line (Figure 2.1b). Ground returns degrades lidar retrievals that intersect with topography, and data from range gates in close vicinity of the surface (0 m to 60 m) are discarded. Hourly averages of the radial velocities from the individual PPI and RHI scans were calculated and interpolated to regular grids with 25 m grid size for further analysis.

Very clean and aerosol-scarce air during the high pressure conditions of 20–28 October 2015 did not allow for wind retrievals in the vicinity of Sattelhorn. However, successful lidar retrievals were recorded during 16 hours of the event from 28 October 2015 07:00 UTC+1 until 23:00 UTC+1 (Figure 2.2). Thereafter, intermittent scanner problems and subsequent weak returns from the vicinity of the Sattelhorn limited the wind retrievals. Hydrometeors and aerosols were either absent along the Sattelhorn ridgeline or the lidar signal was attenuated in the near field by thick clouds and fog (see Appendix A.2).

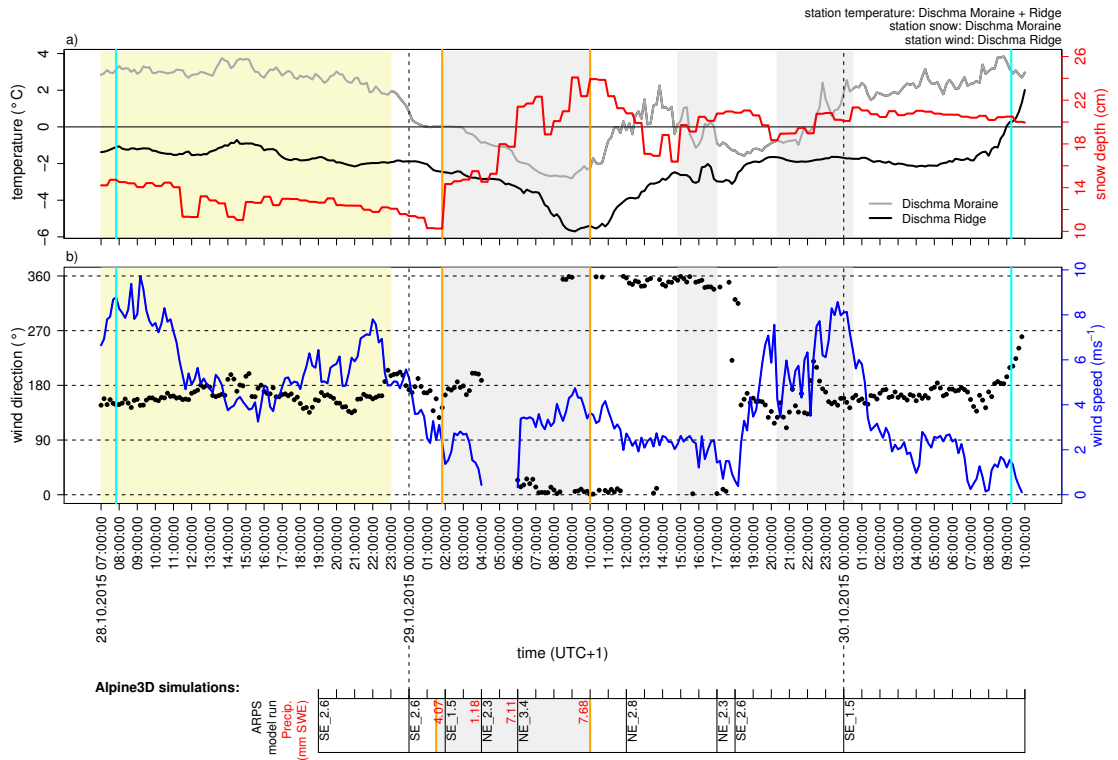


Figure 2.2: Overview of meteorological conditions and snow depth measurements for the study period (28 October 2015 07:00 UTC+1 to 30 October 2015 09:00 UTC+1). a) Temperature is given for the two stations Dischma Moraine (gray) and Dischma Ridge (black). Snow depth (red) is given for station Dischma Moraine. b) Wind direction (black dots) and wind speed (blue) are given for the meteorological station Dischma Ridge. Snow accumulation periods are marked by gray shading. The main snowfall event on 29 October 2015 started around 01:50 UTC+1 and lasted until about 10:00 UTC+1 (orange lines). Cyan lines: Terrestrial laser scans before and after the snowfall event. Yellow shading: Period during which a good lidar signal was obtained from the vicinity of the Sattelhorn north slope. The time line shows the Advanced Regional Prediction System (ARPS) wind fields (Table 2.1) chosen for the Alpine3D simulations (black). Precipitation (calculated from snow depth changes) is given as snow water equivalent (red).

2.2.3 Terrestrial Laser Scanning

Snow depths on the Sattelhorn north slope, which spans from the Sattelhorn in the west to Chlein Sattelhorn in the east (Figure 2.1), were measured with a terrestrial laser scanner (TLS, Riegl VZ-6000) on 28 and

30 October 2015, both before and after the snowfall event (Figure 2.2). All data was post-processed following the procedure by Sommer et al. (2015). However, we calculate snow depth (vertically measured) instead of snow thickness (perpendicular to the terrain) to ensure comparability with modeled snow depth (see Section 2.2.4). Net accumulation during the snowfall event is calculated as the difference between the snow depths from the two TLS scans. Similar procedures have been used in previous studies (e.g. Grünwald et al., 2010; Wirz et al., 2011; Sommer et al., 2015), but the present study used the Riegl VZ-6000 TLS (beam divergence of 0.12 mrad), which operates at a near infrared wavelength (1064 nm), making it exceptionally well-suited to measure snow covered terrain (Riegl, 2015).

For visualization, the processed data is interpolated on a two-meter grid. Measurement uncertainties are both due to acquisition and post-processing. Errors due to acquisition are larger for large ranges, large incidence angles and for rough surfaces (Deems et al., 2013) and may be on the scale of decimeters (Sommer et al., 2015). They are partially reduced by multi station adjustment (Sommer et al., 2015), after which the remaining standard error of the constant surfaces is about 2 cm. More details on the TLS measurements and post-processing is given in the Appendix A.3.

2.2.4 Advanced Regional Prediction System and Alpine3D

Measurements with the single Doppler wind lidar provide temporally and spatially highly resolved wind observations, but resolve only the radial or along-beam wind components, but not the full 3D wind field. To gain a better understanding of the wind components resolved by the lidar (Section 2.2.2), to address the complex nature of the flow field, and as boundary conditions for snow distribution simulations, model simulations for the upper Dischma valley were conducted with ARPS (Xue et al., 2001). A set of simulations (Table 2.1 and Appendix A.4) for different wind speeds, wind directions, and atmospheric stability regimes is conducted to cover the flow conditions at station *Dischma Ridge* during the snowfall event between 28 and 30 October 2015 (Figure 2.2). The naming convention of the simulations is “WD_RWS”, where WD indicates the wind direction and RWS the maximum ridge wind speed.

The ARPS model setup closely follows the setup described by Raderschall et al. (2008), Mott and Lehning (2010) and Mott et al. (2014). All simulations (Table 2.1) are run with a horizontal resolution of 25 m on a domain covering the upper Dischma valley (Figure 2.1), which has an extent of 6.25 km \times 4.55 km. The topography (digital elevation model: dh25 © 2018 swisstopo (5704 000 000)) is slightly smoothed using a low-pass filter.

The simulations have 35 vertical terrain-following levels with the first level at an average height of 2.35 m. The first 100 m of the atmosphere contain 8 to 12 levels. Simulations are integrated up to between 160 s and 250 s (see Appendix A.4) with an integration timestep of 0.01 s and an acoustic wave mode time step of 0.001 s. An intermediate integration time has been chosen to make sure turbulent flow characteristics evolve, even though they may not be fully developed (Raderschall et al., 2008). Longer integration times, however, lead to numerical instabilities caused by the highly complex terrain in the model domain. For all simulations the solar zenith angle corresponds to noon. Simulations over bare ground are run with a roughness length of 0.01 m, while for simulations with a snow cover the roughness length is 0.005 m, as discussed in Mott et al. (2015).

All except for three simulations are initialized with a neutrally stratified atmosphere and a near-surface potential temperature of 295 K over bare ground, as no high resolution information on snow cover, the atmospheric stability, and surface temperatures is available for the whole simulation domain (Section 2.2.1). Bare-ground conditions were chosen as many slopes were snow-free prior to the snowfall event. The combination of data from three meteorological stations at varying altitudes (stations *Dischma Ridge*, *FLU2* and *DAVI*) suggest a slightly stable stratification (Brunt-Väisälä frequency $N_{stat} \approx 0.01 \text{ s}^{-1}$). At station *WFJ2*, temperature differences between the surface and the air at 4.5 m above ground of 1.3 °C to 5.3 °C suggest the temporary occurrence of a strongly stable, near-surface atmosphere. Therefore, three simulations (SE_1.5stable, SE_3.9stable and S_1.5stable) with a more stable near-surface atmosphere were run to evaluate the impact of atmospheric stability on flow structures. SE_1.5stable and SE_3.9stable are initialized with a stability profile as determined from the meteorological stations and a snow cover above 2300 m asl, while S_1.5stable is initialized with a near-surface potential temperature of 285 K instead of 295 K. The simulations initialized with a neutral atmosphere develop slightly stable conditions

Table 2.1: ARPS simulations. All simulations (except for *S_1.5stable*, *SE_1.5* and *SE_3.9stable*) are initialized over bare ground for neutral conditions with a near-surface potential temperature of 295 K. Eddy height gives the vertical extent of the upslope flow in the eddy. Eddy upslope flow gives the mean wind speed in the eddy at the lowest level above ground (about 2 m). For *S_1.5stable* it is the wind speed at the lowest level of the eddy. Simulations initiated with north-easterly wind are only used as input for the Alpine3D simulations.

Simulation	Wind direction °	mean max. ridge wind (m s ⁻¹)	Eddy height (m)	Eddy upslope flow (m s ⁻¹)
SE_0.8	145°	0.76	134	0.5
SE_1.5	145°	1.45	50	0.4
SE_2.6	145°	2.64	8	0.7
SE_1.5stable ^a	145°	1.47	–	–
SE_3.9stable ^a	145°	3.90	–	–
S_3.2	180°	3.24	–	–
S_1.5stable ^a	180°	1.46	13–26	0.2
NE_2.3	15°	2.31		
NE_2.8	15°	2.81		
NE_3.4	15°	3.38		

^aSimulation with a more stable near-surface atmosphere.

near the surface (Brunt Väisälä frequency $N \approx 0.01 \text{ s}^{-1}$) while simulations *SE_1.5stable*, *SE_3.9stable* and *S_1.5stable* develop a strongly stable stratification close to the ground. Considering all model levels up to the 20th level ($\approx 580 \text{ m}$ above ground), the mean Brunt-Väisälä frequency in the area of the Sattelhorn (Figure 2.1) in these simulations is $N = 0.02 \text{ s}^{-1}$, $N = 0.03 \text{ s}^{-1}$ and $N = 0.03 \text{ s}^{-1}$ for *S_1.5stable*, *SE_1.5stable* and *SE_3.9stable*, respectively. Regarding only model level 7 ($\approx 20 \text{ m}$ above ground) to model level 20 over the same area, all simulations have a mean Brunt-Väisälä frequency of $N \approx 0.01 \text{ s}^{-1}$, which corresponds to the Brunt-Väisälä frequency computed from station data ($N_{stat} \approx 0.01 \text{ s}^{-1}$). Given the very short integration time, the influence of radiation on the atmospheric stability and corresponding flow fields is very weak. Thus, slightly stable atmospheric conditions are likely to occur as measured surface temperatures at the reference station *WFJ2* stayed below atmospheric temperatures during the period of the lidar measurements, which is likely for cloudy conditions in late October.

To classify the simulations, maximum ridge wind speeds at the lowest model level are calculated (Figure 2.1). Furthermore, we analyze flow conditions of the different ARPS simulations and the lidar scans using the framework of flow regimes by Baines (1995) to evaluate flow conditions. These regimes are characterized by the Froude Number (Nh_m/U) and the slope characteristic (I_d/h_m), where N is the Brunt-Väisälä frequency, h_m is the maximum height of the obstacle, I_d the downstream half length of the obstacle, and U the wind speed. For the ARPS simulations, the average Brunt-Väisälä frequency in the vicinity of the Sattelhorn (Figure 2.1) is calculated, and the mean maximum ridge wind speed at the lowest model level ($\approx 1.68 \text{ m}$ above ground) is used as wind speed U . For the conditions during the lidar measurements, we calculate the Brunt-Väisälä frequency from air temperatures at meteorological stations located at different elevations in the close surrounding of the Sattelhorn area. Wind speed U is taken from station *Dischma Ridge*. The cross section is chosen as marked in Figure 2.1, while the resolution for the ARPS simulations is 25 m and the resolution for the evaluation of conditions during the lidar measurements is 2 m. This framework allows for the comparison between the flow regime over the Sattelhorn in the ARPS simulations with the flow regime determined for the period of lidar measurements. Additionally, the wind components corresponding to the radial velocities measured by the lidar in the PPI scans and the RHI scans across the valley (227° azimuth) are extracted from the different simulations and are used to validate the representativeness of the ARPS simulations.

To evaluate the influence of the local flow field on snow deposition and to address the process of preferential deposition, the highly resolved ARPS mean flow fields are used as input for the alpine surface processes model Alpine3D (Lehning et al., 2008, Appendix A.4), run with a horizontal resolution of 25 m

on the same domain as the ARPS simulations (Figure 2.1). Because of the very complex topography, numerical instabilities in the ARPS simulations already occur after intermediate integration times. Thus, ARPS simulations, and consequently Alpine3D simulations, are restricted to a resolution of 25 m. As mean flow fields from ARPS are not available for every timestep of Alpine3D (every hour), the use of flow fields representing several timesteps saved computational time, as described in e.g. Mott and Lehning (2010) and Groot Zwaaftink et al. (2011). Overall, the Alpine3D simulations were forced by lower wind speeds at the Sattelhorn ridge than observed at station *Dischma Ridge* (Figure 2.2 and Appendix A.5), because the Sattelhorn ridge is not as exposed as the station *Dischma Ridge* and ARPS simulations with higher wind speeds show numerical instabilities. Precipitation is based on snow depth measurements of the station *Dischma Moraine* (assuming a snow density of 100 kg m^{-3} , approximately corresponding to the density calculated in the Alpine3D simulations) during the main snowfall period. The same snowfall is applied on the whole domain, which is relatively small and therefore this assumption should be reasonable. The two periods with increasing snow depth (Figure 2.2) later on 29 October 2015 are likely due to snow redistribution, as no snowfall is registered at the snow gauge on Weissfluhjoch (*WFJ2*). During the second period, highly variable winds with wind gusts $>4 \text{ m s}^{-1}$ are registered at both stations *Dischma Ridge* (Figure 2.2) and *Dischma Moraine* (not shown). Wind speeds during the first period are lower at both stations. Missing data in the wind measurements at station *Dischma Moraine* could, however, indicate rimed instruments, which might result in an underestimation of wind speeds. Additionally, some fluctuation in the snow measurements are likely due to measurement errors.

To compare snow deposition simulations to measured snow depth, a simulation is run with the full snow drift module of Alpine3D (using the parameterization for saltation developed by Doorschot and Lehning, 2002). An additional Alpine3D simulation without snow drift (as in Mott et al., 2014) is performed to distinguish pure snow deposition due to precipitation (i.e. preferential deposition) from snow redistribution. In the snow drift module of Alpine3D, snow transport by suspension and preferential deposition is modeled based on the 3D wind field calculated by ARPS. Saltation serves as the lower boundary condition of the suspension layer, i.e. snow needs to be entrained from the ground by saltation to potentially enter the suspension layer.

2.3 Results and Discussion

First we give a general overview of the meteorological conditions in the upper Dischma valley during the snowfall event on 28–30 October 2015 (Section 2.3.1), followed by an analysis of the radial velocity patterns in the lidar planes (Section 2.3.1) and a discussion in the light of 3D flow fields from the ARPS simulations (Section 2.3.1). Furthermore, we discuss the flow over Sattelhorn as a stably stratified flow over an obstacle (Section 2.3.1). Corresponding snow accumulation maps are introduced (Section 2.3.2 and 2.3.2) and the relationship of snow accumulation patterns and the flow field is discussed (Section 2.3.2).

2.3.1 The flow field in the vicinity of the Sattelhorn

Flow conditions and precipitation measured by meteorological stations

The mean wind direction at the ridge (station *Dischma Ridge*) in the upper Dischma valley was south to south-east for the first 21 hours of the event (Figure 2.2). Ridgetop wind speeds began to weaken around midnight (00:00 UTC+1) of 28 to 29 October 2015, turned to a northerly direction between 04:00 and 06:00 UTC+1, and back to south-easterly flow on 29 October 2015 around 18:00 UTC+1. The air temperature at 2532 m asl dropped below 0°C shortly after midnight on 29 October 2015 (station *Dischma Moraine*), while ridgetop temperatures at 3034 m asl remained below 0°C (station *Dischma Ridge*). Precipitation measurements at the meteorological station *WFJ2* at the Weissfluhjoch show the onset of snowfall at 23:00 UTC+1 on 28 October 2015 which lasted until 08:00 UTC+1 on 29 October 2015 (not shown). Snow depth measurements at station *Dischma Moraine* in the upper Dischma basin indicate that snow accumulation started around 01:50 UTC+1 on 29 October 2015, and lasted until about 10:00 UTC+1 on 29 October 2015 (Figure 2.2). The difference in precipitation onset times for Weissfluhjoch and the

upper Dischma valley may be because the stations are located in complex terrain separated by a distance of about 13 km or due to above freezing temperatures at the station *Dischma Moraine* until around midnight on 29 October 2015.

Radial velocity patterns in the lidar scans and the ARPS simulations

Radial velocity fields from the lidar PPI scans (Figure 2.3) and velocity azimuth display (VAD) retrievals of the horizontal winds (Appendix A.2) on 28 October 2015 between 07:00–23:00 UTC+1 confirm the prevailing southerly wind direction. PPI scans at an elevation angle of 25° show a radial wind component that is directed away from the lidar on the leeward (northern) side of the Sattelhorn ridge line (Figure 2.3a), while at a higher elevation angle of 28° the cross-barrier flow component over the Sattelhorn is visible (Figure 2.3b). Radial velocities from the RHI scans confirm this pattern (Figure 2.4). Hourly mean radial lidar velocity fields reveal a very persistent flow structure, with a near-surface flow away from the lidar along the upper slopes of the Sattelhorn, while the flow above the ridgeline is directed toward the lidar.

This eddy-like structure develops for southerly to south-easterly wind directions and ridge-top wind speeds between 4 m s^{-1} and 10 m s^{-1} and is observed over a period of 16 hours. Maximum wind speeds in the upslope flow toward the ridge are between 4 m s^{-1} and 10 m s^{-1} , and thus of the same magnitude as the ridge-level flow speeds. The horizontal extent of the eddy-like structure typically varies between 400 m and 1000 m (Figure 2.5) but periods exist where the structure seems to be split into two or more eddy-like cells. The vertical extent of the eddy-like structure reaches up to about 200 m above ground.

Due to the alignment of the RHI scans relative to the Sattelhorn ridge (Figure 2.1), the observed structure in the radial flow field may either represent a lee-side eddy or result from a strong easterly along-slope flow at elevations below the Sattelhorn ridgeline undercutting the cross-barrier flow. With observations from a single lidar, the two patterns cannot fully be distinguished, and will hereafter be referred to as eddy-like structure.

Since our simulation setup is based on many assumptions (Section 2.2.4) and is not covering the full range of measured ridge wind speeds due to numerical instabilities arising for high wind velocity cases, we concentrate the comparison between simulated and observed flow fields on the mean flow field characteristics of the flow fields showing most agreement in the radial velocity fields compared to the lidar retrievals.

The characteristics of the PPI lidar flow field (Figure 2.3a-b) is well represented by the radial flow field in the PPI planes extracted from the ARPS simulations (Figure 2.3c-d). The flow away from the lidar on the leeward side of Sattelhorn at a PPI angle of 25° is most pronounced in SE_1.5, while it is missing, very small or connected to the flow away from the lidar to the north-west of the lidar in the other simulations. The ARPS based radial wind fields corresponding to the RHI scans of the lidar (Figure 2.6a-c) show similar eddy-like structures as observed in the RHI retrievals (Figure 2.4). For the analysis of these synthetic radial velocity cross sections, eddy-like structures are defined by the occurrence of a change in sign of the radial velocity (black line in Figure 2.6) in the vicinity of the surface. Most ARPS simulations show smaller (length and especially height) eddy-like structures than those identified in the lidar data (Figure 2.5). Furthermore, in the ARPS simulations initiated with southeasterly winds, the eddy-like structures tend to become smaller as the ridge wind speeds increase, except for simulations with a strongly stable near-surface atmosphere. The lidar observations did not show such a relationship between wind speed and the size of the eddy-like structures. The length and vertical extent of the eddy-like structure is best represented by SE_1.5, while for stronger wind speeds the vertical extent of the eddy-like structure is much better reproduced by SE_3.9stable compared to SE_2.6. The simulations SE_1.5stable, SE_3.9stable and S_1.5stable show strong downslope flow in the lowest model levels, which is likely thermally induced due to a layer of very cold air in the lowest 20 m. Due to limitations in the lidar retrievals (topographic shielding, ground returns), near-surface features (up to 0 m to 60 m above ground), such as these drainage flows, cannot be resolved.

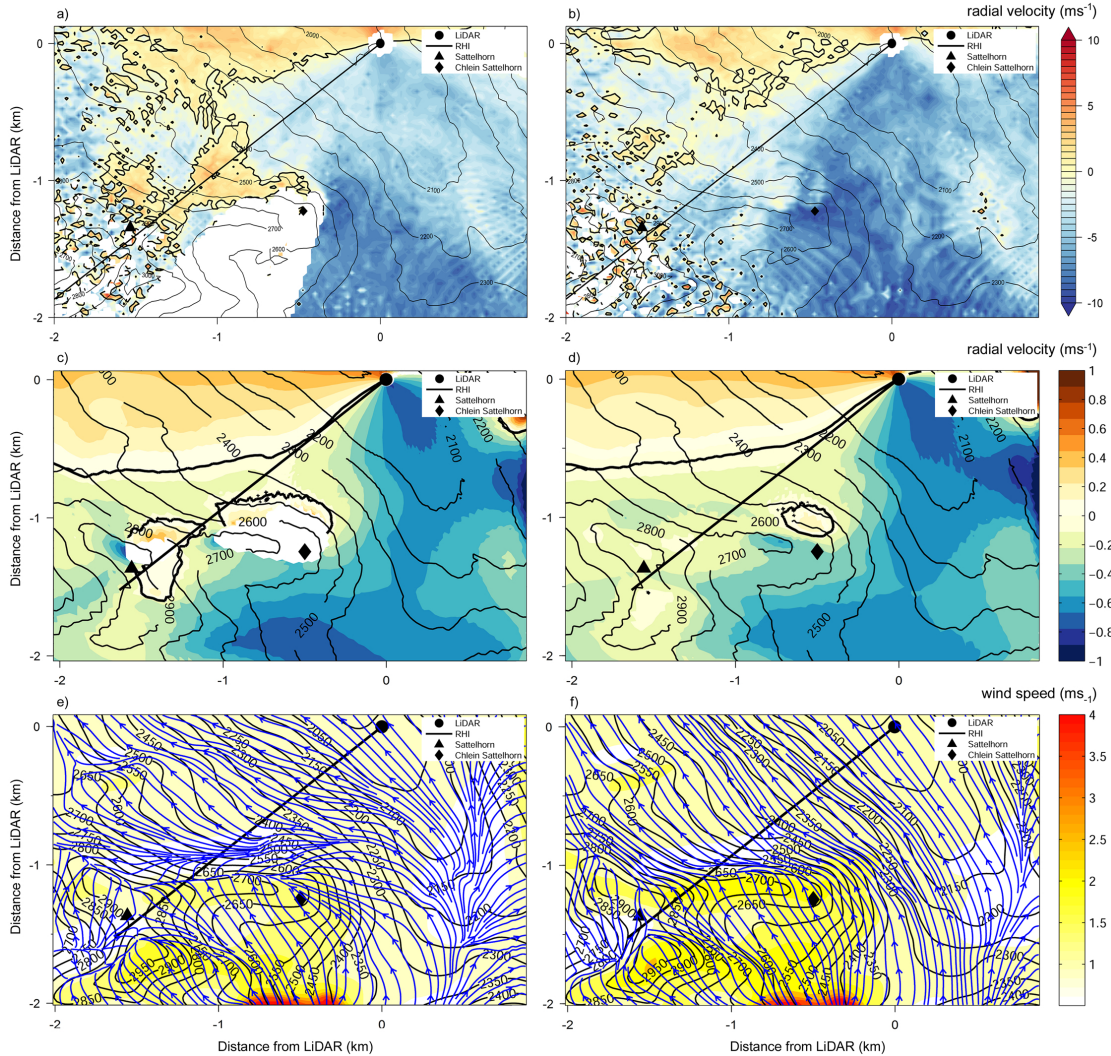


Figure 2.3: Hourly mean a) 14:00–15:00 UTC+1 and b) 17:00–18:00 UTC+1 radial velocity fields in the upper Dischma valley from plane position indicator (PPI) Doppler wind lidar scans on 28 October 2015. The PPI angles are a) 25° and b) 28°. c) and d) PPI radial velocity extracted from the Advanced Regional Prediction System (ARPS) simulation SE_1.5 for the PPI angles c) 25° and d) 28°. Positive radial velocity (red) shows flow away from the lidar and negative radial velocity (blue) shows flow toward the lidar. e) and f) Flow field (wind speed shaded) on the lowest model level over the Sattelhorn simulated by ARPS for simulation e) SE_1.5 and f) SE_2.6. The black dot marks the position of the lidar. Sattelhorn and Chlein Sattelhorn are marked by a triangle and diamond, respectively. The scan direction of the range height indicator (RHI) scan is marked by the black line. Contour lines in a and b: dh25 © 2018 swisstopo (5740 000 000).

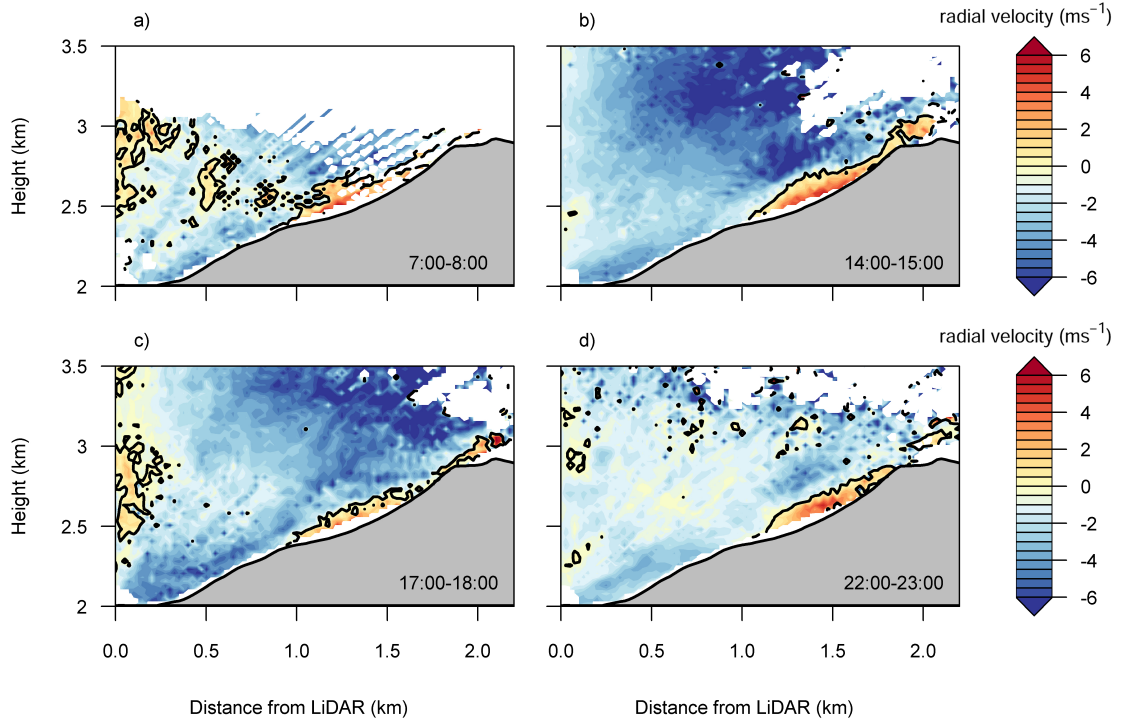


Figure 2.4: Hourly mean radial velocity fields over the Sattelhorn in the range height indicator (RHI) Doppler wind lidar scan on 28 October 2015. Positive radial velocity shows flow away from the lidar and negative radial velocity shows flow toward the lidar. Times are in UTC+1. Topography: dhbm25 © 2018 swisstopo (5740 000 000).

Radial velocity patterns in context of the 3D flow field

To put the radial velocity patterns in the context of the 3D flow field, we concentrate on the simulations with the best representation of the observed radial flow patterns. A more complete description of the flow fields of all simulations is given in the Appendix A.6.

Higher level flow in the ARPS simulations is from a southerly to south-easterly direction, which corresponds to the prevailing wind direction measured at station *Dischma Ridge* during the lidar retrievals. The flow at the lowest atmospheric level in the ARPS simulations initiated with southerly or south-easterly flow (Figure 2.3e-f) confirms a flow across the Sattelhorn ridgeline. Additionally, simulations initiated with south-easterly winds show flow blocking upwind of the Sattelhorn ridge, forcing a bending of the flow around the Chlein Sattelhorn, which initiates a near-surface along-ridge flow on the leeward side of the Sattelhorn ridgeline. This near-surface flow, while very weak, corresponds to the radial velocities directed away from the lidar on the leeward slopes of Sattelhorn. On the other hand, some simulations are able to reproduce the formation of a lee-side eddy behind the east-west oriented Sattelhorn ridge (Figure 2.6b). In all simulations initiated with south-easterly winds and a neutral atmosphere, the eddy-like structure found in the radial velocities, consists of an along-slope flow component and a lee-side eddy, which is smaller for stronger wind speeds and has a small vertical extent (Table 2.1, Figure 2.4). Simulations with a strongly stable near-surface atmosphere show an eddy-like structure in the radial velocity field above the close-ground downslope flows. For S_1.5stable the eddy-like structure is very small and mainly due to a lee-side eddy, as no along-slope flow develops. For SE_1.5stable and SE_3.9stable, a larger eddy-like structure develops with a vertical extent of about 80 m and 100 m, respectively (above about 27 m above ground), which only consists of an along-slope flow component and has a vertical extent that is comparable to the extent of the eddy-like structure in simulation SE_2.6, but slightly shifted downslope (Figure 2.5). The larger vertical extent of the eddy-like structure compared to simulation SE_2.6 (in which the vertical

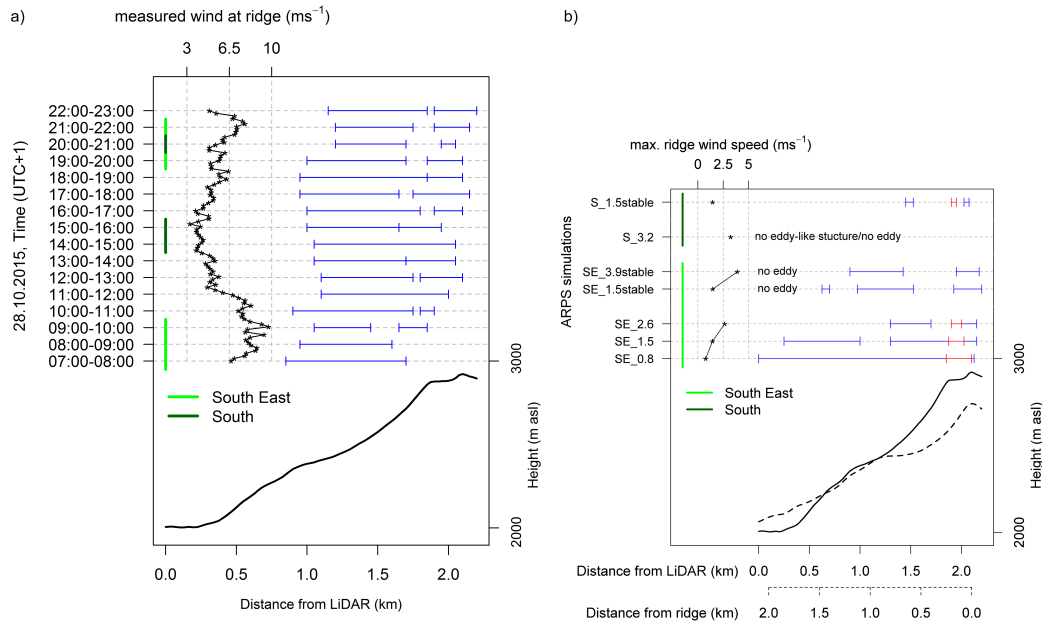


Figure 2.5: Blue bars show estimated horizontal extent of the eddy-like structure a) for the hourly mean Doppler wind lidar range height indicator (RHI) radial velocity across the Sattelhorn and b) radial velocity from Advanced Regional Prediction System (ARPS) simulations. Several blue bars indicate a splitting of the eddy-like structure in several cells. Eddy-like structures are shown a) for the time period 07:00 UTC+1 till 23:00 UTC+1 on 28 October 2015 and b) for the ARPS simulations (Table 2.1) with different ridge wind speeds and wind directions. Wind speeds at the ridge are given as a black curve. In a) wind speeds measured at the meteorological station Dischma Ridge (Figure 2.1) are plotted. Periods with constant southerly (south-easterly) wind direction are marked with a dark (light) green bar. Red bars in b) show the eddy size defined from a north-south cross section through the Sattelhorn (dashed black profile, Figure 2.1). Topography: dhm25 © 2018 swisstopo (5740 000 000).

extent is about 30 m) occurs because the bending of the flow around Chlein Sattelhorn reaches a higher vertical extent for the simulation with a more stable atmosphere, which is typical for a strongly stably stratified atmosphere, as more stably stratified air is more resistant to vertical motions and thus favors the flow around obstacles (Whiteman, 2000).

Besides showing lower wind speeds compared to the lidar flow fields, the ARPS simulations are all (except for SE_1.5stable and SE_3.9stable) initiated with bare ground for the whole domain, even though meteorological stations and photographs indicate a snow-cover in some areas of the simulation domain. Furthermore, given the short integration time of the simulations (Section 2.2.4) eddy size and location are likely to change for longer integration times. Additionally, the real terrain is more complex compared to the ARPS topography. All these factors may contribute to the fact that the model is not exactly able to represent the flow field in the lidar scans.

Overall, our simulations confirm the occurrence of flow separation on the leeward side of Sattelhorn. The flow separation and development of a lee-side eddy appears to be supported by along-slope flows, which were previously found to occur in complex alpine terrain (Hug et al., 2005; Wirz et al., 2011). The interaction with the cross-ridge flow and the along-slope flow may favor or strengthen a lee-side eddy. The along-slope flow may further be forced to lift at the western edge of the Sattelhorn ridge enhancing this interaction. This possible interaction agrees well with highly resolved flow simulations over an idealized pyramid-shaped mountain by Voigt and Wirth (2013), who find a lee-side bow vortex, which is built and maintained by flow over and around the pyramid. Based on the above analysis, the flow structure observed in the lidar scans is best represented by simulation SE_1.5, while the vertical extent of the eddy-like structure is better represented by simulations SE_1.5stable and SE_3.9stable. Additionally, a lee-side eddy forms in the lee of Sattelhorn in simulation S_1.5stable but not in SE_1.5stable. This shows that

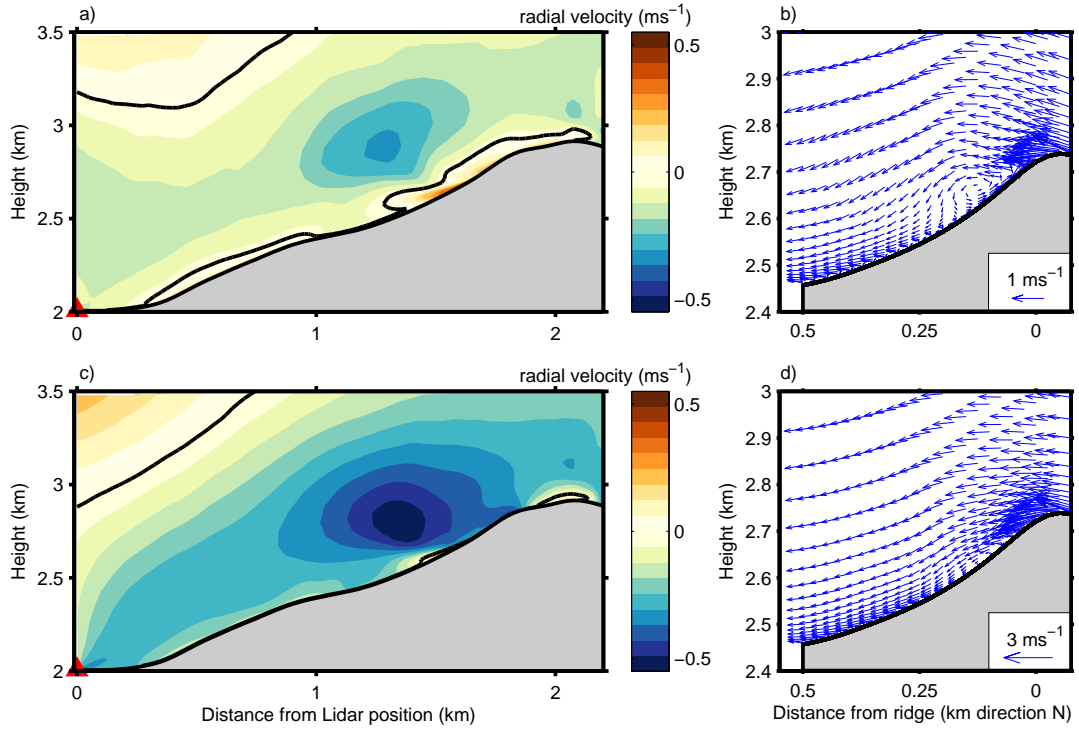


Figure 2.6: Flow field over the Sattelhorn simulated by the Advanced Regional Prediction System (ARPS) for the two simulations SE_1.5 (panels a and b) and SE_2.6 (panels c and d). a) and c) show the simulated radial velocities that would be recorded with a RHI scan (azimuth angle of 227°) of the Doppler wind lidar. The red triangle shows the position of the lidar. b) and d) show a cross section of the north-south flow field for the top 500 m over the Sattelhorn ridge, where a lee-side eddy forms in some of the simulations. The location of the cross section is marked in Figure 2.1.

the small-scale flow field in the lee of the Sattelhorn ridge is strongly sensitive to both wind direction and stability, as already found for the less steep and more ideal area of Gaudergrat (Hug et al., 2005).

Lee side flow regimes

While the flow regime concept by Baines (1995) is developed for a 2D flow over an obstacle with ideal shape, the framework is used here to attempt a classification of the observed flow regimes in the ARPS simulations and the lidar retrievals (Section 2.2.4). The concept may thus not exactly be applicable to our situations of flow across complex 3D topography. Baines (1995) states that the boundaries between the regimes are only approximate and their exact position strongly depends on the shape of the obstacle. Thus, we perform a classification based on two different definitions of the downstream half-width of the terrain obstacle (i.e. the slope). The first classification takes into account the *entire slope* (i.e. from the ridge top down to the valley floor) and the second takes into account the *upper slope* (i.e. from the ridge top to the first terrain step, Figure 2.7a-b).

Depending on the definition of the slope, the flow fields fall into different regimes (Figure 2.7c). For the *entire slope*, all ARPS simulations are in the regime of “post-wave separation”. For the *upper slope*, the hill is steeper and thus the flow in the simulations is close to the transition between the three regimes. Based on the observations the flow regime, during which the eddy-like structure is observed in the lidar retrievals, stretches over the regimes “complete attachment” and “post-wave separation” when taking into account the *entire slope* and falls under the regime of “lee-side bluff body boundary-layer separation” when regarding the *upper slope* (Figure 2.7).

As the eddy-like structure observed in the lidar retrievals is mainly located in the area of the *upper*

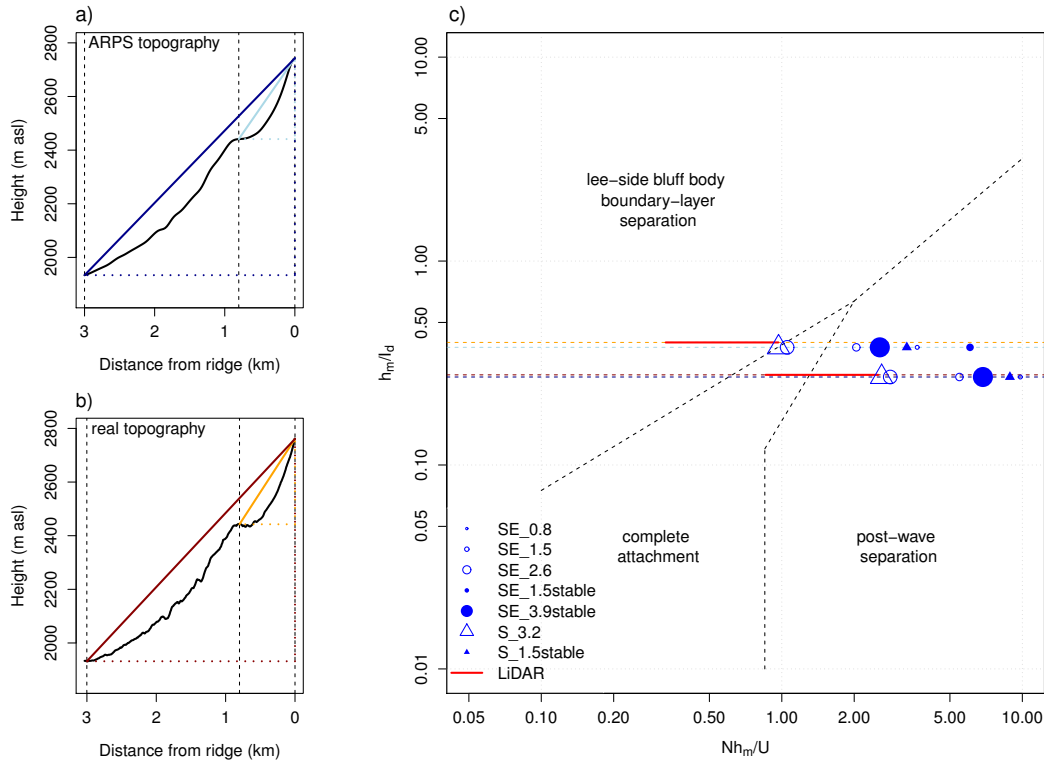


Figure 2.7: a-b) Cross sections from the Sattelhorn ridge to Dischma valley (Figure 2.1) for a) ARPS topography and b) real topography. Two different slopes are shown: upper slope (light blue/orange) and the entire slope (dark blue/dark red). c) ARPS simulations and lidar measurements in the classification scheme of Baines (1995) developed for 2D stratified flow over an obstacle. South-easterly (southerly) flows are marked with blue dots (triangles) and are scaled by wind speed. Filled (open) markers are for simulations with a slightly stable (strongly stable near-surface) atmosphere. The red bars show the position in the diagram for the lidar measurements spanning the wind speeds observed. The dashed lines mark approximately the boundaries as defined by Baines (1995). Real topography: dhm25 © 2018 swisstopo (5740 000 000).

slope and develops directly at the ridge (Figure 2.4) it is likely a “lee-side bluff body boundary-layer separation”. This agrees well with the strong wind speeds observed during the lidar measurements and the classification regarding the *upper slope*. On the other hand, the flow structure observed in the ARPS simulations is mainly identified as “post-wave separation”, which is in agreement with the separation starting about 100 m downstream of the ridge (Figure 2.6b). Additionally, a change in wind direction on the leeward side of the Sattelhorn ridge, could be a sign of a developing wave. The main reason for this, and for the compression of the eddy for larger wind speeds, are the lower ridge wind speeds compared to the wind speeds in the lidar retrievals. However, simulations with higher wind speeds are not available as they become numerically unstable (Section 2.2.4). Steeper slopes of the real terrain compared to ARPS topography slightly enhance this effect.

Given the large vertical extent of the eddy-like structure and the classification in the Baines (1995) diagram, the eddy-like structure observed in the lidar scans is likely a combination of an along-slope flow and a “lee-side bluff body boundary-layer separation” eddy. Thus, the eddy-like structure likely develops in an atmosphere stable enough to favor along-slope flow up to about 100 m to 200 m above ground but weak enough for a lee-side eddy to develop. A “lee-side bluff body boundary-layer separation” eddy may further be favored by the stronger wind speeds in reality compared to our ARPS simulations (Section 2.3.1). Additionally, the wind direction, which is fluctuating between about 130° and 200° may play a crucial role. The eddy in some of the ARPS simulations is, however, more likely to be a “post-wave separation” eddy.

2.3.2 Snow accumulation on lee slopes

Snow depth

At the meteorological station *Dischma Moraine*, an increase in snow depth of 6.0 cm is measured between 28 October 2015 07:50 UTC+1 and 30 October 2015 09:10 UTC+1 (i.e. in the time period between the two TLS measurements, Figure 2.2). During the snowfall event (29 October 2015 01:50–10:00 UTC+1), an increase in snow depth of 13.67 cm is measured at station *Dischma Moraine*, while cumulative snow accumulation is 20.04 cm. Decreases in snow depth during the snowfall period (Figure 2.2) may be due to measurement errors, settling or snow drift. Station *Dischma Moraine* lies just outside our Alpine3D simulation area. However, modeled snow depth changes in the vicinity of station *Dischma Moraine* are between 5 cm and 10 cm in the same period and therefore the observation is within the range of the simulations. The average new snow depth over the TLS area is about 3.1 cm with a standard deviation (σ) of 27 cm, which is on the same order of magnitude as the standard deviation of TLS snow depth measurements in Wirz et al. (2011). This is, however, less than the modeled mean snow accumulation in the TLS area on the north slope of the Sattelhorn (preferential deposition only: 16.8 cm, $\sigma = 2.6$ cm; including wind drift: 16.9 cm, $\sigma = 2.7$ cm).

The uncertainty of the TLS snow depth measurements is as high as the average snow depth change (Section 2.2.3). Additionally, the input of snow precipitation in the Alpine3D simulations is a rough estimation based on snow depth measurements. However, snowfall is likely to be overestimated as settling, snow drift and measurement errors cannot be distinguished in the observations. Thus, we stick to the maximum possible precipitation used as input for Alpine3D. Compared to the snow precipitation at the reference station *WFJ2* (9.4 mm snow water equivalent, SWE) the estimated snowfall is large. However, a difference in snow accumulation is reasonable as the *WFJ2* site is located about 13 km further north. Thus, we concentrate our discussion on the relative distribution. There may be a loss of mass out of the accumulation area by avalanches, which is not modeled in Alpine3D (Section 2.2.4). Additionally, enhanced snow accumulation on the north slope of the Sattelhorn in the Alpine3D simulations might be due to missing inertia in the model, meaning that particles travel too strictly with the flow in the model. This may lead to deposition zones either on the windward slope (i.e. on the Sattelhorn south slope (Figure 2.1) for southerly winds) or further downstream on the leeward slopes, depending on topography, advection and atmospheric stability (Wang and Huang, 2017).

Snow accumulation patterns

TLS new snow accumulation of the snowfall event on 29 October 2015 shows a ridge-to-valley decrease in new snow depth and a pattern of larger accumulation at the eastern and western edge of the Sattelhorn north slope (Figure 2.8a). On top of this, a pattern of ridge-to-valley stripes is observed. The pattern of stripes with reduced snow accumulation (gray) may have two causes. On the one hand, it may be a pattern of small avalanches and snow slides. On the other hand, it may be a sign of cross-slope loading, i.e. filled gullies and chutes on the leeward side of terrain features and eroded areas due to along-slope winds (Figure 2.8c). A sign for avalanches and snow slides is enhanced snow accumulation at the bottom of the stripes with reduced snow accumulation. This is visible for many of the stripes with reduced accumulation. On the other hand, for cross-slope loading no distinct accumulation is expected at the slope toe. Some of the ablation bands show parallel accumulation on the leeward slopes of secondary features, which might be a sign of cross-slope loading. Cross-slope loading may further enhance the possibility of avalanches, where snow is accumulated excessively. No such stripes are seen on Alpine3D snow accumulation maps (Figure 2.8b). On the one hand, the model does not simulate avalanches. Simulating avalanches by gravitational models (Bernhardt et al., 2012; Warscher et al., 2013) might thus be a valuable extension in future studies. On the other hand, cross-slope loading structures are mainly driven by snow drift processes that are not captured well by the model with a 25 meter resolution (Mott and Lehning, 2010). The ridge-to-valley gradient in snow accumulation on the TLS snow map is, however, visible in both Alpine3D simulations for 30 October 2015 at 09:00 UTC+1. A pattern of enhanced snow accumulation at the eastern and western edge of the Sattelhorn north slope is visible, too. On top of this, there is a distinct pattern of enhanced snow accumulation on the north slope of Sattelhorn, which is not visible in

the TLS snow depth change map. This pattern is slightly more distinctive in the simulation with snow drift (Appendix A.7, as differences are almost invisible). The ridge-to-valley gradient most likely is an elevation effect as temperatures are only slightly below zero (Figure 2.2). The west to east pattern is most likely defined by the terrain shape and may be a sign of strong along-slope winds.

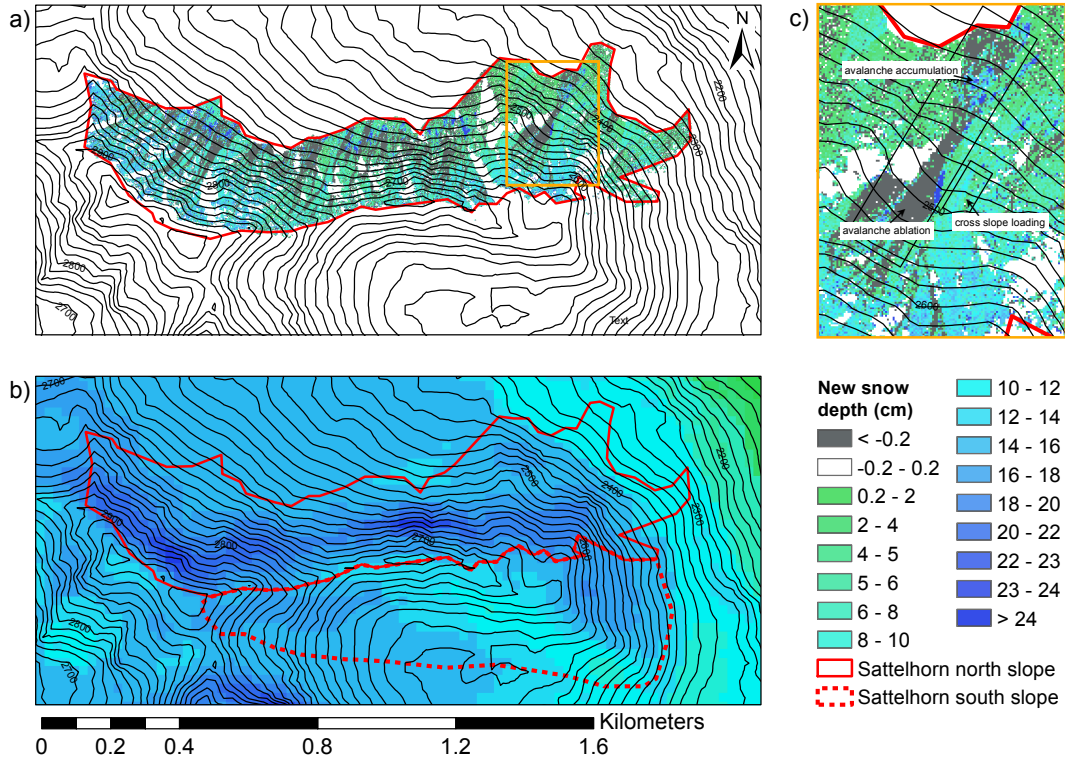


Figure 2.8: a) Snow depth changes (cm) between 28 October 2015 and 30 October 2015 measured by TLS (resolution 2 m). b) Snow accumulation (cm) in the area of the Sattelhorn from the Alpine3D simulation without snow drift (resolution 25 m) for the same period as in a). c) Detailed view of the area marked by an orange square in a) illustrating signs of an avalanche and of cross-slope loading. Positive snow depth changes are given by green to blue colors. Negative snow depth changes are given in gray. The red contour shows the area of the Sattelhorn north slope, which is covered by the terrestrial laser scan (TLS) measurements. The dashed red contour marks the Sattelhorn south slope. The area of the Sattelhorn north and south slope (red) are marked in Figure 2.1. Contour lines: dhm25 © 2018 swisstopo (5740 000 000).

The local flow field and snow accumulation

Based on snow accumulation periods at the station *Dischma Moraine*, 31 % to 81 % of the snowfall on 29 October between 01:50 and 10:00 UTC+1 occurred during southerly winds (measured at station *Dischma Ridge*, Figure 2.2). The large uncertainty comes from missing wind measurements on 29 October 2015 between 04:00 and 06:00 UTC+1, during which period 50 % of the precipitation has fallen, when regarding the total snow depth changes. The last period of snow accumulation at station *Dischma Moraine* was during relatively strong southerly winds (mean wind speed 6.3 m s^{-1}). However, this is likely a sign of snow drift due to strong southerly winds without snowfall. Overall, the northern slope of the Sattelhorn cannot be judged as pure lee or windward slope during this snowfall event. In the Alpine3D simulations snowfall during the period of missing wind measurements is treated as north-easterly wind, because lidar measurements indicate that the wind has already turned. Thus, in the Alpine3D simulations (where SWE is calculated from incremental snow accumulation) only 26 % of the snowfall is for southerly flow.

The analysis of the flow field for southerly winds gives evidence for flow separation on the leeward side (north slope) of Sattelhorn (Section 2.3.1), where based on the theory of preferential deposition (Lehning et al., 2008) an enhanced snow accumulation is expected. Even though in the Alpine3D simulations only 26 % of the snowfall was during southerly winds, a distinct snow accumulation on the north slope of Sattelhorn is observed (Figure 2.8b), which is likely a sign of preferential deposition. The signs of preferential deposition on the Sattelhorn south slope (Figure 2.2) are weaker in the Alpine3D simulations (Figure 2.8b), even though 74 % of the snowfall is simulated during northerly winds. The patterns are almost erased by 30 October 2015 09:00 UTC+1 (Figure 2.8b), mainly because strong incoming solar radiation leads to strong settling and melt on the southern slope (Appendix A.7). Furthermore, snow accumulation due to preferential deposition on the windward side would be expected in the area of the slope toe due to blocking (i.e. outside of the area measured by TLS). Thus, we mainly focus on the interaction of the flow field with snow accumulation during southerly winds, which are furthermore stronger than the northerly winds.

The patterns found in the Alpine3D simulations and the lack of small-scale structures like a cornice and other patterns due to snow drift are generally in agreement with results in Mott and Lehning (2010), who show that the influence of snow drift on snow deposition for a grid resolution of 25 m is rather weak and a resolution of 10 m or less is needed for small-scale structures to develop. Unfortunately, due to the complexity of the terrain and size of the domain our ARPS and therefore Alpine3D simulations are restricted to 25 m resolution.

Slope-scale snow accumulation patterns on the north slope of Sattelhorn measured by TLS show some agreement compared to Alpine3D simulations except for the band of enhanced snow accumulation, which is missing in TLS snow accumulation (Section 2.3.2), i.e. a ridge to valley decrease in snow depth and a pattern of larger snow accumulation at the eastern and western edge of the Sattelhorn ridge. One reason for the missing enhanced snow accumulation by preferential deposition in the TLS snow accumulation map might be the steepness of the Sattelhorn north slope (average slope angle: 42.7° , max slope angle: 79.7° , with steepest slopes in the area of preferential deposition in the Alpine3D simulations). As very steep slopes cannot keep as much snow as less steep slopes, some signal of preferential deposition might be removed by avalanches, which are likely the main process of snow redistribution (Sommer et al., 2015). Furthermore, the band of enhanced snow accumulation on the north slope of Sattelhorn occurs where a “post-wave separation” eddy occurs. Strong winds at the ridge down to about 100 m away from the ridge may prevent snow from depositing or may even erode snow and transport it to the area of the eddy where wind speeds are strongly reduced. In contrast, for the situation observed by lidar, it is more likely to have a “lee-side bluff body boundary-layer separation” eddy. Thus, snow may be transported over the ridge to the lower end of the eddy-like structure (i.e. outside of the area covered by TLS), as winds are separating directly at the ridge. In the area of the eddy-like structure, erosion of snow by strong back flow in the eddy may add to a reduction of snow accumulation. Additionally, processes leading to enhanced snow accumulation on the windward side of the slope (Wang and Huang, 2017) or a transport of particles further downwind, which are not captured in the model, such as particle inertia, could further add to a missing sign of preferential deposition.

After the main snowfall event some snow accumulation occurs at the station *Dischma Moraine* again later between 29 October 2015 20:20 and 30 October 2015 00:30 during relatively strong southerly winds. This is most likely a sign of snow redistribution. As wind conditions during this period are very similar to wind conditions when the eddy-like structure is observed, it is likely that during this period an eddy-like structure developed in the vicinity of the Sattelhorn north slope, which was likely stronger than the eddy-like structure in the ARPS simulations and thus used to force Alpine3D. This indicates that either a stronger lee-side eddy builds during the event compared to ARPS or along-slope winds are stronger than in the ARPS simulations (Section 2.3.1). Strong winds in an eddy-like structure may thus cause redistribution of snow, either strengthening cross loading of the slope, or transport snow to places where winds are weaker. This might be an additional reason why the signal of preferential deposition is further diluted in reality compared to the simulations.

2.4 Conclusion and Outlook

A unique new dataset from the Dischma Experiment (DISCHMEX) combines high-resolution Doppler wind lidar measurements during a snowfall event with TLS-based snow accumulation retrievals. The complex interaction between cross-barrier flow and snow deposition on the northern slope of the Sattelhorn, an alpine mountain ridge close to Davos, Switzerland, is evaluated during the 28–29 October 2015 snowfall event. Lidar and TLS observations are combined with numerical simulations from ARPS and Alpine3D to investigate the detailed 3D wind field and the complex snow accumulation patterns.

Doppler wind lidar measurements resolve the complex flow interactions with the Sattelhorn ridge and show strong evidence for the formation of an eddy-like structure on the leeward side of Sattelhorn. ARPS simulations reproduce this structure, but with a smaller spatial extent and weaker mean flow. Based on these simulations the observed flow field is likely a combination of a cross-ridge and an along-slope flow, which may support the development of a lee-side eddy due to topographic forcing. Similar flow patterns were found for simulations over an idealized pyramid (Voigt and Wirth, 2013) giving evidence for the flow pattern to probably occur more generally for steep alpine peaks and ridges.

Our ARPS simulations show that atmospheric stability, wind direction, and wind speed all have a strong influence on the development of the local near-surface flow field over the northern slope of Sattelhorn and thus the development of a lee-side eddy. The fluctuation between southerly and south-easterly wind directions and the temporary occurrence of a strong near-surface stability may be crucial for the development of a strong eddy-like structure on the leeward side of the Sattelhorn. A dependence on local inflow direction was presented by Hug et al. (2005) for flow over less complex terrain such as the Gaudergrat. A strong dependence on stability was further presented by Wang and Huang (2017).

Due to the lack of detailed atmospheric stability measurements, the simulations are initialized based on stability estimates from weather stations at different altitudes. A more stable near-surface atmosphere may contribute to the large vertical extent of the eddy-like structure in the lidar retrievals as it may maintain along slope flows up to higher elevations. Additionally, stronger wind speeds and the higher complexity of the real terrain make it likely that the flow is in the regime of “lee-side bluff body boundary-layer separation” as shown in our analysis of flow regimes, while the flow in the ARPS simulations is likely in the regime of “post-wave separation”.

Snow accumulation patterns on the northern slope of Sattelhorn measured by terrestrial laser scanning (TLS) show some agreement to modeled snow accumulation, but they do not show a clear sign of preferential deposition. This might be because excess snow accumulation in very steep terrain is unloaded by avalanches (Sommer et al., 2015) or by redistribution of snow due to stronger winds (Wirz et al., 2011) over the northern slope of Sattelhorn compared to our ARPS simulations. Additionally, different flow regimes may play a crucial role on the exact location of snow deposition on the leeward side of the ridge. The stronger sign of preferential deposition on the northern compared to the southern slope of Sattelhorn in the Alpine3D simulations is likely due to stronger southerly winds and because of weaker solar irradiation, even though only 26 % of the snowfall was during southerly winds.

Unfortunately, an initial problem with the lidar scanner and the subsequent lack of successful lidar retrievals due to a lack or over-abundance of scattering particles limited the observations to before 23:00 UTC+1 and did not cover the entire snowfall event. A more complete picture of the influence of the small scale wind field on snow accumulation would require a more continuous lidar dataset and corresponding snow accumulation measurements. Actual measurements of the 3D wind field would require the use of multiple lidars, and would overcome the limitations and difficulties arising from the interpretation of a single lidar-based radial velocity field. However, such measurements are hard to achieve due to the complex logistics of placing, powering, and maintaining several lidars in sub-freezing, avalanche-prone, and steep environments.

The unique combination of observations of snow distribution, meteorological variables, and of the fine-scale wind field, further augmented with high-resolution ARPS model simulations, shows the state-of-the-art process understanding in complex mountainous terrain. One of the objectives was to investigate preferential deposition in the vicinity of the steep and complex Sattelhorn ridge, but our results could only partially confirm the findings previously reported from less steep terrain such as the Gaudergrat ridge (Mott et al., 2010) or the Wannengrat area (Mott and Lehning, 2010). We note that TLS–Alpine3D agreement of

snow distribution in these previous publications was remarkably good in some areas but already pointed out that quantitative agreement is poor in very steep parts most notably on top of steep ridges. Preferential deposition in less steep terrain was further found to be responsible for increased deposition at the lower half of windward slopes due to blocking or at leeward slopes due to flow separation (Lehning and Mott, 2016). Snow transport was further identified to be the main driver for smaller scale drifts such as cornices. Overall, we show that snow accumulation structures in very steep terrain are more complex than previously found for less steep and less complex terrain. This study as well as recent investigations by Wang and Huang (2017) suggest that over steep terrain the process of preferential deposition becomes more complex. The deposition patterns with reduced accumulation at the windward slope and enhanced accumulation at the upper leeward slope, may thus be less important for steep slopes compared to less steep slopes. This could be either due to different processes dominating during snowfall or due to modulation of the accumulation patterns by snow drift and redistribution of snow by gravitational processes (Sommer et al., 2015). Future work will include measurements over a larger area and for several storm periods to address open questions on the relative importance of the different processes shaping the snow cover. It may also be required to use higher resolution numerical simulations and/or work with a flow model that is better suited for very steep and rough terrain. A well suited model for future studies may be the WRF model when it becomes available in an IBM (Immersed Boundary Method) version.

Acknowledgments *The work is funded by Swiss National Science Foundation (Project: Snow-atmosphere interactions driving snow accumulation and ablation in an Alpine catchment: The Dischma Experiment; SNF-Grant: 200021_150146). Some funding for S.W. Hoch came from Office of Naval Research Award N00014-11-1-0709. For organizational assistance thanks go to Charles Fierz, for field assistance we thank Sebastian Schlögl and for technical assistance with Alpine3D many thanks go to Mathias Bavay. Further, we thank the Swiss Federal Office of Meteorology and Climatology (MeteoSwiss) for providing meteorological data. Topographic data is reproduced by permission of swisstopo (JA100118). Data presented in this article are published as Gerber et al. (2017b). Additionally, we thank the anonymous reviewers for their questions, comments and recommendations, which helped to improve the paper.*

Spatial variability of snow precipitation and accumulation in COSMO–WRF simulations and radar estimations over complex terrain

revised version of the discussion paper in *The Cryosphere Discussions*, 2018, doi:[10.5194/tc-2018-50](https://doi.org/10.5194/tc-2018-50)^{*}, Franziska Gerber¹², Nikola Besic³⁴, Varun Sharma¹, Rebecca Mott⁵², Megan Daniels⁶, Marco Gabella⁴, Alexis Berne³, Urs Germann⁴, Michael Lehning¹²

Candidates contribution: *The candidate performed the analysis together with NB and worked on the development and has run the COMSO-WRF coupling and simulation setup. The concept was developed together with the co-authors. The candidate wrote the manuscript together with all co-authors.*

Abstract Snow distribution in complex alpine terrain and its evolution in the future climate is important in a variety of applications including hydro-power, avalanche forecasting and fresh water resources. However, it is still challenging to quantitatively forecast precipitation especially over complex terrain, where the interaction between local wind and precipitation fields strongly affects snow distribution at the

^{*}Slight changes to the resubmitted version are applied to assure consistency throughout the thesis.

¹Laboratory of Cryospheric Sciences, School of Architecture and Civil Engineering, École Polytechnique Fédérale de Lausanne, Lausanne, Switzerland.

²WSL Institute for Snow and Avalanche Research SLF, Davos, Switzerland.

³Environmental Remote Sensing Laboratory, School of Architecture and Civil Engineering, École Polytechnique Fédérale de Lausanne, Lausanne, Switzerland.

⁴Radar, Satellite, Nowcasting Departement, MeteoSwiss, Locarno, Switzerland.

⁵Institute of Meteorology and Climate Research, Atmospheric Environmental Research (KIT/IMK-IFU), KIT-Campus Alpin, Garmisch-Partenkirchen, Germany.

⁶unaffiliated, Sydney, Australia.

mountain ridge scale. Therefore, it is essential to retrieve high-resolution information about precipitation processes over complex terrain. Here, we present very high resolution Weather Research and Forecasting model (WRF) simulations (COSMO–WRF), which are initialized by 2.2 km resolution Consortium for Small-scale Modeling (COSMO) analysis. To assess the ability of COSMO–WRF to represent spatial snow precipitation patterns, they are validated against operational weather radar measurements. Estimated COSMO–WRF precipitation is generally higher than estimated radar precipitation, most likely due to an overestimation of orographic precipitation enhancement in the model. The high precipitation amounts also lead to a higher spatial variability in the model compared to radar estimates. Overall, an autocorrelation and scale analysis of radar and COSMO–WRF precipitation patterns at a horizontal grid spacing of 450 m show that COSMO–WRF captures the spatial variability normalized by the domain-wide variability of precipitation patterns down to the scale of few kilometers. However, simulated precipitation patterns systematically show a lower variability on the smallest scales of a few 100 m compared to radar estimates. A comparison of spatial variability for different model resolutions gives evidence for an improved representation of local precipitation processes at a horizontal resolution of 50 m compared to 450 m. Additionally, differences of precipitation between 2830 m above sea level and the ground indicate that near-surface processes are active in the model.

3.1 Introduction

In many regions of the world, e.g. the Alps or the Californian Sierra Nevada, snow is the main source of fresh water. Additionally, it is an important resource for hydro-power and is crucial for winter tourism in skiing areas (Schmucki et al., 2017). Thus, especially in a changing climate, it is essential to improve the understanding of processes forming the seasonal snow cover. Improving the ability of weather forecast models to represent the spatial variability of snowfall is further crucial to efficiently manage fresh water and hydro-power. Moreover, as snow is a potential danger in terms of avalanches, improved knowledge about the distribution of snow is crucial for avalanche forecasting and prevention.

Snow accumulation patterns at a mountain-range scale are known to be strongly dependent on blocking and lifting processes including large-scale orographic precipitation enhancement (e.g. Houze, 2012; Stoelinga et al., 2013), which is related to the large-scale atmospheric circulation. However, for a long time little knowledge was available about the spatial distribution of snow on a mountain-slope or river-catchment scale. Only in recent years improvements in technology allowed the investigation of mountain-slope scale snow distribution (e.g. Deems et al., 2006; Prokop, 2008; Grünwald et al., 2010). Terrestrial and airborne laser scanning reveal annually persistent patterns of peak-of-winter snow accumulation distribution on river-catchment scales (Schirmer et al., 2011; Scipión et al., 2013), which is found to be consistent with few dominant snowfall events of the season. Reported scale breaks in fractal analysis of snow accumulation patterns are mainly at scales <100 m and represent the occurrence of a change in dominant processes (e.g. Deems et al., 2008). On very small-scales snow accumulation patterns are assigned to wind redistribution of snow (e.g. Mott et al., 2011; Vionnet et al., 2017). Vegetation effects were found to be dominant at small scales and terrain effects dominate on scales up to 1 km (Deems et al., 2006; Trujillo et al., 2012; Tedesche et al., 2017). Different dominant scales are reported for different slope expositions relative to the wind direction (Schirmer and Lehning, 2011). Furthermore, Schirmer et al. (2011) could show that snow accumulation smooths the underlying terrain, reducing the small-scale spatial variability of topography. While most studies addressed variability of snow accumulation, the combined scale analysis of snow accumulation and snow precipitation patterns by Scipión et al. (2013) reveals much smoother patterns in snow precipitation at about 300 m to 600 m above ground compared to final snow accumulation at the ground on scales up to 2 km. This stresses the importance of pre-depositional near-surface and post-depositional processes for snow accumulation patterns.

Driving processes of snow accumulation on the mountain-ridge scale were addressed in numerous studies, which reveal two main pre-depositional processes. On the one hand, mountain-ridge scale precipitation and accumulation are influenced by local cloud-dynamical processes (Choularton and Perry, 1986; Dore et al., 1992; Zängl, 2008; Zängl et al., 2008; Mott et al., 2014). On the other hand, particle-flow interactions (i.e. the influence of the local flow field on the pathways of snow particles and the particle

distribution in the air) determine snow accumulation patterns in mountainous terrain (Colle, 2004; Zängl, 2008; Lehning et al., 2008; Dadić et al., 2010b; Mott et al., 2010; Mott et al., 2014). On the mountain-ridge scale, Mott et al. (2014) documented the occurrence of a local event of orographic snowfall enhancement. In their case study, the presence of a low-level cloud gives evidence for precipitation enhancement favored by the seeder-feeder mechanism (e.g. Bergeron, 1965; Purdy et al., 2005). On similar scales, preferential deposition (Lehning et al., 2008) was found to cause enhanced snow accumulation on leeward slopes (e.g. Mott et al., 2010; Mott and Lehning, 2010). However, snow depth measurements in very steep terrain and corresponding local flow field measurements reveal even more complex particle-flow interactions (Chapter 2, Gerber et al., 2017a) than previously suggested by model studies. On even smaller scales the main driver of snow accumulation patterns is post-depositional snow transport by drifting and blowing snow, which is dependent on local topographic features and wind gusts (Lehning and Fierz, 2008; Mott et al., 2010).

Complex terrain-flow-precipitation interactions (i.e. the effect of terrain-induced flow field variations on the precipitation formation and distribution), especially on the mountain-ridge scale, still leave the relative importance of the different pre-depositional processes for snow accumulation and the frequency of occurrence barely known (Mott et al., 2014; Vionnet et al., 2017). Running a coupled simulation of the snowpack model Crocus and the atmospheric model Meso-NH in large-eddy simulation (LES) mode, Vionnet et al. (2017) addressed the question of the relative importance of these different processes including snow redistribution by wind. Their results show that post-depositional snow transport dominates snow accumulation variability, but leaves the question of the relative importance of pre-depositional processes open.

Given the small scale of these processes their relative importance may either be addressed based on very high resolution numerical simulations or based on spatially highly resolved precipitation measurements. Therefore, accurate model results and radar measurements at high resolution are essential. Both, however, are challenging to achieve and very high resolution simulations are still rare especially over complex terrain. Remote sensing techniques, on the other hand, are the most important methods to obtain high-resolution spatial measurements of atmospheric properties at different atmospheric levels. They permit to gain information about both the small- and the large-scale properties of the atmospheric processes. The particular place among these techniques belongs to the weather radar, due to its wide coverage, fine spatial resolution, and interaction of microwaves with the precipitation. These properties have been used to infer orographic precipitation enhancement, particularly in the case of liquid precipitation (Panziera et al., 2015).

In this study, we present very high resolution WRF simulations, which are forced by 2.2 km resolution Consortium for Small-scale Modeling (COSMO) analysis and high resolution radar estimates making use of the recently renewed MeteoSwiss radar network (Germann et al., 2015) and its adequate technical performances which allow observing precipitation in the challenging, complex alpine environment. Combining the COSMO–WRF simulations with operational radar measurements, we perform a variability analysis for snow precipitation at a regional to mountain-ridge scale to address the question: How much snow precipitation variability is represented by very high resolution WRF simulations?

Model simulations, radar measurements and analysis techniques are presented in Section 3.2. In a first part of the results and discussion (Section 3.3), we validate COSMO–WRF simulations against point measurements of temperature, relative humidity, wind speed and direction (Section 3.3.1). Spatial precipitation patterns in both radar estimates and COSMO–WRF simulations, are presented in Section 3.3.2. Subsequently, we address the question how well the overall precipitation variability is represented in the model by analyzing the domain-wide statistics (Sections 3.3.3). To address the spatial variability of precipitation patterns we present a discussion of dominant processes based on variograms and 2D-autocorrelation maps (Sections 3.3.4). Variograms and autocorrelation analysis are widely used to address the spatial variability of snow accumulation and precipitation (e.g. Deems et al., 2008; Mott et al., 2011; Schirmer and Lehning, 2011; Scipión et al., 2013; Vionnet et al., 2017). While scale analysis has been performed multiple times for snow accumulation patterns on a local scale, we address measured and modeled snow precipitation patterns at the approximate elevation of the operational weather radar on Weissfluhgipfel at 2830 m above sea level (m asl) on a mountain-ridge to regional scale. Additionally, we analyze modeled ground precipitation without taking into account any post-depositional processes.

Given the different scales of analysis compared to previous studies, here we address scales at which local cloud dynamics and particle-flow interactions are expected to occur but leave out scales at which snow accumulation is expected to be dominated by post-depositional snow redistribution. Following this analysis of spatial precipitation variability, which includes a discussion of dominant processes driving the spatial variability of precipitation patterns, Section 3.3.5 addresses the question if an increased model resolution may improve the representation of spatial variability in the model. Finally, our findings about the model performance, our analysis of the spatial variability of precipitation and future perspectives are wrapped up in a conclusion and outlook (Section 3.4).

3.2 Data and Methods

3.2.1 WRF model setup

Atmospheric simulations are performed with the non-hydrostatic and fully compressible Weather Research and Forecasting (WRF) model (Skamarock et al., 2008) version 3.7.1 for the region of Eastern Switzerland (Figure 3.1). Simulations are set up with four one-way nested domains (d01–d04, Figure 3.1). Domain d01 has a horizontal resolution of 1350 m, with 40 vertical levels and covers a region of about 250 km times 320 km including eastern Switzerland and a portion of the neighboring countries (Figure 3.1, Table 3.1). The three nests have horizontal resolutions of 450 m, 150 m and 50 m using a nesting ratio (dx_{parent}/dx_{nest}) of 3. Domains d02–d04 have 40, 60 and 90 vertical levels, respectively, with the model top at 150 hPa using a preliminary version of vertical nesting (Daniels et al., 2016). Twenty and 40 vertical levels are refining the whole atmosphere in domains d03 and d04, respectively. Ten vertical levels in d04 are introduced to additionally refine the boundary layer. To make sure that there is plenty of domain for the model to adapt to the refined topography, domain d02 is shifted toward the eastern boundary of domain d01 as dominant wind directions are from a north-westerly and southerly direction. Domain d02 covers the central northern part of the Grisons, while domains d03 and d04 cover the surroundings of Davos and the upper Dischma valley, respectively (Figure 3.1). Simulations are performed for three snow precipitation events on 31 January 2016, 4 February 2016 and 5 March 2016 (Section 3.2.5).

The parent domain is run with a planetary boundary layer (PBL) scheme (non-large eddy simulation (non-LES) mode), while the three nests are run in the LES mode. No strong differences were found when running domains d02 and d03 in non-LES mode (not shown). Therefore and as we are interested in having an as good as possible representation of small-scale winds, we decided to run our simulations in the LES mode for all nested domains. Domains d02 and d03 are within the “gray zone” (Wyngaard, 2004). There are approaches omitting simulation in the “gray zone” by the choice of a higher grid refinement ratio (MunozEsparza2017), which would be worth a sensitivity study. However, we use the well-tested 1:3 grid refinement ratio and keep our model setup consistent with the very high resolution simulations by Talbot et al. (2012), except that they perform separate simulations for the non-LES and LES domains, while we run a nested simulation with one-way feedback for all four domains. Running a nested simulation of the non-LES and LES domains turned out to be necessary for precipitation to evolve properly in the LES domains, as hydrometeors cannot be used as a boundary condition for the parent domain but are fed to nested domains in WRF simulations. Subgrid scale turbulence is parametrized by the 1.5 order turbulent kinetic energy closure (Skamarock et al., 2008). For the non-LES setup the Yonsei University PBL parameterization (YSU PBL, Hong et al., 2006) is used, which is considered to be one of the schemes showing the best performance over complex terrain (Gómez-Navarro et al., 2015). An adapted version of YSU PBL was shown to perform even better when taking into account subgrid-scale variability of the terrain (Jiménez and Dudhia, 2012; Gómez-Navarro et al., 2015). However, given our high model resolution we decided to keep the model simple and run the simulations with the standard YSU PBL. Landuse data is taken from the Corine dataset (European Environmental Agency, 2006) and translated to the USGS conventions (Pineda et al., 2004; Arnold et al., 2010). Soil type is set to *silty clay loam* for the whole domain. The link between the soil, which is modeled by the Noah land-surface model with multi-parameterization options (Noah-MP, Niu et al., 2011; Yang et al., 2011), and the atmosphere is given by the MM5 Monin-Obukhov surface layer model (Paulson, 1970; Dyer and Hicks, 1970; Webb,

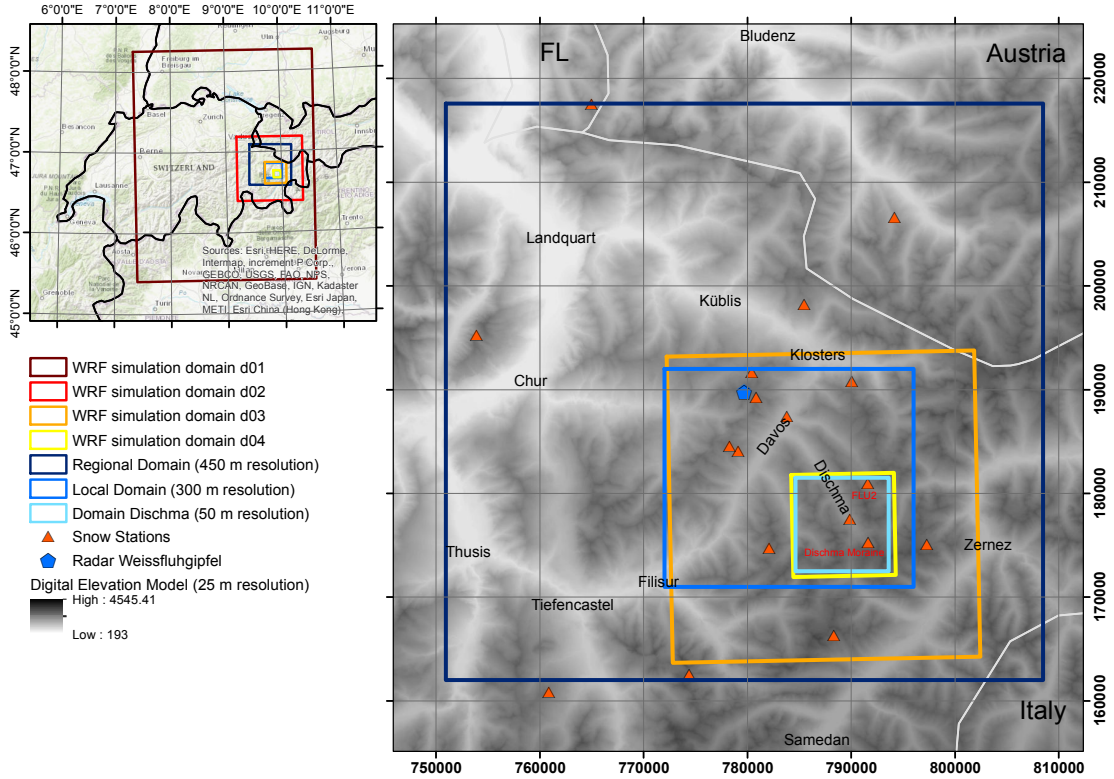


Figure 3.1: Overview over the study area in the eastern part of Switzerland surrounding Davos. WRF simulation domains (d01–d04, dark red to yellow) and evaluation domains (blue) give information on the simulation and evaluation setup. The 18 meteorological stations (red triangles) are within or very close to the regional domain. The two stations Dischma Moraine and FLU2, which are used to validate the model, are within domain Dischma. The operational weather radar is located on Weissfluhgipfel at approximately 2830 m above sea level (m asl, blue pentagon). Coordinates in the right panel are in Swiss coordinates CH1903LV03 (unit: m). Shaded topography: dhm25 © 2018 swisstopo (5740 000 000).

1970; Zhang and Anthes, 1982; Beljaars, 1994), which is based on the Monin-Obukhov similarity theory (Obukhov, 1971). For microphysics the Morrison 2-moment precipitation scheme (Morrison et al., 2005; Morrison et al., 2009) is used, which was found to be one of the schemes, which most adequately simulate snow precipitation over complex terrain (Liu et al., 2011). Details about processes in the Morrison parameterization are given in Appendix B.1. An investigation of different microphysical parameterizations would be interesting, but is beyond the scope of this study. Given the high horizontal resolution no sub-grid parameterization for cumulus clouds is used.

The 2.2 km horizontally resolved Consortium for Small-scale Modeling (COSMO–2) analysis by MeteoSwiss are used as initial and boundary conditions for the parent domain. For COSMO–2 analysis data to be readable by the WRF pre-processing system a regridding of the rotated COSMO-coordinates to latitude-longitude coordinates is required. COSMO preprocessing, model adaptations and details about the model simulations are given in Gerber and Sharma (2018, Appendix D).

Topography in the model is based on the Aster Global Digital Elevation Model V002 with a resolution of one arc-second (METI/NASA, 2009). Terrain smoothing has been applied for all domains due to the very steep terrain in the simulation area. Four cycles of the WRF 1–2–1 smoothing (i.e. a moving window filter with a window length of 3 and weights of 1:2:1 for the grid points $i-1$, i and $i+1$) are applied to all four domains to keep all slopes in domain d04 (50 m horizontal grid spacing) below 45° . Additionally, the boundaries of the parent domain are smoothed to match COSMO-topography (Gerber and Sharma, 2018, Appendix D.). Test simulations are run with 14 cycles of WRF 1–2–1 smoothing, which allows

Table 3.1: Setup for the four nested domains (d01–d04) used in the WRF simulations. For the planetary boundary layer (PBL) the simulation mode is given, distinguishing between non-large eddy simulation (LES) and LES settings. For non-LES settings the PBL scheme is given. Additionally, the subgrid scale (SGS) turbulence parameterization is given for all four domains. dx, dy give the horizontal resolution. Vertical levels (total) gives the number of vertical levels in the different domains. Vertical levels (<1000 m) gives the number of vertical levels in the lowest 1000 m of the atmosphere. The time step (dt) and the maximum slope angles (Max. slope) are given for simulations with 4 (14) smoothing cycles.

Domain	PBL mode	PBL scheme	SGS scheme	dx, dy (m)	Vertical levels		dt (s)	Max. slope °
					total	<1000 m		
d01	non-LES	YSU ¹	TKE clos. ²	1350	40	8	1 (6)	17.5 (9.9)
d02	LES	-	TKE clos. ²	450	40	8	1/3 (2)	35.2 (26.5)
d03	LES	-	TKE clos. ²	150	60	9	1/9 (1/2)	39.8 (36.8)
d04	LES	-	TKE clos. ²	50	90	21	1/27 (1/4)	44.5 (37.4)

¹YSU: Yonsei University PBL scheme

²TKE clos.: 1.5 order turbulent kinetic energy (TKE) closure

for a longer computational timestep and therefore saves computational time (Table 3.1). Maximum slope angles for all domains and different smoothing are given in Table 3.1. Simulations with different precision of topography further allow us to address the importance of the representation of topography in the model. To allow the simulations to adapt to higher resolution topography domains d01–d04 are run with a spin-up of 43 h, 19 h, 7 h and 1 h, respectively.

As the snow cover in complex alpine terrain is likely rougher than for a flat field and to account for non-resolved topography and additional smoothing, snow surface roughness length has been changed to 0.2 m. The chosen roughness length is much larger than roughness lengths assumed by e.g. Mott et al. (2015). However, grid spacing in our simulations is larger and the roughness length is chosen such that it accounts for roughness elements in complex terrain (e.g. large rocks) and non-resolved topography, which are assumed to have an average size of about 2 m. This estimate is based on a comparison of a 2-m digital terrain model (DTM-AV © 2018 swisstopo (5704 000 000)) to a 25-m resolution digital elevation model (dhm25 © 2018 swisstopo (5740 000 000)), which reveals an average difference on the order of 2.5 m for bare ground conditions in domain d04 between 2200 and 2700 m asl. Hence, the estimate of 2 m is rather conservative but takes into account smoothing of the terrain by the snow cover.

For the model validation (Section 3.3.1) WRF variables are linearly interpolated to the coordinates of the meteorological station (see Section 3.2.2). Temperature is corrected for elevation due to terrain smoothing using a moist-adiabatic temperature gradient of -0.0065 K m^{-1} . Modeled wind speeds are extrapolated to the measurement height by applying a logarithmic wind profile, as wind measurements at the automatic weather stations are not taken at 10 m but 4 or 5 m above ground (Section 3.2.2). This is a rough approximation given the assumption of a neutral atmosphere. For simulation domains d01–d03 10-m wind speeds are extrapolated to the elevation of the sensor above the snow cover, while for domain d04 wind speeds at the lowest model level (approximately 3 m above ground) are used for the correction. The dynamic reference roughness length is chosen to be 0.2 m (corresponding to the surface roughness length in the model simulations). For wind direction comparisons wind directions at 10 m and 3 m above ground are chosen for the simulation domains d01–d03 and d04, respectively. As a reference COSMO-2 variables of the closest grid point to the station are included in the model validation and hence in Figure 3.2 and Figure 3.3. Two-meter temperature and 10-m wind speed of COSMO-2 are corrected for elevation by the same procedure as for the WRF simulations.

3.2.2 Automatic weather stations

Snow depth measurements from a total of 18 automatic weather stations in the central northern part of the Grisons (Figure 3.1) are used. Two stations, (*Dischma Moraine* and *Dischma Dürrboden*), were installed as part of the Dischma Experiment (DISCHMEX), in which processes of snow accumulation and ablation

in the Dischma valley near Davos (Switzerland) are addressed (Chapter 2, Gerber et al., 2017a; Mott et al., 2017; Schlögl et al., *in review*). 16 stations are part of the Intercantonal Measurement and Information System (IMIS). The 18 stations are located between 1560 m asl and 2725 m asl. The stations measure snow depth in addition to the standard meteorological parameters. All stations have shielded temperature and humidity sensors, but are unheated. Biased temperatures around midday and occasional data gaps due to iced instruments may therefore occur (Huwald et al., 2009; Grünewald et al., 2012). Two stations (*Dischma Moraine* and *FLU2*), which are located in the WRF domain with a horizontal grid spacing of 50 m, are used for the model validation. The variables evaluated are 2-m temperature, 2-m relative humidity, wind speed and wind direction. Wind measurements at IMIS stations are taken about 5 m above ground, while the wind sensor at station *Dischma Moraine* is located at about 4 m above ground.

3.2.3 Operational weather radar data

Weather radar datasets employed in the presented analyses are acquired by the MeteoSwiss operational radar located at the Weissfluhgipfel (2850 m asl), in the proximity of Davos. It is a dual-polarization Doppler weather radar, providing complementary information about the detected hydrometeors by considering their interaction with the incident electromagnetic radiation in both, horizontal and vertical, polarization planes. This complementary information leads to an enhanced clutter detection, which makes the radar measurements in such a complex mountainous terrain significantly more reliable. The polarimetry also makes it possible to identify the type of hydrometeors (Besic et al., 2016), which allows us to be confident that in the zone of interest for the presented study we deal with solid precipitation, consisting mostly of aggregates and crystals, and partly of rimed ice particles.

The radar operates in 5-minutes cycles during which it scans the surrounding atmosphere by performing complete rotations at twenty different elevations, from -0.2° to 40° (Germann et al., 2015). Operationally, the size of a radar sampling volume is 500 m in range, whereas the size observed in the perpendicular plane depends on the half-power beamwidth and increases with range. The acquired data undergo an elaborated procedure of corrections (Gabella et al., 2017). Before the quantity of precipitation at the ground level is estimated by averaging over 1 km^2 the observations are corrected for the Vertical Profile of Reflectivity (VPR) with the weight assigned to volumes being inversely proportional to their height above the ground (Germann et al., 2006).

In the framework of our study, rather than relying on the operational radar product, we use data with the highest available resolution of 83 m in range. We also adopted a more conservative, non-operational method of clutter identification, which relies exclusively on the polarimetry and leaves very little residual clutter, however, sometimes at the expense of removing some precipitation. Given that we consider only radar measurements at low elevation angles in the vicinity of the radar and that the bright band is not present in our case studies (all radar measurements are from above 2800 m asl during the winter season), the observations are not corrected for the VPR. Furthermore, given the strong influence of wind on the snow precipitation, we restrict our precipitation estimate to only four elevations, from the second to fifth (0.4° , 1° , 1.6° , 2.5°), avoiding the first one, judged to contain too little information due to the abundant rejected ground clutter areas.

Polarimetry helps to identify non-meteorological scatterers, to distinguish between different types of hydrometeors, to correct for signal attenuation and to make quantitative estimates of intense to heavy rainfall. For snowfall measurements it is common to use reflectivity Z at horizontal polarization and convert it into snow water equivalent S using a so-called Z - S relationship (Saltikoff et al., 2015):

$$Z = 100S^2. \quad (3.1)$$

The coefficients used in this formula account for the dielectric properties and fall velocities of snow and convert reflectivity Z in snow water equivalent S . The radar provides an indirect estimate of snowfall, rather than a direct measurement. Applied on each radar sampling volume scanned by the four selected elevations in the zone of interest (up to 40 km around the radar), the formula gives an estimate of liquid precipitation equivalent in the three-dimensional volume. By vertically averaging estimates from the four elevation sweeps using equal weights, we obtain the estimate of precipitation in polar (range, azimuth)

coordinates at a flat plane at the height level of the radar. These estimates are summed up over 24 h to get the accumulation maps used in the study.

Further on, the polar accumulation maps are re-sampled by means of the bi-linear interpolation to the Cartesian grid of the regional domain (450 m resolution) and the local domain (300 m resolution). The obtained Cartesian maps are finally processed to remove the residual clutter using a 3×3 median filter, partly or entirely. The former means that only the isolated high values in the original map are replaced with the corresponding value of the filtered map, at the positions where the difference between the original and the filtered map appears to be larger than 5 mm (hereafter “partly-filtered”). The latter means that the entire map is influenced by the median filtering (hereafter denoted as “entirely-filtered”).

3.2.4 Autocorrelation and variogram analysis

To investigate the variability of snow precipitation and accumulation patterns and their relation to topography a scale analysis, based on 2-dimensional (2D) autocorrelation maps and variograms, is performed. 2D-autocorrelation maps and variograms are further used to relate variability in radar and WRF precipitation. Given the resolution restriction by the radar measurements (Section 3.2.3) we analyze two different domains using horizontal resolutions of 450 m and 300 m, respectively. The domain with a resolution of 450 m covers an area of about 58 km times 56 km centered over the radar on Weissfluhgipfel (hereafter regional domain, Figure 3.1). The domain with a resolution of 300 m covers an area of 24 km times 21 km to the south of Davos (Switzerland) including the Dischma valley (hereafter local domain). Radar data (300 m resolution) and WRF precipitation on three resolutions (450 m, 150 m and 50 m) are additionally, evaluated on domain Dischma to address the influence on the spatial resolution of variability. Domain Dischma covers the upper Dischma valley with an extent of 9 km times 9 km.

To produce variograms the semivariance (γ) is calculated at 50 logarithmic lag distance bins (h , i.e. a set of distance ranges) by

$$\hat{\gamma}(h) = \frac{1}{2|N(h)|} \sum_{(i,j) \in S(h)} (a_j - a_i)^2, \quad (3.2)$$

where $S(h)$ are the point pairs (i, j) and $N(h)$ gives the number of point pairs of the evaluated variable a . WRF and radar snow precipitation and topography are evaluated at 450 m and 300 m resolutions with a maximum lag distances of 25 km and 10 km, respectively. Variograms for domain Dischma are calculated with a maximum lag distance of 5 km. Minimum numbers of point pairs in one lag distance bin for the local and regional domain are 18317 and 8035, respectively. For domain Dischma the minimum number of point pairs is between 677 and 55419, depending on the resolution.

To determine scaling properties an empirical log-linear model is fit to the variogram by least square optimization (Schirmer et al., 2011). The model used is not a valid variogram model but used to describe the experimental variograms and chosen to be consistent with Schirmer et al. (e.g. 2011). For all variograms three empirical log-linear models are fit:

$$y(x) = \begin{cases} \alpha_1 * \log(h) + \beta_1, & \text{for } \log(h) < l_1 \\ \alpha_2 * \log(h) + \beta_2, & \text{for } l_1 \geq \log(h) < l_2 \\ \alpha_3 * \log(h) + \beta_3, & \text{for } \log(h) \geq l_2 \end{cases} \quad (3.3)$$

using the constraint that each log-linear model needs to contain a minimum of four data points and the continuity constraint(s)

$$\begin{aligned} \alpha_1 \log(l_1) + \beta_1 &= \alpha_2 \log(l_1) + \beta_2 \\ \alpha_2 \log(l_2) + \beta_2 &= \alpha_3 \log(l_2) + \beta_3 \end{aligned} \quad (3.4)$$

where $\alpha_{1,2,3}$ and $\beta_{1,2,3}$ are the slopes and intercepts of the three log-linear models, respectively. Scale breaks (l_1 , l_2) are the lag distances of the intersections of the first and second, and second and third log-linear model, respectively. Scale breaks were previously found to determine the scale of a change of dominant processes (e.g. Deems et al., 2006). To address the variability with respect to the overall variability in the respective domain, all variograms are normalized by the total domain-wide variance.

2D-autocorrelation is calculated based on Pearson's correlation coefficient r of all grid point pairs for a maximum lag distance of ± 40 grid points in x- and y-direction. This results in maximum lag-distances of 18 km for the regional domain.

3.2.5 Snowfall events

This study is based on three precipitation events in winter 2016. On 31 January 2016 the Azores high and a low-pressure area over Scandinavia induce westerly flow over central Europe and relatively mild temperatures with about -3°C at 2500 m asl. A shift of the Azores high toward northern Spain and a trough over eastern Europe lead to a change in wind direction toward northerly advection and a decrease of temperature (about -12°C at 2500 m asl) on 4 February 2016. On 5 March 2016 a low-pressure area over France, which is part of a large depression area over central Europe, causes southerly advection over Switzerland. Temperatures are about -7°C at 2500 m asl. Given the relatively high temperatures on 31 January 2016, which resulted in quite substantial liquid precipitation at the lowest elevations, total (solid and liquid) ground precipitation is evaluated. This does not make a big difference for the precipitation events on 4 February 2016 and 5 March 2016 but is essential for the precipitation event on 31 January 2016. For precipitation patterns at the elevation of the radar (2830 m asl) we only analyze solid precipitation from WRF.

3.3 Results and Discussion

3.3.1 Point validation of WRF simulations

Two-meter air temperature, and 4- or 5-m wind speed and direction at two stations (Section 3.2.2) are compared to WRF to validate the model (Figure 3.2a-c and Figure 3.3a-c). For both stations 2-m temperature matches reasonably with observations although especially for the precipitation event on 4 February 2016 substantial temperature deviations occur around midday. Deviations of the WRF model from station measurements during midday are likely caused by errors in station measurements due to radiative heating of the multiplate shielded temperature sensors (Huwald et al., 2009, Section 3.2.2). Additionally, offsets in simulated temperatures may be linked to offsets in the input by COSMO-2.

Relative humidity shows partially good agreement, but shows a strong temporal variability (Figure 3.2d-f and Figure 3.3d-f). Some disagreement of relative humidity simulated by WRF compared to station measurements might be induced by COSMO input, which for some cases shows an offset compared to station measurements. This bias can sometimes be reduced by WRF simulations but for other cases WRF introduces an additional bias. WRF is generally able to capture main drops in relative humidity at the two investigated stations but it introduces additional drops compared to measurements. The microphysics parameterization is originally developed for simulations with a coarser resolution, which produce less vertical motions. Thus, the introduction of a higher variability in relative humidity in our WRF simulations may be due to strong subsidence and lifting, which lead to an overestimation of adiabatic cooling or warming and hence to an overestimation of humidity generation or decay. Additionally, differences between modeled and measured relative humidity may be due to measurement uncertainties.

Simulated wind direction shows good agreement with measured wind direction (Figure 3.2g-i and Figure 3.3g-i). In complex terrain, simulations are often limited to resolutions, which are too coarse to resolve smaller-scale terrain features that affect near-surface wind direction (e.g. due to lack of high resolution terrain data, or computational resources), and thus cannot accurately capture changes in wind direction close to the surface where weather stations are located. Good agreement in wind direction modeling in our COSMO-WRF simulations in complex terrain is likely due to the high resolution of topography. For some cases wind directions in the WRF simulations additionally improve for higher resolutions although for others terrain smoothing is likely to have adverse effects on modeled wind direction.

Compared to the good agreement of wind direction, wind speeds show only partially good agreement with station measurements (Figure 3.2k-m and Figure 3.3k-m). Wind speeds were found to strongly depend

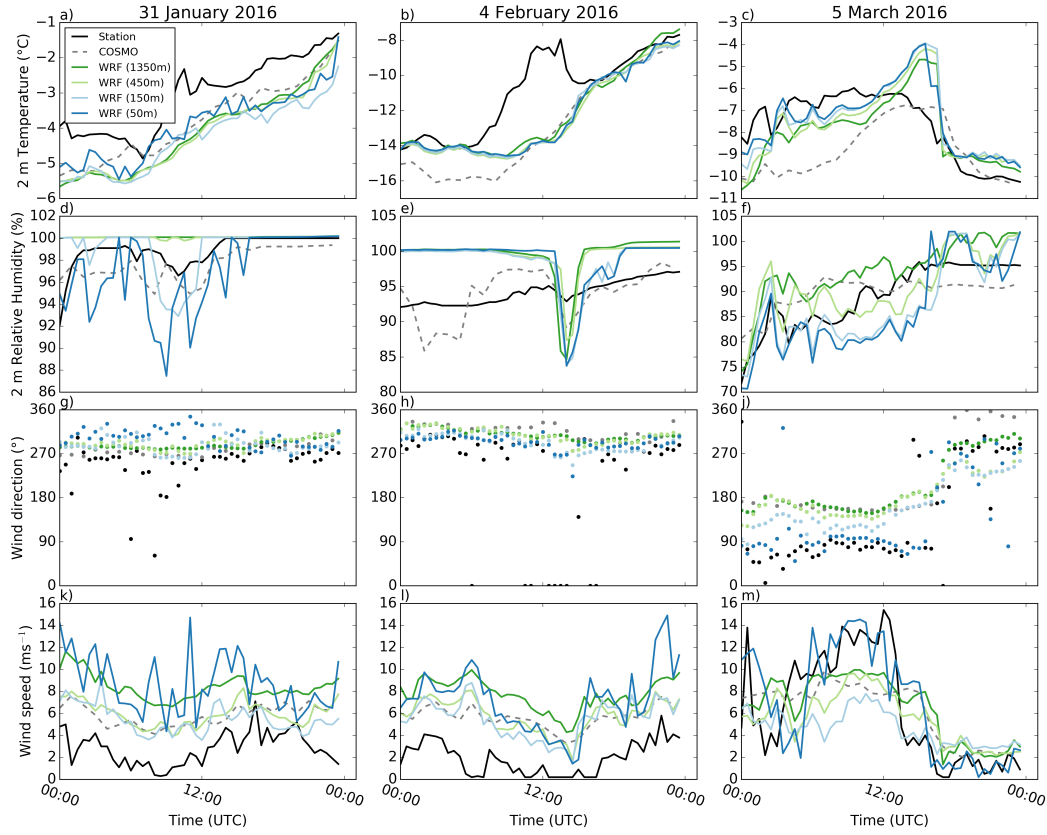


Figure 3.2: Comparison of 2-m temperature (°C), 2-m relative humidity (%), 4-m wind speed (m s⁻¹) and wind direction (°) at station Dischma Moraine (black) to WRF simulations interpolated to the coordinates of station Dischma Moraine for the three precipitation events on 31 January 2016, 4 February 2016 and 5 March 2016 for all four simulation domains (d01: dark green, d02: light green, d03: light blue, d04: dark blue). For comparison COSMO-2 is added for the closest grid point (dashed gray). Two-meter temperature in WRF and COSMO are corrected for elevation based on a moist-adiabatic temperature gradient.

on the subgrid-scale turbulence parameterization and a strong overestimation of wind speeds was observed for different simulation setups (not shown). Applying the improved non-linear subgrid-scale turbulence parameterizations (Mirocha et al., 2010; Mirocha et al., 2014) leads to instabilities in the current model setup. The use of a snow surface roughness length of 0.2 m, representing the combined roughness of snow and surface features (e.g. rocks) compared to simulations with standard WRF roughness length of snow of 0.002 m, could partially reduce overestimated wind speeds (Appendix D, Gerber and Sharma, 2018). While we address non-resolved topography based on an increased snow roughness length, another approach to improve wind speeds in WRF simulations has been introduced by Jiménez and Dudhia (2012), who use a sink term in the momentum equation based on subgrid-scale topography. They demonstrate the ability of their approach to improve surface wind speeds. However, the effect of the subgrid scale topography is only respected for simulations using a PBL parameterization. As in our model setup a PBL parameterization is only applied for domain d01, we decide to address the non-resolved topography by increasing the surface roughness, which allows us to include the effect of non-resolved topography for all four simulation domains. Furthermore, our simulations are run over snow covered terrain, which implies that the standard roughness length used in WRF is much lower than roughness lengths for complex terrain.

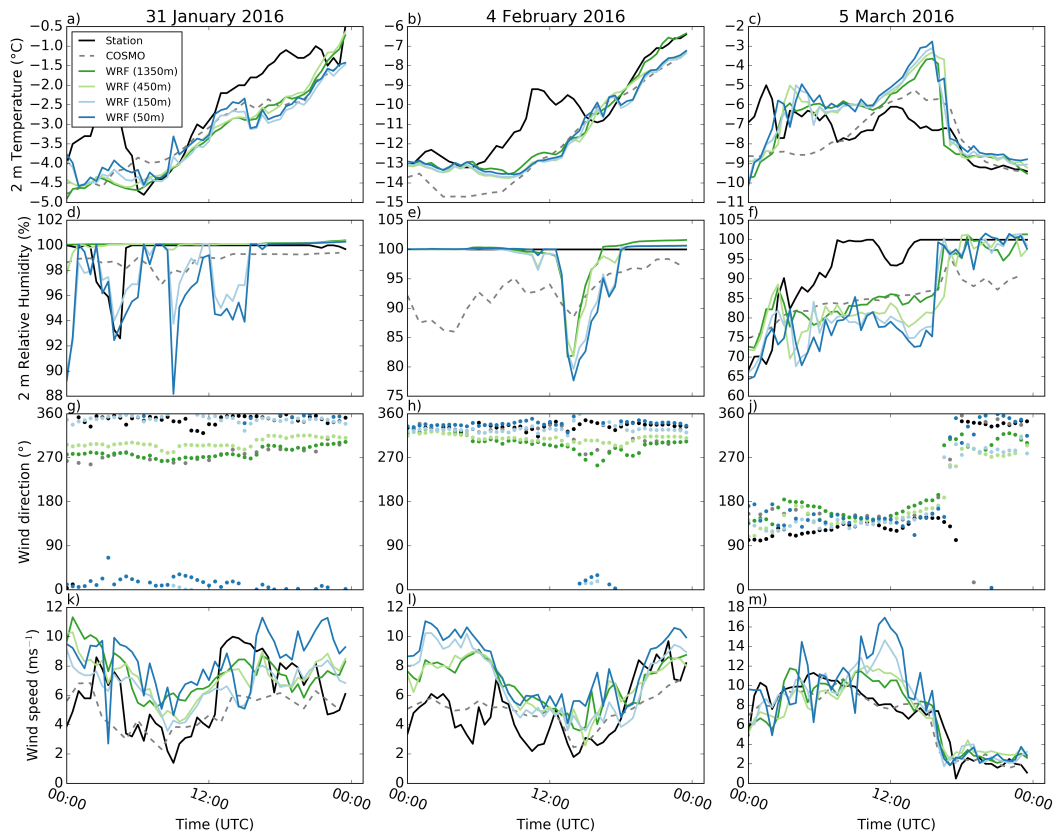


Figure 3.3: As Figure 3.2 but for the station FLU2 on the Flüelapass with 5-m wind speed and direction.

Still, applying the PBL version of Jiménez and Dudhia (2012) might be a possibility to reduce excess wind speeds in domain d01, which might also impact wind speeds in the domains d02–d04. However, such a sensitivity study is out of scope of the presented study.

Based on our approach COSMO–WRF still simulates excess wind speeds for the two precipitation events on 31 January 2016 and 4 February 2016. This overestimation is assumed to be connected to the upwind location of both stations during these two precipitation events, as speed up over windward slopes and ridges are a known problem (Mott et al., 2010; Gómez-Navarro et al., 2015). Hence, the exact location of the station relative to the ridge is important to verify wind speeds. Furthermore, local terrain features upstream of the station may disturb the wind field. For example station Dischma Moraine is located on a moraine on the northern side of the ridge between Piz Grialetsch and Scalettahorn. Station FLU2 is located on the northern side of Flüelapass above a small rock face and to the east of a terrain knoll. Such terrain features, while not represented in the model, may strongly reduce wind speeds in reality. For station Dischma Moraine on the 31 January 2016 and the 4 February 2016 an overestimation of wind speed is already observed in COSMO–2, which might be an additional reason for wind speed overestimation at this station. However, given the fetch distances and spin-up times of our model simulations (Section 3.2.1), we expect the atmosphere to develop independently. Still, if COSMO wind speeds are constantly overestimated WRF may not be able to correct for excess wind speeds. Furthermore, station measurements are prone to measurement uncertainties and riming of the unheated instruments may lead to an underestimation of wind speeds (Grünwald et al., 2012).

Generally, reasons for an overestimation of wind speeds may be manifold. An exact estimation of wind speeds at stations in the model is not expected. An additional source of uncertainty – though unlikely to be on the order of the strong excess wind speeds – is the extrapolation of wind speeds based on the assumption of a neutral atmosphere. While different potential causes of wind speed overestimation are discussed above, actual reasons for deviations in wind speed remain unknown.

Overall, we show that the presented simulation setup reasonably captures temperature, relative humidity and wind conditions in complex terrain at two stations. Wind speeds on the windward side of the mountain ridges tend to be overestimated. Temperature deviations around midday are likely due to measurement uncertainties.

3.3.2 Spatial snow precipitation and accumulation patterns

Radar precipitation maps of the regional domain covering an area of about 58 km times 56 km centered over the radar on Weissfluhgipfel (Figure 3.1) tend to show wind direction (Figure 3.2g-i, Figure 3.3g-i and Figure 3.4d-f) dependent precipitation patterns (Figure 3.4). The precipitation field on 31 January 2016 shows a strong south-north gradient (Figure 3.4a), while the precipitation field on 4 February 2016 shows a more homogeneous distribution (Figure 3.4b). For the precipitation event on 5 March 2016 radar precipitation maxima are observed over the mountain ridges in the southern part of the domain (Figure 3.4c). Although our regional domain does not represent a cross section across the whole alpine mountain range, a north-south (south-north) precipitation gradient for southerly (northerly) advection are apparent. This is in good agreement with large-scale orographic precipitation enhancement (Houze, 2012; Stoelinga et al., 2013), which favors precipitation on the upwind side of a mountain range due to topographically induced lifting and a drying due to sinking air masses downwind of the mountain range.

These large-scale patterns of orographic precipitation enhancement are partially captured in the WRF simulations (Figure 3.4d-f). Especially, for southerly advection (precipitation event on 5 March 2016) this large-scale effect is well represented in COSMO-WRF, where precipitation maxima occur over mountain ridges in the southern part of the domain and a north-south precipitation gradient is present. For northerly to north-westerly advection (precipitation events on 31 January 2016 and 4 February 2016), however, snow precipitation maxima in the WRF simulations are shifted eastward compared to radar precipitation estimates, i.e. toward the outflow boundary.

Microphysics and precipitation dynamics in the model are likely to be a limiting factor in terms of small-scale precipitation patterns. Disagreement between radar and WRF precipitation patterns may further be connected to the strong terrain smoothing in the model. Despite of the high resolution of our simulations, slope angles are relatively low with maximum slope angles of 35.2° in the regional domain due to the application of terrain smoothing (Table 3.1). Given even lower slope angles in domain d01 precipitation fed to domain d02 may already be too weak and thus needs to develop within domain d02. As mountains in the north-western part of the domain are shallower than mountains in the south-eastern area (Figure 3.1), lifting condensation may not be strong enough in the north-western area of the domain, leading to precipitation generation further downstream in the domain, where steeper and higher mountains may even lead to too strong precipitation enhancement. Additionally, if the tendency of overestimated wind speeds sustains up to higher atmospheric levels in the model, this may lead to an overestimation of the advection of hydrometeors in the microphysics scheme (Morrison et al., 2005). This would result in a downstream shift of the precipitation maximum. However, we do not expect this to have a strong impact on the regional scale precipitation distribution. Thus, there are likely additional reasons for the observed downstream shift of WRF precipitation compared to radar precipitation, which remain difficult to explain.

On a mountain-valley scale (local domain) the same tendencies emerge with good agreement in overall gradients for southerly advection and partially reversed gradients for northerly to north-westerly advection when comparing WRF to radar precipitation patterns (not shown). WRF precipitation patterns generally show a stronger dependency on topography expressed in higher precipitation rates over higher elevations. Radar precipitation patterns additionally reveal small-scale precipitation patterns. Very small-scale patterns are visible on the partly-filtered radar maps (Section 3.2.3, not shown), while in entirely-filtered radar estimates (Figure 3.4a-c) smallest-scale patterns are eliminated but patterns of about 1 km size emerge. Patterns in the entirely-filtered data could be small-scale precipitation cells, while the very small-scale

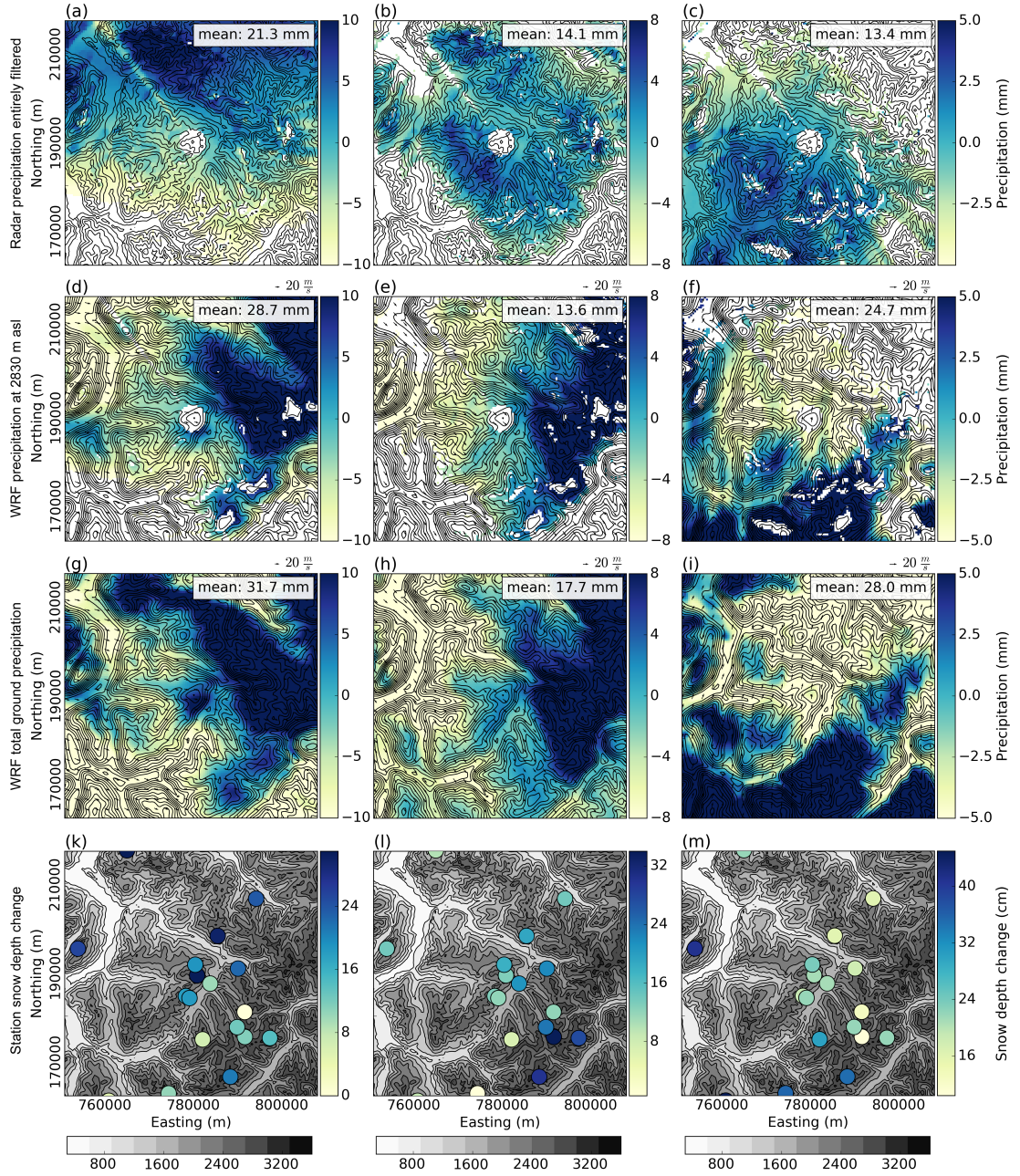


Figure 3.4: Twenty-four hour snow precipitation (mm) from a-c) MeteoSwiss entirely-filtered radar measurements, d-f) Weather Research and Forecasting (WRF) snow precipitation at 2830 m above sea level (m asl), g-i) WRF total ground precipitation and k-m) 24 h snow depth changes (cm) at meteorological stations on 31 January 2016 (left), 4 February 2016 (middle) and 5 March 2016 (right) with a resolution of 450 m in the regional domain (Figure 3.1). Radar precipitation is estimated from different radar elevations (Section 3.2.3). White areas in a-f mark areas where clutter is removed and small values in the radar data are masked. The same mask is applied for WRF solid precipitation at 2830 m asl (approximate elevation of the radar, d-f), for which additionally areas where WRF topography is higher than 2830 m asl are masked. Arrows in d-f indicate wind direction and speed at an elevation of 2830 m asl. Northing and easting are given in the swiss coordinate system (CH1903LV03). Note different colorbars. Contour lines in a-c) and k-m): dh25 (c) 2018 swisstopo (5740 000 000). Gray shading in k-m) represent topography.

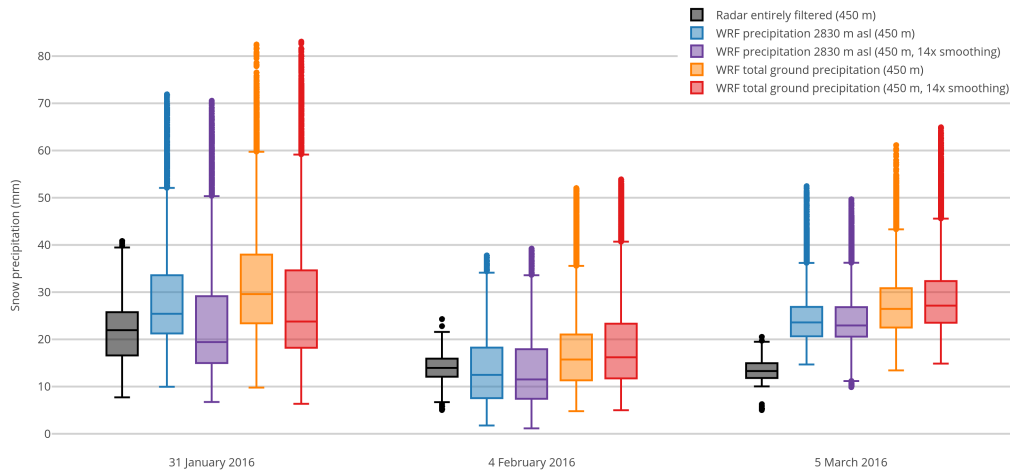


Figure 3.5: Domain-wide 24 h precipitation statistics for the regional domain (450 m resolution, Figure 3.1) for the three precipitation events on 31 January 2016, 4 February 2016 and 5 March 2016. Gray colors show entirely-filtered radar precipitation. WRF precipitation at 2830 m above sea level (m asl) for simulations with weak terrain smoothing (Section 3.2.1) and strong terrain smoothing are given in blue and violet, respectively. Orange (red) shows boxplots of WRF total ground precipitation for weak (strong) terrain smoothing. Radar precipitation and WRF precipitation at 2830 m asl are masked (as shown in Figure 3.4).

patters are most likely noise in the radar data (see Section 3.3.4).

New snow depth measured at 18 automatic weather stations in the regional domain (Figure 3.4k-m) over 24 h shows a distinct elevation gradient, which is quite well represented by WRF total ground precipitation (Figure 3.4g-i). For 31 January 2016 and 5 March 2016 the large-scale precipitation trend observed in the radar data is generally represented in station measurements. On 4 February 2016 station measurements suggest a precipitation peak in the upper Dischma valley (lower left quadrant in Figure 3.4l), which agrees with WRF simulations. Radar estimates, however, show a more homogeneous distribution of precipitation on 4 February 2016. Snow depth changes at the stations are very local and strongly affected by wind redistribution of snow, which may disturb the large-scale gradient. Additionally, the distribution of stations is not homogeneous over the regional domain and fewer stations are available in the western part of the domain.

The visual comparison of radar and WRF precipitation patterns for all three events (Figure 3.4) reveals that precipitation patterns are influenced by wind direction and topography. Large-scale precipitation patterns are in agreement with station measurements, although the latter are strongly influenced by the local wind field and snow redistribution processes.

3.3.3 Mean variability

Radar precipitation distributions at 2830 m asl on the regional domain (450 m resolution, Figure 3.5) show a larger interquartile range (IQR) than radar precipitation on the local domain (300 m resolution, Appendix B.2), confirming that local precipitation is more uniform than regional precipitation. Radar median precipitation over 24 h is on the order of 10 mm to 20 mm water equivalent for all three precipitation events in the regional domain. The median of radar precipitation in the local domain can be both, higher or lower than in the regional domain. Although radar estimates are based on a reference S-Z relationship, the employed formula (Equation 3.1) is not immune to potential estimation errors. Therefore, despite reasonably assuming that the potential estimation errors should not significantly influence the variability and the relative intensity of the precipitation fields, we consider potential inaccuracies in our interpretations.

For the precipitation event on 31 January 2016 and 4 February 2016 median precipitation at 2830 m asl in the COSMO-WRF simulations is in reasonable agreement with radar median precipitation (Figure 3.5),

even though WRF and radar precipitation patterns are different (Section 3.3.2). However, for the precipitation event on 5 March 2016 the median of precipitation in the regional domain is higher in WRF simulations compared to radar measurements while the large-scale precipitation gradient is in good agreement (Figure 3.4c and Figure 3.4f). The IQR of WRF precipitation is generally larger compared to the IQR of radar precipitation and the domain-wide WRF precipitation distribution has longer tails compared to the radar precipitation distribution. These tendencies are even stronger for the domain-wide WRF precipitation distribution on the local domain (Appendix B.2). This confirms the hypothesis that the model tends to overestimate precipitation for higher resolutions with steeper and more complex topography.

The domain-wide median and IQR of precipitation at 2830 m asl in WRF simulations with weaker terrain smoothing and stronger terrain smoothing (Section 3.2.1) are similar with a slight tendency of higher median values for weaker smoothing, indicating that the accuracy of topography does not have a strong influence on the domain-wide statistics of precipitation on the regional scale. Enhanced precipitation for weaker terrain smoothing compared to stronger terrain smoothing could be explained by enhanced precipitation production due to steeper topography.

An overestimation of precipitation in WRF simulations was previously reported (e.g. Mass et al., 2002; Leung and Qian, 2003; Silverman et al., 2013) and could be due to various reasons. Mass et al. (2002) and Leung and Qian (2003) among others report that WRF tends to show stronger overestimation of precipitation for higher model resolutions compared to coarser model resolutions. Additionally, they document a dependency on the intensity of precipitation. An overestimation of orographic precipitation enhancement in more complex terrain or an overestimation of moisture in the model were further reported by Silverman et al. (2013). An overestimation of orographic precipitation enhancement would be in agreement with a stronger overestimation of precipitation for the local domain compared to the regional domain and for weaker smoothing compared to stronger smoothing. Furthermore, it is likely to occur for simulations with high horizontal resolution as higher peaks and steeper slopes are preserved (Silverman et al., 2013). Compared to a shallow topography, higher peaks and steeper slopes may cause stronger lifting and subsidence, which is also a likely cause for additional drops in relative humidity in WRF compared to measured relative humidity (Section 3.3.1, Figures 3.2 and 3.3). This tendency seems to only apply for the highest elevations. For lower elevations strong smoothing may result in elevation differences, which are too small for precipitation to evolve by lifting condensation (Section 3.3.2). As additional reasons for precipitation overestimation in WRF an overestimation of precipitation in the driving model (Caldwell et al., 2009) and underlying landuse characteristics (Silverman et al., 2013) were mentioned. The latter was, however, previously found to only have a weak influence on the precipitation amount (Pohl, 2011). Humidity in COSMO-2 is an unlikely reason as COSMO-2 shows rather a tendency of underestimating relative humidity compared to station measurements (Figures 3.2 and 3.3).

Even though there are many possible reasons for overestimation of precipitation in WRF, the estimation of solid precipitation from radar measurements is also subject to uncertainties (e.g. Cooper et al., 2017). Given uncertainties in radar precipitation estimates the comparison of median domain-wide precipitation should be taken with care. An in depth analysis of spatial variabilities is given in Section 3.3.4.

At the ground level WRF precipitation tends to show higher median values of precipitation compared to WRF precipitation at 2830 m asl for both domains. The IQR is similar. From this we hypothesize that there are precipitation formation or enhancement processes taking place between the elevation of the radar and the ground. This is in good agreement with the fact that near-surface processes can strongly enhance snow precipitation (e.g. riming). Overall, this analysis shows that WRF tends to overestimate domain-wide precipitation and precipitation variability at 2830 m asl compared to radar estimates.

3.3.4 Spatial variability

To address spatial patterns and variability of precipitation a scale analysis is performed augmented with a 2D-autocorrelation analysis (Section 3.2.4). Given the overestimation of precipitation in the model and the large differences in domain-wide variability between the model and radar precipitation estimates (Section 3.3.3), all variograms are normalized by the domain-wide variability, which allows analysis of spatial patterns with respect to the overall range of precipitation values. From the analysis of precipitation patterns (Section 3.3.2), we further know that there are strong large-scale precipitation gradients in the

Table 3.2: Large-scale linear trends of radar (Radar entirely filtered) and WRF precipitation patterns on the regional domain (Figure 3.1). WRF precip. at 2830 m asl refers to solid precipitation in WRF simulations at 2830 m above sea level and WRF total ground precip. refers to the total (solid and liquid) precipitation at the ground level. Orient. gives the direction of the slope and Intensity the strength of inclination. 0° would indicate a slope pointing toward the East. WRF snow precipitation is from simulations with weak terrain smoothing (Section 3.2.1).

	31 January 2016		4 February 2016		5 March 2016	
	Orient.	Intensity	Orient.	Intensity	Orient.	Intensity
Radar entirely filtered	86.9°	0.17	-125.9°	0.01	-114.8°	0.04
WRF precip. (2830 m asl)	16.7°	0.22	-5.1°	0.21	-98.2°	0.12
WRF tot. ground precip.	25.0°	0.18	5.4°	0.26	-103.3°	0.19

regional domain. In the variogram analysis small- and intermediate-scale structures may be hidden by the large-scale gradient. To avoid this and non-stationarity of patterns, we first present variograms of detrended precipitation fields (Section 3.3.4). However, to assess processes acting at different scales, variograms of non-detrended precipitation patterns are subsequently analyzed in a scale analysis (Section 3.3.4). Finally, a 2D-autocorrelation analysis is used to comment on directional dependencies of precipitation patterns (Section 3.3.4).

Large-scale precipitation trends

Large-scale precipitation patterns show a strong gradient (Figure 3.4). Therefore a plane is fit linearly to the precipitation fields describing the large-scale precipitation trend (Table 3.2). The trend on the 31 January 2016 roughly points toward the North. For the precipitation event on 5 March 2016 the trend points roughly to the South. Given a southerly advection on 5 March 2016 this direction corresponds to the main wind direction and therefore agrees with the theory of large-scale orographic precipitation enhancement or rather the drying trend due to sinking air further downstream within the mountain range. The south-north gradient on 31 January 2016 roughly agrees with the main wind direction but points out that regional trends of larger-scale patterns may not exactly be aligned with wind direction. For the precipitation event on 4 February 2016 the intensity of the trend (i.e. the strength of inclination of the linearly fitted plane) is, however, weak and therefore the orientation of the slope is arbitrary. For this day, we hypothesize that either dynamics were more variable preventing the evolution of a strong gradient or lifting condensation due to the orography was not as efficient as for the other two events. For two events (31 January 2016 and 4 February 2016) the model has trouble reproducing the trend (i.e. orientation and intensity of the linearly fitted plane). For 31 January 2016 the deviation of orientation between the trends of radar precipitation and WRF precipitation at 2830 m asl is about 70° but with a similar intensity of the trend. For 4 February 2016 the model shows a strong trend of precipitation, while the intensity of the trend is weak in the entirely-filtered radar data. However, for the precipitation event on 5 March 2016 the trend is reasonably captured by the model with a deviation of the orientation of 16.6° and a slightly stronger intensity of the trend in the model compared to the radar estimation.

Disagreement in precipitation patterns, trend orientation and intensity on 4 February 2016 (quite homogeneous precipitation distribution in the radar estimate (Figure 3.4) compared to the strong downstream shift of precipitation in WRF) and the overestimation of precipitation in the model give evidence for a too simplistic representation of precipitation in the model (i.e. simplified microphysics and cloud dynamics), which tends to overestimate the effect of highest topographic features but misses precipitation over shallower areas. Good agreement in the intensity of the trend on 31 January 2016 and good agreement of the orientation of the trend on 5 March 2016, however, show that the model is able to capture large-scale precipitation trends, which may be connected to a large-scale orographic enhancement.

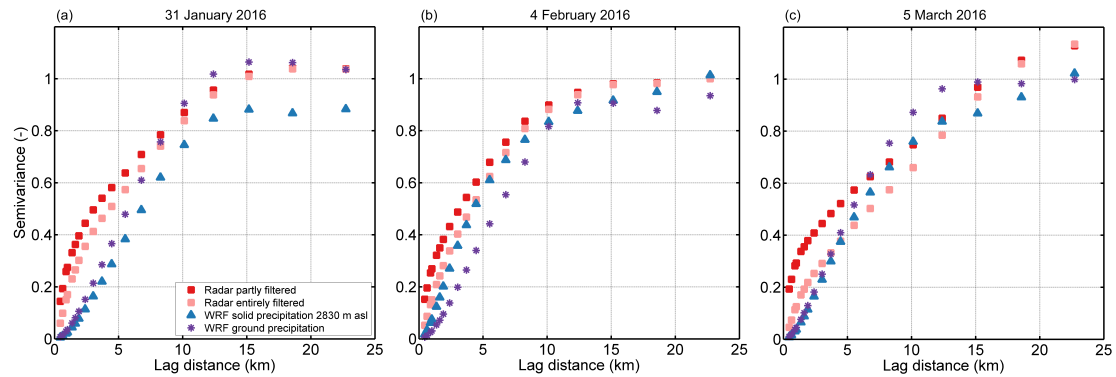


Figure 3.6: Variograms of detrended snow precipitation normalized by the domain-wide variance of precipitation for the precipitation events on a) 31 January 2016, b) 4 February 2016 and c) 5 March 2016 for the regional domain (Figure 3.1). Variograms are given for partly-filtered (red) and entirely-filtered (orange) radar snow precipitation, WRF snow precipitation at 2830 m above sea level (m asl, blue) and WRF total ground precipitation (violet). WRF precipitation is from simulations with weak terrain smoothing (Section 3.2.1). All precipitation fields are masked.

Spatial variability of detrended precipitation fields

On the smallest scales a strong difference is visible in variograms of detrended entirely-filtered and detrended partly-filtered radar precipitation, with weaker variability for entirely-filtered data (Figure 3.6). Smallest-scale structures in the radar data are likely an indicator of residual noise in the partly-filtered radar data (Section 3.2.3). However, it could also imply micro-scale precipitation features. This stresses the challenge of processing high-resolution radar data (Section 3.2.3) to get a reasonable radar precipitation field. In any case the entirely-filtered radar precipitation estimates may be regarded as clean concerning residual clutter and will therefore be used for all subsequent analysis.

Variograms of entirely-filtered and detrended radar precipitation show a steep increase of variability on the smallest scales, while the increase in variability gets weaker for larger scales (less steep slope in the variograms). Small-scale patterns are likely driven by small-scale precipitation cells induced by local cloud dynamics and microphysics. Such small-scale structures are repeated on intermediate scales and lead to a weaker increase in variability, as less new spatial features are added. At larger scales variability reaches the total variability of the detrended data.

Compared to radar precipitation WRF precipitation at 2830 m asl shows a lower variability and a flatter increase in variability at small scales giving evidence for a smoother precipitation distribution at the smallest scales compared to radar precipitation patterns. The lack of small-scale patterns clearly shows that the radar sees more variability at the smallest scales, while WRF likely misses the smallest-scale processes. Variability of radar and WRF precipitation at 2830 m asl at large scales (>5 km), especially on 4 February 2016, show less systematic differences than at small scales. This indicates that, with respect to total variability, patterns at these scales are well represented. Total ground precipitation shows a higher variability compared to precipitation at 2830 m asl (except for 4 February 2016), which is an indication that near-surface processes are active in the model.

Variograms of precipitation in the local domain (300 m resolution, Figure 3.1) look similar to variograms of the regional domain (450 m resolution), but reach domain-wide variability at about 5 km lag distance (Appendix B.2), while on the regional scale the domain-wide variability is reached at a distance of about 15 km to 20 km (Figure 3.6). Furthermore, the difference between radar and WRF precipitation variability at small scales is larger on the local domain compared to the regional domain. This and a systematic underestimation of precipitation variability at scales <5 km (on the regional domain) compared to precipitation variability in radar estimates indicate that mountain ridge-scale precipitation processes are under-represented in the model.

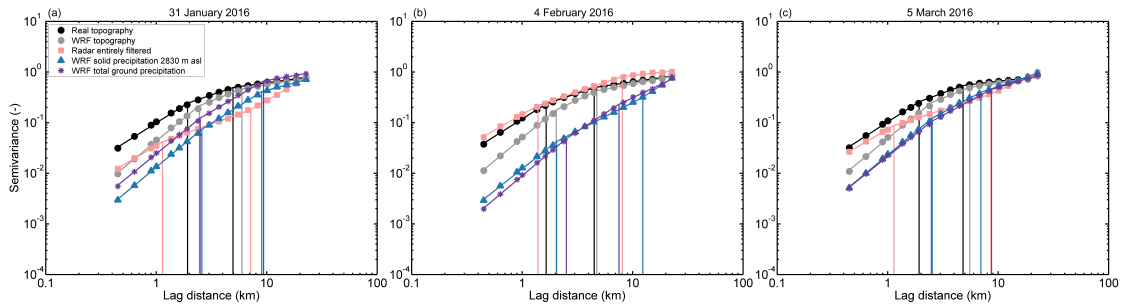


Figure 3.7: Normalized variograms of the snow precipitation events on a) 31 January 2016, b) 4 February 2016 and c) 5 March 2016 for the regional domain (Figure 3.1). Variograms are given for entirely-filtered radar snow precipitation (orange), WRF snow precipitation at 2830 m above sea level (m asl, blue) and WRF total ground precipitation (violet). Additionally, variograms are given for real topography (based on dh25 © 2018 swisstopo (5740 000 000), black) and WRF topography (gray). WRF topography and precipitation are from simulations with weak terrain smoothing (Section 3.2.1). All precipitation fields are masked.

Scale breaks and dominating processes

Scale breaks were previously found to be connected to changes in dominant processes (e.g. Deems et al., 2006). Here, we present a scale analysis including variability due to large-scale precipitation processes. Therefore, we present variograms of non-detrended precipitation fields, being aware that a certain portion of the small- and intermediate-scale precipitation variability may become hidden. As precipitation patterns are known to be driven by topography and wind, we present variograms of topography together with the variograms of precipitation. Variograms of topography clearly reveal two scale breaks (Figure 3.7). The first scale break is between 1 and 2.5 km depending on the resolution, the second scale break is at 5 km and 6 km for real topography and weakly smoothed WRF topography, respectively. For topography the two scale breaks are separating the mountain-slope scale ($< \sim 1$ km to 2 km), mountain-ridge-to-valley scale (between ~ 1 km to 2 km and ~ 5 km) and the scale of repeated mountain ridges and valleys (> 5 km).

For consistency reasons, all variograms in Figure 3.7 are presented with two scale breaks. Scale breaks for all events and both resolutions are basically grouped in two areas (~ 1 km to 2.5 km and 5 km to 10 km for 450 m resolution, Figure 3.7 and ~ 800 m to 1.2 km and 2.5 km to 5 km for 300 m resolution, Appendix B.2), even though for precipitation some scale breaks are arbitrary. Albeit scale breaks of precipitation do not exactly match scale breaks of topography, breaks at similar scales as well as similar slopes of topography and precipitation at small scales support the interpretation of topography dependent precipitation patterns. On the smallest scales (< 1 km to 2 km) the slopes of precipitation variograms are similar to the slopes of the variograms of corresponding topography. This is an indication that precipitation patterns on mountain-slope scales may be terrain-driven. Processes acting at these scales could be small-scale cloud-dynamical processes such as the seeder-feeder mechanism (Bergeron, 1965; Purdy et al., 2005) or preferential deposition (Lehning et al., 2008). The latter is, however, for most mountain ridges unlikely to be seen in precipitation fields at 2830 m asl as it happens close to the ground. For the precipitation event on 5 March 2016, on scales > 5 km to 7 km (i.e. for the scales above the second scale break) the slopes of the normalized variograms of radar and WRF precipitation at radar elevation are similar. Large-scale gradients at these scales are most likely driven by large-scale orographic precipitation enhancement (e.g. Stoelinga et al., 2013). Good agreement of the slopes in normalized variograms between radar and WRF precipitation is an indicator that the model has the potential to properly represent the strength of the large-scale gradient with respect to the overall variability, i.e. large-scale orographic precipitation enhancement. Disagreement of variograms of precipitation and topography at these scales further support the hypothesis that largest-scale precipitation is mainly determined by large-scale orographic precipitation enhancement, which introduces an increase in variability of precipitation at large scales, while large-scale topography reveals a repeated pattern of valleys and peaks (i.e. constant variability). Overall, this analysis supports the hypothesis in Section 3.3.2 that precipitation patterns in the regional domain are topography driven.

2-dimensional variability patterns

Finally, the combined influence of topography and the general wind direction on snow precipitation patterns in the regional domain is assessed by spatial 2D-autocorrelation maps (Figure 3.8). Like variograms, autocorrelation is dependent on large-scale trends. The general direction of 2D-autocorrelation patterns is the same for detrended (Figure 3.8) and non-detrended (not shown) precipitation patterns. However, autocorrelation patterns of detrended precipitation fields show much shorter decorrelation lengths. This is due to the spatial coherence introduced by large-scale trends in precipitation. To avoid biased autocorrelation data, only 2D-autocorrelation maps of detrended precipitation fields are shown. However, we keep in mind that large-scale trends are present.

Autocorrelation maps of topography (Figures 3.8a and 3.8e) represent a north-west to south-east oriented pattern which is, although weaker, repeated in south-west to north-east and west to east direction. For snow precipitation events with dominating north-westerly to northerly advection, the main axis of the snow precipitation 2D-autocorrelation pattern is oriented in a north-west to south-east direction and therefore in alignment with both topography and the main wind direction (Figures 3.8b-c and 3.8f-g). Patterns of WRF precipitation at 2830 m asl are rotated toward a north-south direction on 4 February 2016. For dominating southerly advection the 2D-autocorrelation map of radar precipitation shows a more homogeneous pattern compared to autocorrelation patterns for northern to north-western advection but a weak south-west to north-east orientation of larger-scale patterns (Figures 3.8d). For the WRF simulations a strong south-west to north-east orientation is present in the autocorrelation map for the precipitation event on 5 March 2016 (Figure 3.8h). Even though isotropic variograms reveal good agreement in domain-wide variability, 2D-autocorrelation maps show that this may not necessarily go along with good agreement of the orientation of patterns. Best agreement in the orientation of patterns is found for 31 January 2016. For the three events, 2D-autocorrelation maps of detrended precipitation reveal a smoother distribution of precipitation on the smallest scales in the model compared to radar data, due to less small-scale structures in the model. On the other hand, a strong decrease in autocorrelation in east-west direction is visible for 5 March 2016. This shows that WRF simulations have a stronger dependency on both wind direction and topography and tend to generate strong precipitation bands in the main wind direction, confirming the overly simplistic behavior of the model.

For ground precipitation 2D-autocorrelation patterns tend to be repeated in south-west to north-east and west to east direction as seen for topography (Figures 3.8j-g). This stresses the hypothesis that the influence of topographic features on WRF ground precipitation is stronger than at radar elevation and gives evidence that these results are likely produced by near-surface topographically driven pre-depositional processes such as e.g. preferential deposition or the seeder-feeder mechanism in the model. While a topography dependency was already found in isotropic variograms, this 2D-autocorrelation analysis reveals that the wind direction additionally strongly impacts the snow precipitation distribution.

3.3.5 Dependence of spatial variability on model resolution and smoothing

Geostatistical analyses presented in this study demonstrate that precipitation on the regional scale (>5 km) is reasonably represented in the WRF model, while small-scale precipitation variability is systematically underestimated in the model simulations with a horizontal grid spacing of 450 m (Section 3.3.4). Variograms up to a maximum lag distance of 5 km on domain Dischma (Figure 3.1) reveal an increase of variability for increasing model resolution (Figure 3.9). However, simulated variability stays far below the variability of entirely-filtered radar precipitation. Depending on the event an increase in variability is present for 150 m and 50 m resolution. This indicates that smallest-scale precipitation dynamics are still not fully resolved at 50 m resolution. A comparison of variograms for simulations with strongly smoothed terrain compared to simulations with weaker terrain smoothing (Section 3.2.1) reveal that a stronger terrain smoothing may result in less explained variability in normalized variograms (not shown). Even though this signal is not consistent for all events, we can show that a better representation of topography due to higher resolution and less smoothing has the potential to increase the explained variability of precipitation patterns. An increase in variability at small scales (<5 km), indicates that more small-scale patterns are resolved at higher resolutions in the model (50 m horizontal grid spacing). Our simulations are currently

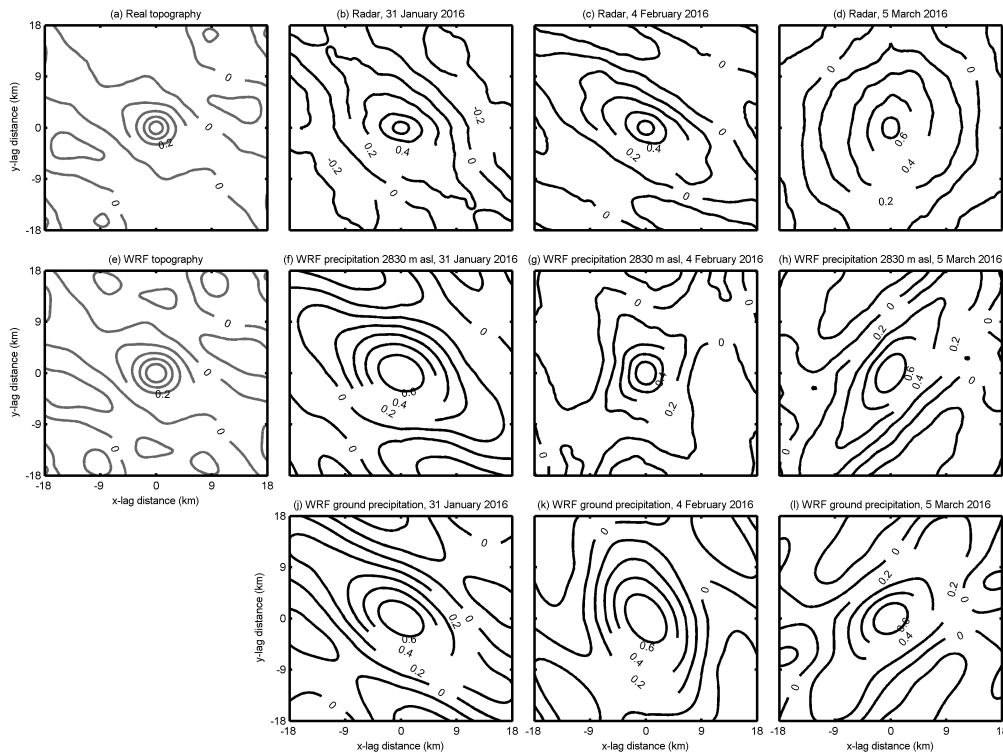


Figure 3.8: Spatial 2D-autocorrelation maps for the regional domain (450 m resolution) of detrended a) real topography (based on dh25 © 2018 swisstopo (5740 000 000)), b)-d) entirely-filtered radar snow precipitation, e) WRF topography, f)-h) WRF snow precipitation at 2830 m above sea level (m asl) and j-l) WRF total ground precipitation. Autocorrelation maps of snow precipitation are for the three snow precipitation events on 31 January 2016, 4 February 2016 and 5 March 2016. WRF topography and precipitation are from simulations with weak terrain smoothing (Section 3.2.1). Radar precipitation and WRF precipitation at 2830 m asl are masked (as shown in Figure 3.4).

limited to the presented resolutions and strong terrain smoothing due to model instabilities. However, based on the presented results, once available, the immersed boundary method version of WRF (e.g. Lundquist et al., 2010; Lundquist et al., 2012; Arthur et al., 2016; Ma and Liu, 2017), will likely be a good tool to allow for steeper slopes in the simulation and going toward higher resolution LES simulations to resolve further small-scale wind fields, which drive the precipitation structures.

3.4 Conclusions and Outlook

The implementation of COSMO–WRF is a further step in performing very-high resolution precipitation simulations in complex alpine terrain to address the question of the relative importance of cloud-dynamics and particle-flow interactions on a mountain-ridge scale. In this validation study, we show that COSMO–WRF is able to reasonably simulate atmospheric conditions, but tends to overestimate near-surface wind speeds, which may be due to many reasons from an overestimation of speed-up effects to an underrepresentation of small terrain features. Relative humidity patterns are highly variable and may be a sign that subsidence and lifting produce too strong effects in the (partially parameterized) cloud dynamics, given the good representation of topography at larger scales.

Regional and local scale precipitation patterns in the COSMO–WRF simulations are in partially good agreement with MeteoSwiss operational radar measurements and automatic weather stations. For the three

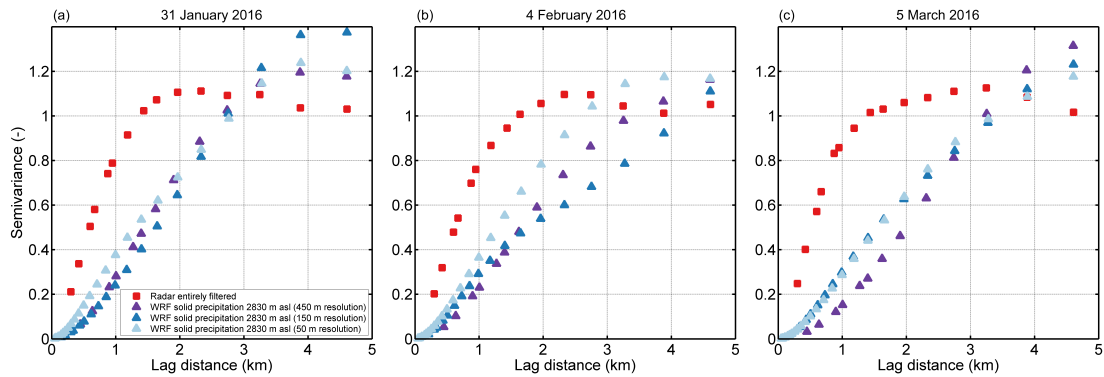


Figure 3.9: Variograms of detrended snow precipitation normalized by the domain-wide variance of precipitation for the precipitation events on a) 31 January 2016, b) 4 February 2016 and c) 5 March 2016 for domain Dischma (Figure 3.1). Variograms are given for entirely-filtered radar snow precipitation (red), and WRF snow precipitation at 2830 m above sea level (m asl) with 450 m (violet), 150 m (blue) and 50 m (light blue) resolution. WRF snow precipitation is from simulations with weak terrain smoothing (Section 3.2.1). Radar precipitation is masked.

events analyzed here, precipitation estimates from WRF simulations are higher compared to precipitation estimates from radar measurements. A general overestimation of precipitation produced by WRF is consistent with an overestimation of subsidence and lifting. Overestimation of precipitation in WRF simulations has been documented previously for snow precipitation over complex terrain (e.g. Silverman et al., 2013), likely due to the high model resolution and therefore more complex topography and higher mountain peaks compared to common high resolution simulations.

An autocorrelation and scale analysis of radar and WRF snow precipitation reveals a good agreement of precipitation patterns on regional scales (>5 km), which are topography and wind driven. These large-scale patterns are in good agreement with the theory of large-scale orographic enhancement (e.g. Stoelinga et al., 2013). Disagreement in precipitation patterns i.e. a downwind shift of snow precipitation in the WRF simulations compared to radar precipitation estimates is likely due to lifting condensation being too weak in areas, where topography is lower and strong smoothing leads to an underrepresentation of topography. On the other hand, over peaks, which are high and steep enough in the model to allow for lifting condensation, the effect of orographic precipitation enhancement tends to be overestimated. An increase of this overestimation of precipitation over high elevations for higher resolution simulations as well as for weaker terrain smoothing supports this hypothesis. Smallest-scale patterns in the radar measurements are likely dominated by noise, which is removed by the application of a median filter. Given these uncertainties the radar data cannot be considered as the absolute reference. In case of critical data analysis, an estimation of high-resolution radar precipitation is, however, useful to improve the understanding of precipitation processes in complex terrain and to validate and improve model simulations. On a local to mountain-valley scale WRF simulations systematically show a lower variability of precipitation compared to radar estimates. This indicates that the model is not able to represent the full spectrum of small-scale precipitation patterns, which are present in the radar measurements. One potential reason for the lack of precipitation variability is the simplification of cloud dynamics and microphysics in the model, typically used to model regional-scale precipitation fields. Additionally, we could show that the underrepresentation of topography may have a strong influence on the formation of local low-level clouds, which are important for orographic precipitation enhancement. This is supported by the fact that precipitation patterns in the model show a stronger dependency on topography and wind direction than precipitation patterns in the radar estimates. However, an increase in precipitation variability at scales <5 km is visible for higher resolution WRF simulations. Furthermore, for simulations with steeper terrain an increase in variability for all resolutions is found. This shows that especially for small-scale variability a better representation of the complex terrain is essential to reproduce precipitation variability. Although the model cannot represent the full variability measured by the radar at small scales, an increase in precipitation between 2830 m asl

and the ground is an indication that the model captures a certain portion of near-surface processes.

To specifically address processes such as the seeder-feeder mechanism or preferential deposition an analysis of hydrometeors and precipitation distributions in vertical profiles across mountain ridges is needed. To connect pre-depositional processes with post-depositional processes even higher resolution WRF simulations would be required. This might be achieved by employing the immersed-boundary method version setup of WRF. A parameterization of post-depositional processes in WRF or using WRF simulations as a boundary condition for simulations with the Alpine surface processes model Alpine3D (Lehning et al., 2008), would then allow validation of modeled snow accumulation patterns compared to measured snow accumulation patterns. Furthermore, simulations of precipitation patterns in complex terrain need to be analyzed with higher temporal resolution (e.g. on the order of minutes), as contributing processes show high temporal variability. Future work will include addressing the temporal variability of precipitation patterns using radar observations, along with an analysis of precipitation growth with respect to topography and wind direction.

Acknowledgements *The work is funded by the Swiss National Science Foundation (Project: Snow-atmosphere interactions driving snow accumulation and ablation in an alpine catchment: The Dischma Experiment; SNF-grant: 200021_150146 and project: The sensitivity of very small glaciers to micrometeorology; SNF-grant: P300P2_164644). Topographic data are reproduced by permission of swisstopo (JA100118). For advice to setup WRF simulations we thank the WRF-help. For supporting our project with computational time many thanks go to the Swiss National Supercomputing Center (CSCS) and their support for technical advice. Additionally, we thank the Swiss Federal Office of Meteorology and Climatology (MeteoSwiss) for providing access to radar data, COSMO-2 analysis and the regridding tool fieldextra. For advice related to COSMO-2 thanks go to Guy de Morsier from MeteoSwiss. Further thanks go to Amalia Iriza and Rodica Dumitrache from MeteoRomania for advice concerning the COSMO-WRF coupling. Additional thanks go to Louis Quéno and Benoit Gherardi for their work on pre-preprocessing steps and data processing to setup WRF simulations. Additionally, we thank Heini Wernli and the two anonymous reviewers for their questions, comments and recommendations, which helped to improve the paper.*

The importance of near-surface winter precipitation processes in complex alpine terrain

partially revised version of the article under review for the *Journal of Hydrometeorology*, Franziska Gerber¹², Rebecca Mott²³, Michael Lehning¹²

Candidates contribution: *The candidate run the model simulations. She did the analysis and wrote the manuscript together with all co-authors.*

Abstract While near-surface atmospheric processes are known to strongly affect final winter precipitation deposition, their relative importance is still discussed. In this study, near-surface snow and graupel precipitation processes in very high-resolution real-case large-eddy simulations are analyzed. The results reveal that a horizontal grid spacing of ≤ 50 m is required to resolve local orographic precipitation enhancement, lee-side flow separation and thereby preferential deposition. At this resolution precipitation patterns across mountain ridges show a high temporal variability. Nevertheless, event mean snow precipitation across three mountain ridges in the upper Dischma valley (Davos, Switzerland) for two precipitation events show distinct patterns, which are in agreement with theoretical concepts, such as small-scale orographic precipitation enhancement or preferential deposition. Terrain-flow-precipitation interactions are estimated to increase snow accumulation on the leeward side of mountain ridges by approximately 26 % to 28 % with respect to snow accumulation on the windward side of the ridge. Cloud dynamics and mean advection may locally increase precipitation on the leeward side of the ridge by up to about 20 % with respect to mean precipitation across a mountain ridge. Near-surface processes, which are likely dominated by particle-flow interactions may increase snow deposition locally on the order of 10 % with respect to mean precipitation across a mountain ridge. However, the effect of terrain-flow-precipitation

¹Laboratory of Cryospheric Sciences, School of Architecture and Civil Engineering, École Polytechnique Fédérale de Lausanne, Lausanne, Switzerland.

²WSL Institute for Snow and Avalanche Research SLF, Davos, Switzerland.

³Institute of Meteorology and Climate Research, Atmospheric Environmental Research (KIT/IMK-IFU), KIT-Campus Alpin, Garmisch-Partenkirchen, Germany.

interactions is strongly dependent on atmospheric humidity. Weak dynamic stability was further shown to be important for graupel production, which is an essential component of solid winter precipitation. A comparison to smoothed measurements of snow depth change reveals a certain agreement with simulated precipitation across mountain ridges.

4.1 Introduction

Snow distribution in complex alpine terrain is determined by many different processes. At a mountain-range scale large-scale orographic precipitation enhancement is dominant, causing enhanced snow accumulation on the upstream side of a mountain range due to forced lifting and condensation (e.g. Stoelinga et al., 2013). Decreasing precipitation occurs downstream, where air masses are sinking and drying. However, at smaller scales, additional processes, such as local orographic precipitation enhancement and particle-flow interactions (i.e. the influence of the local flow field on the pathways of snow particles and the particle distribution in the air), become important due to the interaction of the local flow field with topography (e.g. Zängl, 2007; Lehning et al., 2008; Mott et al., 2014; Grazioli et al., 2015). Knowledge about small-scale processes is important for mountain-ridge to mountain-valley scale snow accumulation. Hence, improved understanding of the importance of these processes is valuable for e.g. water resources management and avalanche forecasting.

The flow over mountain ridges may introduce low-level clouds due to lifting condensation (e.g. Banta, 1990). Particles falling through such low-level clouds may strongly grow at the expense of cloud droplets by depositional growth or form rimed particles or graupel by collision (Stoelinga et al., 2013). This process is also known as seeder-feeder mechanism (Bergeron, 1965). Due to small-scale orographic precipitation enhancement without taking into account precipitation advection a precipitation peak is expected over the mountain ridge (Mott et al., 2014). For the same flow field over a mountain ridge particle-flow interactions additionally act on the precipitation distribution (Lehning et al., 2008; Mott et al., 2014). On the one hand, mean advection may lead to a downstream shift of peak precipitation. On the other hand, close-ground modifications of the flow field may interact with particle fall velocities. The influence of particle-flow interactions on snow deposition in complex terrain has been introduced as preferential deposition by Lehning et al. (2008). Close-ridge updrafts on the windward side of the mountain ridge are expected to reduce the terminal fall velocity of precipitation. Hence, snow accumulation on the windward side of the mountain ridge is reduced and precipitation particles are transported over the ridge. On the leeward side of the ridge, where precipitation faces flow separation, snow will be preferentially deposited. Small-scale flow blocking (e.g. Carruthers and Hunt, 1990) can further lead to enhanced snow accumulation typically at the foot of the mountain ridge, which is often a local depression (Lehning and Mott, 2016). In contrast to pre-depositional precipitation processes, which shape the snow distribution already during snowfall in and below the clouds, post-depositional processes may additionally alter snow accumulation patterns by redistribution of snow by wind (Vionnet et al., 2017) and avalanches (e.g. Bernhardt et al., 2012; Sommer et al., 2015).

There are different approaches to investigate winter precipitation over complex topography. Simple, though based on physical principles, the linear theory model (Smith and Barstad, 2004) may represent orographic precipitation over complex terrain (Roth et al., 2018). The linear theory model as well as numerical weather prediction models are usually used at horizontal grid spacings of ≥ 1 km for precipitation studies (e.g. Richard et al., 2007; Rasmussen et al., 2011; Pontoppidan et al., 2017), as these approaches fairly capture precipitation patterns due to large-scale processes and as they have high computational cost. For mountain-range scale orographic precipitation enhancement only weak improvement of precipitation representation was found when increasing the model resolution from 3 km to 1 km (Pontoppidan et al., 2017). The small-scale variability of snow accumulation has been addressed with atmospheric numerical models, based on semi-idealized conditions (real topography and idealized or partially idealized boundary conditions) either coupled to or used as input for a snow model (e.g. Mott et al., 2014; Vionnet et al., 2017). Based on this approach, different studies found evidence for preferential deposition in numerical simulations, which could be verified by means of snow depth measurements (e.g. Mott and Lehning, 2010; Mott et al., 2010; Mott et al., 2014). However, effects of different atmospheric conditions and terrain on

preferential deposition are still under debate (e.g. Chapter 2, Mott et al., 2010; Mott et al., 2014; Gerber et al., 2017a; Vionnet et al., 2017; Wang and Huang, 2017; Comola et al., 2018). Mott and Lehning (2010) could reproduce snow accumulation patterns which agree fairly well with the original definition of preferential deposition and their simulations show good correspondence to field measurements. Recent studies show that preferential deposition strongly depends on the local flow field and atmospheric stability (e.g. Wang and Huang, 2017; Comola et al., 2018). Wang and Huang (2017) report a shift of peak snow precipitation from the windward toward the leeward side of the ridge for increasing advection strength. Recently, Comola et al. (2018) confirmed that deposition patterns strongly depend on the strength of advection, while precipitation patterns are qualitatively preserved for varying slope angles, based on idealized large eddy simulations (LES). Furthermore, they addressed particle inertia, which is disregarded by many models. Their results showed that snow accumulation patterns resulting from simulations with inertialess particles are similar to patterns simulated for inertial dendritic particles. However, simulations based on inertialess particles do not properly represent snow accumulation patterns as expected for rounded particles with inertia. While it is well known that post-depositional particle-flow interactions have a strong impact on the small-scale snow distribution in complex terrain (e.g. Vionnet et al., 2017), the relative importance of cloud-dynamical effects and pre-depositional particle-flow interactions is still hardly known (Mott et al., 2014; Vionnet et al., 2017).

Regional simulations are usually limited to a horizontal grid spacing of ≥ 1 km. A comparison of Weather Research and Forecasting (WRF) model simulations driven by Consortium for Small-scale Modeling (COSMO-2) analysis (COSMO-WRF) to high-resolution radar measurements indicates that winter-time precipitation patterns over complex terrain are not fully captured by model simulations even at a horizontal grid spacing of 450 m, while some additional small-scale variability is resolved at a horizontal grid spacing of 50 m (Chapter 3, Gerber et al., 2018). Furthermore, Gerber et al. (2018) found differences in precipitation patterns between 2830 m above sea level (m asl) and the ground, indicating the presence of near-surface processes.

In this study, we address the question at which resolution the model starts to resolve mountain-ridge scale precipitation processes. Therefore, we analyze the sensitivity of mountain-ridge scale precipitation processes to the model resolution (Section 4.3.1). Based on very high resolution simulations (50 m horizontal grid spacing) we then estimate the relative importance of pre-depositional precipitation processes. To this end, we first present and discuss topographically induced precipitation processes in the COSMO-WRF setup (Section 4.3.2 and Section 4.3.3). Subsequently, we compare modeled precipitation patterns with photogrammetrically determined snow accumulation measurements (Section 4.3.4). Finally, we estimate the importance of pre-depositional precipitation processes on the snow accumulation distribution in COSMO-WRF simulations (Section 4.3.5). Conclusions and an outlook wrap up this study in Section 4.4.

4.2 Data and Methods

4.2.1 COSMO-WRF simulations

For this study simulations are performed with the non-hydrostatic and fully compressible Weather Research and Forecasting (WRF) model (Skamarock et al., 2008). The simulations are run with specified boundary conditions, initialized and driven by Consortium for Small-scale Modeling (COSMO-2) analysis by MeteoSwiss. The simulation setup corresponds to the one described in Gerber et al. (2018, Chapter 3). All simulations have four one-way nested domains (d01–d04) with horizontal grid spacings of 1350 m, 450 m, 150 m and 50 m, respectively (Figure 4.1). The four simulation domains have 40, 40, 60 and 90 vertical levels, respectively, with the model top at 150 hPa. Analysis of near-surface processes are based on domain d04 (50 m horizontal grid spacing), which covers the upper Dischma valley (Davos, Switzerland). To address the resolution sensitivity of processes, precipitation patterns are compared in the model output at the different horizontal grid spacings of 50 m, 150 m and 450 m. The coarsest horizontal grid spacing of 1350 m is not used in the analysis as even at a horizontal grid spacing of 450 m mountain-ridge to mountain-valley scale precipitation processes may not be resolved (Section 4.3.1).

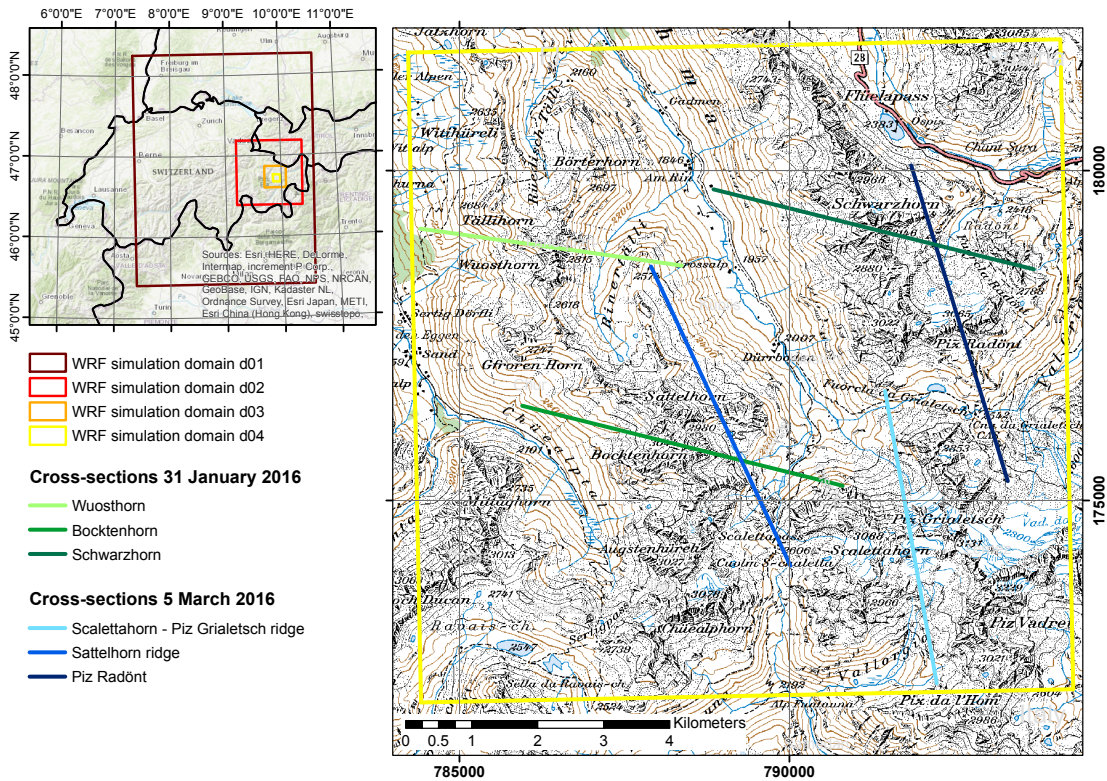


Figure 4.1: Overview of the study area over the eastern part of Switzerland and surrounding countries. The simulation domains d01–d04 (dark red to yellow) with 1350 m, 450 m, 150 m and 50 m horizontal grid spacing, respectively, show the simulation setup. Domain d04 covers the upper Dischma valley (Davos, Switzerland). Cross-sections analyzed for the two precipitation events on 31 January 2016 (greens) and 5 March 2016 (blues) are approximately centered over the respective mountain peak or ridge. Basemap (right panel): pixmaps © 2018 swisstopo (5704 000 000).

Using this simulation setup, two precipitation events on the 31 January 2016 and 5 March 2016 are simulated. The simulations are run for 24 h with a spin-up time of 43 h, 19 h, 7 h and 1 h for the domains d01–d04, respectively. The 31 January 2016 and 5 March 2016 are chosen because these were two significant precipitation events within the time period, for which photogrammetrically determined airplane-based snow depth measurements are available (Section 4.2.5). Additionally, simulations for these two dates showed better performance compared to simulations for another precipitation event on 4 February 2016 (Gerber et al., 2018). For the variability analysis with respect to radar estimates, the simulations were chosen to cover full calendar days due to the processing of radar measurements.

Boundary-layer processes in the parent domain (d01) are parametrized by the Yonsei University planetary boundary layer (YSU PBL) scheme (Hong et al., 2006), while all the nested domains are run in large-eddy simulation (LES) mode. For subgrid-scale turbulence the 1.5-order turbulent kinetic energy parametrization is used (Skamarock et al., 2008).

Microphysical processes are parameterized by the Morrison 2-moment parameterization (Morrison et al., 2005; Morrison et al., 2009). Land-surface processes are parametrized by the Noah land-surface model with multi-parametrization options (Noah-MP, Niu et al., 2011; Yang et al., 2011) and linked to the atmosphere by the MM5 Monin-Obukhov surface layer parameterization (Paulson, 1970; Dyer and Hicks, 1970; Webb, 1970; Zhang and Anthes, 1982; Beljaars, 1994). Terrain smoothing (four smoothing cycles using the 1–2–1 smoothing option of the WRF preprocessing system, Chapter 3, Gerber et al., 2018) is applied to keep all slope angles in domain d04 below 45°, to avoid pressure-gradient errors (De Wekker, 2002). The same number of smoothing cycles is applied for all four nested domains to keep topography consistent across domain boundaries. To take missing topography and missing roughness elements into

account, the snow surface roughness length is increased to 0.2 m (Chapter 3, Gerber et al., 2018).

The simulations have been validated against two meteorological stations in domain d04. Gerber et al. (2018, Chapter 3) could show that the simulations perform well, especially in terms of wind direction, but with largely overestimated wind speeds for some time periods and expositions, especially for the precipitation event on 31 January 2016. Additionally, precipitation tends to be overestimated with respect to radar estimates. Further information about the simulation setup and the validation can be found in Gerber and Sharma (2018, Appendix D) and Gerber et al. (2018, Chapter 3).

Additionally, two simulations are run to address the impact of different simulation resolutions but eliminating the effect of additional smoothing. The first simulation includes domains d01 and d02, and has maximum slope angles of 45° in domain d02. The second simulation has three domains (d01, d02 and d03), and restricts slope angles to $<45^\circ$ in domain d03. Keeping all slope angles below 45° in domain d02 (horizontal grid spacing of 450 m) requires one smoothing cycle. Three smoothing cycles are needed to keep all slope angles below 45° in domain d03 (horizontal grid spacing of 150 m). The specified number of smoothing cycles is applied to all nested domains of the respective simulation.

4.2.2 Precipitation events

To analyze close-ground terrain-flow-precipitation interactions (i.e. the influence terrain-induced flow field variations on the precipitation formation and distribution), we investigate two precipitation events on 31 January 2016 and 5 March 2016. On 31 January 2016 a westerly flow induced by the Azores high and a low pressure system over Scandinavia dominated the weather over central Europe. Temperatures were about -3°C at 2500 m asl. Temperatures on 5 March 2016 were slightly lower with about -7°C at 2500 m asl. The general flow direction over the eastern part of Switzerland was from the South due to a large depression area over central Europe. The events further differ in their relative humidity (RH). While RH is high over the whole domain d04 for the precipitation event on 31 January 2016, saturation is only achieved in the vicinity of the mountain peaks on 5 March 2016, and a RH gradient is observed with higher humidity toward the southern boundary of the domain. The dry static stability of the atmosphere in the area of the different mountain ridges is weakly stable for both precipitation events, as expected for winter conditions over snow covered terrain. For the precipitation event on 31 January 2016 precipitation over 24 h (31 January 2016, 00:00 UTC until 1 February 2016 00:00 UTC) is analyzed. For the precipitation event on 5 March 2016 only 10 h are analyzed between 07:00 UTC and 17:00 UTC covering the precipitation period during southerly advection. For the sensitivity study only the event on 31 January 2016 is analyzed.

4.2.3 Study area and cross-sections across mountain ridges

This study is part of the Dischma experiment (DISCHMEX), which was launched to investigate the effect of atmospheric processes on snow accumulation (Chapter 2, Chapter 3, Gerber et al., 2017a; Gerber et al., 2018) and ablation (Mott et al., 2017; Schlögl et al., *in review*) in alpine terrain. The upper Dischma valley is located within the eastern Swiss Alps to the south of Davos (Figure 4.1).

The effect of the flow field on precipitation processes and final snow deposition is analyzed based on cross-sections across 6 mountain peaks or ridges. The mountain peaks and ridges as well as the direction of the cross-sections were chosen depending on the event and the main wind direction in domain d04 (Figure 4.1). For the precipitation event on 31 January 2016, with a main wind direction from north-west to west, cross-sections across the Wuosthorn, Schwarzhorn and Bocktenhorn are analyzed. For the precipitation event on 5 March 2016 cross-sections across the Sattelhorn ridge, the ridge between Scalettahorn and Piz Grialetsch and Piz Radönt are chosen.

The direction of each cross-section is determined by the mean wind for the respective precipitation event over a square with side lengths of 500 m centered over the simulation grid point closest to the main mountain peak or ridge crest, taking into account the lowest ~ 350 m above ground (ag, 11 lowest model levels, Table 4.1) in domain d04. The cross-sections have a length of 5 km and are approximately centered over the main mountain peak or ridge. Two exceptions are the cross-sections across Wuosthorn, which has a length of 4 km, and the cross-section across the ridge between Scalettahorn and Piz Grialetsch with a

Table 4.1: Characteristics of the wind conditions and peak snow precipitation distances for mean advection and orographic precipitation enhancement (precipitation distribution at ~ 95 m above ground, ag), and near-surface preferential deposition (precipitation distribution in the lowest ~ 95 m ag) for the six cross-sections Wuosthorn, Schwarzhorn, Bocktenhorn, Sattelhorn ridge, Piz Radönt and ridge between Scalettahorn and Piz Grialetsch (Figure 4.1) in the simulation domain d04 with a horizontal grid spacing of 50 m. Wind speed (m s^{-1}) and wind direction (Wind dir., $^{\circ}$) are mean values over the lowest ~ 350 m ag in domain d04 over a square with side lengths of 500 m centered over the closest grid point of the ridge. Adv. max. (m) gives the distance of the first precipitation maximum on the leeward side of the mountain ridge at ~ 95 m ag (Figure 4.2). Pref. Dep. max. (m) gives the distance of relative precipitation maxima closest to the ridge on the windward side of the ridge (negative values) and on the leeward side of the ridge (positive values) of the precipitation distribution in the lowest ~ 95 m ag (Figure 4.2). Values show averages over the respective precipitation event, i.e. for 31 January 2016 values are averaged over 24 h (31 January 2016 00:00 UTC – 1 February 2016 00:00 UTC) and for 5 March 2016 values are averaged over 10 h (5 March 2016 07:00–17:00 UTC).

Date	Ridge	Wind dir. $^{\circ}$	Wind speed m s^{-1}	Adv. max. m	Pref. Dep. max. m
31 January 2016	Wuosthorn	278	13.7	600	250
	Schwarzhorn	284	19.6	1100	-50/300
	Bocktenhorn	284	15.7	650	250
5 March 2016	Sattelhorn ridge	155	11.2	0	100
	Piz Radönt	163	14.1	200	50
	Scaletta-Grialetsch	170	22.8	500	0/200

cross-section length of 4.5 km, restricted by the extent of domain d04. The same cross-sections are used for the sensitivity analysis of different model resolutions.

4.2.4 Quantification of preferential deposition and cloud-dynamical processes

To retrieve an estimate of near-surface preferential deposition and cloud-dynamical processes, we separate the two processes based on a simple approach. Previous studies showed that preferential deposition mainly acts at the lowest ~ 100 m of the atmosphere, while cloud-dynamical processes are dominant above this height (Mott et al., 2014). In agreement with these results our model simulations show only a weak precipitation formation and growth or even a reduction (due to sublimation) below ~ 93 m to ~ 410 m ag (depending on the cross-section) in the cross-section and event mean precipitation rates (Table C.1 and Table C.2 in Appendix C.1). Above ~ 93 m to ~ 410 m ag the cross-section and event mean precipitation rate per elevation ($\text{mm h}^{-1} \text{m}^{-1}$) strongly increases (by up to 50 % to 60 %) or changes from a precipitation reduction to a precipitation increase with respect to the level below. A weak increase of precipitation with increasing model level within the lowest part of the atmosphere (below ~ 96 m ag for cross-sections across Wuosthorn, Schwarzhorn and Bocktenhorn and ~ 93 m ag for cross-sections across Sattelhorn ridge, Piz Radönt and the ridge between Scalettahorn and Piz Grialetsch, hereafter called ~ 95 m ag) over the main ridge, confirms that precipitation formation and growth (by cloud-dynamical processes) below the lowest ~ 95 m ag are of minor importance (Figure 4.2c, Figure C.1g-i and Figure C.2g-i).

Therefore, we assume that precipitation patterns above ~ 95 m ag (7th model level) are dominated by the combined effect of cloud dynamics and mean advection. The difference between precipitation distribution at ~ 3 m ag (1st model level) and ~ 95 m ag is assumed to show the effect of near-surface preferential deposition (red line in Figure 4.2, Figure C.1 and Figure C.2).

Slightly different elevations are chosen for the comparison of different model resolutions, due to differences in the number of (eta-)levels in our simulations. Cloud-dynamical processes and mean advection are estimated at ~ 80 m ag for domains d02 and d03 (2nd model level) and are compared to ~ 95 m ag in domain d04. The lowest model level in domains d02 and d03 is at ~ 20 m ag. Therefore, we use the 3rd model level (~ 20 m ag) of domain d04 when addressing differences between model resolutions.

This technique has a few limitations. The separation of processes is not entirely exclusive and small precipitation changes in the lowest ~ 95 m ag show that cloud-dynamical and microphysical processes are

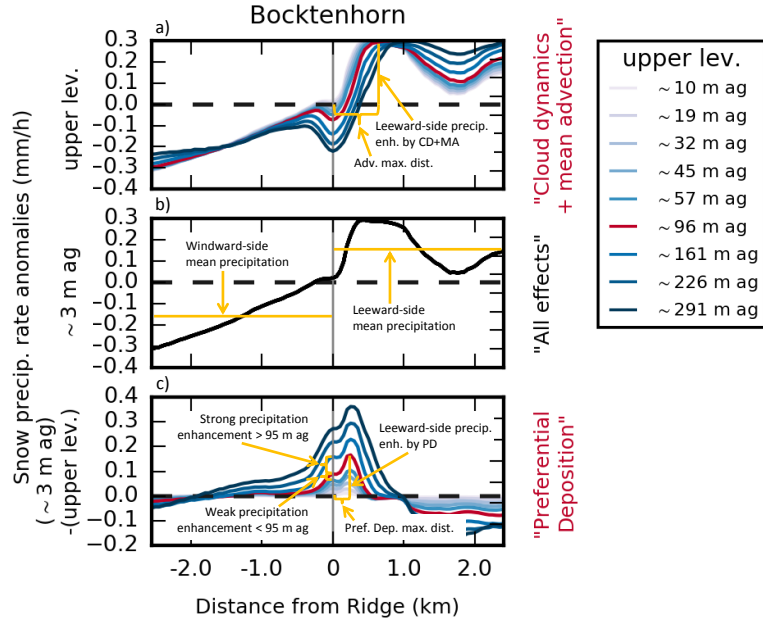


Figure 4.2: Illustration of the precipitation processes and precipitation patterns at different levels above ground (ag). The illustration is based on the example of the cross-section across Bocktenhorn for the precipitation event between 31 January 2016 00:00 UTC and 1 February 2016 00:00 UTC (50 m horizontal grid spacing). a) shows event mean precipitation rate anomalies with respect to cross-section and event mean precipitation rates at 9 different model levels (upper lev.) between ~10 m ag and ~291 m ag. Darker blue lines go along with increasing model levels. The ~96 m ag level is shown by the red line (illustrating the effect of Cloud dynamics + mean advection). Adv. max. dist. illustrates the distance of maximum advection of precipitation. Leeward-side precip. enh. by CD+MA gives the precipitation enhancement due to cloud dynamics (CD) and mean advection (MA). b) shows the event mean precipitation rate anomalies with respect to the cross-section and event mean precipitation rate at the lowest model level ~3 m ag. Windward-side mean precipitation (Leeward-side mean precipitation) illustrates the windward-(leeward-)side and event mean precipitation. c) shows the precipitation distribution due to processes between the lowest model level ~3 m ag (shown in b) and the upper level (shown in a). Darker blue lines in c) go along with increasing vertical model elevation of the upper level as for a). Precipitation distribution due to processes in the lowest ~96 m ag is shown by the red line (showing the effect of near-surface preferential deposition). Strong precipitation enhancement >95 m ag (Weak precipitation enhancement <95 m ag) illustrate the change in precipitation enhancement ~95 m ag at the mountain ridge. Pref. Dep. max. dist. shows the distance of the maximum preferential deposition. Leeward-side precip. enh. by PD illustrates the precipitation enhancement due to near-surface preferential deposition (PD). Gray vertical lines mark the position of the mountain ridge (i.e. the absolute elevation maximum in topography).

active in the lowest ~95 m ag. However, in the cross-section and event mean precipitation the effect of precipitation generation or reduction is weak, justifying the assumption that cloud-dynamical precipitation enhancement is less important in the lowest ~95 m ag and hence particle-flow interactions dominate. Results based on this approach should still be regarded as a rough approximation and the analysis intends to give a first estimate of the importance of the different local precipitation processes.

Maximum precipitation enhancement due to cloud-dynamics and mean advection at ~95 m ag is defined as the first local maximum of event mean precipitation rate downstream of the main mountain ridge (Figure 4.2a). Analogously, maximum precipitation enhancement by near-surface preferential deposition due to processes below the lowest ~95 m ag is defined as the first relative maximum of event mean precipitation rate on the leeward side (and if applicable on the windward side) of the main mountain ridge (Figure 4.2c). The local importance of cloud dynamics and mean advection (near-surface preferential deposition) is estimated as the positive precipitation anomaly at the first local maximum downstream of

the main mountain ridge with respect to the cross-section and event mean precipitation rate at ~ 95 m ag (~ 3 m ag). The effect of near-surface preferential deposition is only estimated for cross-sections, for which sublimation in the lowest ~ 95 m does not induce a snow precipitation decrease $> 0.02 \text{ mm h}^{-1}$ (i.e. excluding Sattelhorn ridge and Piz Radönt on 5 March 2016). The cumulated effect of cloud dynamics, mean advection and near-surface preferential deposition is estimated as the leeward-side and event mean precipitation with respect to the windward-side and event mean precipitation at ~ 3 m ag (Figure 4.2b).

4.2.5 Photogrammetrically determined snow depth distribution

Snow depth maps with a resolution of 2 m, retrieved from airplane-based photogrammetry, are available for the Dischma valley for two days in winter 2015/16. Flights have been performed on 26 January 2016 and 9 March 2016, covering the Dischma valley and the Wannengrat area. Absolute snow depth is calculated by the difference of the winter flights and a snow-free flight in September 2013 and is corrected for buildings, vegetation (> 1 m), outliers and pixels, which are obviously snow free on the pictures (Bühler et al., 2015). To evaluate snow accumulation patterns, the difference between the winter snow depth maps on 9 March 2016 and on 26 January 2016 is calculated.

The uncertainty of the snow depth maps is about ± 30 cm (Bühler et al., 2015). However, both flights were performed during slightly cloudy conditions, which lead to weak image matching, resulting in a high number of interpolated snow depth values in certain areas. This introduces additional uncertainty. Furthermore, about 1.5 months passed between the two measurements, implying that several snowfall events, post-depositional snow redistribution and snow settling shape the observed snow accumulation patterns.

Based on snow depth change and corresponding wind direction measurements of five automatic weather stations in the surroundings of the Dischma valley, about 67.6 % of the summed snow accumulation between 26 January 2016 and 9 March 2016 happened during north-easterly, northerly, north-westerly and westerly advection and 32.4 % during easterly, south-easterly, southerly and south-westerly advection. To compare measured snow accumulation patterns to modeled snow precipitation patterns, solid precipitation simulated for the two precipitation events on 31 January 2016 (northerly to north-westerly advection) and 5 March 2016 (southerly advection, Section 4.2.2) is weighted by these percentages. This implies the assumption that the precipitation distribution is similar for different precipitation events with the same main wind direction. Individual storms likely result in different precipitation patterns (e.g. due to different atmospheric conditions). However, end-of-winter snow accumulation was found to be consistent with few major storms (Schirmer et al., 2011). The two analyzed precipitation events were two out of three major snow precipitation events between the 26 January 2016 and 9 March 2016 and thus likely representative for the precipitation distribution during this period.

The snow depth measurements and simulated snow precipitation are compared along four transects within the simulation domain d04: two in north-westerly to south-easterly direction and two in southerly to northerly direction. They are chosen such that areas of interpolated snow depths (i.e. areas with weak image matching) are best possibly avoided. Snow depth measurements are smoothed using a 500 m and a 100 m moving average filter to make large-scale trends visible.

4.3 Results and Discussion

Results are presented and discussed as follows: first, precipitation patterns are analyzed with respect to different model resolutions (Section 4.3.1). Subsequently, precipitation patterns developing due to the combined effect of cloud dynamics and mean advection (Section 4.3.2) and near-surface preferential deposition (Section 4.3.3) are discussed. A comparison of modeling results with spatial snow depth measurements is provided in Section 4.3.4. Finally, we estimate the contribution of the different precipitation processes to snow accumulation patterns in the COSMO-WRF model (Section 4.3.5). Bear in mind that the effects of different precipitation processes are estimated based on the assumption that cloud-dynamical precipitation growth and mean advection are dominant above the lowest ~ 95 m ag, while in the lowest ~ 95 m ag near-surface preferential deposition is dominant (Section 4.2.4).

4.3.1 Effects of model resolution on the representation of snow precipitation processes

Model resolution has as strong effect on the topography and thus, especially in complex terrain, on the representation of valleys and mountain peaks. This affects terrain-flow interactions, which have a strong influence on precipitation formation and distribution (e.g. Lehning et al., 2008; Mott et al., 2014). Therefore, we illustrate the importance of very high resolution simulations, to address mountain-ridge to mountain-valley scale precipitation distribution in complex alpine terrain.

In our COSMO–WRF simulations with a horizontal grid spacing of 450 m no clear sign of local orographic precipitation enhancement or near-surface preferential deposition is found (Figures 4.3a and 4.3g). Mountain ridges are quite flat for a horizontal grid spacing of 450 m (Figure 4.3k). Consequently, updrafts are weak going along with a low cloud-droplet concentration (i.e. weak low-level cloud formation) and a weak precipitation production over shallow mountain peaks, which is in agreement with findings in Gerber et al. (2018, Chapter 3).

Up- and downdrafts become more pronounced for simulations with a horizontal grid spacing of 150 m (Figure 4.3l). This results in slightly enhanced precipitation on the leeward side of the mountain ridge (Figure 4.3b and Figure 4.3e) and indicates that the combined effect of local cloud dynamics and mean advection starts to be resolved. Slightly enhanced precipitation deposition over the mountain peak is further visible, likely due to reduced updrafts over the mountain ridge (Figure 4.3h) preventing the transport of snow over the ridge. Lee-side flow separation is not resolved, which leads to a quite homogeneous precipitation distribution in the lowest ~95 m ag.

For simulations with a horizontal grid spacing of 50 m updrafts are even stronger than for simulations with a horizontal grid spacing of 150 m (Figure 4.3m). Downdrafts on the leeward side of the mountain ridge become weaker and lee-side flow separation or even a lee-side eddy start to be resolved. Small-scale flow features such as lee-side eddies are in agreement with flow fields observed during field measurements and in large-eddy simulations with a horizontal grid spacing of 25 m (e.g. Gerber et al., 2017a). They may strongly affect snow precipitation patterns. Flow separation on the leeward side of the mountain ridge results in peak precipitation in the area of weak wind speeds on the leeward side of the mountain ridge. This peak precipitation due to terrain-flow interactions in the lowest ~95 m ag is in good agreement with preferential deposition (Lehning et al., 2008, Section 4.3.3). Larger elevation differences in topography on the windward side of the mountain ridge at a horizontal grid spacing of 50 m compared to a horizontal grid spacing of 150 m allow for enhanced condensation and precipitation production. Mean advection leads to a downstream shift of the precipitation peak toward the leeward side of the ridge (Mott et al., 2014, Section 4.3.2). Similar precipitation patterns and flow fields emerge for three mountain ridges for two precipitation events (not shown).

A sensitivity study is performed to address the effect of stronger versus weaker smoothing of the model topography (Section 4.2.1). Restricting maximum slope angles in domain d04 to 45° yields maximum slope angles of 39.8° and 35.2° in domains d03 and d02, respectively (strong smoothing). They are compared to simulations with weaker smoothing i.e. maximum slope angles of 45° in domains d03 and d02 (Figure 4.3). When regarding the whole simulation domain d02 an upstream shift of precipitation is observed for weaker smoothing. This confirms the finding by Gerber et al. (2018, Chapter 3) that too small slope angles in the north-western part of domain d02 are responsible for weak precipitation in this area. In the Dischma valley, we observe the opposite behavior (less precipitation for weaker smoothing), which is likely a consequence of the upstream “rain out”. However, weaker smoothing (i.e. more pronounced valleys and ridges) compared to stronger smoothing, reveals a stronger elevation gradient of precipitation, which is in agreement with enhanced condensation due to larger elevation differences. The variability of precipitation across the investigated mountain ridges does not strongly change for different smoothing strengths.

Overall, these simulation results reveal that precipitation patterns across mountain ridges strongly depend on the grid resolution in COSMO–WRF simulations (Figure 4.3). The spatial variability of precipitation patterns increases with increasing model resolution, and a horizontal grid spacing of 50 m is required to resolve local cloud-dynamical effects and near-surface preferential deposition. This is in agreement with Mott and Lehning (2010), who found that effects of preferential deposition on the leeward

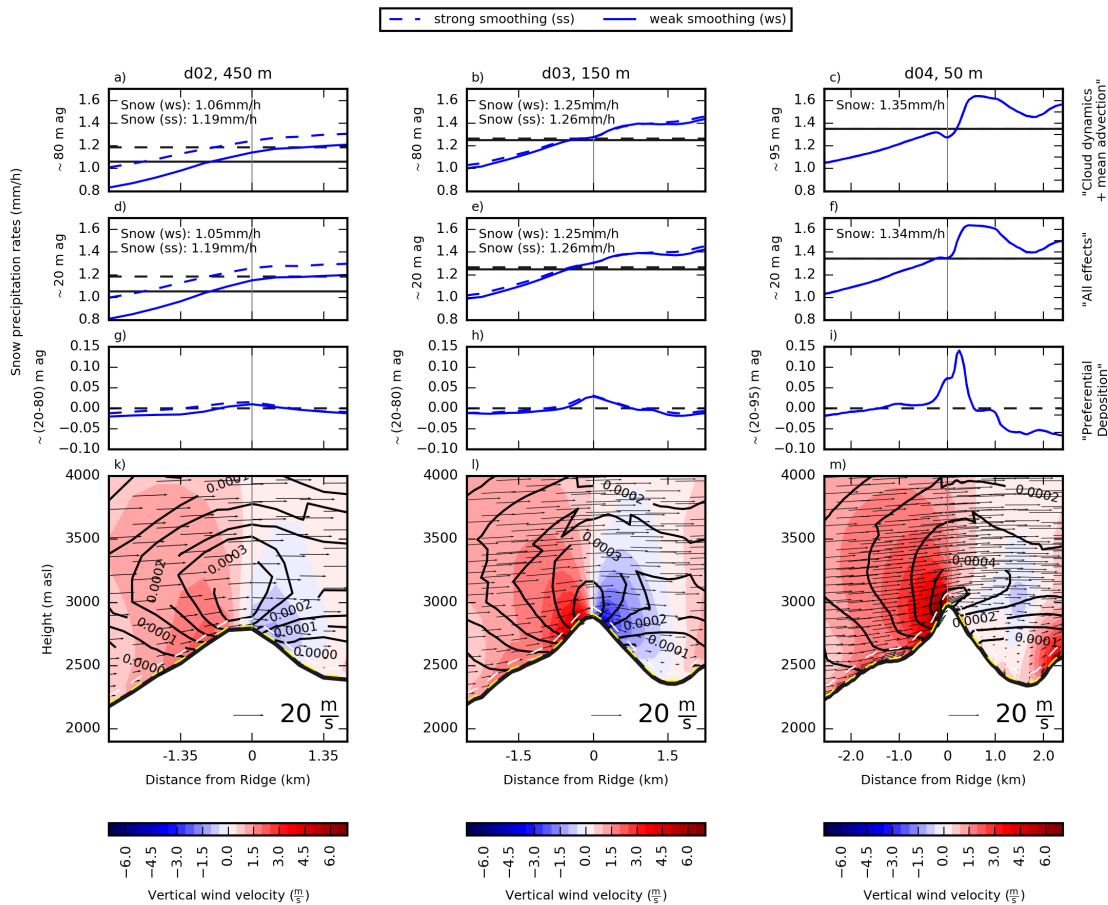


Figure 4.3: Cross-sections across Bocktenhorn (Figure 4.1) for 450 m (left), 150 m (middle) and 50 m horizontal grid spacing (right) for the 24-h precipitation event on 31 January 2016 (31 January 2016 00:00 UTC – 1 February 2016 00:00 UTC). a)-c) and d)-f) represent the event mean snow precipitation rates at ~80 m ag or ~95 m ag and ~20 m ag, respectively. g)-i) show the difference of the event mean snow precipitation rates between ~20 m ag and ~80 m or ~95 m ag. For simulations with 450 m and 150 m horizontal grid spacing event mean snow precipitation rates are given for weaker smoothing (solid blue line, maximum slope angles of 45° in d04) and strong smoothing (dashed blue line, maximum slope angles of 45° in d02 and d03, respectively). Solid (dashed) black lines in a)-f) mark the cross-section and event snow precipitation rate mean for weak (strong) terrain smoothing, which are given in the upper left corner as “Snow (ws)” and “Snow (ss)”, respectively. The dashed black line in g)-i) marks the zero-line. k)-m) show topography (m above sea level, m asl), vertical wind velocities (shading), plane wind (arrows) and cloud droplet mixing ratio (black contours). The yellow (white) dashed lines mark the ~80 m ag or ~95 m ag (~20 m ag level). Gray vertical lines mark the mountain ridges (i.e. relative elevation maxima of topography).

slope may be represented at a horizontal grid spacing of 50 m. However, to fairly represent deposition on windward slopes and post-depositional patterns even higher model resolutions and a coupling to an alpine surface processes model (e.g. Alpine3D, Lehning et al., 2008) would be required.

4.3.2 Cloud-dynamical effects and mean advection

To determine main features of cloud dynamics and advection we analyze precipitation patterns at ~95 m ag in domain d04 (50 m horizontal grid spacing, Section 4.2.4). Cloud-dynamical effects are expected to lead to precipitation enhancement over the mountain ridge, e.g. by the seeder-feeder mechanism (e.g. Mott et al., 2014). Low-level clouds are likely to produce graupel by accretion of cloud droplets on falling ice

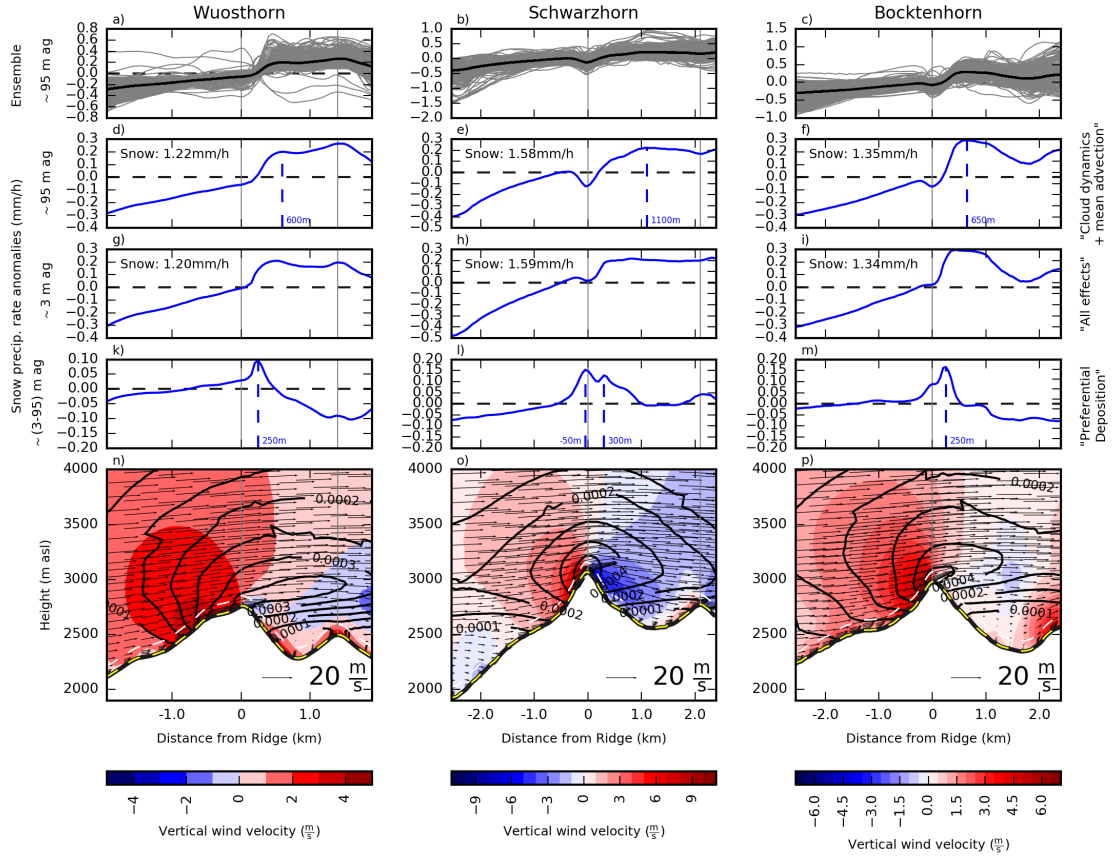


Figure 4.4: Cross-sections across Wuosthorn (left), Schwarzhorn (middle) and Bocktenhorn (right, Figure 4.1) for the 24-h precipitation event between 31 January 2016 00:00 UTC and 1 February 2016 00:00 UTC (50 m horizontal grid spacing). a)-c) show the 288 individual 5-minute snow precipitation rate anomalies (gray) and the 24-h mean snow precipitation rate anomaly (black) with respect to the cross-section and snow precipitation event mean. d)-f) and g)-i) show event mean snow precipitation rate anomalies with respect to cross-section and event mean precipitation rates (upper left corner) at ~95 m above ground (ag) and ~3 m ag, respectively (solid blue lines). k)-m) show the difference of snow precipitation rates between ~3 m ag and ~95 m ag (solid blue lines). Dashed blue lines and distances given to the right of the lines in d)-f) mark the position of peak snow precipitation downstream of the mountain ridge due to cloud dynamics and mean advection. Analogously, dashed blue lines in k)-m) mark snow precipitation peaks due to near-surface preferential deposition downstream (positive values) and upstream (negative values) of the mountain ridge. n)-p) show topography (m above sea level, m asl), vertical wind velocities (shading), plane wind (arrows) and cloud droplet mixing ratio (black contours). The white (yellow) dashed lines mark the ~95 m ag (~3 m ag level). Gray vertical lines mark the mountain ridges (i.e. relative elevation maxima of topography). Note different scales.

or snow particles (e.g. Grazioli et al., 2015). However, small-scale precipitation enhancement may also enhance snow precipitation by depositional growth (Stoelinga et al., 2013). The two precipitation events on 31 January 2016 and 5 March 2016 show strong differences with respect to graupel production. Therefore, we separately analyze snow and graupel precipitation patterns (hereafter called snow precipitation and graupel precipitation, respectively).

Snow precipitation patterns across mountain ridges show a strong temporal variability (Figure 4.4a-c and 4.5a-c). This indicates that snow precipitation and its interaction with the local flow field are very dynamic and sensitive to the upstream flow conditions. However, some distinct patterns are observed in the event mean snow precipitation rates across the investigated mountain ridges (Figure 4.4 and 4.5).

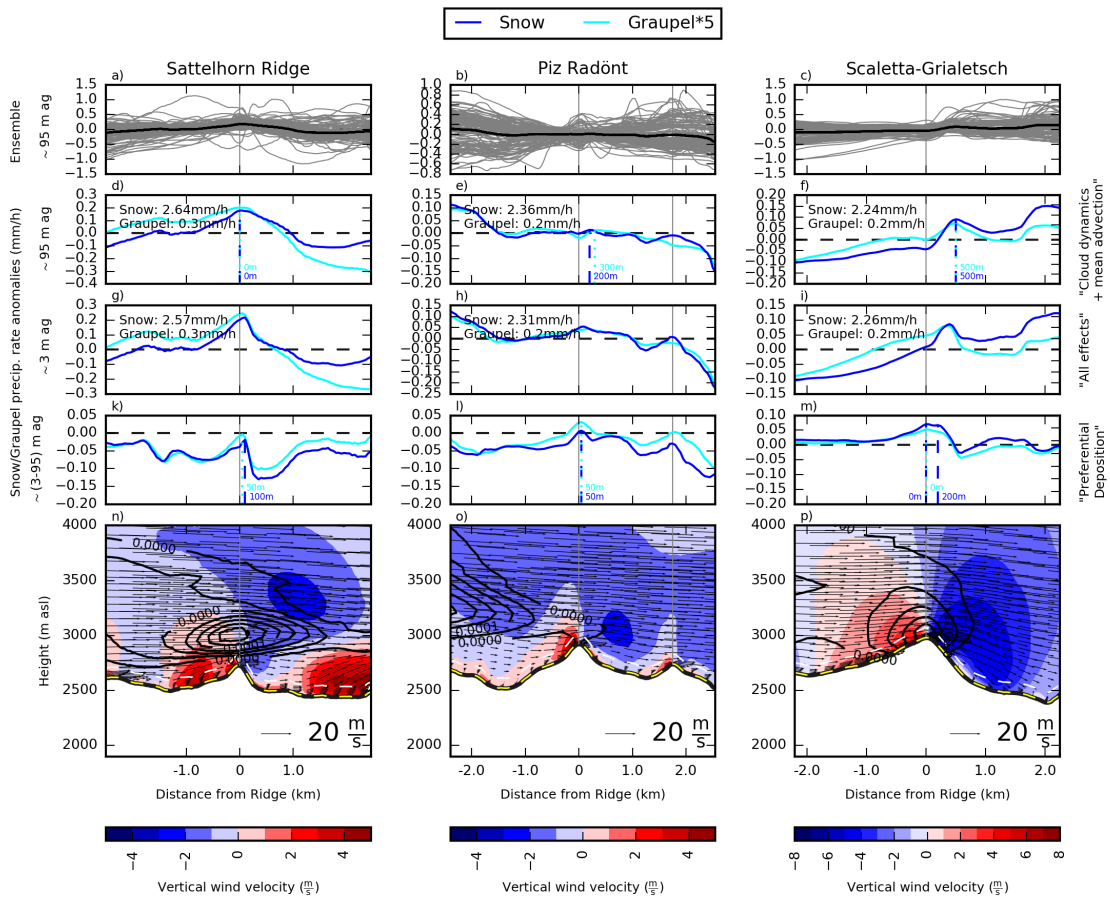


Figure 4.5: Cross-sections across Sattelhorn ridge (left), Piz Radönt (middle) and the ridge between Scalettahorn and Piz Grialetsch (right, Figure 4.1) for the 10-h precipitation event on 5 March 2016 between 07:00 UTC and 17:00 UTC (50 m horizontal grid spacing). a)-c) show the 120 individual 5-minute snow precipitation rate anomalies (gray) and the 10-h mean snow precipitation rate anomaly (black) with respect to the cross-section and snow precipitation event mean. d)-f) and g)-i) show mean precipitation rate anomalies at ~ 95 m above ground (ag) and ~ 3 m ag, respectively. k)-m) show the difference of precipitation rates between ~ 3 m ag and ~ 95 m ag. Snow precipitation is given by solid blue lines. Graupel precipitation (solid cyan lines) is exaggerated by a factor of 5. Snow and graupel precipitation anomalies in d)-i) are given with respect to the cross-section and event mean of snow or graupel precipitation, respectively (given in the upper left corner). Dashed blue (cyan) lines and distances given to the right of the lines in d)-f) mark the position of peak snow (graupel) precipitation downstream of the mountain ridge due to cloud dynamics and mean advection. Analogously, dashed blue (cyan) lines in k)-m) mark snow (graupel) precipitation peaks due to near-surface preferential deposition downstream of the mountain ridge. n)-p) show topography (m above sea level, m asl), vertical wind velocities (shading), plane wind (arrows) and cloud droplet mixing ratio (black contours). The white (yellow) dashed lines mark the ~ 95 m ag (~ 3 m ag level). Gray lines mark the mountain ridges (i.e. relative elevation maxima of topography). Note different scales.

Mean snow precipitation patterns across four mountain ridges show a peak in precipitation few 100 m downstream of the main mountain ridge (Figure 4.4d-f and 4.5f). This represents the combined effect of small-scale orographic precipitation enhancement and mean advection. In the WRF model snow may grow by deposition, collection of cloud droplets or autoconversion of ice (i.e. when ice reaches a certain size by vapor diffusion growth, Morrison et al., 2005). For Wuosthorn, Schwarzhorn and Bocktenhorn (Figure 4.4d-f) local snow precipitation production at higher elevations is in agreement with the presence of a high cloud-droplet concentration (i.e. depositional precipitation growth or precipitation growth by

riming) over and downstream of the mountain ridge (Figure 4.4n and 4.4p). On the one hand, snow precipitation produced over the mountain ridge may be transported downstream. On the other hand, a downstream transport of condensates (cloud droplets) may enhance snow precipitation growth downstream of the main ridge.

Snow precipitation distribution across the ridge between Scalettahorn and Piz Grialetsch on 5 March 2016 (Figure 4.5f) is similar to the distribution across Wuosthorn, Schwarzhorn and Bocktenhorn on 31 January 2016 with peak snow precipitation few 100 m downstream of the ridge, likely due to the combined effect of local orographic precipitation enhancement and mean advection. For the Sattelhorn ridge, peak snow precipitation is very close to the ridge (Figure 4.5d). This may be due to weaker advection of hydrometeors due to lower wind speeds (Table 4.1) or efficient downstream sublimation. No snow precipitation peak emerges for Piz Radönt on 5 March 2016. The precipitation event on 5 March 2016 shows southerly advection. The relatively dry air is a sign that at the large scale the Dischma valley is downstream of main precipitation for a southerly event and strongly influenced by a downstream drying of the atmosphere. This is in agreement with its location in the interior of the alpine mountain range (Figure 4.1). Downstream drying is confirmed by precipitation patterns observed on a larger scale, both in the model and in radar precipitation estimates (Chapter 3, Gerber et al., 2018). Additionally, a general sinking of air masses is observed at 4000 m asl for 5 March 2016 (Figure 4.5n-p), while air masses are lifted on a large-scale on 31 January 2016 (Figure 4.4n-p). Piz Radönt is the northernmost of the three investigated mountain ridges for the precipitation event on 5 March 2016 and may hence be located in too dry air to face local snow precipitation enhancement.

Strong differences between the two precipitation events are apparent for graupel. The precipitation event on 31 January 2016 does not show any significant graupel formation ($<1\%$ of mean solid precipitation across the three investigated cross-sections, not shown). On 5 March 2016, on the other hand, graupel formation makes up 5 % to 10 % of mean solid precipitation across the three investigated cross-sections (Figure 4.5). Graupel production in the model is based on (i) conversion of ice or snow to graupel by riming with cloud droplets, (ii) collision of rain with snow or ice, or (iii) freezing of rain (Reisner et al., 1998; Morrison et al., 2005). The two winter precipitation events addressed in this study produce a negligible amount of liquid precipitation in the upper Dischma valley and therefore processes including rain are irrelevant. For both events snow and cloud droplets do not coexist widely. However, there is a higher amount of ice available for the precipitation event on 5 March 2016 compared to the precipitation event on 31 January 2016, which may be a reason for stronger graupel production. Additionally, lower Richardson numbers up to higher atmospheric levels indicate stronger vertical shear of the horizontal wind and a lower dynamic stability of the atmosphere on 5 March 2016 compared to 31 January 2016 (Appendix C.2). A lower dynamic stability may be an effect of the general sinking of air masses on 5 March 2016, which interact with small-scale terrain-induced lifting upstream of the mountain ridges. This is in agreement with Grazioli et al. (2015), who found wind shear to be an important component of precipitation enhancement and the formation of rimed particles. Turbulent updrafts due to wind shear may lead to a continuous feeding of supercooled liquid water (i.e. cloud droplets) and ice crystals to the layer above the shear layer, where precipitation growth may take place consequently (Hogan et al., 2002). Once present, graupel may grow at the expense of cloud droplets or by deposition (Reisner et al., 1998). Another source of graupel may be the transport of graupel into the domain by mean advection, which is, however, not very likely due to their high fallout rates.

Overall, snow and graupel precipitation on 5 March 2016 shows similar precipitation patterns with enhanced precipitation few 100 m downstream of the mountain ridge. Differences in precipitation distribution across different mountain ridges for the two investigated precipitation events are attributed to different humidity conditions. When regarding the combined effect of cloud-dynamical processes and particle-flow interactions throughout the whole atmosphere (i.e. precipitation distribution ~ 3 m ag, Figure 4.4g-i and 4.5g-i) precipitation patterns across mountain ridges are similar to precipitation patterns ~ 95 m ag. The patterns agree well with the expected asymmetric precipitation distribution across a mountain ridge with peak precipitation downstream of the main ridge (Mott et al., 2014).

4.3.3 Near-surface particle-flow interactions

For Wuosthorn and Bocktenhorn on 31 January 2016 and for Sattelhorn ridge on 5 March 2016 a snow precipitation peak on the leeward side of the mountain ridge is observed due to processes in the lowest ~ 95 m ag (Figure 4.4k,m and Figure 4.5k). Assuming that precipitation patterns in the lowest ~ 95 m ag are dominated by particle-flow interactions, the simulated precipitation patterns may be regarded as near-surface preferential deposition. Peak precipitation as observed is in agreement with the concept of preferential deposition (Lehning et al., 2008). The snow distribution patterns represent the expected precipitation distribution for a precipitation transport over the mountain ridge and peak accumulation on the leeward side of the mountain ridge, where the flow field shows weak downdrafts or even a lee-side eddy. However, reduced snow precipitation due to reduced fall speeds on the windward side of the mountain ridge is not represented in the model. The assumption of dominant particle-flow interactions in the lowest ~ 95 m ag is supported by the fact that there is no strong increase in cross-section and event mean snow precipitation between ~ 95 m ag and the ground (Section 4.2.4). However, weak local snow precipitation growth may still take place and lead to snow precipitation enhancement in the vicinity of the mountain ridge, where the air is saturated. This might be a reason for increasing snow precipitation on the windward side close to the mountain ridge. For some cross-sections (Wuosthorn, Bocktenhorn, Sattelhorn ridge and Piz Radönt), a slight decrease in mean snow precipitation is observed in the lowest ~ 95 m ag (Appendix C.1), which is a sign for sublimation of precipitation. This effect is stronger on 5 March 2016 compared to 31 January 2016 due to dryer air masses (Section 4.2.2).

For Schwarzhorn on 31 January 2016 (Figure 4.4l) and the ridge between Scalettahorn and Piz Grialetsch on 5 March 2016 (Figure 4.5m) a double peak of snow precipitation is observed with the main snow precipitation peak at the mountain ridge and a second snow precipitation peak behind the mountain ridge. The second snow precipitation peak is likely a sign of preferential deposition as reported above. The snow precipitation peak over or slightly upstream of the mountain ridge may occur in this case but not in the other cases because terrain-induced updrafts are restricted to the windward side of Schwarzhorn and the ridge between Scalettahorn and Piz Grialetsch (Figure 4.4o and Figure 4.5p), while above the mountain peak vertical wind speeds are almost zero. Thus, precipitation may be deposited over the mountain ridge. In contrast, for the mountain ridges discussed above, updrafts are still active over the mountain ridge top.

Graupel precipitation on 5 March 2016 shows similar precipitation patterns as snow precipitation but graupel precipitation peaks show a tendency to be slightly shifted upstream compared to peaks of snow precipitation. The most likely reason for this is that graupel has higher fall speeds and therefore reaches the ground earlier than snow (Zängl, 2007).

In a recent study by Comola et al. (2018) the particle shape (expressed by particle inertia) has been reported to strongly affect precipitation distribution across an idealized hill. Flow conditions and snow precipitation patterns for the three mountain ridges Wuosthorn and Bocktenhorn on 31 January 2016 and Sattelhorn ridge on 5 March 2016 in our (inertialess) simulations are consistent with accumulation patterns for inertialess particles and strong advection in Comola et al. (2018), for which they found a precipitation peak on the leeward side of the mountain ridge. Based on Comola et al. (2018) this would imply that precipitation patterns in our simulations are representative for dendritic particles. For rounded particles (e.g. graupel) different patterns would, however, be likely. Similar precipitation patterns for mountain ridges with different slope angles confirm the finding by Comola et al. (2018) that steepness may not be a main factor determining snow precipitation patterns due to particle-flow interactions. Still, differences in snow and graupel precipitation patterns across different mountain ridges due to particle-flow interactions are likely linked to the complex topography, leading to irregular cross-sections and different flow fields.

Overall, snow and graupel precipitation patterns in the lowest ~ 95 m ag show a precipitation peak at the mountain ridge or slightly downstream for all investigated mountain ridges. For the precipitation event on 5 March 2016 a much weaker sign of preferential deposition and a smaller downstream shift of peak precipitation are observed compared to precipitation patterns on 31 January 2016. Different patterns are attributed to different flow conditions: constrained updrafts to the windward side of the mountain ridge versus updrafts over the leeward side of the mountain ridge and dry conditions leading to sublimation versus a saturated atmosphere.

4.3.4 Modeled precipitation patterns versus measured snow depth changes

Snow depth measurements with a resolution of 2 m based on airborne photogrammetry (Figure 4.6a) show a very high spatial variability of snow accumulation. A high spatial variability of snow accumulation patterns is expected, especially in steep terrain, due to the effect of post-depositional snow redistribution by wind and avalanches (e.g. Sommer et al., 2015).

A comparison of filtered snow accumulation measurements (500 m and 100 m moving average, solid and dashed red lines in Figure 4.6b-e) to precipitation patterns from COSMO-WRF simulations with a horizontal grid spacing of 50 m (solid blue lines in Figure 4.6b-e) reveals that COSMO-WRF simulations show a lower spatial variability but a stronger enhancement of snow precipitation over the south-western part of domain d04. The former confirms that very high resolution simulations are essential to capture snow accumulation patterns over complex terrain (Section 4.3.1). The latter may be an indication that local orographic precipitation enhancement over the highest mountain ridges is overestimated in the model simulations (Chapter 3, Gerber et al., 2018). This is likely due to an overestimation of precipitation production in the microphysics parameterization, which was originally developed for simulations with a much coarser resolution. On the other hand, a flattening of the snow distribution toward mountain ridges based on snow depth measurements was reported before (Grünwald et al., 2014; Kirchner et al., 2014) and could be a sign for post-depositional snow redistribution at high-elevation sites, which is not represented in the model. Although there are various reasons for disagreement, for two transects local precipitation trends on the order of a few kilometers show a certain agreement with filtered snow accumulation trends (Figure 4.6b and 4.6e).

Precipitation patterns due to processes in the lowest ~95 m ag (Figure 4.6b-e, dashed blue lines) do not show strongly enhanced precipitation rates over higher elevations but more small-scale precipitation variability. Some snow accumulation peaks based on measurements are in agreement with precipitation peaks due to near-surface precipitation processes in the model, which are likely dominated by near-surface preferential deposition (Section 4.2.4), while others are shifted, likely due to post-depositional snow transport in reality. Overall, it is interesting to note that for two transects (Figure 4.6c-d) large-scale precipitation patterns due to near-surface precipitation processes in the model show a closer agreement with measured snow accumulation than modeled total snow precipitation distribution. This may be an indication that, at a mountain-ridge scale, near-surface precipitation processes are more important for the final snow accumulation distribution than precipitation distribution farther above ground.

Differences may have manifold reasons from missing post-depositional snow redistribution in the model to measurement uncertainties (Section 4.2.5). Furthermore, aspect and slope of the mountain ridges are important parameters, e.g. determining snow settling and ablation (e.g. Grünwald et al., 2013; Kirchner et al., 2014). However, the presented comparison reveals that precipitation patterns at a mountain-ridge to mountain-valley scale in COSMO-WRF simulations at a horizontal grid spacing of 50 m partially represent snow depth measurements based on airborne photogrammetry. Precipitation parameterizations with a weak scale dependency and even higher resolution simulations would be required to further improve the representation of local precipitation patterns in complex terrain. Additionally, a coupling to an alpine surface processes model (e.g. Alpine3D, Lehning et al., 2008) would be beneficial for a refined comparison.

4.3.5 Estimation of the relative importance of different processes

Based on our analysis, we estimate the relative importance of different processes on the snow precipitation distribution across mountain ridges, being aware that the processes may not be fully distinguishable (Section 4.2.4). Therefore, we always refer to the levels, for which estimates are made, claiming that processes we refer to may not be the only processes leading to the observed patterns, and values presented below should be regarded as indicative (Section 4.2.4).

Small-scale orographic precipitation enhancement and mean advection, which are likely dominant above the lowest ~95 m ag may locally lead to an increase in snow precipitation of up to about 20 % with respect to cross-section and event mean precipitation (Section 4.2.4). The strength of local orographic precipitation enhancement and mean advection shows a strong variability between mountain peaks and precipitation events. The strongest dependency is observed with respect to the precipitation event. While

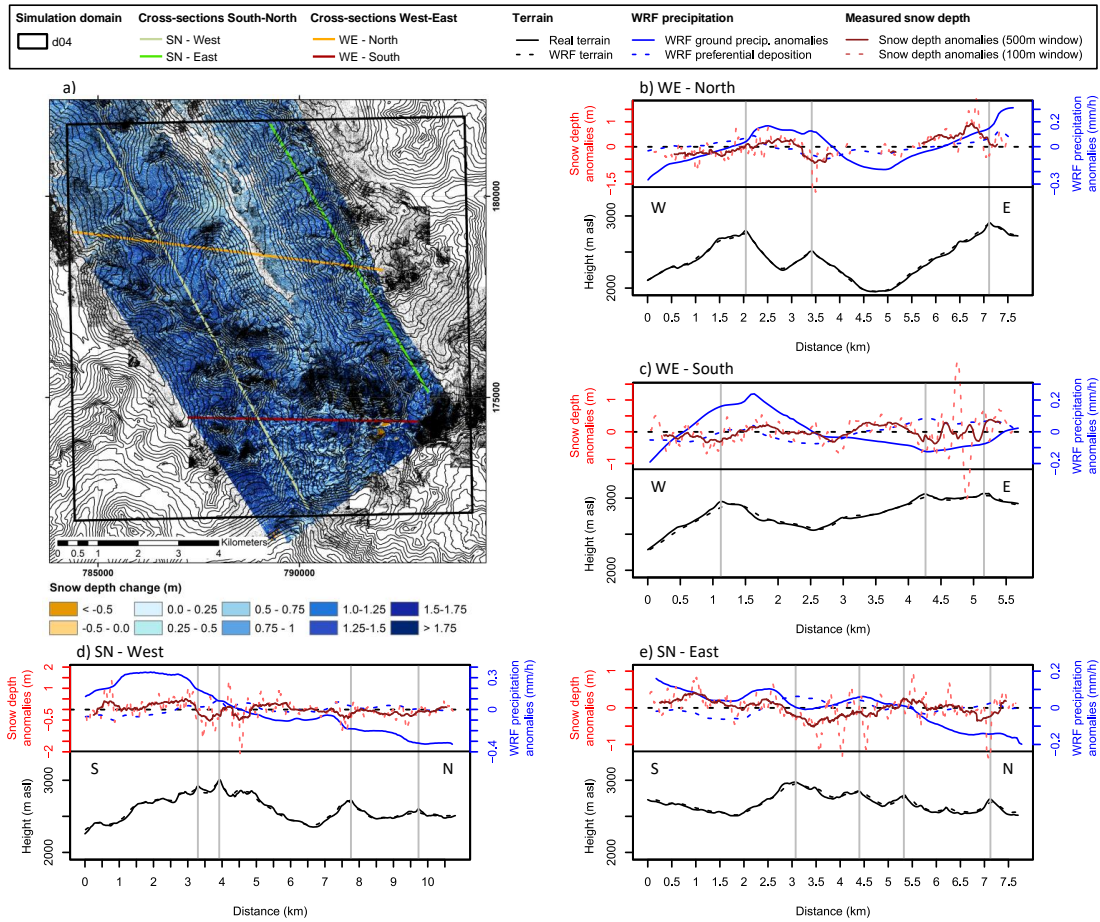


Figure 4.6: Cross-sections of COSMO–WRF precipitation patterns (50 m horizontal grid spacing) versus airborne photogrammetric snow depth change measurements with a resolution of 2 m. a) Snow depth changes (m) in the upper Dischma valley between 26 January 2016 and 9 March 2016. Four transects (b–e) within the simulation domain d04 (black box in a) are marked by solid lines in a). b)–c) show the northern and southern transect from west (W) to east (E). d)–e) show the western and eastern transect from south (S) to north (N). The directions of the transects is chosen such that they approximately fit one of the dominating wind directions (northwest to southeast and south to north) and to best possibly avoid areas of interpolated snow depth estimates (black dots in a, Section 4.2.5). COSMO–WRF ground precipitation anomalies (mm h^{-1} , solid blue line) with respect to transect mean precipitation and precipitation difference between ~ 3 m above ground (ag) and ~ 95 m ag (dashed blue line) are compared to measured snow depth patterns (m, red lines). Measured snow depth is smoothed using a moving average with a window length of 100 m (dashed red line) and 500 m (solid red line). Real and modeled topography are shown by black solid and dashed lines, respectively. Contour lines in a) are based on dh25 © 2018 swisstopo (5704 000 000).

local orographic precipitation enhancement and mean advection increase snow precipitation by 14 % to 22 % on 31 January 2016, the enhancement is only responsible for differences by 1 % to 7 % on 5 March 2016. The most likely reason for this difference is that the precipitation event on 5 March 2016 goes along with much dryer air compared to the precipitation event on 31 January 2016 (Section 4.3.2). For strong advection the precipitation peak is not expected over the ridge but shifted a few hundred meters downstream of the main ridge (Figure 4.4 and Figure 4.5, Section 4.3.2, Mott et al., 2014). Mean advection and peak snow precipitation distance from the ridge show a tendency of an increasing downstream shift of peak snow precipitation with increasing wind speeds (Table 4.1). However, this trend is only valid when comparing patterns for the same precipitation event.

The effect of particle-flow interactions in the lowest ~ 95 m ag (Section 4.2.4) may induce local changes

of snow precipitation patterns on the order of 10 % with respect to mean snow precipitation across the respective mountain ridge. As for local orographic precipitation enhancement and mean advection the effect is stronger for the precipitation event on 31 January 2016 where near-surface preferential deposition changes snow precipitation patterns by 8 % to 12 %. The effect estimated for the ridge between Scalettahorn and Piz Grialetsch accounts for 3 %. Sublimation, which is likely strengthened on the leeward side of the mountain ridge due to descending air, is again the likely reason for a weaker snow precipitation peak induced by preferential deposition on the 5 March 2016 compared to the 31 January 2016.

The cumulated effect of orographic precipitation enhancement, mean advection and near-surface preferential deposition results in asymmetric snow accumulation patterns across mountain ridges (Mott et al., 2014). In our simulations the strength of this asymmetry is strongly dependent on the atmospheric conditions. For the two case studies, we attribute the differences to the humidity of the atmosphere. However, there are likely other factors which determine the snow precipitation distribution across mountain ridges. While we report a weak asymmetry – even reversed for the Sattelhorn ridge and Piz Radönt – of –2 % to 6 % enhancement of event mean snow precipitation on the leeward side of the mountain ridge with respect to event mean snow precipitation on the windward side of the mountain ridge (Section 4.2.4), we can show that for humid conditions (as presented for the precipitation event on 31 January 2016) terrain-flow-precipitation interactions may increase snow precipitation on the leeward side of the ridge with respect to snow precipitation on the windward side of the mountain ridge by 26 % to 28 %.

4.4 Conclusion and Outlook

In this study, we investigate near-surface pre-depositional precipitation processes shaping snow accumulation patterns in COSMO–WRF large-eddy simulations with a horizontal grid spacing of 50 m. Additionally, the representation of terrain-flow-precipitation interactions is analyzed with respect to the model resolution.

The evaluation of different model resolutions reveals that near-surface precipitation processes are not resolved at a horizontal grid spacing of 450 m. Horizontal grid spacings as high as 50 m are required to represent small-scale terrain-flow-precipitation interactions (i.e. local orographic precipitation enhancement and preferential deposition) shaping mountain-ridge scale snow accumulation patterns, as flow separation on the leeward side of mountain ridges starts to be resolved at this resolution. Smoothing of topography does not have a strong effect on the spatial variability of snow precipitation across mountain ridges.

Based on simulations with a horizontal grid spacing of 50 m, the contribution of near-surface preferential deposition to snow deposition patterns is estimated to be on the order of 10 %, assuming that the contribution of cloud-dynamical precipitation formation in the lowest ~95 m above ground (ag) is negligible. The combined effect of cloud-dynamical processes and mean advection may introduce a precipitation peak a few 100 m downstream of the main ridge, enhancing precipitation by up to about 20 %. Overall, precipitation patterns show a strong temporal and spatial variability, which confirms that precipitation processes in the model are very dynamic. No clear relationship between wind speed and advection distance of precipitation is found. However, in our case studies weaker effects of terrain-flow-precipitation interactions go along with a dryer atmosphere.

These analyses are based on a simple approach to distinguish particle-flow interactions and cloud-dynamical processes. However, no clear separation of the processes is possible based on conventional WRF model output. As preferential deposition already starts at higher atmospheric levels than the lowest ~95 m ag as assumed in our study, the total contribution of preferential deposition is likely underestimated. On the other hand, the contribution of cloud dynamics is likely lower than our estimate of the combined effect, which includes local cloud dynamics and mean advection. Additionally, the model shows a tendency of overestimating orographic precipitation enhancement over the highest mountain peaks. A tracer experiment using a passive tracer, which is transported with the flow could be valuable for a more rigorous distinction between particle-flow interactions and cloud-dynamical effects on precipitation patterns. Furthermore, given that the model does not include post-depositional snow redistribution and is not coupled to an alpine surface processes model, we cannot address post-depositional snow redistribution, which has a strong impact on total snow accumulation variability (e.g. Vionnet et al., 2017).

Nevertheless, precipitation patterns in COSMO–WRF simulations resemble theoretical concepts of precipitation distribution due to pre-depositional precipitation processes (e.g. Lehning et al., 2008; Mott et al., 2014; Comola et al., 2018). Moreover, we could show that there is a certain agreement of filtered snow distribution from airborne photogrammetrically determined snow maps and modeled precipitation patterns for two transects in the Dischma valley. For two different transects measured snow depth patterns show a closer agreement with precipitation patterns due to processes in the lowest ~95 m ag. This comparison is based on numerous assumptions and could be improved by measurements of a single precipitation event. Additionally, measurements should be taken shortly before and after a snowfall event to best possibly avoid post-depositional redistribution and snow settling. Going toward higher resolution simulations, the development of a snow drift module for WRF or coupling WRF to an alpine surface processes model, would add to a refined comparison.

For a precipitation event with high humidity, 26 % to 28 % snow accumulation enhancement on the leeward side of three mountain ridges with respect to the windward side of the mountain ridges is reported. Snow accumulation patterns were found to be very persistent for different winters and were found to be dominated by few major snowfall events (Schirmer et al., 2011). However, given the inter-annual variability or even a shift in prevailing wind directions going along with climate change, a strong asymmetry of snow accumulation across mountain ridges may result in modified accumulation between different river catchments.

Acknowledgments *This work is funded by the Swiss National Science Foundation (Project: Snow-atmosphere interactions driving snow accumulation and ablation in an Alpine catchment: The Dischma Experiment; SNF-Grant: 200021_150146 and SNF-Grant: P300P2_164644). We thank the Swiss Federal Office of Meteorology and Climatology (MeteoSwiss) for providing COSMO–2 analysis and to let us use the regridding software fieldextra. Topographic data is reproduced by permission of swisstopo (JA100118). Special thanks go to Leica Geosystems for providing ADS80 data and to Yves Bühler and Mauro Marty for the processing of ADS80 data to obtain snow depth maps. Furthermore, we thank the Swiss National Supercomputing Center (CSCS) for providing computing time on their super computer and for technical assistance. For assistance with setting up COSMO–WRF additional thanks go to Varun Sharma, Megan Daniels and Louis Quéno. Additionally, we thank Heini Wernli and the anonymous reviewer for their questions, comments and recommendations, which helped to improve the paper.*

Conclusions and outlook

5.1 Conclusions

To estimate catchment runoff it is essential to have information about the spatial distribution of seasonal snow on mountain-ridge to mountain-valley scale (few hundred meters to few kilometers). However, the importance of local orographic precipitation enhancement and preferential deposition at these scales is barely known. Therefore, effects of terrain-flow-precipitation interactions on snowfall and the corresponding snow distribution at a mountain-ridge to mountain-valley scale are investigated, aiming to improve the knowledge about the relative importance of different pre-depositional precipitation processes on the seasonal snow distribution in complex alpine terrain. Nevertheless, complex process interactions and the fact that cloud-dynamical processes and particle-flow interactions are active at about the same scale make it challenging to decompose the processes acting on the snow distribution. Furthermore, processes are strongly dependent on various atmospheric conditions, the shape of the complex terrain and the chaotic behavior of the atmosphere.

Generally, there are two approaches to shed light on atmospheric processes. Atmospheric numerical models are used to run sensitivity studies of atmospheric processes and are used to reconstruct or predict atmospheric conditions for real-case studies. Yet, discretization and required parameterizations of unresolved processes are required. Thus, models show a strong simplification of reality. Due to the wide range of scales and non-linearities, modeling errors are hardly avoidable. The second approach is to perform in situ or remote sensing measurements, which have the advantage that they give information on actual conditions in reality. However, they are usually strongly restricted in spatial coverage or in spatial resolution and suffer from measurement uncertainties. Additionally, different measurements are required for different processes and interacting processes may not be distinguished. Furthermore, due to interferences of measurements with the solid surface and the complexity of alpine terrain, especially near-surface processes are hard to measure. Nevertheless, field measurements are essential for advances in process understanding and to investigate the ability and accuracy of model simulations in capturing reality. Thus, combined analysis of numerical simulations and field measurements are a valuable combination of information to understand the complex nature of precipitation processes in alpine terrain.

In this thesis, different processes, acting on snow precipitation and snow accumulation distribution at a mountain-ridge to mountain-valley scale, are addressed. Therefore, field measurements and corresponding numerical simulations are analyzed in combination to improve the process understanding of terrain-flow-precipitation interactions and their effects on snow distribution in complex alpine terrain.

Lee-side flow and snow accumulation To address the question on *how the small-scale lee-side flow field may affect preferential deposition in very steep terrain* a unique combination of field measurements and numerical simulations for a snowfall event in the upper Dischma valley (Davos, Switzerland) is analyzed (Chapter 2, Gerber et al., 2017a). To this end, high-resolution Doppler wind lidar flow field measurements and spatial snow distribution data, based on terrestrial laser scans, for a snowfall event in October 2015 are augmented with very high-resolution (25 m horizontal grid spacing) Advanced Regional Prediction System (ARPS) large-eddy simulations of the atmosphere based on a semi-idealized approach (real topography and idealized boundary conditions) to analyze the flow field and to force the alpine surface processes model Alpine3D.

Results reveal the complexity of terrain-flow-precipitation interactions over a very steep slope in the upper Dischma valley. By the means of a Doppler wind lidar radial velocity fields, we could document a very persistent eddy-like structure, which is likely a combination of a lee-side eddy and an along-ridge flow. Observations and corresponding model simulations confirm that the development of a lee-side eddy strongly depends on the slope, atmospheric stability, wind speed and direction. The type of flow separation and corresponding lee-side eddy development are shown to be important for snow accumulation patterns. In the model, moderate wind speeds and a near-neutral or slightly-stable atmosphere result in “postwave flow separation” and reveal a clear sign of preferential deposition. However, based on our measurements “lee-side bluff body boundary-layer” flow separation emerges for strong wind speeds and does not show a clear sign of close-ridge preferential deposition. This analysis shows that the interaction of the small-scale wind field and precipitation in steep mountainous terrain are more complex than previously found over flatter terrain. The study further confirms the finding that post-depositional processes are especially important in very steep terrain. Snow distribution by wind or avalanches are even likely to extenuate the signal of preferential deposition.

Semi-idealized numerical simulations are a good tool for sensitivity analysis and as boundary conditions to run an alpine surface processes model, linking atmospheric circulation to snow accumulation and redistribution. Nevertheless, given the very high horizontal resolution of 25 m and the highly complex topography, they are limited to relatively small domains and low wind speeds due to numerical issues. Given the periodic boundary conditions they represent a snapshot of atmospheric conditions. To include precipitation processes and the effect of larger scale atmospheric variability on the local precipitation distribution, high-resolution real-case simulations are essential. To this end, we coupled Consortium for Small Scale Modeling (COSMO) analysis with the Weather Research and Forecasting (WRF) model to downscale 2.2 km COSMO analysis to 50 m horizontal grid spacing large-eddy simulations based on a nesting approach.

Snow precipitation and accumulation variability To reveal if *real-case high-resolution large-eddy simulations can represent the spatial variability of precipitation in complex terrain* they are validated against automatic weather station data and compared to precipitation radar estimates (Chapter 3, Gerber et al., 2018). Especially wind direction strongly profits from high-resolution simulations when compared to automatic weather station measurements, due to the improved representation of topography at higher resolutions. Furthermore, a scale analysis based on variograms reveals that at large scales (>5 km) the model (at a horizontal grid spacing of 450 m) is able to capture a good portion of spatial variability compared to spatial variability observed by radar measurements. Based on two-dimensional autocorrelation maps, precipitation patterns in both, radar and model data, show a topography and wind direction dependency. This is in agreement with similar scale breaks at 5 km to 6 km in variograms of precipitation and topography. An increase of precipitation variability but constant variability of topography due to repeated mountain ridges and valleys above this scale indicate that the model captures the process of large-scale orographic enhancement although the agreement with radar precipitation patterns strongly depends on the precipitation event.

A second scale break in topography at ~1 km to 2.5 km separates the mountain-slope scale from the mountain-ridge to mountain-valley scale. Again scale breaks in both, variograms of radar estimates and modeled precipitation, emerge at similar scales. Similar slope angles of radar and COSMO–WRF precipi-

tation and their respective topography indicate that precipitation processes are topography driven, giving evidence for small-scale orographic enhancement at the mountain-ridge scale. However, COSMO–WRF simulations at a horizontal grid spacing of 450 m miss substantial small-scale variability, which is represented in radar precipitation estimates. This implies that the horizontal grid spacing of 450 m is not high enough to capture mountain-ridge to mountain-valley scale precipitation patterns. For higher resolution (50 m) simulations an increase in small-scale variability in the model is observed and demonstrates the potential of COSMO–WRF to capture local precipitation processes in complex terrain. Furthermore, differences in precipitation patterns between the elevation of the radar and the ground give evidence for near-surface processes in the model.

The scale analysis and 2-dimensional autocorrelation maps reveal that high-resolution COSMO–WRF simulations have potential to fairly represent large-scale precipitation processes over complex terrain at a resolution of 450 m. An increase in variability in precipitation patterns at higher resolution is an indication that additional precipitation processes are resolved with higher model resolution.

Near-surface winter precipitation processes over complex terrain To get further insight *at which resolution the small-scale flow field and mountain-ridge scale precipitation processes start to be resolved*, cross sections across several mountain ridges have been analyzed in the COSMO–WRF simulations (Chapter 4, Gerber et al., [in review](#)). A comparison of flow fields and snow accumulation patterns across different mountain ridges reveals that precipitation patterns across mountain ridges are strongly dependent on the model resolution. To clearly resolve mountain-ridge scale precipitation patterns associated with small-scale orographic precipitation enhancement, a model resolution of ≤ 50 m is required. At the same resolution lee-side flow separation starts to be resolved, resulting in preferential deposition of snow precipitation. A resolution of 50 m is by far higher than used in most studies addressing snow water resources in complex terrain and we highlight that resolutions ≤ 50 m are essential if mountain-ridge to mountain-valley scale processes are important.

Furthermore, we estimate *the relative importance of mountain-ridge scale processes on snow distribution*. To this end, we separate preferential deposition and local cloud-dynamical processes by assuming that preferential deposition is the dominant process within the lowest ~ 90 m above ground, while cloud-dynamical processes and mean advection are dominating above. Local precipitation enhancement by the combined effect of cloud-dynamical processes and mean advection lead to a downstream precipitation enhancement of up to 20 %. However, this strongly depends on the cross section and the precipitation event. Peak precipitation is advected downstream by a few hundred meters, which is in agreement with previous studies. Near-surface preferential deposition (lowest ~ 90 m of the atmosphere), on the other hand, was found to change snow accumulation on the order of 10 %, with peak deposition over the ridge or slightly downstream. Based on our approach, we likely underestimate the effect of total preferential deposition, as particle-flow interactions above the lowest ~ 90 m above ground count to the combined effect of cloud-dynamics and mean advection.

A comparison with snow depth measurements from airborne photogrammetric measurements was used to compare cross-ridge snow distribution to precipitation patterns in COSMO–WRF simulations. From this comparison, we conclude that COSMO–WRF simulations tend to overestimate the elevation gradient of precipitation. Nevertheless, some smaller scale patterns in the measurements are in good agreement with precipitation peaks due to near-surface preferential deposition in the model revealing that the importance of preferential deposition for the final snow accumulation patterns may even be higher than the importance of local orographic enhancement, which is in agreement with previous studies. Differences are likely due to post-depositional processes, which would require a coupling of COSMO–WRF to a surface processes model and even higher model resolutions.

Overall, the three presented studies, confirm the high complexity and variability of snow precipitation and accumulation due to interacting cloud-dynamical processes and particle-flow interactions as well as post-depositional processes in both, space and time. COSMO–WRF simulations at a resolution of 50 m underline the importance of the lee-side flow field, which is strongly determined by flow separation and

potentially the formation of a lee-side eddy, for snow distribution across a mountain ridge. However, such small-scale flow structures are not resolved in simulations with coarser resolution. Thus, we highlight that simulations with a model resolution of at least 50 m are essential if mountain-ridge to mountain-valley scale precipitation patterns need to be resolved.

The concept of preferential deposition has been addressed in this thesis. When the concept was introduced, preferential deposition clearly showed a snow deposition pattern with reduced snow accumulation on the windward side of the mountain ridge and enhanced snow accumulation on the leeward side of the mountain ridge. Different studies found evidence for this snow accumulation distribution across mountain ridges. However, recently it was found that the snow distribution across mountain ridges may be more complex than previously suggested. Different factors such as stability or particle shape can importantly affect the final snow distribution (Section 1.2.2). In this study, we highlight the impact of the lee-side flow field. We could show that the lee-side eddy formation in very steep terrain may play a crucial role for snow distribution and may together with post-depositional processes potentially erase peak snow accumulation on the leeward side of the mountain ridge. Additionally, our analysis reveals that the atmospheric humidity is an important factor acting on the snow distribution due to sublimation. Overall, further sensitivity studies are required to determine the exact role of preferential deposition in complex terrain.

To the best of the authors' knowledge, the relative importance of pre-depositional snow precipitation processes has been quantitatively estimated for the first time. Based on the presented estimate small-scale orographic precipitation enhancement and mean advection account for about twice as much precipitation enhancement on the leeward side compared to near-surface preferential deposition. However, preferential deposition is likely underestimated based on this approach, as mean advection and cloud dynamical effects cannot be distinguished. Estimating the combined effect of local orographic precipitation enhancement, mean advection and preferential deposition result in approximately 25 % enhanced snow accumulation on the leeward side compared to the windward side of a mountain ridge, although strongly dependent on atmospheric humidity. Especially in a changing climate modified atmospheric circulation might result in a change in wind direction for dominant snowfall events. As mountain ridges may separate different river catchments a change in dominant wind directions might strongly affect river runoff based on this estimate, which would be of paramount importance for water resources management, flood prevention or hydropower companies. Given high atmospheric variability, model assumptions, and uncertainties the presented estimates have to be refined based on additional case studies and field measurements. Overall, this thesis underlines the importance of very high-resolution simulations to address terrain-flow-precipitation interactions and contributes to the understanding of processes shaping mountain-ridge to mountain-valley scale snow distribution.

5.2 Outlook

Although it was possible to retrieve an estimation of the importance of near-surface preferential deposition and the combined effect of small-scale orographic enhancement and mean advection based on a modeling study (Chapter 4, Gerber et al., *in review*), it still needs to be proven that estimated values are valid. Thus, complementary studies are required to verify presented results. Furthermore, based on a variability analysis of precipitation patterns, we could show that current models – even at a resolution of 50 m – cannot capture the full variability of snow precipitation in complex terrain (Chapter 3, Gerber et al., 2018). Accordingly, it would be beneficial to study orographic precipitation enhancement based on high-resolution radar estimates. Additionally, the wide variety of atmospheric conditions is likely to strongly influence terrain-flow-precipitation interactions and resulting snow accumulation patterns (e.g. Chapter 2, Gerber et al., 2017a; Wang and Huang, 2017). Hence, it is important to perform additional sensitivity studies specifically addressing atmospheric conditions (e.g. stability, mean advection, humidity) as well as terrain characteristics (e.g. slope, curvature, elevation difference). Furthermore, increased model resolution and the use of a flow model, which performs better for very steep and complex terrain, would be beneficial.

Orographic enhancement in radar precipitation estimates

High-resolution radar snow precipitation estimates reveal precipitation patterns with a scale of about 1 km over complex terrain (Chapter 3, Gerber et al., 2018). These patterns may be linked to very local updrafts. However, they may also be a sign of small-scale orographic processes. This implicates that high-resolution radar precipitation estimates are valuable to investigate orographic precipitation structures. A growth and decay analysis may be based on the mean advection by the use of a Lagrangian approach. The precipitation field at one time step is shifted based on the flow field, which can be determined based on Doppler velocity analysis from the radar. The shifted precipitation field is then compared to the measured precipitation field after the respective time interval. Differences may be accounted as precipitation growth and decay and can be analyzed with respect to the underlying topography. In addition, hydrometeor classification, which allows to distinguish up to 9 different hydrometeor types (Besic et al., 2016), is further applied to identify regions of strong riming and aggregation co-occurring with ice crystals, which might be a sign of seeder-feeder precipitation growth. A wavelet decomposition analysis (Vetterli and Kovačević, 1995) will be performed to address the relation of precipitation growth and topography. First results reveal interesting patterns of snowfall growth, riming and co-occurring ice crystals and aggregates (Besic et al., *in prep.*). In addition to the spatial relationship, the authors plan to additionally assess the temporal resolution of precipitation processes.

Sensitivity studies

Model parameterizations Although the presented COSMO–WRF simulations fairly agree with measurements of automatic weather stations (Chapter 2, Gerber et al., 2017a), it would be extremely valuable to run sensitivity studies testing different model setups. There is a huge number of model parameters, which may be chosen in WRF simulations and may potentially make strong differences. Model simulations presented in this thesis are based on a standard approach, keeping the settings simple but being aware that they are likely to be improved by more advanced settings. Below, four examples of potential improvements are listed, which would be worth a sensitivity study in comparison with the presented simulation setup.

- COSMO–WRF simulations in this study are based on the 1.5-order turbulent kinetic energy sub-grid scale turbulence parameterization. However, this scheme does e.g. not account for the advection of turbulent kinetic energy (Mirocha et al., 2010). Advanced parameterizations of the sub-grid scale turbulence closure for LES simulations are available (e.g. Mirocha et al., 2010; Mirocha et al., 2014), which allow for different turbulent kinetic energy production and dissipation, which is likely to occur in complex terrain, and for backscatter (i.e. energy transport from smaller to larger scales). First tests using this non-linear option, however, introduced numerical instabilities in our current model setup, but would be worth to be investigated.
- Additionally, it has been shown that turbulence needs quite some distance from the boundary fetch to properly evolve in nested domains with higher model resolution (Mazzaro et al., 2017). There are approaches for faster turbulence generation, based on induced perturbations at the domain boundaries (Faure, 2008; Mirocha et al., 2014; Muñoz-Esparza et al., 2017). However, rougher terrain was shown to create turbulence quicker compared to flat terrain (Talbot et al., 2012; Mirocha et al., 2014). Given the high complexity of the terrain an investigation of turbulence evolution would be interesting.
- In our study the roughness length of snow has been strongly increased compared to standard settings in WRF, arguing that snow roughness in complex terrain is much higher compared to a snow covered flat field and to account for some unresolved sub-grid scale orography (Chapter 2, Gerber et al., 2017a). There is an alternative approach which takes into account unresolved variability of the topography (Jiménez and Dudhia, 2012; Lee et al., 2015). The unresolved variability of the topography is taken into account in the planetary boundary layer scheme. It would therefore be interesting to evaluate the impact of this option on wind speeds in the parent domain of our simulation setup and its effect on the nested LES domains.

- Moreover, a sensitivity study of precipitation in different microphysics schemes would be extremely valuable, as it has previously been shown that different microphysics schemes may produce quite strong differences (Liu et al., 2011). It would be interesting to evaluate precipitation over extremely complex topography at very high resolution and to investigate how they represent precipitation across mountain ridges, for different microphysics schemes.

Terrain-flow-precipitation interactions Except from sensitivity analysis based on model parameterizations, sensitivity analysis of processes would allow a systematic analysis of the impact of atmospheric conditions on preferential deposition or cloud-dynamical processes. It would e.g. be interesting to analyze the impact of different wind speeds on the downstream advection of snow precipitation. Based on idealized conditions, Comola et al. (2018) analyze preferential deposition for different flow regimes. They address the effect of rounded versus dendritic particles and the steepness of the hill. Systematic studies would, further, be beneficial to e.g. address the impact of static and dynamic stability of the atmosphere, temperature conditions or different hill shapes (concave versus convex) on local orographic precipitation enhancement and preferential deposition.

Tracer experiment to decompose process interactions

We applied a simple method to distinguish preferential deposition and small-scale orographic precipitation enhancement based on the assumption that orographic precipitation enhancement mainly takes place above the lowest ~90 m above ground, while preferential deposition is the dominant process in the lowest ~90 m above ground (Mott et al., 2014, Chapter 4). However, orographic precipitation enhancement is likely to still be active in the lowest atmospheric levels while preferential deposition is also active above and thus the two processes may not exclusively be distinguished. To achieve an improved decomposition of processes acting on the precipitation distribution across mountain ridges, a tracer experiment might be beneficial. This would imply adding a passive tracer with the same properties (density, size distribution, fall speed, mixing ratio, number concentration) into the atmosphere at an initial time. The distribution of the passive tracer would then indicate particle-flow interactions and the corresponding passive tracer distribution would reveal the expected “snow” distribution due to preferential deposition. Differences between the distribution of the passive tracer and solid precipitation could then be attributed to cloud-dynamical precipitation enhancement.

Coupled atmosphere-snow model

While standard atmospheric models are able to represent atmospheric processes fairly well, most of them still have a rudimentary representation of snow on the ground. As mentioned in Chapter 1, there are different ways how to model alpine surface processes. An alpine surface processes model may be run based on measurements by automatic atmospheric weather stations (Lehning et al., 2006). In more sophisticated approaches atmospheric input is based on high-resolution numerical simulations (Lehning et al., 2008; Raderschall et al., 2008). Information from spatial snow depth measurements may be used to distribute snow precipitation to retrieve an improved snow distribution in the model (Vögeli et al., 2016). Moreover, the coupling of an alpine surface processes model to a numerical model of the atmosphere was tested by Vionnet et al. (2014) and Vionnet et al. (2017) revealing encouraging results. Given a fairly good representation of precipitation patterns in COSMO-WRF simulations it would be interesting to couple this WRF setup to an alpine surface processes model such as Alpine3D.

Based on such a coupling, it would be possible to look at pre- and post-depositional processes in combination. This would be beneficial for comparison to field measurements of snow depth, which are always affected by post-depositional processes (Chapter 4). While we only address the relative importance of pre-depositional processes, a coupling of COSMO-WRF to an alpine surface processes model would further allow to take into account all pre- and post-depositional precipitation processes (Vionnet et al., 2017) that are forming final snow accumulation patterns.

Comprehensive field campaign

As demonstrated in this thesis and in previous studies (e.g. Mott and Lehning, 2010; Schirmer and Lehning, 2011; Scipión et al., 2013; Grazioli et al., 2015), field measurements are a valuable source of information to validate model simulations and to improve the process understanding of snow precipitation and snow accumulation. One big challenge in addressing the importance of pre-depositional precipitation processes on snow distribution is that the different processes take place simultaneously. Furthermore, terrain-flow-precipitation interactions are very dynamic and snow accumulation patterns are strongly influenced by post-depositional snow redistribution. Furthermore, changing wind directions may erase distinct accumulation patterns as expected from preferential deposition. Thus, airborne laser scans or photogrammetrically determined snow depth measurements should ideally be retrieved directly before and after a snowfall event, which is shaped by one main wind direction.

In this thesis, results from various measurements have been presented, which were performed during the Dischma-Experiment (DISCHMEX, Gerber et al., 2017a; Mott et al., 2017; Schlögl et al., *in review*; Gerber et al., 2018; Gerber et al., *in review*) in the Dischma valley (close to Davos, Switzerland). Terrestrial laser scans performed during DISCHMEX are restricted to one side of a mountain ridge and strongly limited in spatial coverage. On the other hand, photogrammetrically determined snow depth information was retrieved with a coarse time resolution of about one month between subsequent measurements, covering different snowfall events with various wind directions, strong snow redistribution and settling. Doppler wind lidar measurements were restricted to a short time period due to a lack of aerosols or attenuation by too strong snowfall during deployment.

All above mentioned and additional limitations concerning field measurements (good weather, strong enough but not too strong snowfall, snowfall with one distinct wind direction, operating and maintaining measurement devices in complex avalanche prone terrain, costs, etc.) make it extremely difficult to retrieve an unbiased picture of pre-depositional precipitation processes. Furthermore, field campaigns are often dedicated to a very specific question and thus only include a small set of measurements.

However, continuous efforts to retrieve a comprehensive field campaign should be taken. Simultaneous measurements including spatial snow depth distribution, radar precipitation measurements, Doppler wind lidar measurements of the flow field, radio soundings for stability analysis and model verification, snow drift measurements using snow particle counters and turbulence measurements and preferably automatic weather stations during a snowfall event with a persistent wind direction, would be extremely valuable to achieve an improved picture of terrain-flow-precipitation interactions.

Given permanent improvement in technology and applications, innovative approaches may emerge in the future enabling to perform insightful in-depth analysis addressing snow precipitation and accumulation patterns in complex terrain. Although, large-scale orographic precipitation enhancement may be modeled fairly accurate at resolutions of ≥ 1 km (Richard et al., 2007; Rasmussen et al., 2011; Pontoppidan et al., 2017), at this resolution models may not become able to accurately represent terrain-flow-precipitation interactions at a mountain-ridge to mountain-valley scale given that numerous mountain-peaks cannot be explicitly resolved. However, it is known that snow distribution may strongly vary across mountain ridges and end of winter snow accumulation patterns are known to be quite consistent between years, dominated by a few major snow precipitation events (Schirmer et al., 2011). As noted before, given the asymmetric snow distribution across mountain ridges, a climate driven change of dominant wind directions might lead to a shift in snow water resources between adjacent river catchments. Additionally, sublimation of drifting and blowing snow may cause a reduction of snow water resources and is prone to change for different atmospheric conditions in a changing climate. Thus, there is an urgent need for various additional studies to complement the current picture of terrain-flow-precipitation interactions and the knowledge about the importance of pre-depositional snow precipitation as well as post-depositional snow redistribution processes in complex terrain.



Supplementary Information for “A Close-Ridge Small-Scale Atmospheric Flow Field and its Influence on Snow Accumulation”

A.1 Meteorological stations

Table A.1 gives information of the geographical position of the meteorological stations used in this study. Additionally, for each station the relevant measured variables are given.

Table A.1: Overview over the meteorological stations. Latitude (Lat) and longitude (Lon) are given in WGS84 coordinates. Measured parameters, which are of interest in the present study (TA: air temperature, TSS: (snow) surface temperature, RH: relative humidity, VW: wind velocity, DW: wind direction, HS: snow depth, PSUM: precipitation in a heated gauge), are indicated by x.

Station	Lat (°N)	Lon (°E)	Elevation (m asl)	TA	TSS	RH	VW	DW	HS	PSUM
Dischma Moraine	46.7016	9.9449	2532	x		x	x	x	x	
Dischma Ridge	46.6939	9.9496	3034	x		x	x	x		
IMIS DAV1	46.6881	9.8146	2871	x		x	x	x		
IMIS DAV2	46.6992	9.8199	2561	x	x	x	x	x	x	
IMIS FLU2	46.7524	9.9467	2404	x	x	x	x	x	x	
WFJ2	46.8300	9.8096	2540	x	x	x	x	x	x	x

A.2 VAD-retrieved wind field and Backscatter

The velocity azimuth display (VAD) technique and assumptions are used to estimate the vertical wind profile from PPI scans with a 75° elevation angle that are repeated every 10 min. Time series of backscatter and VAD-retrieved winds for 28 October 2015 and 29 October 2015 are shown in Figure A.1 and Figure A.2, respectively.

A.3 TLS measurement and post-processing

The two terrestrial laser scans on 28 and 30 October 2015 (using a Riegl VZ-6000) have been performed with a line- and frame resolution of 0.007° corresponding to the beam divergence of the VZ-6000. This results in a resolution of about 30 cm (i.e. approximate distance between points in the point cloud) at a distance of 2500 m (approximate maximum distance in our measurements). All data was post-processed following the procedure by Sommer et al. (2015). The raw data are filtered by an octree filter to achieve evenly distributed data points. To calculate changes in snow depth, the two scans are aligned by 6 reference points and outliers and isolated points are removed. Additionally, a multi station adjustment is performed on the bare rock faces. Bare rock faces are filtered by an amplitude filter based on the blue portion of the color information, which is later on used to eliminate unchanged areas of the slope. The amplitude filter depends on the exposure of the pictures and is set to 150 dB and 400 dB for the TLS on 28 October 2015 and on 30 October 2015, respectively. To run the multi station adjustment rock faces are triangulated by a plane triangulation with a maximum triangle edge length of 5 m, a maximum triangle tilt angle of 90° and a minimum triangle angle of 2° . The multi station adjustment is done for a search radius of 1.5 m and a maximum tilt angle of 75° with the least square fitting mode. Based on this analysis the standard error resulting after multi station adjustment for the two scans is 1.61 cm.

A.4 Technical information about ARPS and Alpine3D simulations

Some general information about the simulation setup is given below, and additional technical information about the individual ARPS simulations used in this manuscript are given in Table A.2. Alpine3D is based on SNOWPACK, which is a physically based 1D column model to simulate energy balance processes of soil, snow and canopy. To account for lateral fluxes additional modules are run to calculate radiation balance, snowdrift, and runoff (while runoff is not included in the current simulation setup). The simulations are run with the Monin-Obukhov stability correction module (Michlmayr et al., 2008) and a roughness length of 0.007 m. The internal calculation time step is 15 min.

Domain: Upper Dischma valley, $6.25 \text{ km} \times 4.55 \text{ km}$, lower left corner: 46.7010°N , 9.8518°E (WGS84).
Grid size: 25 m

Vertical levels in ARPS: 35 generalized terrain-following levels

The Advanced Regional Prediction System simulations are run on Six Core AMD Opteron 2439 compute nodes. Necessary computational times are about 0.8 CPUh per simulated second on 96 nodes. Alpine3D simulations are run on intel i7-4770 compute nodes. The necessary computational time for the simulation without snowdrift is about 1.0 CPUh per simulated hour, while for the simulation with snowdrift it is about 6.5 CPUh per simulated hour on average on 2 nodes.

A.5 Alpine3D input

Table A.3 gives information on wind and precipitation input for the simulations with the alpine surface processes model Alpine3D. Wind fields are based on wind conditions measured at station *Dischma Ridge*. Precipitation is based on snow accumulation at station *Dischma Moraine*.

Table A.2: Technical details about the initial conditions in the ARPS simulations. The initial stability (Init. stability) used for the simulations is either neutral or slightly stable, which is determined based on meteorological stations in the surrounding of the upper Dischma valley. Initial wind speeds (Init. wind spd.) are given for 2700 m above sea level. Pot. temp. gives the near-surface potential temperature and wind dir. the initial wind direction.

Simulation	Wind dir.	Init. wind spd. (m s ⁻¹)	Pot. temp. (K)	Init. stability	Snow cover	Integration time (s)
SE_0.8	145°	0.8	295	neutral	–	250
SE_1.5	145°	1.3	295	neutral	–	250
SE_2.6	145°	1.8	295	neutral	–	160
SE_1.5stable	145°	1.0	295	slightly stable	yes	190
SE_3.9stable	145°	3.0	295	slightly stable	yes	190
S_3.2	180°	0.8	295	neutral	–	250
S_1.5stable	180°	1.3	285	neutral	–	250
NE_2.3	15°	0.2	295	neutral	–	250
NE_2.8	15°	0.4	295	neutral	–	250
NE_3.4	15°	0.8	295	neutral	–	250

Table A.3: Advanced Regional Prediction System (ARPS) wind fields used as input for the Alpine3D simulations. More information about the ARPS simulations is given in Table A.2. Precipitation is given as snow water equivalent, calculated from snow depth changes at the station Dischma Moraine assuming a snow density of 100 kg m⁻³. Wind speeds give the mean maximum wind speed at the Sattelhorn ridge (Figure 2.1 in the main manuscript). The period between 04:00 and 06:00 UTC+1 on 29 October 2015, where wind measurements at station Dischma Ridge are missing, is chosen to be NE_2.3, as the lidar measurements already indicate northerly winds for this period.

Day	Time UTC+1	Run	Wind direction	Wind speed (m s ⁻¹)	Snow water equivalent (mm)
28 Oct 2015	19:00–00:00	SE_2.6	145°	2.64	
29 Oct 2015	00:00–02:00	SE_2.6	145°	2.64	4.07
	02:00–04:00	SE_1.5	145°	1.45	1.18
	04:00–06:00	NE_2.3	15°	2.31	7.11
	06:00–12:00	NE_3.4	15°	3.38	7.68
	12:00–17:00	NE_2.8	15°	2.81	
	17:00–18:00	NE_2.3	15°	2.31	
	18:00–00:00	SE_2.6	145°	2.64	
30 Oct 2015	00:00–06:00	SE_2.6	145°	2.64	
	06:00–10:00	SE_1.5	145°	1.45	

A.6 Flow conditions in the ARPS simulations

Depending on the wind direction, ridge wind speed, and near-surface stability different flow patterns develop in the ARPS simulations for the upper Dischma valley (Figure 2.3e-f). For increasing ridge level wind speeds in simulations with a slightly stable stratification throughout the atmosphere (Section 2.2.4), the flow through the Dischma valley becomes more channeled, and southerly flow becomes dominant in the valley. Uphill flow components on both valley sides become smaller compared to simulation SE_0.8, where they are dominating the low-level flow-field (not shown). At higher levels easterly winds dominate for weaker ridge wind speeds, while for stronger ridge wind speeds the southerly component is pre-dominant. Under stronger ridge-level wind, blocking and an associated bending of the flow field around the Chlein Sattelhorn is still present, producing a weak along-slope flow on the leeward side of Sattelhorn in the lowest model levels (Figure 2.3d). Similar to weak ridge-level wind speed conditions, an eddy is forming on the leeward side of Sattelhorn (Figure 2.6), but this eddy becomes more compressed and slightly shifted to lower elevations along the lee-side slope (red bars in Figure 2.5). The vertical extent of the uphill flow toward the ridge ranges between 0 m to 134 m above ground and wind speeds in the lowest level of the eddy are between 0.2 m s^{-1} to 0.7 m s^{-1} (Table 2.1). Given the short integration time of the simulations (Section 2.2.4) eddy size and location are, however, likely to change for changing integration times.

Contrary, in the simulation initiated with a southerly flow and a neutral atmosphere (S_3.2) the flow is slightly bending to the east, when passing the Sattelhorn ridge. No eddy is observed in simulation S_3.2 (Figure 2.5). The simulations with a strongly stable near-surface atmosphere (S_1.5stable, SE_1.5stable and SE_3.9stable) show a different behavior compared to simulations with a slightly stable stratification throughout the atmosphere, with a downslope flow developing close to the leeward slopes. At higher levels the flow field is dominated by the initial wind direction (southerly winds in S_1.5stable and south-easterly wind in SE_1.5stable and SE_3.9stable). In simulation SE_1.5stable and SE_3.9stable, a blocking and associated turning of the flow around Chlein Sattelhorn is observed, similar to results from simulations under neutral south-easterly flow. However, the turning flow is weaker but has a greater vertical extent, and no eddy forms on the leeward side of the Sattelhorn. Simulation S_1.5stable shows the development of an eddy, but the along slope flow component is missing.

A.7 Alpine3D snow accumulation

Figure A.3 illustrates the evolution of snow accumulation in the Alpine3D simulation including drifting and blowing snow. Snow accumulation is calculated both with and without drifting and blowing snow in Alpine3D (Section 2.2.4). Figure A.3 and Figure 2.8 in the manuscript show that there is very little difference between the simulation with and without snow drift, as the model resolution of 25 m is too coarse to capture the small scale processes of snow redistribution (Mott and Lehning, 2010).

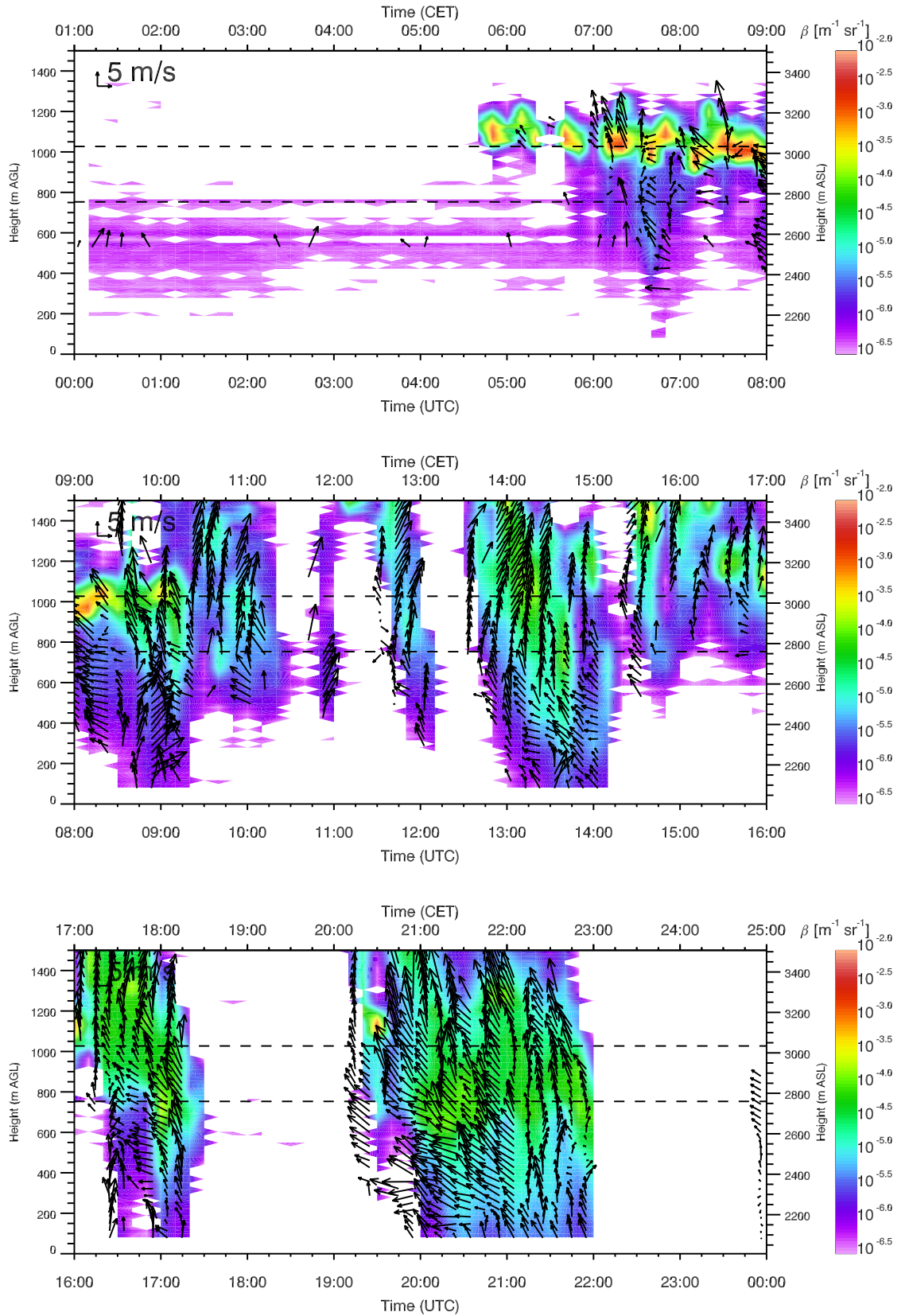


Figure A.1: Lidar backscatter and VAD-retrieved vertical profile of horizontal winds on 28 October 2015.

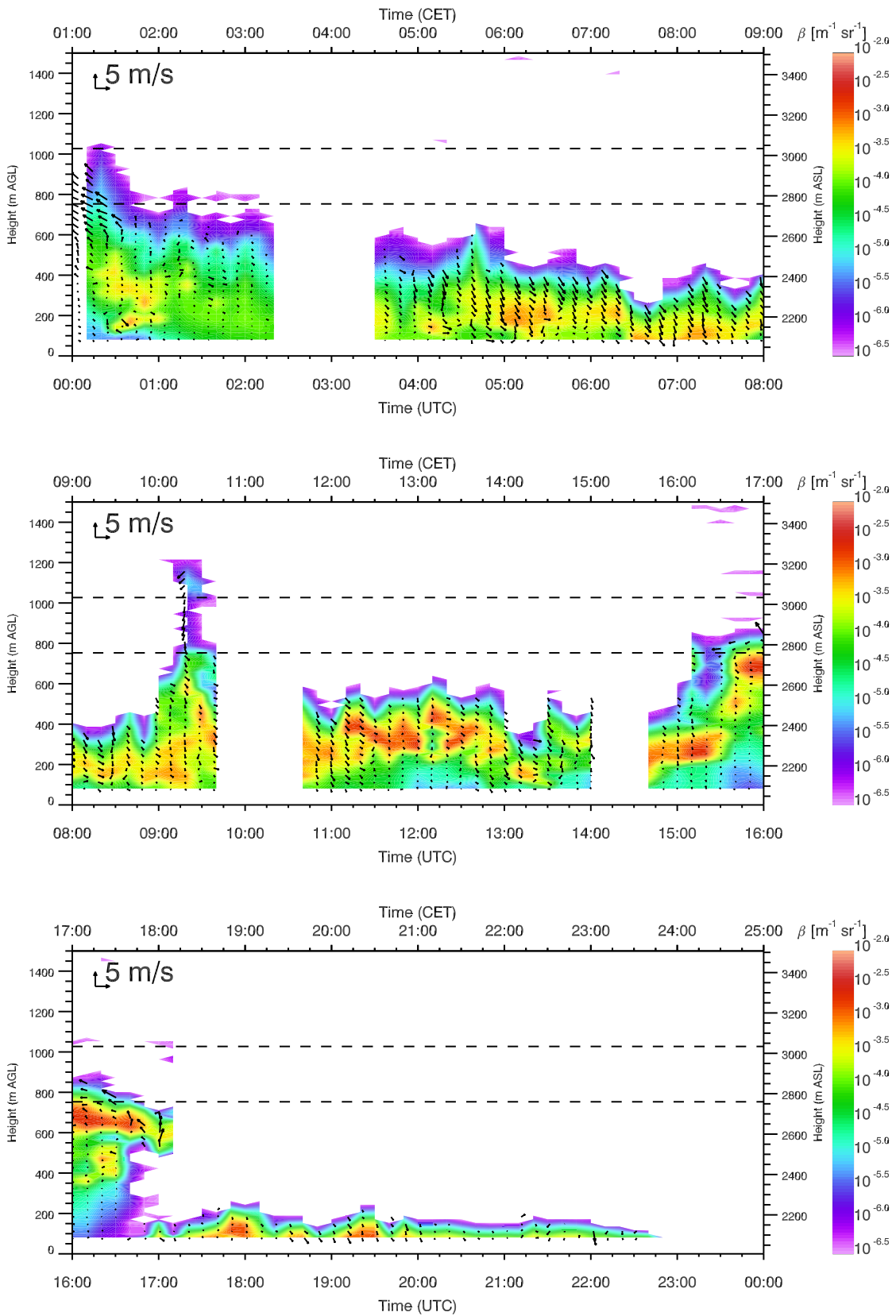


Figure A.2: Lidar backscatter and VAD-retrieved vertical profile of horizontal winds on 29 October 2015.

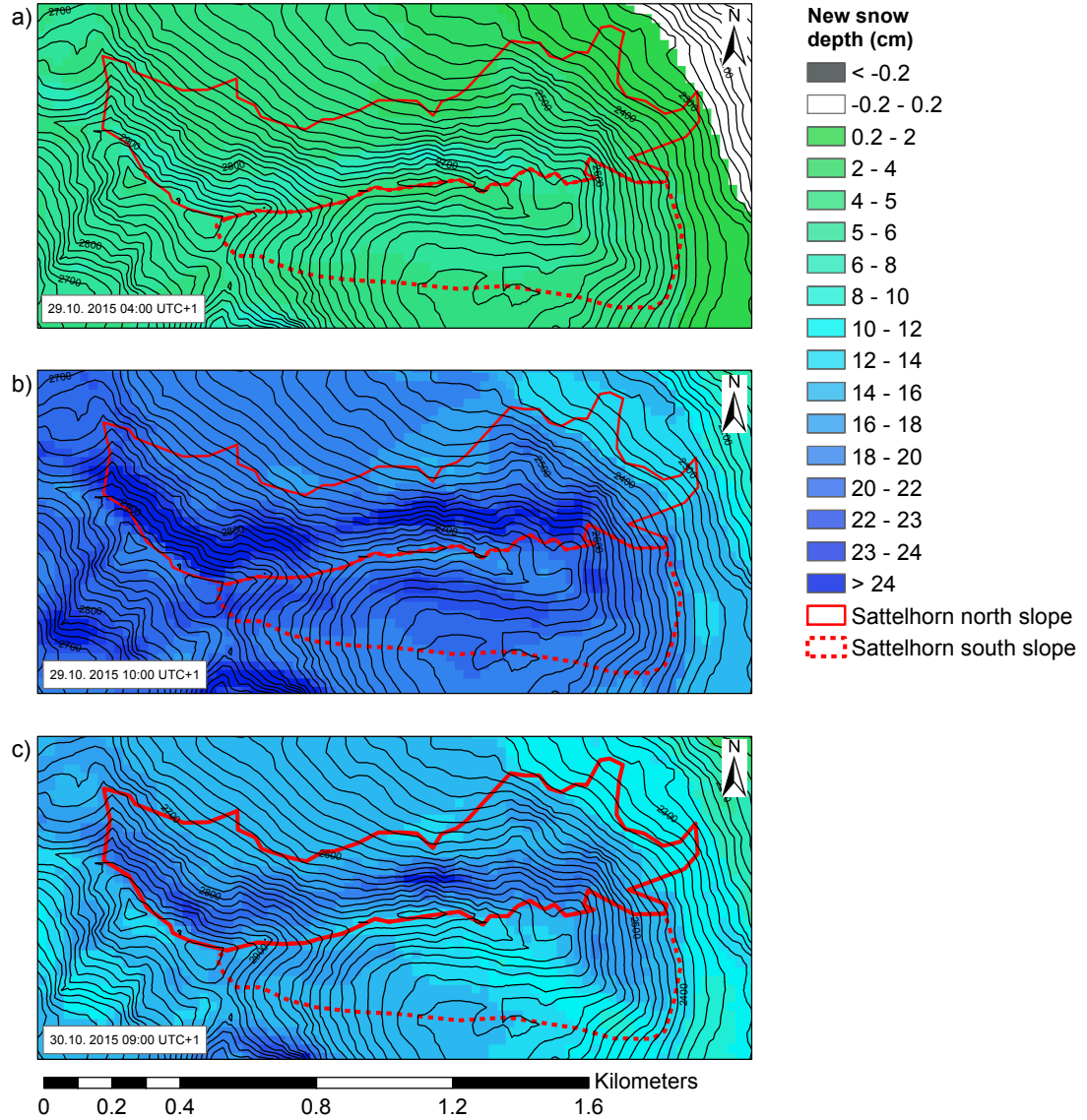


Figure A.3: Snow depth changes (cm) from the Alpine3D simulation with snow drift (resolution 25 m) between 28 October 2015 (before the snowfall event starts) and a) 29 October 2015 04:00 UTC+1, when the period of southerly winds ends, b) 29 October 2015 10:00 UTC+1, when the snowfall stops, and c) 30 October 2015 09:00, when the second terrestrial laser scan has been taken. Positive snow depth changes are given by green to blue colors. The red contour shows the area of the Sattelhorn north slope, which is covered by the terrestrial laser scan (TLS) measurements. The dashed red contour marks the Sattelhorn south slope. The area of the Sattelhorn north and south slope (red) are marked in Figure 2.1 of the main text. Contour lines: dhm25 © 2018 swisstopo (5740 000 000).

B

Supplementary Information for “Spatial variability of snow precipitation and accumulation in COSMO–WRF simulations and radar estimations over complex terrain”

B.1 Morrison microphysics in WRF

The Morrison microphysics scheme includes prognostic equations of number concentration and mass mixing ratio of 5 precipitation species (rain, snow, ice, graupel and cloud droplets). The parametrization of rain, snow, ice and cloud droplets is based on Morrison et al. (2005). The implementation of graupel follows Reisner et al. (1998), except for minimum mixing ratios, which are required to produce graupel from the collision of rain and snow, snow and cloud water, and rain and cloud ice, which are based on Rutledge and Hobbs (1984).

The kinetic equations include advection, sedimentation and turbulent diffusion as well as source and sink terms of ice nucleation and droplet activation, condensation and deposition, coalescence and diffusional growth, collection, melting and freezing as well as ice multiplication (Morrison et al., 2005). For graupel deposition, collection, collision, accretion, freezing and melting processes are parameterized (Reisner et al., 1998).

Size distribution functions are gamma functions:

$$N(D) = N_0 D^\mu e^{-\lambda D}, \quad (\text{B.1})$$

where D is the particle diameter, μ is the shape parameter of the distribution function, which is $\mu = 0$ for rain, snow, ice and graupel, resulting in an exponential function for $N(D)$. λ and N_0 are the slope and

intercept, respectively, of the size distribution, evaluated by the predicted number concentration N and mass mixing ratio q :

$$\lambda = \left[\frac{cN\Gamma(\mu + d + 1)}{q\Gamma(\mu + 1)} \right]^{1/d} \quad (\text{B.2})$$

and

$$N_0 = \frac{N\lambda^{\mu+1}}{\Gamma(\mu + 1)}, \quad (\text{B.3})$$

where Γ is the gamma-function. c and d are the parameters of the power-law function $m = cD^d$ indicating the mass-diameter relationship. Terminal fallspeeds are as well assumed to have a power-law form of $v(D) = \frac{\rho_{sur}}{\rho} aD^b$, with individual parameters a and b for the different species. ρ is the air density and ρ_{sur} the air density at sea level. For simplification all species are assumed to be spheres. Additionally, the particles do not have any particle inertia.

B.2 Variability at the local domain

Figure B.1 show the domain-wide statistics of the local domain, for which data has a resolution of 300 m (Figure 3.1). Variograms analogously to Figure 3.6 and Figure 3.7 are presented for the local domain. Trends removed from the data to produce the variograms in Figure B.2 are given in Table B.1. For Figure B.3 no trends are removed and small as well as intermediate scale patterns may be hidden by the domain-wide trends.

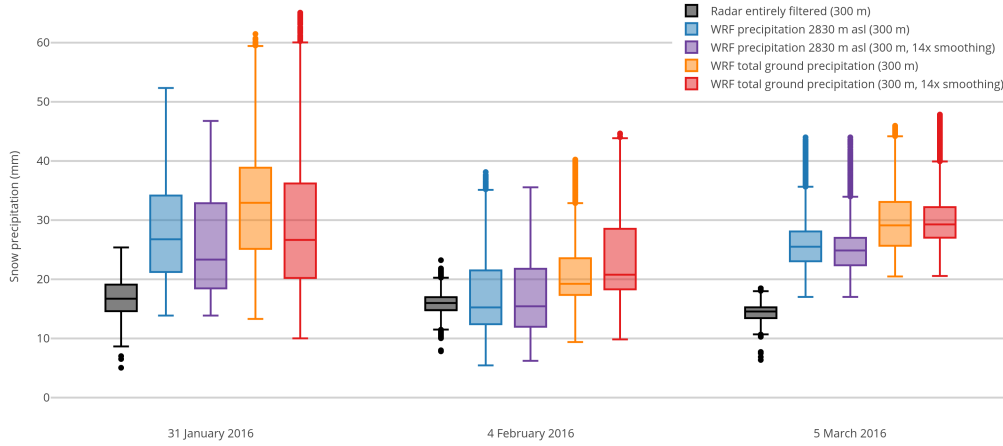


Figure B.1: Domain-wide 24 h precipitation statistics for the local domain (300 m resolution, Figure 3.1) for the three precipitation events on 31 January 2016, 4 February 2016 and 5 March 2016. Gray colors show entirely-filtered radar precipitation. WRF precipitation at 2830 m above sea level (m asl) for simulations with weak terrain smoothing (Section 3.2.1) and strong terrain smoothing are given in blue and violet, respectively. Orange (red) shows boxplots of WRF total ground precipitation for weak (strong) terrain smoothing. Radar precipitation and WRF precipitation at 2830 m asl are masked (as shown in Figure 3.4).

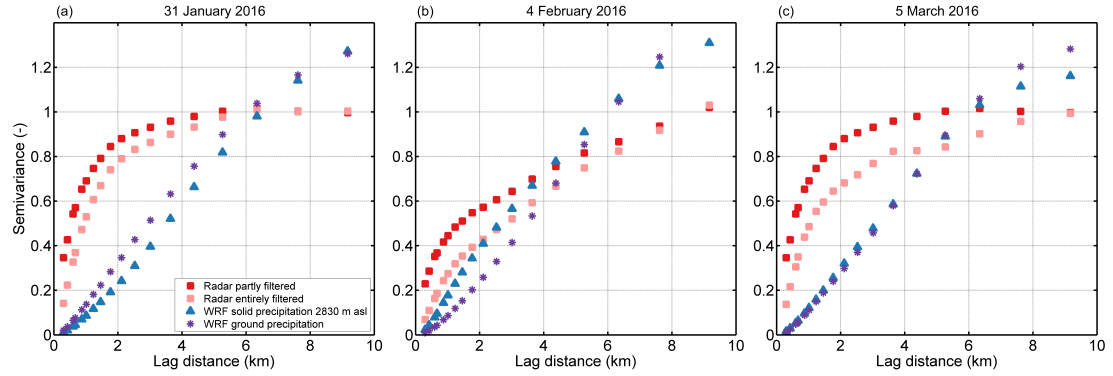


Figure B.2: Normalized variograms of detrended snow precipitation for the precipitation events on a) 31 January 2016, b) 4 February 2016 and c) 5 March 2016 for the local domain (Figure 3.1). Variograms are given for partly-filtered (red) and entirely-filtered (orange) radar snow precipitation, WRF snow precipitation at 2830 m above sea level (m asl, blue) and WRF total ground precipitation (violet). WRF precipitation is from simulations with weak terrain smoothing (Section 3.2.1). All precipitation fields are masked.

Table B.1: Large-scale linear trends of radar (Radar entirely filtered) and WRF precipitation patterns on the local domain (Figure 3.1). WRF precip. at 2830 m asl refers to solid precipitation in WRF simulations at 2830 m above sea level and WRF total ground precip. refers to the total (solid and liquid) precipitation at the ground level. Orient. gives the direction of the slope and Intensity the strength of inclination. 0° would indicate a slope pointing toward the East. WRF snow precipitation is from simulations with weak terrain smoothing (Section 3.2.1).

	31 January 2016		4 February 2016		5 March 2016	
	Orient.	Intensity	Orient.	Intensity	Orient.	Intensity
Radar entirely filtered	68.5°	0.14	150.5°	0.03	-135.4°	0.04
WRF precip. 2830 m asl	22.6°	0.26	5.8°	0.24	-79.6°	0.19
WRF total ground precip.	30.6°	0.32	24.2°	0.24	-67.6°	0.21

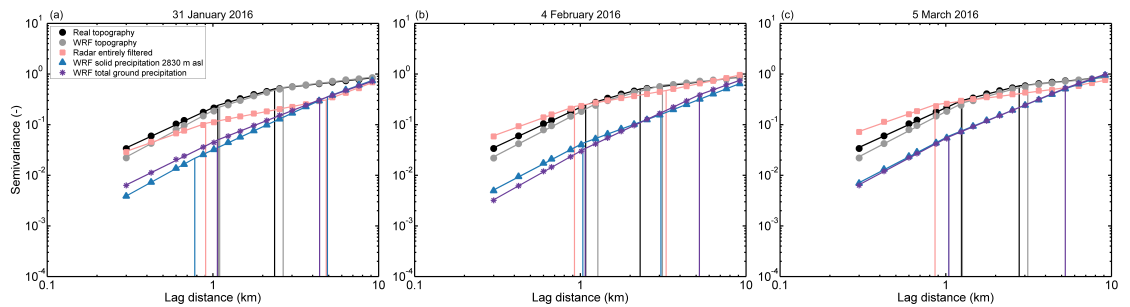


Figure B.3: Normalized variograms of the snow precipitation events on a) 31 January 2016, b) 4 February 2016 and c) 5 March 2016 for the local domain (Figure 3.1). Variograms are given for entirely-filtered radar snow precipitation (orange), WRF snow precipitation at 2830 m above sea level (m asl, blue) and WRF total ground precipitation (violet). Additionally, variograms are given for real topography (based on dh25 © 2018 swisstopo (5740 000 000), black) and WRF topography (gray). WRF topography and precipitation are from simulations with weak terrain smoothing (Section 3.2.1). All precipitation fields are masked.



Supplementary Information for “The importance of near-surface winter precipitation processes in complex alpine terrain”

C.1 Model level dependency and precipitation growth

Table C.1 and Table C.2 give summed event and cross-section mean precipitation growth between the 9 lowest adjacent model levels. Figure C.1 and Figure C.2 illustrate corresponding precipitation patterns across the six investigated mountain ridges for the two precipitation event on 31 January 2016 and on 5 March 2016, respectively. Patterns show a consistent change with increasing elevation above ground (increasing intensity of the blue color). The ~95 m ag level (which is used for the analysis in the manuscript) is marked by a red line.

C.2 Stability analysis

The dry static stability is analyzed based on the Brunt-Väisälä frequency N :

$$N = \sqrt{\frac{g}{\theta} \frac{d\theta}{dz}}, \quad (\text{C.1})$$

where g is the acceleration of gravitation, θ is the potential temperature and z is the elevation. To analyze the dynamic stability the Richardson number (Ri) is calculated, which is buoyancy squared divided by the square of vertical shear of the horizontal velocity:

$$Ri = \frac{-g \frac{d\rho}{dz}}{\rho_0 [(\frac{du}{dz})^2 + (\frac{dv}{dz})^2]}, \quad (\text{C.2})$$

Table C.1: Cross-section and event mean precipitation rate changes between the given model level (Level) and the level below for the precipitation event on 31 January 2016 00:00 UTC and 2 February 2016 00:00 UTC. The Elevation above ground (m ag) gives the cross-section mean elevation above ground averaged over all three cross-sections analyzed for the 31 January 2016 (i.e. Wuosthorn, Schwarzhorn and Bocktenhorn). Precipitation rate changes (Precip. rate change) are given in mm h^{-1} and $\text{mm h}^{-1} \text{m}^{-1}$. Precipitation rate changes in mm h^{-1} give the precipitation rate change between the adjacent levels for the cross-section and event mean precipitation rate. Precipitation rate change in $\text{mm h}^{-1} \text{m}^{-1}$ gives the precipitation rate change per elevation change of the cross-section and event mean precipitation.

Level	Elevation m ag	Wuosthorn		Schwarzhorn		Bocktenhorn	
		Precip. rate change mm h^{-1}	Precip. rate change $\text{mm h}^{-1} \text{m}^{-1}$	Precip. rate change mm h^{-1}	Precip. rate change $\text{mm h}^{-1} \text{m}^{-1}$	Precip. rate change mm h^{-1}	Precip. rate change $\text{mm h}^{-1} \text{m}^{-1}$
2	~ 10	-0.001	-2.1×10^{-4}	-5.0×10^{-5}	-7.9×10^{-6}	-0.0004	-6.7×10^{-5}
3	~ 19	-0.002	-2.2×10^{-4}	0.0002	2.4×10^{-5}	-0.0007	-7.3×10^{-5}
4	~ 32	-0.004	-3.1×10^{-4}	0.0006	4.5×10^{-5}	-0.001	-1.0×10^{-4}
5	~ 45	-0.004	-3.5×10^{-4}	0.001	9.5×10^{-5}	-0.002	-1.2×10^{-4}
6	~ 58	-0.005	-3.5×10^{-4}	0.002	1.7×10^{-4}	-0.001	-1.1×10^{-4}
7	~ 96	-0.005	-1.4×10^{-4}	0.006	1.6×10^{-4}	-0.0006	-1.6×10^{-5}
8	~ 161	-0.009	-1.4×10^{-4}	0.019	3.0×10^{-4}	0.003	5.0×10^{-5}
9	~ 226	-0.0002	-3.0×10^{-6}	0.029	4.5×10^{-4}	0.013	2.0×10^{-4}
10	~ 291	0.012	1.6×10^{-4}	0.037	5.7×10^{-4}	0.020	3.1×10^{-4}

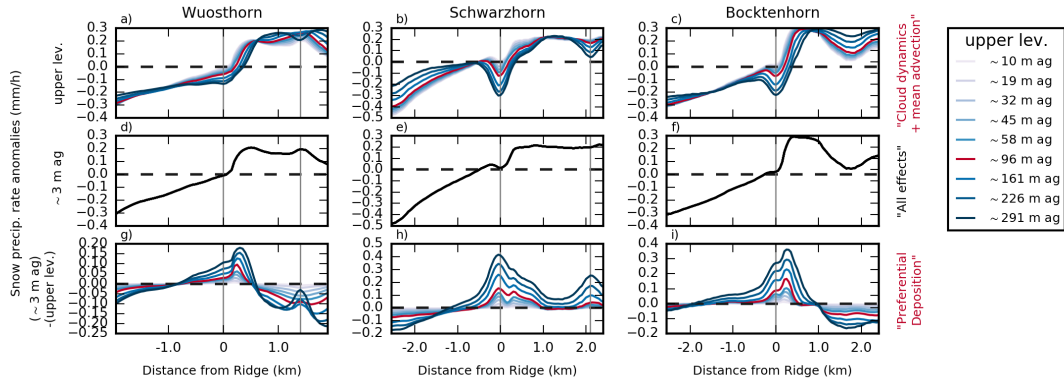


Figure C.1: Cross-section precipitation patterns across Wuosthorn (left), Schwarzhorn (middle) and Bocktenhorn (right, Figure 4.1) for the 24-h precipitation event between 31 January 2016 00:00 UTC and 1 February 2016 00:00 UTC (50 m horizontal grid spacing). a)-c) show event mean snow precipitation rate anomalies with respect to cross-section and event mean precipitation rates at 9 different model levels (upper lev.) between ~10 m ag and ~291 m ag. Darker blue lines go along with increasing model levels. The ~96 m ag level is shown by the red line. d)-f) show the event mean precipitation rate anomalies with respect to the cross-section and event mean precipitation rate across the three cross-sections at the lowest model level ~3 m ag. g)-i) show the precipitation distribution due to processes between the upper level (shown in a)-c) and the lowest model level ~3 m ag (shown in d)-f). Darker blue lines in g)-i) go along with increasing vertical model elevation of the upper level as for a)-c). Precipitation distribution due to processes in the lowest ~95 m ag (96 m ag in the legend) is shown by the red line. Gray vertical lines mark the positions mountain ridges (i.e. relative elevation maxima of topography). Elevations of the upper level are the average elevation of the respective level across all three cross-sections.

where ρ is the air density and ρ_0 the reference air density. u and v are the west-east and south-north components of horizontal wind velocity. Critical Richardson numbers for turbulence generation are between 0.2 and 1 but turbulence may even be sustained at higher Richardson numbers (Galperin et al., 2007).

Table C.2: Cross-section and event mean precipitation rate changes between the given model level (Level) and the level below for the precipitation event on 5 March 2016 between 07:00 UTC and 17:00 UTC. The Elevation above ground (m ag) gives the cross-section mean elevation above ground averaged over all three cross-sections analyzed for the 5 March 2016 (i.e. Sattelhorn ridge, Piz Radönt and the ridge between Scalettahorn and Piz Grialetsch). Precipitation rate changes (Precip. rate change) are given in mm h^{-1} and $\text{mm h}^{-1} \text{m}^{-1}$. Precipitation rate changes in mm h^{-1} give the precipitation rate change between the adjacent levels for the cross-section and event mean precipitation. Precipitation rate change in $\text{mm h}^{-1} \text{m}^{-1}$ gives the precipitation rate change per elevation change of the cross-section and event mean precipitation.

Level	Elevation m ag	Sattelhorn ridge		Piz Radönt		Scaletta-Grialetsch	
		Precip. rate change mm h^{-1}	Precip. rate change $\text{mm h}^{-1} \text{m}^{-1}$	Precip. rate change mm h^{-1}	Precip. rate change $\text{mm h}^{-1} \text{m}^{-1}$	Precip. rate change mm h^{-1}	Precip. rate change $\text{mm h}^{-1} \text{m}^{-1}$
2	~ 9	-0.005	-7.3×10^{-4}	-0.004	-6.1×10^{-4}	2.3×10^{-4}	3.7×10^{-5}
3	~ 18	-0.006	-6.9×10^{-4}	-0.005	-5.7×10^{-4}	6.5×10^{-4}	7.0×10^{-5}
4	~ 31	-0.010	-8.3×10^{-4}	-0.008	-6.7×10^{-4}	0.002	1.7×10^{-4}
5	~ 43	-0.011	-9.2×10^{-4}	-0.009	-6.9×10^{-4}	0.003	2.6×10^{-4}
6	~ 56	-0.011	-9.0×10^{-4}	-0.008	-6.5×10^{-4}	0.004	3.5×10^{-4}
7	~ 93	-0.017	-4.6×10^{-4}	-0.011	-3.0×10^{-4}	0.007	1.8×10^{-4}
8	~ 156	-0.029	-4.7×10^{-4}	-0.015	-2.3×10^{-4}	0.027	4.3×10^{-4}
9	~ 219	-0.030	-4.7×10^{-4}	-0.006	-9.0×10^{-5}	0.032	5.1×10^{-4}
10	~ 282	-0.031	-4.9×10^{-4}	0.007	1.1×10^{-4}	0.030	4.7×10^{-4}

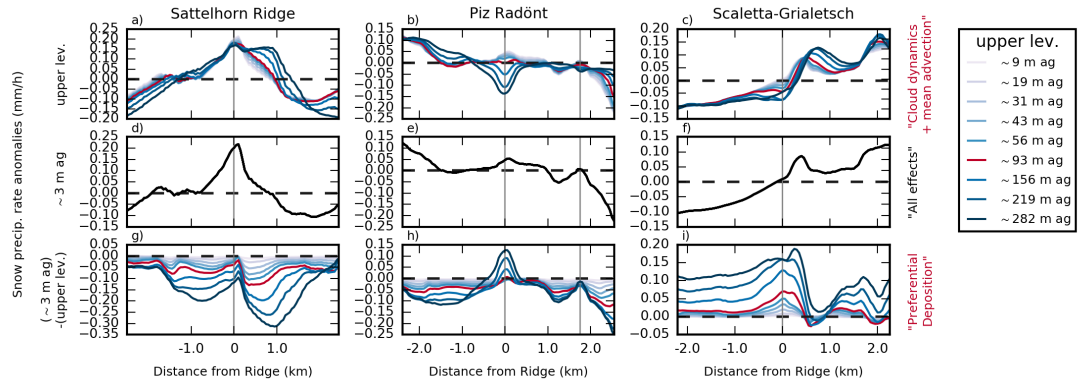


Figure C.2: Cross-section precipitation patterns across Sattelhorn ridge (left), Piz Radönt (middle) and the ridge between Scalettahorn and Piz Grialetsch (right, Figure 4.1) for the 10-h precipitation event on 5 March 2016 between 07:00 UTC and 17:00 UTC (50 m horizontal grid spacing). a)-c) show event mean snow precipitation rate anomalies with respect to cross-section and event mean precipitation rates at 9 different model levels (upper lev.) between ~9 m ag and ~282 m ag. Darker blue lines go along with increasing model levels. The ~93 m ag level is shown by the red line. d)-f) show the event mean precipitation rate anomalies with respect to the cross-section and event mean precipitation rate across the three cross-sections at the lowest model level ~3 m ag. g)-i) show the precipitation distribution due to processes between the upper level (shown in a-c) and the lowest model level ~3 m ag (shown in d-f). Darker blue lines in g)-i) go along with increasing vertical model elevation of the upper level as for a)-c). Precipitation distribution due to processes in the lowest ~95 m ag (~92 m ag in the legend) is shown by the red line. Gray vertical lines mark the positions of the mountain ridges (i.e. relative elevation maxima of topography). Elevations of the upper level are the average elevation of the respective level across all three cross-sections.

The static stability above all ridges and both simulations is about $N = 0.01 \text{ s}^{-1}$. Low Richardson numbers are sustained to higher elevations above ground for the precipitation event on 5 March 2016 (Figure C.3) compared to the precipitation event on 31 January 2016, for which low Richardson numbers are restricted to the lowest 500 m of the atmosphere (Figure C.4).

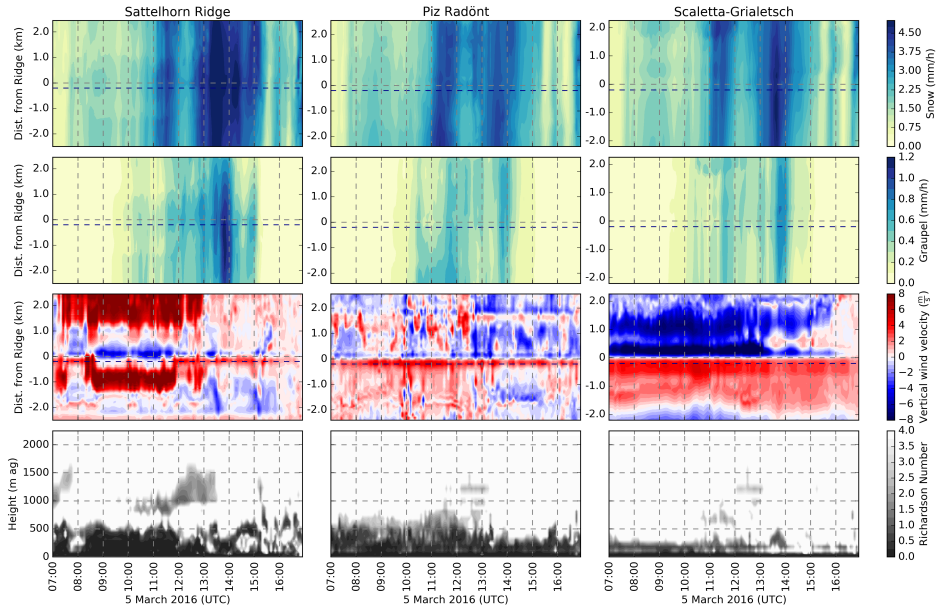


Figure C.3: Time-cross section diagrams of snow (top) and graupel (second row) precipitation (mm h^{-1}), vertical wind velocity at $\sim 95 \text{ m}$ above ground (m s^{-1} , third row) on 5 March 2016 across the Sattelhorn ridge (left), Piz Radönt (middle) and the ridge between Scaletthorn and Piz Grialetsch (right). Horizontal grey dashed lines mark the mountain ridge. Richardson numbers 200 m upstream of the ridge (blue dashed line) are shown with respect to elevation above ground (bottom). All panels show 24-h mean values for simulations with a horizontal grid spacing of 50 m.

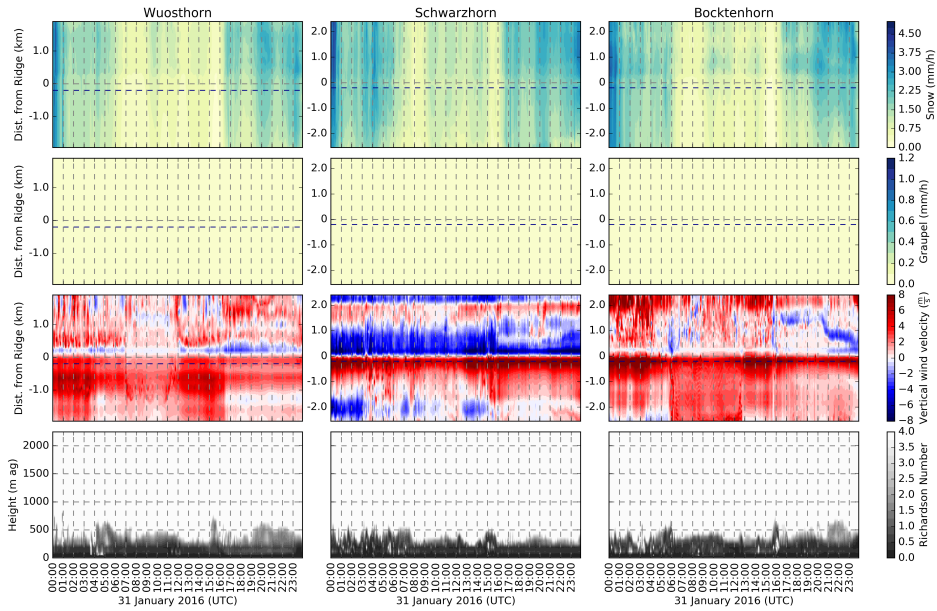


Figure C.4: Time-cross section diagrams of snow (top) and graupel (second row) precipitation (mm h^{-1}), vertical wind velocity at $\sim 95 \text{ m}$ above ground (m s^{-1} , third row) on 31 January 2016 for the Wuosthorn (left), Schwarzhorn (middle) and Bocktenhorn (right). Horizontal grey dashed lines mark the mountain ridge. Richardson numbers 200 m upstream of the ridge (blue dashed line) are shown with respect to elevation above ground (bottom). All panels show 24-h mean values for simulations with a horizontal grid spacing of 50 m.



Running COSMO-WRF on very high resolution over complex terrain

published version of the COSMO–WRF documentation by the *Laboratory for Cryospheric Sciences CRYOS, École Polytechnique Fédérale de Lausanne, Lausanne, Switzerland, 2018, doi:10.16904/enviadat.35*, Franziska Gerber^{1,2}, Varun Sharma¹

***Candidates contribution:** The candidate has setup the COSMO-WRF setup to run high resolution simulations over complex terrain with the help of the co-author and others and wrote the documentation.*

Abstract This is a technical documentation of the procedure to run the Weather Research and Forecasting (WRF) Model over complex alpine terrain using Consortium for Small-Scale Modeling (COSMO) analysis by the Federal Office of Meteorology and Climatology (MeteoSwiss) as initial and boundary conditions (COSMO-WRF). The setup is adapted for very-high resolution simulations based on COSMO-2 (2.2 km resolution) analysis. This document gives an overview over steps to setup COSMO-WRF and adaptations needed to run COSMO-WRF. Additionally, the calculation of precipitation rate at a horizontal plane and remapping of COSMO–WRF output on Swiss Coordinates are documented.

D.1 Introduction

To run the atmospheric model Weather Research and Forecasting (WRF) model version 3.7.1 (Skamarock et al., 2008) over complex alpine terrain using Consortium for Small-Scale Modeling (COSMO-2) analysis (2.2 km resolution) by the Federal Office of Meteorology and Climatology (MeteoSwiss) as initial and boundary conditions, numerous adaptations are needed. Several pre-preprocessing steps are required to get the data ready for standard WRF pre-processing. Here, we provide a description of these steps and illustrate the WRF setup presented in Gerber et al. (2018, Chapter 3). Information in boxes is additional information, which may be specifically for a certain software or system or is not necessarily needed

¹Laboratory of Cryospheric Sciences, School of Architecture and Civil Engineering, École Polytechnique Fédérale de Lausanne, Lausanne, Switzerland.

²WSL Institute for Snow and Avalanche Research SLF, Davos, Switzerland.

to run a WRF simulation, but may be of interest. Some parts of the description are specifically for retrieving COSMO-2 analysis and the setup of WRF on Piz Daint on the Swiss National Supercomputing Center (CSCS) and are likely different for different computing systems. COSMO-2 analysis data is available on Piz Daint. MeteoSwiss has to be contacted for permission and access. A list of software, scripts, files and data, needed to get through the whole procedure, is given in Section D.8. Users who have not worked with WRF before are strongly encouraged to work through the WRF online tutorial (<http://www2.mmm.ucar.edu/wrf/OnLineTutorial/index.htm>, accessed 20 November 2017) to familiarize themselves with the WRF model. Prior to performing the standard WRF procedure, several additional steps are needed to run COSMO-WRF over complex terrain, which will be described in Sections D.2 and D.3, commenting on pre-preprocessing steps for meteorological data and static data, respectively. Section D.4 gives information about installing WRF and the WRF pre-processing system (WPS). Information about adaptations and recommended settings for WPS and WRF are given in Sections D.5 and D.6, while Section D.7 gives some information on post-processing procedures.

Note

This document is intended as a guideline. It does not claim to be complete. No responsibility will be taken in case of damage or loss of any kind.

D.2 Meteorological data

COSMO-2 analysis are given on a rotated coordinate system, which is not readable by the WRF preprocessing system (WPS). Therefore, COSMO-2 data needs to be regridded to regular latitude-longitude coordinates. Additionally, several grib parameters need to be changed to make COSMO-2 input readable by WPS. The rotation is performed using the program `fieldextra` by MeteoSwiss, which is available on the CSCS computing system.

Location `fieldextra`: `/users/oprusers/osm/opr/abs/fieldextra` (subject to changes)

Location COSMO-2: `/store/archive/mch/msopr/owm/COSMO/LA<YEAR>/<DATE>.tar`

Note

Fieldextra is a licensed software which belongs to MeteoSwiss and is the official COSMO post-processing software. Free license may be granted to R&D institutions, but without support; if you are interested contact MeteoSwiss. Additionally, COSMO-2 analysis belong to MeteoSwiss and to access and use the data MeteoSwiss must be asked for permission.

D.2.1 Get COSMO-2 files

Download `.tar` files for chosen dates.

Run `./cosmo_untar.sh`

Note

All COSMO output is given in UTC (Daniel Leuenberger, MeteoSwiss, 21 August 2017, per email).

D.2.2 Run `fieldextra`

Basic instruction about the use of `fieldextra` was provided by A. Iriza and R. Dumitrache from Meteo Romania (personal communication), who previously implemented a COSMO-WRF version to assess the

accuracy of high resolution WRF simulations (Iriza et al., 2016). Advice about namelist setting was further provided by G. de Morsier from MeteoSwiss (personal communication). In `fieldextra` surface (2-dimensional) and atmospheric (3-dimensional) data need to be processed separately. The domain, variables, vertical levels, format, in- and output folder for the transformation are specified in the namelists `2Ddata.nl` and `3Ddata.nl`.

In `2Ddata.nl` and `3Ddata.nl`:

- `in_file = '<path_to_input_files>'`
- `out_file = '<path_for_output_files>'`
- `out_regrid_target = 'getlatlon, 4000000, 43000000, 12000000, 4900000, 20000, 20000',` specifies the domain, which is processed 'getlatlon, llon, llat, rlon, ulat, gridx, gridy', with llon and rlon the left and right longitude, llat and ulat the lower and upper latitude, and gridx and gridy the cellsize in x- and y-direction, respectively.
- Specify variables to be read and vertical levels, to which they should be interpolated (see example in `2Ddata.nl` and `3Ddata.nl`).

For a single day:

```
> /users/oprusers/osm/opr/abs/fieldextra 3Ddata.nl # for
    3D data
> /users/oprusers/osm/opr/abs/fieldextra 2Ddata.nl # for
    surface data
```

Note

When paths change, all paths and lines 45-48 in `3Ddata.nl` need to be adapted (analogously for `2Ddata.nl`).

For a series of days:

- Adapt `create_list.sh` and `rot_vel_from_raw_for_WRFinput.py` (runs over 24h for all given dates)
- run the script


```
> python rot_vel_from_raw_for_WRFinput.py
```

 or submit batch job (on CSCS):


```
> sbatch rot_vel_from_raw_for_WRFinput.job
```
- Additionally adapt and run `2Ddata.nl` for surface data:


```
> /users/oprusers/osm/opr/abs/fieldextra 2Ddata.nl
```

Create netcdf from COSMO grib

Adapt output format in `3Ddata.nl` and `2Ddata.nl` and run `fieldextra`.

```
out_type = 'NETCDF'
out_file = '<outfile_path_and_name>.nc'
```

D.2.3 Change grib parameters

The following grib parameters (`indicatorofParameter`) have to be changed for WPS, as COSMO and WRF use different conventions for grib codes.

Mixing ratio

- Ice mixing ratio (QI): 33 → 178 (because U has also GRIB code 33)

Calling

```
> ./change_vals_day.bash <DATE>
```

changes mixing ratio values for each hour of the specified <DATE>, which has the format YYYYMMDD.

Soil parameters The following soil parameters need to be adapted:

- Soil temperature (T_SO): 197 → 85
- Soil moisture (W_SO): 198 → 86

Additionally, `indicatorOfTypeOfLevel` and the `levels` of the soil parameters need to be adapted (Table D.1). Calling

```
./change_vals_day_soil.bash <DATE>
```

changes soil values for each hour of the specified day, where <DATE> has the format YYYYMMDD.

Table D.1: Transformation of soil levels from COSMO to WRF.

COSMO		→	WRF	
top	bottom		top	bottom
1	1	→	0	1
2	2	→	1	3
6	6	→	3	9
18	18	→	9	27
54	54	→	27	81
162	162	→	81	243
486	486	→	243	729
1458	1458	→	729	2187

D.3 Geographical/static data

To run WRF on very-high resolutions (up to 50 meters) over very steep and complex terrain, high-resolution static data (topography, landuse, soiltype) is necessary. The WRF package provides only static data up to a resolution of 2 arc min. Here, we use topographic data with a resolution of 1 arc sec (~30 m). Additionally, landuse data and soil type data are pre-preprocessed for the same resolution. Before the data can be used by WPS it needs to be translated to the binary format readable by WPS.

D.3.1 Topography

The topography is retrieved from the Aster 1 s digital elevation model (METI/NASA, 2009). To get a smooth transition between the COSMO topography and the WRF topography, a transitional topography is generated at the edges of the WRF domain. This is important to prevent strong boundary effects, which eventually cause instabilities in the simulations.

Note

There are even higher resolution digital elevation models available for Switzerland. However, they do not cover the whole domain of the parent domain of our simulation setup. We did not use the higher quality topography for the inner domains, to avoid inconsistencies of topography at the boundaries of the nests. However, as strong smoothing (see Section D.5.1) is applied during the WRF preprocessing, we would most likely not benefit much from the higher quality digital elevation model.

- Download 1 s resolution topography: <https://gdex.cr.usgs.gov/gdex/> (accessed: 18 August 2017). Dataset: ASTER Global DEM V2 (<https://lpdaac.usgs.gov/node/1079>, accessed: 15 November 2017, METI/NASA, 2009)
- Extract a slightly larger domain than the parent domain in ArcGIS and save it as ascii-file. The domain extracted from the digital elevation model should be slightly larger to make sure the whole domain, which will be simulated, is inside the extracted digital elevation model. The domain extracted for the simulations in Gerber et al. (2018, Chapter 3) was about 0.1° larger in each direction. As the coordinates of COSMO-2 all end with an equal number at the second decimal place, the domain has to be chosen such that its boundaries are at coordinates ending with an equal number at the second decimal place (e.g. 46.00, 64.02, 64.04, etc., and 9.86, 9.88, 9.90, etc.).

Note

When smoothing the boundaries (see next step) the outermost grid points are set to COSMO topography. This range should approximately cover the excess part of the extracted digital elevation model (e.g. ~0.1°).

Steps for extraction of topographic data in ESRI ArcGIS

In ArcCatalogue:

- Create new polygon (specify coordinates, e.g. WGS84 coordinates for Aster topography)

In ArcMap:

- Open Map
- Add digital elevation model (e.g. Aster 1 s resolution)
- Add polygon
- Draw polygon: Start editing → choose polygon → draw the approximate polygon → save
- Move edges to chosen position/coordinates:
 - use 'Edit Tool'
 - double click on polygon → right click on edge → Move to . . .
 - specify coordinate → Enter
 - Save & stop editing
- Extract domain from digital elevation model:
 - Arc Toolbox → Spatial Analyst Tools → Extraction → Extract by mask
- Save as Ascii:
 - Arc Toolbox → Conversion Tools → From Raster → Raster to Ascii

- Run boundary smoothing to adapt topography boundaries of the extracted e.g. Aster topography to COSMO topography.
To run the boundary smoothing (`toposmoothtest_wgs_84_cosmobound.nc1`), one COSMO file in .nc format is required (see box in Section D.2.2). The date does not matter, as only the

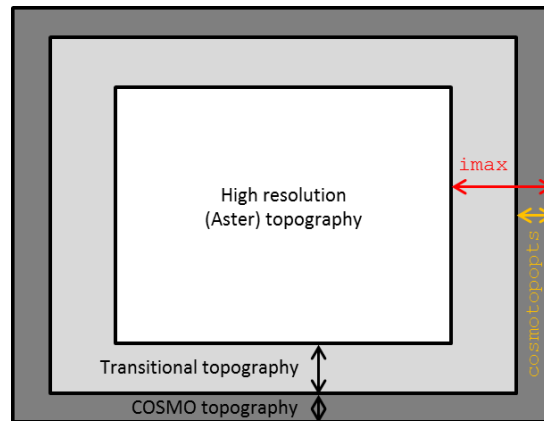


Figure D.1: Illustration of boundary smoothing. Dark grey shows the boundary, which is changed to COSMO topography. Light grey shows the transitional zone, which changes by a linear interpolation from COSMO to the high resolution topography. *imax* and *cosmotopopts* are the variables in *toposmoothtest_wgs_84_cosmobound.ncl* specifying the boundaries.

static (topographic) information is needed. *toposmoothtest_wgs_84_cosmobound.ncl* is converting topography at the boundary of the domain to COSMO topography. A transitional topography zone between COSMO and Aster topography is additionally added (Figure D.1). The width of the two zones can be chosen by the user. For the domain used in Gerber et al. (2018, Chapter 3) (using Aster topography with a resolution of 1 arc second) a COSMO topography boundary of 0.1° (360 grid points) and a transitional boundary of 0.3° (~ 30 km, 1080 grid points) are used. Depending on the domain and the complexity of the topography these boundaries may need to be adapted.

Adapt the file *toposmoothtest_wgs84_cosmobound.ncl*:

- Choose input and output directories
- Choose the domain: *y1*, *y2* = min./max. latitude, *x1*, *x2* = min./max. longitude
- Choose number of grid points for COSMO-topography: *cosmotopopts* (row 17). This should approximately cover the area, which will be outside of the model domain.
- Choose number of grid point for the COSMO-topography and transitional topography: *imax* (row 18)

→ Output will be written to: *outputdirectory+ '/WRFmatrix_0.txt'*

- Create binary file and adapt index file.

Run *ascii_to_bin_topo_wgs84_ws2sf1.f90* to create the binary file needed by WPS (adapt folder and file name in row 23):

```
> gfortran -o ascii_to_bin_topo_wgs84_ws2sf1.exe
  ascii_to_bin_topo_wgs84_ws2sf1.f90 write_geogrid.o
> ./ascii_to_bin_topo_wgs84_ws2sf1.exe
```

This generates the binary file 00001-XXXXX.00001-YYYYY, where XXXXX is the number of grid points in x-direction and YYYYY is the number of grid points in y-direction. Copy the binary file to *topo_RES* (*RES* gives the resolution of the data) folder in your *geog* folder.

Adapt the index file (see example file *index_topo*) in */geog/topo_RES/* folder. When choosing topography from Aster with 1 s resolution the values *known_lat*, *known_lon*, *tile_x* and *tile_y* have to be adapted. For the *known_lat*, *known_lon*, *tile_x*, and *tile_y* the total contained domain has to be specified, i.e. the domain including the extra 0.1° .

D.3.2 Landuse

High resolution landuse data is retrieved from the Coordination of Information on the Environment (Corine) dataset (European Environmental Agency, 2006). Corine landuse categories cannot be read by WPS directly. Thus, we did a transformation of Corine landuse categories to United States Geological Survey (USGS) landuse categories. Furthermore, Corine landuse is projected to the Aster grid.

- Download Corine landuse data: <https://www.eea.europa.eu/data-and-maps/data/clc-2006-raster> (downloaded: 15 June 2016, accessed: 18 August 2016, new version available)
- Reclassify Corine categories to USGS categories and remap on chosen resolution and project on WGS84.

For this step, we follow the description by Arnold et al. (2010) provided on <http://forum.wrfforum.com/viewtopic.php?f=22&t=2266> (accessed: 18.8.2017), which is based on the reclassification from Corine to USGS landuse categories by Pineda et al. (2004). As Pineda et al. (2004) defines USGS landuse categories between 101 and 124 an additional conversion (subtraction of 100) is needed for landuse categories to fit WRF requirements, which defines USGS landuse categories between 1 and 24. Furthermore, the data needs to be remapped on the chosen resolution if the resolution of the digital elevation model is different from the resolution of the Corine landuse data (additional step to description by Arnold et al., 2010) and finally needs to be projected to WGS84 coordinates.

Steps for transformation and extraction of Corine data (adapted from Arnold et al., 2010), ESRI ArcGIS

In ArcMap:

- Open Map (document, which was produced while processing the digital elevation model)
 - Add landuse data
 - Remap:
 - ArcToolbox → Spatial Analyst Tools → Reclass → Reclassify (or any of the other Reclass tools, based on Pineda et al. (2004), subtracting 100 for each category.)
 - Resample:
 - ArcToolbox → Data Management Tools → Raster → Raster Processing → Resample: Choose cell size of digital elevation model; choose nearest neighbor interpolation
 - Reproject to WGS84 coordinates:
 - ArcToolbox → Data Management Tools → Projections and Transformations → Raster → Project Raster
 - Extract domain (same as for digital elevation model) from landuse data:
 - Arc Toolbox → Spatial Analyst Tools → Extraction → Extract by mask
 - Save as Ascii:
 - Arc Toolbox → Conversion Tools → From Raster → Raster to ASCII
-
- Create binary file and adapt index file.
Run `ascii_to_bin_landuse.f90` to create the binary file needed by WPS (adapt folder and file name in row 23):
- ```
> gfortran -o ascii_to_bin_landuse.exe
 ascii_to_bin_landuse.f90 write_geogrid.o
> ./ascii_to_bin_landuse.exe
```
- This generates the binary file `00001-XXXXX.00001-YYYYY`, where `XXXXX` is the number of grid points in x-direction and `YYYYY` is the number of grid points in y-direction. Copy the binary file to `landuse_RES` (RES gives the resolution of the data) folder in your `geog` folder.

Adapt the index file (see example file `index_landuse`) in `/geog/landuse_RES/` folder. When choosing topography from Aster with 1s resolution the values `known_lat`, `known_lon`, `tile_x` and `tile_y` have to be adapted. For the `known_lat`, `known_lon`, `tile_x` and `tile_y` the total contained domain has to be specified, i.e. the domain including the extra 0.1°.

### D.3.3 Soil type

Keeping the model simple, we only use one soil type (*silty clay loam*) for the whole domain. This is not exactly accurate but as we are mainly simulating over a snow cover, the soil type should not make a strong difference for our simulations. The same file is used for the top and bottom layer soil, which are distinguished in WRF (`SOIL_TOP` and `SOIL_BOT`).

- Create soil type file for whole domain.  
Run the script `soiltype_writing.py` to create a soiltype file consisting of *silty clay loam* (category 8) or any other chosen category (to be changed in row 42) for the whole domain on the resolution of the topography data. Adapt the input and output file names and folders (rows 12 and 29).
- Create binary file and adapt index file.  
Run `ascii_to_bin_soiltype.f90` to create the binary file needed by WPS (adapt folder and file name in row 23):

```
> gfortran -o ascii_to_bin_soiltype.exe
 ascii_to_bin_soiltype.f90 write_geogrid.o
> ./ascii_to_bin_soiltype.exe
```

This generates the binary file `00001-XXXXX.00001-YYYYY`, where `XXXXX` is the number of grid points in x-direction and `YYYYY` is the number of grid points in y-direction. Copy the binary file to `soiltype_bot_RES` and `soiltype_top_RES` (`RES` gives the resolution of the data) folder in your `geog` folder.

Adapt the index file (see example file `index_soiltype`) in `/geog/soiltype_bot_RES/` and `/geog/soiltype_top_RES/` folders. When choosing topography from Aster with 1s resolution the values `known_lat`, `known_lon`, `tile_x` and `tile_y` have to be adapted. For the `known_lat`, `known_lon`, `tile_x` and `tile_y` the total contained domain has to be specified, i.e. the domain including the extra 0.1°.

## D.4 Installation of WRF and WPS

Generally, WRF and WPS are installed following the instruction given by the WRF tutorial: <http://www2.mmm.ucar.edu/wrf/OnLineTutorial/> (accessed: 18 August 2017). However, to make WPS run with COSMO input some adaptations are necessary.

Compiling WRF:

1. `./configure` – choose the distributed memory (`dmpar`) option for INTEL compiler: `INTEL (ftn/icc): CRAY XC` option (the exact option number varies with WRF version)
2. `./compile -j 8 em_real`

#### Note

WPS is compiled *after* compilation of WRF. Before compiling WPS, it is critical that the changes suggested in Section D.4.1 are implemented. Compile WPS using the INTEL compiler - *but only in serial mode!*

### Setup environment to install WRF and WPS on Piz Daint CSCS

WRF and WPS were compiled using INTEL compilers provided by the CSCS Programming Environment

The following steps were carried out by modifying the `~/ .bashrc` script:

1. Change the programming environment from Cray to Intel (`module switch PrgEnv-cray/6.0.4 PrgEnv-intel`)
2. Load the netcdf module (`module load cray-netcdf`)
3. Set path for the netcdf library specific for the compiler (INTEL) used: (`export NETCDF=/opt/cray/pe/netcdf/4.4.1.1.3/INTEL/16.0/`)

## D.4.1 Adaptations for WPS

`./ungrib/src/rrpr.f90`

- Add lines to specify soil moisture and soil temperature variables
- Convert soil moisture values to the unit of WRF ( $\text{m}^{-1}$  to  $\text{m}^3 \text{m}^{-3}$ ).
- Change all lake temperatures  $>300 \text{ K}$  to  $285 \text{ K}$  as lake temperatures in COSMO are unrealistically high.

`./ungrid/src/rd_grib1.f90`

- line 397 was edited and the variables `map%dx` and `map%dy` were hard-coded to be equal to the resolution of the incoming COSMO data in the units of degrees.
- The resolution of the incoming COSMO data is set in the field extra script - in the present case it is  $0.02^\circ$  and thus `map%dx = 0.02` and `map%dy = 0.02`.

## D.4.2 Problem with Morrison microphysics in WRF version 3.7.1

Running the Morrison microphysics scheme without cumulus scheme in WRF version 3.7.1 requires some adaptation, as described in <http://www2.mmm.ucar.edu/wrf/users/wrfv3.7/known-prob-3.7.1.html> (accessed 18 August 2017).

**Problem with Morrison Scheme** (posted January 15, 2016, <http://www2.mmm.ucar.edu/wrf/users/wrfv3.7/known-prob-3.7.1.html>)

**“Problem:** When using the Morrison scheme without any cumulus turned on in any of the domains (for example, running a single domain with Morrison scheme only), problems exist because the Morrison scheme uses some tendency arrays from output with a cumulus scheme. However, these arrays were not allocated when no cumulus scheme is used.

**Solution:** If you wish to use this scheme without any cumulus, you must edit `Registry.EM_COMMON`, and update this line, from:

```
package morr_two_moment mp_physics==10 - moist:qv,qc,
 qr,qi,qs,qg; scalar:qni,qns,qnr,qng
to
package morr_two_moment mp_physics==10 - moist:qv,qc,
 qr,qi,qs,qg; scalar:qni,qns,qnr,qng; state:rqrcuten,
 rqscuten,rqicuten
```

Once you update the file, save the file, and then you will need to go back to the `WRFV3/` directory, issue a `clean -a`, then reconfigure, and recompile the code.”

## D.5 Running WPS

To create meteorological and geographic input on a user defined grid, three pre-processing steps need to be performed prior to running WRF. `geogrid` interpolates the geographic (static) data, i.e. topography, landuse, soil type etc. to the chosen horizontal grid for the parent domain and all nests. `ungrib` reads meteorological data given in `grib1` or `grib2` format. Finally, `metgrid` horizontally interpolates the meteorological data to the horizontal grid produced by `geogrid`. Vertical interpolation will be done by the program `real`, which is the last pre-processing step but part of WRF (see Section D.6). General information about WPS and WRF namelist settings are based on Wang et al. (2016).

### D.5.1 Geogrid

To run `geogrid.exe` static data must be available in the `/geog/` folder (Section D.3) and the index file in the `/geog/` folder must be adapted for the desired domain. In the `namelist.wps` the `&share` and `&geogrid` section must be specified. An example of `namelist.wps` is given in Section D.10. Suggestions and information about some namelist options are listed in Table D.2.

**GEOGRID.TBL (in /WPS/geogrid/)** For `geogrid.exe` to be able to read the static data provided in the newly created folders for topo, landuse and soiltype, in `/geog/` the `GEOGRID.TBL` file needs to be adapted.

- Add `interp_option` and `rel_path` for all static data (`HGT_M`, `HGT_U`, `HGT_V`, `LANDUSEF`, `SOILCTOP`, and `SOILCBOT`).
- Change the default path to the new folder.
- For `LANDUSEF` additionally add line `land_mask_water`.

**Terrain smoothing** For complex topography and very high resolution simulations maximum slope angles are likely very high. Large slope angles are critical for simulations with eta-coordinates, as too steep slopes may cause problems when calculating the pressure gradient, as height differences between neighboring grid points may become up to an order of magnitude larger than the elevation difference between neighboring eta levels (Doyle et al., 2013). Therefore, it is recommended to apply a terrain smoothing to keep all slope angles below 45°. For the simulations in Gerber et al. (2018, Chapter 3) a minimum number of four smoothing cycles with WPS 1-2-1 smoothing is needed. WPS 1-2-1 smoothing applies a moving window filter with a window length of 3. Grid points `i-1`, `i`, and `i+1` are weighted with a ratio of 1:2:1. However, a very small simulation timestep is needed for a simulation with maximum slope angles of 45° (see Section D.6). To speed up simulations a stronger smoothing may be applied. To check maximum slopes in the `geo_em.d*.nc` files `see_slopes.ncl` may be used. The smoothing type and the number of smoothing cycles need to be chosen in `GEOGRID.TBL`:

- Chose smoothing type (`smooth_option`) and number of smoothing cycles (`smooth_passes`) in `GEOGRID.TBL`.

Run `geogrid`: > `./geogrid.exe`

### D.5.2 Ungrib

To run `ungrib` on COSMO-2 data all the steps described in Section D.2 need to be performed in advance. As COSMO-2 is not a standard input for WRF, a variable table translating COSMO-2 grib codes is required and needs to be linked to WPS/Vtable (`Vtable.COSMO.mixing.landuse`, see Section D.9).

Run `ungrib`:

```
> ./link_grib.csh <path_to_COSMO_files>/laf # (no * to add
 all files)
> ./ungrib.exe
```



**Table D.2:** Description and suggestions for some options in `namelist.wps`. An example of `namelist.wps` can be found in Section D.10.

| Section  | Option                        | Description                                                                                                                                                                                                                                                                                                                                                                                                                                                                                                                                                                 |
|----------|-------------------------------|-----------------------------------------------------------------------------------------------------------------------------------------------------------------------------------------------------------------------------------------------------------------------------------------------------------------------------------------------------------------------------------------------------------------------------------------------------------------------------------------------------------------------------------------------------------------------------|
| &geogrid | Parent_grid_ratio             | An odd parent grid ratio is recommended because the WRF grids are Arakawa C-staggered and therefore mass and velocity points of the parent and nest will be coincident. A ratio of 1:3 is recommended as it is most tested (Skamarock et al., 2008; Gill and Pyle, 2010).                                                                                                                                                                                                                                                                                                   |
|          | e_we/e_sn                     | For nested domains the ending point of the domain in west-east (we) and south-north (sn) direction must be chosen "one greater than some integer multiple of the nesting ratio" (Wang et al., 2016), to make sure that the upper right corner coincides with a grid point of the parent domain.<br>e_we and e_sn must be chosen such that they are inside the domain available for topography, landuse and soiltype, but not too far from the boundary, such that the smooth transition between COSMO and the high resolution topography is inside the domain (Figure D.1). |
|          | geog_data_res                 | Give the name of your newly created folder in /geog/, which contains your topography binaries.                                                                                                                                                                                                                                                                                                                                                                                                                                                                              |
|          | dx, dy                        | dx and dy are given in meters except when using 'lat-lon' projection, where dx and dy are given in degrees.                                                                                                                                                                                                                                                                                                                                                                                                                                                                 |
|          | map_proj                      | For mid-latitude domains 'lambert' projection is most accurate. However, the output will not be on regular output coordinates. For some applications 'mercator' projection may thus be preferred.                                                                                                                                                                                                                                                                                                                                                                           |
|          | ref_lat/ref_lon               | Specifies the lower left corner (ref_x = 1, ref_y = 1) of the parent domain and must be chosen such that it is inside the domain provided by static data but not too far from the edge such that the transitional topography is inside the domain.                                                                                                                                                                                                                                                                                                                          |
|          | geog_data_path                | Path of the /geog/ folder.                                                                                                                                                                                                                                                                                                                                                                                                                                                                                                                                                  |
| &metgrid | fg_name                       | Should correspond to the prefix in &ungrib, except if the intermediate files from ungrib were moved to a different directory.                                                                                                                                                                                                                                                                                                                                                                                                                                               |
|          | %opt_output_from_metgrid_path | A path for met_em.d*.nc files may be specified.                                                                                                                                                                                                                                                                                                                                                                                                                                                                                                                             |
| &share   | Opt_output_from_geogrid_path  | A path for the output files geo_emd0*.nc can be specified.                                                                                                                                                                                                                                                                                                                                                                                                                                                                                                                  |

### D.5.3 Metgrid

Once `geogrid.exe` and `ungrib.exe` were run successfully, `metgrid.exe` can be run. Sections `&geogrid` and `&ungrib` should be left unchanged. Section `&share` should stay unchanged except for `start_date` and `end_date` for the nested domains, for which the start and the end date can be set to the start date and time for the nests. For the nests only the start date and time needs to be processed, because the nests are only initialized with COSMO input but boundary conditions will always be taken from the parent domain.

**METGRID.TBL**(in `/WPS/metgrid/`) When running a simulation with a land surface model, `METGRID.TBL` needs to be adapted such that `metgrid` is able to read soil temperatures and soil moisture. For `name=ST` and `name=SM` the new soil levels need to be added as conditional statement:

```
=====
name=ST
...
ELSE IF
 fill_lev = 1 : T_SO0001 (200100)
 fill_lev = 3 : T_SO0002 (200100)
 fill_lev = 9 : T_SO0006 (200100)
 fill_lev = 27 : T_SO0018 (200100)
 fill_lev = 81 : T_SO0054 (200100)
 fill_lev = 243 : T_SO0162 (200100)
=====
name=SM
...
ELSE IF
 fill_lev = 1 : W_SO0001 (200100)
 fill_lev = 3 : W_SO0002 (200100)
 fill_lev = 9 : W_SO0006 (200100)
 fill_lev = 27 : W_SO0018 (200100)
 fill_lev = 81 : W_SO0054 (200100)
 fill_lev = 243 : W_SO0162 (200100)
=====
```

Additionally, for each soil level a block specifying soil temperature and soil moisture properties needs to be added:

```
=====
name=T_SO0000
 interp_option=sixteen_pt+four_pt+wt_average_4pt+
 wt_average_16pt+search
 masked=water
 interp_mask=LANDSEA(0)
 missing_value=-1.E30
 fill_missing=285.
 flag_in_output=FLAG_T_SO0000
=====
name=W_SO0001
 interp_option=sixteen_pt+four_pt+wt_average_4pt+
 wt_average_16pt+search
 masked=water
 interp_mask=LANDSEA(0)
 missing_value=-1.E30
 fill_missing=1.
```

```
flag_in_output=FLAG_W_S00001
=====
```

Run metgrid:

```
> ./metgrid.exe
```

### Semi-idealized simulations for sensitivity studies

**Option 1** To perform simulation over real complex topography but with constant meteorological input, one possibility is to use a certain meteorological field from COSMO-2 and repeatedly feed it to WRF as boundary condition. A test has been run but no thorough analysis has been performed. To make a certain meteorological condition available for every boundary input timestep, `met_em.d*.nc` files can be multiplied and the timestamp of the files may be adapted. To adapt the timestamp in the multiplied `.nc`-files `change_Times_netcdf.ncl` is available. However, before using this approach the following short-comings should be addressed:

- Are the chosen atmospheric conditions representative?
- Are the chosen nighttime/daytime conditions problematic when repeated for day/night times?

**Option 2** Another option to address the sensitivity of precipitation to different wind speeds would be to adapt wind speeds for a certain flow field. For this analysis wind speeds could be reduced to a certain percentage of the original wind speeds. To ensure thermodynamic equilibrium additional variables such as temperature need to be adapted. To adapt wind speeds in the `met_em*.nc` files `change_wind_netcdf.ncl` is available. Other variables can be adapted based on the same procedure.

## D.6 Running WRF

Setting up a very-high resolution simulation over complex terrain for snow covered conditions is challenging. Different settings and changes to standard settings are needed to run COSMO-WRF simulations. Below, the settings used for simulations presented in Gerber et al. (2018, Chapter 3) are mentioned and described. An example of `namelist.input` is given in Section D.11.

**Vertical nesting in version 3.7.1** As vertical nesting (Daniels et al., 2016) is not fully implemented in version 3.7.1, the `eta_levels` have to be determined manually. The simplest procedure to do this is to run a very short simulation for each number of vertical levels on a single domain.

### Note

This issue has been fixed in newer versions of WRF (Megan Daniels, personal communication).

- Choose vertical levels
- For each domain, i.e. for all different numbers of vertical levels:
  - Run a very short simulation (2s, setting `history_interval_s = 1`) on only one domain with the chosen number of vertical levels.
  - Use `ncdump -v ZNW wrfout_d01_<DATE> > dumpETA.txt`
  - Copy and paste the ZNW (eta levels) into the `namelist.input`

**Additional refinement of vertical levels on 50 meter resolution** A refinement of vertical levels in the boundary layer was performed to get a higher resolution of close-ground processes in very-high resolution simulations. The refinement is performed as suggested in a WRF tutorial about `real` by Gill (2015). For the refinement 10 additional eta-levels are added to the boundary layer.

**Large Eddy Simulations (LES)** To run WRF simulation in the LES mode different settings are required. Generally, the LES mode of WRF is based on choosing no boundary layer parametrization (`bl_pbl_physics = 0`). Depending if the simulation is run with or without a land surface model, different additional settings need to be chosen (Dudhia, 2012). The use of the LES mode is basically recommended for simulation with  $dx \ll 1$  km. Recommended namelist settings for complex topography and high resolution simulations are given in (Dudhia, 2012).

Settings chosen for simulations in Gerber et al. (2018, Chapter 3) are based on Dudhia (2012):

```
diff_opt = 2

isfflx = 1 # drag and heat flux from physics
sf_sfclay_physics = 1
sf_surface_physics # 0

km_opt = 2 # or 3
mix_isotropic = 0 # set to 1 for $dx \approx dz$
gwd_opt = 0
```

Alternatively, the following may be chosen:

```
isfflx = 2 # drag from physics, heat flux from
 tke_heat_flux
sf_sfclay_physics = 1
```

#### Note

`mix_isotropic` has been set to 0 for all simulation domains for the simulation in Gerber et al. (2018, Chapter 3). It might be valuable to change `mix_isotropic` to 1 for the two innermost domains with resolutions of 150 m and 50 m, respectively.

**Mesoscale setting** Given the setup with resolutions of 1350 m, 450 m, 150 m, and 50 m in the parent domain and the three nests, a mesoscale setting is appropriate for the parent domain with a grid size of 1350 m. For mesoscale simulations a planetary boundary layer (PBL) scheme (`bl_pbl_physics`) has to be chosen. For complex terrain the Yonsei University (YSU) PBL scheme (Hong et al., 2006) was found to be one of the best schemes for simulations over complex terrain (Gómez-Navarro et al., 2015). A more sophisticated version of YSU PBL is available, which takes into account subgrid scale orography (Jiménez and Dudhia, 2012). This is claimed to correct for negative (positive) wind speed biases over mountainous (flat) terrain (Jiménez and Dudhia, 2012; Lee et al., 2015). Comparing the influence of a parent domain with and without corrections for subgrid scale orography would be very interesting. To keep the simulation setup simple, simulations in Gerber et al. (2018, Chapter 3) were run with the uncorrected YSU PBL scheme for the parent domain.

#### Note on model resolutions

In numerical modeling different zones are distinguished. Large-scale and mesoscale simulations are commonly used for simulations with horizontal resolutions of  $> 10$  km. For these coarse resolutions no turbulence is resolved and a boundary layer parameterization is needed. At small scales ( $< \text{few } 100 \text{ m}$ ) large eddy simulations (LES) are used, which allow to resolve all major eddies. The zone in between is usually referred to as the “grey zone” or “terra incognita” (Wyngaard, 2004). This is the zone where a certain part of turbulent kinetic energy is resolved but not all. The “grey zone” is most challenging in numerical simulations. Approaches have been proposed to skip the “grey zone” by choosing the grid ratio accordingly (Rai et al., 2017).

**Roughness length of snow in complex terrain** Snow cover is often assumed to have a very low roughness length, which is good for relatively flat and gentle terrain. However, snow cover in alpine terrain is likely rough due to large rocks and the complex topography, which is only partially smoothed out by the snow cover. Therefore, for simulations over snow in complex terrain, we suggest to increase the roughness length of snow to 0.2 m instead of the default value of 0.002 m, as the size of roughness elements of 2 m seems to be reasonable to account for missing terrain features and roughness due to large rocks in snow covered complex terrain. Roughness was determined by the comparison of a 2 m digital terrain model (DTM-AV © 2018 swisstopo (5704 000 000)) with a 25 m digital elevation model (dhm25 © 2018 swisstopo (5740 000 000)). To evaluate the roughness of complex alpine terrain, the average of the absolute difference of the two terrain models for a domain covering the upper Dischma valley (Davos, Switzerland, innermost domain in simulations by Gerber et al. (2018, Chapter 3) between 2200 and 2700 meter above sea level has been taken. The average difference is 2.5 m. To account for smoothing due to snow coverage, we estimate the size of roughness elements to 2 m.

Depending on the chosen surface model, different tables need to be adjusted to change the roughness length properties. When using `sf_surface_physics = 4` (see next paragraph) the file `MPTABLE.TBL` is used. In `MPTABLE.TBL` the roughness length of snow is specified as `Z0SNO`. We suggest changing `Z0SNO` from 0.002 m to 0.2 m.

**Land-surface model** The most common land surface model in WRF is the Noah land surface model (Tewari et al., 2004). However, this model has been further developed and a more recent version Noah with multiple parametrization (Noah-MP Niu et al., 2011; Yang et al., 2011) is available. Noah-MP has a more sophisticated treatment of snow. Therefore, COSMO-WRF in Gerber et al. (2018, Chapter 3) is run with Noah-MP surface physics (`sf_surface_physics = 4`). When running a simulation with a surface model, the number of input soil layers (`num_metgrid_soil_levels`), the input source (`surface_input_source`), the number of soil levels in WRF (`num_soil_layers`), and the number of land categories (`num_land_cat`) have to be specified. For `sf_surface_physics = 4` the parameter `ifsnow` is irrelevant as it is only used for `sf_surface_physics = 1` (Wang et al., 2016).

**Simulation timestep** The simulation timestep is strongly dependent on the steepness and complexity of the topography and may therefore differ for different domains. Based on the timestep requirements of simulations over complex terrain in the surroundings of Davos (Switzerland, Chapter 3, Gerber et al., 2018), with maximum slope angles of 45° at a 50 m resolution (simulation set up with parent domain and three nest with horizontal resolutions of 1350 m, 450 m, 150 m, and 50 m and 40, 40, 60, and 90 vertical levels and a model top at 150 mbar) we recommend to start with:

```
timestep = 1 # second
parent_time_step_ratio = 1,3,3,3,
```

For a simulation with the same simulation setup but stronger terrain smoothing (maximum slope angles for 50 m resolution of 37.4°), the following setup is recommended to start with:

```
timestep = 6 # seconds
parent_time_step_ratio = 1,3,4,2,
```

#### Note

Time steps should always be chosen such that they end up to round numbers to avoid stability problems in the model (M. Daniels, personal communication).

**Horizontal resolution and domain** The specifications for horizontal resolution and the domain have to be set corresponding to the settings chosen in WPS (Section D.5).

**Radiation** The simplest schemes are chosen for radiation. `slope_radiation` and `topo_shading` make sure shadows due to topography in complex terrain are properly simulated. The radiative time step `rad_t` is 5 min. Based on the WRF User Guide it is recommended to choose `rad_t` as “1 min per km of `dx`” (Wang et al., 2016). However, calculating radiation more frequently than every 5 min to 15 min is not necessary as radiation is not a quickly changing process. The parameter `icloud` allows for cloud effects on radiation.

**Precipitation** The microphysics scheme (`mp_physics`) is set to the Morrison 2-moment scheme (Morrison et al., 2005; Morrison et al., 2009). The Morrison 2-moment scheme (option 10) and the Thompson graupel scheme (option 8) have been found to most properly simulate solid precipitation in complex terrain (Liu et al., 2011). The cumulus parameterization (`cu_physics`) is set to zero, as it is recommended to run simulations without a cumulus parameterization for grid sizes <4 km (e.g. Wang, 2015).

**Run a simulation** Prior to running `wrf.exe`, the input data has to be interpolated to the chosen vertical levels by `real.exe`. Namelist setting in `namelist.input` for `real.exe` and `wrf.exe` are identical (Section D.10 and Section D.11). Once all settings in the `namelist.input` are chosen, `real.exe` can be run and if successful, `wrf.exe` can be run.

To restart a simulation the `namelist.input` has to be adapted:

- Change `run_days`, `run_hours`, `run_minutes` and `run_seconds` to the remaining time.
- Change `start_year`, `start_month`, `start_day`, `start_hour`, `start_minute` and `start_second` to the date and time of the last available restart file. The frequency of restart files can be determined by `restart_interval`.
- Change `restart` to `.true.` if it is the first restart.
- Restart the simulation.

### Running a simulation on Piz Daint at CSCS

To run a simulation a batch job needs to be submitted. Therefore, batch scripts are required for both, to run `real` and `wrf` (`real.job` and `wrf.job`). On Piz Daint, any simulation can run over a maximum of 24 h. Therefore, longer WRF simulations need to be restarted every 24 h. To run the simulation, the batch script has to be submitted:

```
> sbatch WRF_real.job
```

To check the status of the simulation:

```
> squeue -u $USER
```

Output from the simulation is written to `rsl.out.0000`. When `real.exe` was successful `SUCCESS COMPLETE REAL_EM INIT` will be written at the end of `rsl.out.0000`. Note: `rsl.out.*` and `rsl.error.*` files are written for each cpu.

When `real` is successful, `wrf.exe` can be run:

```
> sbatch WRF_wrf.job
```

To restart the simulation, the `namelist.input` needs to be adapted and another batch job needs to be submitted.



## D.7 Post processing

Different post-processing methods will be described. The list does not cover all aspects of post-processing that may be valuable for any kind of analysis. However, we provide some post-processing information for more complex analysis.

### D.7.1 Map WRF output on Swiss Coordinates

For comparison to e.g. operational radar data by MeteoSwiss, it is helpful to display the same domain as the radar. However, radar data comes in Swiss Coordinates (CH1903LV03). This requires mapping of WRF output on the Swiss Coordinate system and plot it in the Swiss Coordinate reference frame.

- create the required lat/lon coordinate grid in swiss coordinates (CH1903LV03)  
→ `create_CH1903LV03_vector.py`
- remap the created ascii-file into global coordinates (ETRF93/CHTRF95 (ETRS89/CHTRS95/ WGS84) using the REFRAME tool by swisstopo (<https://www.swisstopo.admin.ch/de/karten-daten-online/calculation-services/reframe.html>, accessed: 22 August 2017)
- interpolate the WRF data onto the new global coordinates, which correspond to the swiss coordinates and plot them in the reference frame of swiss coordinates  
→ `plane_2dfield_snowacc24h_everyoutputtime_raddom.py`

### D.7.2 Precipitation rate at horizontal level

Precipitation rate (RAINNC: total precipitation, SNOWNC: solid precipitation without graupel and GRAUPELNC: graupel only) in WRF is only given as a ground level output. To analyze precipitation fields with respect to radar precipitation fields, WRF precipitation needs to be extracted at the radar elevation level. Given the particle size distribution  $N(D)$

$$N(D) = N_0 D^\mu e^{-\lambda D}, \quad (\text{D.1})$$

where  $D$  is the particle diameter,  $N_0$  is the intercept,  $\lambda$  the slope and  $\mu$  the shape parameter of the size distribution, precipitation rate ( $R_i$ ) can be calculated from the predicted mixing ratios ( $q_i$ ) and the predicted number concentration ( $N_i$ ) of hydrometeors ( $i$ ) as:

$$R_i = \int_0^\infty v_i(D) m_i(D) N_i(D) dD \quad (\text{D.2})$$

with terminal fall velocity  $v(D) = \alpha D^\beta$  and mass  $m(D) = a D^b$ , where  $D$  is the particle diameter and  $\alpha$ ,  $\beta$ ,  $a$ , and  $b$  are constants (Table D.3). Integration of  $R_i$  results in:

$$R_i = N_{0,i} a_i \alpha_i \frac{\Gamma(b_i + \beta_i + 1 + \mu_i)}{\lambda_i^{(b_i + \beta_i + 1 + \mu_i)}} \quad (\text{D.3})$$

with

$$\lambda_i = \left[ \frac{a_i \Gamma(\mu_i + b_i + 1)}{q_i \Gamma(\mu_i + 1)} \right] \quad (\text{D.4})$$

and

$$N_{0,i} = \frac{N_i \lambda_i^{(\mu_i + 1)}}{\Gamma(\mu_i + 1)} \quad (\text{D.5})$$

Due to the terrain-following vertical coordinates all WRF parameters need to be interpolated to the radar elevation, which is done by inverse-weighted interpolation between the two closest eta-levels to the required elevation.

**Note**

The precision of the output fields strongly depends on the output-timestep. Strong differences between e.g. SNOWNC and calculated precipitation at the ground level may arise with an output timestep of 30 minutes, as WRF updates summed precipitation every simulation timestep.

**Table D.3:** Constants for precipitation rate calculation for the ice, snow and graupel hydrometeors.  $\rho$  is the density of the different hydrometers.  $a$  and  $b$  are the constants for the mass and  $\alpha$  and  $\beta$  are the constants for the terminal fall velocity equation.  $\mu$  is the shape parameter of the particle size distribution. Values for graupel are given for simulations run without hail (i.e. option `IHAIL` = 0).

| Hydrometeor | $\rho$ | $a$                                   | $b$ | $\alpha$ | $\beta$ | $\mu$ |
|-------------|--------|---------------------------------------|-----|----------|---------|-------|
| Ice         | 500    | $\rho_{\text{ice}} \frac{\pi}{6}$     | 3   | 700.00   | 1.00    | 0     |
| Snow        | 100    | $\rho_{\text{snow}} \frac{\pi}{6}$    | 3   | 11.72    | 0.41    | 0     |
| Graupel     | 400    | $\rho_{\text{graupel}} \frac{\pi}{6}$ | 3   | 19.30    | 0.37    | 0     |

## D.8 Requirements

### Software

- fieldextra (available on CSCS, owned by MeteoSwiss: /users/oprusers/osm/opr/abs/fieldextra, location may change)
- WRF version 3.7.1 (including WPS, [http://www2.mmm.ucar.edu/wrf/users/download/get\\_source.html](http://www2.mmm.ucar.edu/wrf/users/download/get_source.html), accessed: 14 March 2018)
- python
- gfortran
- NCL
- GIS software (e.g. ArcGIS)

### Data

- COSMO-2 analysis (available on CSCS, owned by MeteoSwiss: /store/archive/mch/msopr/owm/COSMO/LA<YEAR>/<DATE>.tar)
- Aster topography: <https://gdex.cr.usgs.gov/gdex/> (accessed: 18 August 2017)
- Corine landuse: <https://www.eea.europa.eu/data-and-maps/data/clc-2006-raster> (downloaded: 15 June 2016, accessed: 18 August 2017, new version available)

### Pre-preprocessing scripts

#### Meteorological data (MeteorologicalData.zip)

- cosmo\_untar.sh
- create\_list.sh
- 2Ddata.nl
- 3Ddata.nl
- rot\_vel\_from\_raw\_for\_WRFinput.py
- rot\_vel\_from\_raw\_for\_WRFinput.job (if running as batch job)
- change\_vals\_day.bash
- change\_vals\_day\_soil.bash
- change\_Times\_netcdf.ncl
- change\_wind\_netcdf.ncl

#### Static data (StaticData.zip)

- toposmoothtest\_wgs84\_cosmobound.ncl
- soiltype\_writing.py
- write\_geogrid.o
- ascii\_to\_bin\_topo\_wgs84\_ws2sf1.f90
- ascii\_to\_bin\_topo\_wgs84\_ws2sf1.exe
- ascii\_to\_bin\_landuse.f90
- ascii\_to\_bin\_landuse.exe
- ascii\_to\_bin\_soiltype.f90
- ascii\_to\_bin\_soiltype.exe
- see\_slopes.ncl

### Adapted Files to compile WPS/WRF

#### WPS (WPSSetup.zip)

- rrpr.f90-soilmoistandtempadapted

- `rd_grib1.f90-COSMO`
- Corrections for WRF3.7.1 when using Morrison microphysics: <http://www2.mmm.ucar.edu/wrf/users/wrfv3.7/known-prob-3.7.1.html> (accessed 18 August 2017)

## Files to run WPS/WRF

### WPS (WPSrun.zip)

- `index_topo`
- `index_landuse`
- `index_soiltype`
- `GEOGRID.TBL-aster-121_4` (example with four smoothing cycles of 1-2-1 smoothing)
- `METGRID.TBL-T_Sofill1285-W_Sofill11`
- `namelist.wps`
- `Vtable.COSMO.mixing.soil`

#### Note

*index* files need to be named *index* in their respective folder (Section D.3).

### WRF (WRRun.zip)

- `MPTABLE.TBL_Z0SNO0.2`
- `namelist.input`
- `WRF_real.job`
- `WRF_wrf.job`

## Postprocessing

### Map WRF output on Swiss Coordinates (Postprocessing.zip)

- Coordinate transformation swiss coordinates to global coordinates for whole grid: <https://www.swisstopo.admin.ch/de/karten-daten-online/calculation-services/reframe.html> (accessed: 22 August 2017)
- `create_CH1903LV03_vector.py`
- `create_arcgis_ascii.py`
- `read_wrf_fields.py`

**Precipitation rate at horizontal level** Python scripts may be made available upon request.

## D.9 Vtable for COSMO-2 data

| GRIb<br>Code | Level<br>Code | Level<br>1 | Level<br>2 | metgrid<br>Name | metgrid<br>Units | METGRID<br>Description                  |
|--------------|---------------|------------|------------|-----------------|------------------|-----------------------------------------|
| 6            | 100           | *          |            | GEOPT           | m2 s-2           |                                         |
|              | 100           | *          |            | HGT             | m                | Height                                  |
| 11           | 100           | *          |            | TT              | K                | Temperature                             |
| 33           | 100           | *          |            | UU              | m s-1            | U                                       |
| 34           | 100           | *          |            | VV              | m s-1            | V                                       |
| 52           | 100           | *          |            | RH              | %                | Relative Humidity                       |
| 11           | 1             | 0          |            | SKINTEMP        | K                | Skin temperature (can use for SST also) |
| 11           | 105           | 2          |            | TT              | K                | Temperature at 2 m                      |
| 52           | 105           | 2          |            | RH              | %                | Relative Humidity at 2 m                |
| 33           | 105           | 10         |            | UU              | m s-1            | U at 10 m                               |
| 34           | 105           | 10         |            | VV              | m s-1            | V at 10 m                               |
| 1            | 1             | 0          |            | PSFC            | Pa               | Surface Pressure                        |
| 2            | 102           | 0          |            | PMSL            | Pa               | Sea-level Pressure                      |
| 66           | 1             | 0          |            | SNOWH           | m                | Physical Snow Depth                     |
| 31           | 100           | *          |            | QC              | kg kg-1          | Cloud water mixing ratio                |
| 36           | 100           | *          |            | QS              | kg kg-1          | Snow water mixing ratio                 |
| 39           | 100           | *          |            | QG              | kg kg-1          | Graupel water mixing ratio              |
| 35           | 100           | *          |            | QR              | kg kg-1          | Rain water mixing ratio                 |
| 178          | 100           | *          |            | QI              | kg kg-1          | Ice mixing ratio                        |
| 85           | 112           | 0          | 1          | T_S00001        | K                | Soil temperature 1 cm below ground      |
| 85           | 112           | 1          | 3          | T_S00002        | K                | Soil temperature 2 cm below ground      |
| 85           | 112           | 3          | 9          | T_S00006        | K                | Soil temperature 6 cm below ground      |
| 85           | 112           | 9          | 27         | T_S00018        | K                | Soil temperature 18 cm below ground     |
| 85           | 112           | 27         | 81         | T_S00054        | K                | Soil temperature 54 cm below ground     |
| 85           | 112           | 81         | 243        | T_S00162        | K                | Soil temperature 162 cm below ground    |
| 86           | 112           | 0          | 1          | W_S00001        | m                | Soil moisture 1 cm below ground         |
| 86           | 112           | 1          | 3          | W_S00002        | m                | Soil moisture 2 cm below ground         |
| 86           | 112           | 3          | 9          | W_S00006        | m                | Soil moisture 6 cm below ground         |
| 86           | 112           | 9          | 27         | W_S00018        | m                | Soil moisture 18 cm below ground        |
| 86           | 112           | 27         | 81         | W_S00054        | m                | Soil moisture 54 cm below ground        |
| 86           | 112           | 81         | 243        | W_S00162        | m                | Soil moisture 162 cm below ground       |

## D.10 namelist.wps

```

&share
 wrf_core = 'ARW',
 max_dom = 1,
 start_date = '2016-01-29_05:00:00', '2016-01-30_05
 :00:00', '2016-01-30_17:00:00', '2016-01-30_23:00:00',
 end_date = '2016-02-01_00:00:00', '2016-01-30_05
 :00:00', '2016-01-30_17:00:00', '2016-01-30_23:00:00',
 interval_seconds = 3600,
 io_form_geogrid = 2,
 opt_output_from_geogrid_path = '/project/s569/gerberf/input_WPS
 /GEO_EM/'
/

&geogrid
 parent_id = 1, 1, 2, 3,
 parent_grid_ratio = 1, 3, 3, 3,
 i_parent_start = 1, 105, 83, 88,
 j_parent_start = 1, 82, 54, 55,
 e_we = 184, 202, 199, 199,
 e_sn = 237, 199, 199, 199,
 geog_data_res = 'topo_1s', 'topo_1s', 'topo_1s', 'topo_1s',
 dx = 1350,
 dy = 1350,
 map_proj = 'lambert',
 ref_lat = 45.4,
 ref_lon = 7.4,
 ref_x = 1,
 ref_y = 1,
 truelat1 = 46.4,
 truelat2 = 47.2,
 stand_lon = 9.0,
 geog_data_path = '/project/s569/gerberf/geog_origWRF'
/

&ungrib
 out_format = 'WPS',
 prefix = '/project/s569/gerberf/input_WPS/FILES/
 COSMO_Jan-Mar_landsurf_ptop100/FILE',
/

&metgrid
 fg_name = '/project/s569/gerberf/input_WPS/FILES/
 COSMO_Jan-Mar_landsurf_ptop100/FILE'
 io_form_metgrid = 2,
 opt_output_from_metgrid_path = '/project/s569/gerberf/input_WRF
 /METFILES/COSMO_Jan-Mar_smoothboundaries1440_cosmo-le-360
 _mixing_1350_lambert_landuse_wrfsmooth14_ptop100/'
/

```



## D.11 namelist.input

```

&time_control
 run_days = 2,
 run_hours = 19,
 run_minutes = 0,
 run_seconds = 0,
 start_year = 2016, 2016, 2016, 2016,
 start_month = 01, 01, 01, 01,
 start_day = 29, 30, 30, 30,
 start_hour = 05, 05, 17, 23,
 start_minute = 00, 00, 00, 00,
 start_second = 00, 00, 00, 00,
 end_year = 2016, 2016, 2016, 2016
 end_month = 02, 02, 02, 02,
 end_day = 01, 01, 01, 01,
 end_hour = 00, 00, 00, 00,
 end_minute = 00, 00, 00, 00,
 end_second = 00, 00, 00, 00,
 interval_seconds = 3600,
 input_from_file = .true., .true., .true., .true.,
 fine_input_stream = 0, 2, 2, 2,
 history_interval = 30, 30, 30, 30,
 frames_per_outfile = 48, 48, 48, 48,
 restart = .false.,
 restart_interval = 60,
 write_hist_at_0h_rst = .true.
 io_form_history = 2,
 io_form_restart = 2,
 io_form_input = 2,
 io_form_boundary = 2,
 io_form_auxinput2 = 2,
 debug_level = 0,
/

&domains
 time_step = 1,
 time_step_fract_num = 0,
 time_step_fract_den = 1,
 max_dom = 4,
 e_we = 184, 202, 199, 199,
 e_sn = 237, 199, 199, 199
 e_vert = 40, 40, 60, 90,
 vert_refine_method = 0, 2, 2, 2,
 eta_levels = 1, 0.993, 0.983, 0.97, 0.954,
 0.934, 0.909, 0.88, 0.8600174, 0.840035, 0.8200524,
 0.8000699, 0.761449, 0.7237018, 0.6868118, 0.6507629,
 0.615539, 0.5811244, 0.5475038, 0.5146619, 0.4825837,
 0.4512546, 0.42066, 0.3907857, 0.3616177, 0.3331423,
 0.3053457, 0.2782149, 0.2517365, 0.2258978, 0.200686,
 0.1760886, 0.1520934, 0.1286884, 0.1058616, 0.08360139,
 0.06189632, 0.0407351, 0.02010664, 0,
1, 0.993, 0.983, 0.97, 0.954, 0.934, 0.909, 0.88, 0.8600174,
 0.840035, 0.8200524, 0.8000699, 0.761449, 0.7237018,
 0.6868118, 0.6507629, 0.615539, 0.5811244, 0.5475038,
 0.5146619, 0.4825837, 0.4512546, 0.42066, 0.3907857,
 0.3616177, 0.3331423, 0.3053457, 0.2782149, 0.2517365,

```

```

 0.2258978, 0.200686, 0.1760886, 0.1520934, 0.1286884,
 0.1058616, 0.08360139, 0.06189632, 0.0407351, 0.02010664, 0,
1, 0.993, 0.983, 0.97, 0.954, 0.934, 0.909, 0.88, 0.8679016,
 0.8558034, 0.8437051, 0.8316067, 0.8079001, 0.7845152,
 0.7614485, 0.7386963, 0.7162551, 0.6941214, 0.6722915,
 0.6507621, 0.6295298, 0.608591, 0.5879425, 0.5675809,
 0.5475029, 0.5277053, 0.5081847, 0.488938, 0.469962,
 0.4512536, 0.4328096, 0.4146269, 0.3967026, 0.3790335,
 0.3616167, 0.3444492, 0.3275281, 0.3108504, 0.2944133,
 0.2782139, 0.2622495, 0.2465171, 0.2310141, 0.2157377,
 0.2006852, 0.1858538, 0.1712411, 0.1568442, 0.1426606,
 0.1286878, 0.1149231, 0.1013641, 0.08800822, 0.074853,
 0.06189599, 0.04913476, 0.03656691, 0.02419006, 0.01200187,
 0,
1, 0.999, 0.998, 0.996, 0.994, 0.992, 0.990, 0.980, 0.970,
 0.960, 0.950, 0.940, 0.930, 0.920, 0.910, 0.900, 0.890,
 0.880, 0.8713248, 0.8626496, 0.8539743, 0.8452992, 0.8282002,
 0.8112669, 0.7944981, 0.7778924, 0.7614484, 0.745165,
 0.7290407, 0.7130743, 0.6972646, 0.68161, 0.6661096,
 0.650762, 0.6355659, 0.6205201, 0.6056233, 0.5908744,
 0.5762722, 0.5618153, 0.5475027, 0.5333331, 0.5193053,
 0.5054182, 0.4916706, 0.4780613, 0.4645893, 0.4512533,
 0.4380522, 0.4249849, 0.4120502, 0.3992472, 0.3865746,
 0.3740314, 0.3616164, 0.3493286, 0.337167, 0.3251304,
 0.3132178, 0.3014282, 0.2897605, 0.2782136, 0.2667867,
 0.2554785, 0.2442882, 0.2332146, 0.2222569, 0.211414,
 0.2006849, 0.1900687, 0.1795644, 0.169171, 0.1588876,
 0.1487132, 0.1386468, 0.1286876, 0.1188346, 0.1090869,
 0.09944359, 0.08990372, 0.0804664, 0.07113075, 0.06189587,
 0.05276088, 0.04372491, 0.03478707, 0.02594652, 0.01720238,
 0.008553809, 0,
p_top_requested = 15000,
num_metgrid_levels = 39,
num_metgrid_soil_levels = 6,
dx = 1350, 450, 150, 50,
dy = 1350, 450, 150, 50,
grid_id = 1, 2, 3, 4,
parent_id = 1, 1, 2, 3,
i_parent_start = 1, 105, 83, 88,
j_parent_start = 1, 82, 54, 55,
parent_grid_ratio = 1, 3, 3, 3,
parent_time_step_ratio = 1, 3, 3, 3,
feedback = 0,
smooth_option = 0,
/

&physics
mp_physics = 10, 10, 10, 10,
ra_lw_physics = 1, 1, 1, 1,
ra_sw_physics = 1, 1, 1, 1,
slope_rad = 1, 1, 1, 1,
topo_shading = 1, 1, 1, 1,
radt = 5., 5., 5., 5.,
sf_sfclay_physics = 1, 1, 1, 1,
sf_surface_physics = 4, 4, 4, 4,
bl_pbl_physics = 1, 0, 0, 0,
bldt = 0, 0, 0, 0,

```

```

cu_physics = 0, 0, 0, 0,
cudt = 0, 0, 0, 0,
isfflx = 1,
ifsnow = 1,
icloud = 1,
surface_input_source = 1,
num_soil_layers = 4,
num_land_cat = 24,
sf_urban_physics = 0, 0, 0, 0,
/

&fdda
/

&dynamics
rk_ord = 3,
diff_opt = 2, 2, 2, 2,
km_opt = 2, 2, 2, 2,
diff_6th_opt = 0, 0, 0, 0,
damp_opt = 3,
zdamp = 5000., 5000., 5000., 5000.,
dampcoef = 0.2, 0.2, 0.2, 0.2,
w_damping = 0,
khdif = 0, 0, 0, 0,
kvdif = 0, 0, 0, 0,
non_hydrostatic = .true., .true., .true., .true.,
moist_adv_opt = 1, 1, 1, 1,
scalar_adv_opt = 1, 1, 1, 1,
epssm = 1, 1, 1, 1,
/

&bdy_control
specified = .true., .false., .false., .false
.,
spec_bdy_width = 5,
spec_zone = 1,
relax_zone = 4,
nested = .false., .true., .true., .true.,
/

&grib2
/

&namelist_quilt
nio_tasks_per_group = 0,
nio_groups = 1,
/

```

**Acknowledgments** Many thanks go to Michael Lehning, Rebecca Mott and Megan Daniels for many fruitful discussions about the WRF setup and outputs. Additionally, we like to thank Benoit Gherardi for his work on the adaptation of WRF topography to COSMO topography at the boundaries and his work on different pre- and post-processing scripts as well as Louis Queno for his work on pre-processing scripts to read topography and prepare soiltype and landuse input files. Additionally, thanks go to Cornelius Hald, Keith Mussleman, Changhai Liu, the help at CSCS and the wrf-help. For allowing us to use *fieldextra* and providing COSMO-2 analysis we further thank MeteoSwiss. Special thanks go to Guy de Morsier from MeteoSwiss for his advice about namelist setting to use *fieldextra*. Additional thanks for instructions about the use of *fieldextra*, go to Amalia Iriza and Rodica Dumitrache from Meteo Romania. Further thanks go to Mathias Hauser for his support with typesetting.



# Bibliography

- Arnold, D., I. Schicker, and P. Seibert (2010). *High-Resolution Atmospheric Modelling in Complex Terrain for Future Climate Simulations(HiRmod), Report 2010*. Tech. rep. Institute of Meteorology (BOKU-Met), University of Natural Resources and Life Sciences, Vienna, Austria (cited on pp. 38, 105).
- Arthur, R., K. A. Lundquist, J. D. Mirocha, S. W. Hoch, and F. K. Chow (2016). “High-resolution simulations of downslope flows over complex terrain using WRF-IBM”. *17th Conference on Mountain Meteorology, Armerican Meteorological Society*, Paper 7.6, 18 pages (cited on p. 54).
- Bader, M. J. and W. T. Roach (1977). “Orographic rainfall in warm sectors of depressions”. *Quarterly Journal of the Royal Meteorological Society*, 103, 269–280. DOI: [10.1002/qj.49710343605](https://doi.org/10.1002/qj.49710343605) (cited on p. 3).
- Baines, P. G. (1995). *Topographic effects in stratified flow*. Ed. by G. K. Batchelor, L. B. Freund, S. Lebovich, and V. Tvergaard. Cambridge University Press, 482 (cited on pp. 16, 21, 27, 28).
- Banta, R. M. (1990). “Atmospheric Processes over Complex Terrain”. Ed. by W. Blumen. Vol. 23. American Meteorological Society, Boston, MA. Chap. The Role of Mountain Flows in Making Clouds, 229–282. DOI: [10.1007/978-1-935704-25-6\\_9](https://doi.org/10.1007/978-1-935704-25-6_9) (cited on p. 58).
- Banta, R. M., C. M. Shun, D. C. Law, W. Brown, R. F. Reinking, R. M. Hardesty, C. J. Senff, W. A. Brewer, M. J. Post, and L. S. Darby (2013). “Mountain Weather Research and Forecasting: Recent Progress and Current Challenges”. Ed. by K. F. Chow, F. S. De Wekker, and J. B. Snyder. Springer Netherlands. Chap. Observational Techniques: Sampling the Mountain Atmosphere, 409–530. DOI: [10.1007/978-94-007-4098-3\\_8](https://doi.org/10.1007/978-94-007-4098-3_8) (cited on pp. 10–12).
- Bárdossy, A. and G. Pegram (2011). “Downscaling precipitation using regional climate models and circulation patterns toward hydrology”. *Water Resources Research*, 47, W04505. DOI: [10.1029/2010WR009689](https://doi.org/10.1029/2010WR009689) (cited on p. 7).
- Barnett, T. P., J. C. Adam, and D. P. Lettenmaier (2005). “Potential impacts of a warming climate on water availability in snow-dominated regions”. *Nature*, 438, 303–309. DOI: [10.1038/nature04141](https://doi.org/10.1038/nature04141) (cited on p. 2).
- Bavay, M., M. Lehning, T. Jonas, and H. Löwe (2009). “Simulations of future snow cover and discharge in Alpine headwater catchments”. *Hydrological Processes*, 23, 95–108. DOI: [10.1002/hyp.7195](https://doi.org/10.1002/hyp.7195) (cited on pp. 1, 9).
- Beljaars, A. C. M. (1994). “The parameterization of surface fluxes in large-scale models under free convection”. *Quarterly Journal of the Royal Meteorological Society*, 121, 255–270. DOI: [10.1002/qj.49712152203](https://doi.org/10.1002/qj.49712152203) (cited on pp. 39, 60).
- Beniston, M. (2003). “Climatic change in mountain regions: A review of possible impacts”. *Climatic Change*, 59, 5–31. DOI: [10.1023/A:1024458411589](https://doi.org/10.1023/A:1024458411589) (cited on p. 2).
- Beniston, M. (1997). “Variations of snow depth and duration in the Swiss Alps over the last 50 years: Links to changes in large-scale climatic forcings”. *Climatic Change*, 36, 281–300. DOI: [10.1023/A:1005310214361](https://doi.org/10.1023/A:1005310214361) (cited on p. 16).

- Bergeron, T. (1965). “On the low-level redistribution of atmospheric water caused by orography.” *Suppl. Proc. Int. Conf. Cloud Phys.*, Tokyo, 96–100 (cited on pp. 3, 37, 52, 58).
- Bernhardt, M. and K. Schulz (2010). “SnowSlide: A simple routine for calculating gravitational snow transport”. *Geophysical Research Letters*, 37, L11502. DOI: [10.1029/2010GL043086](https://doi.org/10.1029/2010GL043086) (cited on p. 5).
- Bernhardt, M., K. Schulz, G. Liston, and G. Zängl (2012). “The influence of lateral snow redistribution processes on snow melt and sublimation in alpine regions”. *Journal of Hydrology*, 424–425, 196–206. DOI: [10.1016/j.jhydrol.2012.01.001](https://doi.org/10.1016/j.jhydrol.2012.01.001) (cited on pp. 5, 29, 58).
- Bernhardt, M., G. Zängl, G. E. Liston, U. Strasser, and W. Mauser (2009). “Using wind fields from a high-resolution atmospheric model for simulating snow dynamics in mountainous terrain”. *Hydrological Processes*, 23, 1064–1075. DOI: [10.1002/hyp.7208](https://doi.org/10.1002/hyp.7208). eprint: <https://onlinelibrary.wiley.com/doi/pdf/10.1002/hyp.7208> (cited on p. 9).
- Besic, N., J. Figueras i Ventura, J. Grazioli, M. Gabella, U. Germann, and A. Berne (2016). “Hydrometeor classification through statistical clustering of polarimetric radar measurements: a semi-supervised approach”. *Atmospheric Measurement Techniques*, 9, 4425–4445. DOI: [10.5194/amt-9-4425-2016](https://doi.org/10.5194/amt-9-4425-2016) (cited on pp. 41, 79).
- Besic, N., F. Gerber, N. Nerini, L. Foresti, J. Figueras i Ventura, M. Gabella, U. Germann, M. Lehning, and A. Berne (in prep.). “Topographic influence on snowfall: A radar based spatio-temporal analysis” (cited on p. 79).
- Blanchet, J., C. Marty, and M. Lehning (2009). “Extreme value statistics of snowfall in the Swiss Alpine region”. *Water Resources Research*, 45, W05424. DOI: [10.1029/2009WR007916](https://doi.org/10.1029/2009WR007916) (cited on p. 16).
- Blöschl, G. (1999). “Scaling issues in snow hydrology”. *Hydrological Processes*, 13, 2149–2175. DOI: [10.1002/\(SICI\)1099-1085\(199910\)13:14/15<2149::AID-HYP847>3.0.CO;2-8](https://doi.org/10.1002/(SICI)1099-1085(199910)13:14/15<2149::AID-HYP847>3.0.CO;2-8) (cited on p. 5).
- Brewer, A. W. and H. P. Palmer (1949). “Condensation processes at low temperatures, and the production of new sublimation nuclei by the splintering of ice”. *Nature*, 164, 312–313. DOI: [10.1038/164312a0](https://doi.org/10.1038/164312a0) (cited on p. 3).
- Brown, R. D. and P. W. Mote (2009). “The Response of Northern Hemisphere Snow Cover to a Changing Climate”. *Journal of Climate*, 22, 2124–2145. DOI: [10.1175/2008JCLI2665.1](https://doi.org/10.1175/2008JCLI2665.1) (cited on p. 2).
- Bühler, Y., M. S. Adams, R. Bösch, and M. Stoffel (2016). “Mapping snow depth in alpine terrain with unmanned aerial systems (UASs): potential and limitations”. *The Cryosphere*, 10, 1075–1088. DOI: [10.5194/tc-10-1075-2016](https://doi.org/10.5194/tc-10-1075-2016) (cited on p. 13).
- Bühler, Y., M. Marty, L. Egli, J. Veitinger, T. Jonas, P. Thee, and C. Ginzler (2015). “Snow depth mapping in high-alpine catchments using digital photogrammetry”. *The Cryosphere*, 9, 229–243. DOI: [10.5194/tc-9-229-2015](https://doi.org/10.5194/tc-9-229-2015) (cited on pp. 13, 64).
- Buzzi, M. (2008). “Challenges in operational numerical weather prediction at high resolution in complex terrain”. PhD thesis. Eidgenössische Technische Hochschule ETH Zürich, Nr. 17714. DOI: [10.3929/ethz-a-005698833](https://doi.org/10.3929/ethz-a-005698833) (cited on p. 7).
- Caldwell, P., H. Chin, D. Bader, and G. Bala (2009). “Evaluation of a WRF dynamical downscaling simulation over California”. *Climate Change*, 95, 499–521. DOI: [10.1007/s10584-009-9583-5](https://doi.org/10.1007/s10584-009-9583-5) (cited on p. 49).
- Carruthers, D. J. and J. C. R. Hunt (1990). “Fluid Mechanics of Airflow over Hills: Turbulence, Fluxes, and Waves in the Boundary Layer”. *Atmospheric Processes over Complex Terrain*. Ed. by W. Blumen. Vol. 23. Meteorological Monographs. American Meteorological Society, Boston, MA. DOI: [10.1007/978-1-935704-25-6\\_5](https://doi.org/10.1007/978-1-935704-25-6_5) (cited on pp. 4, 58).
- Chen, Y., F. L. Ludwig, and R. L. Street (2004). “Stably stratified flows near a notched transverse ridge across the Salt Lake Valley”. *Journal of Applied Meteorology*, 43, 1308–1328. DOI: [10.1175/1520-0450\(2004\)043<1308:SSFNAN>2.0.CO;2](https://doi.org/10.1175/1520-0450(2004)043<1308:SSFNAN>2.0.CO;2) (cited on p. 9).



- Choukulkar, A., R. Calhoun, B. Billings, and J. D. Doyle (2012). “A Modified Optimal Interpolation Technique for Vector Retrieval for Coherent Doppler LIDAR”. *IEEE Geoscience and Remote Sensing Letters*, 9, 1132–1136. DOI: [10.1109/LGRS.2012.2191762](https://doi.org/10.1109/LGRS.2012.2191762) (cited on p. 11).
- Choularton, T. W. and S. J. Perry (1986). “A model of the orographic enhancement of snowfall by the seeder-feeder mechanism”. *Quarterly Journal of the Royal Meteorological Society*, 112, 335–345. DOI: [10.1002/qj.49711247204](https://doi.org/10.1002/qj.49711247204) (cited on pp. 3, 16, 36).
- Chow, F. K., A. P. Weigel, R. L. Street, M. W. Rotach, and M. Xue (2006). “High-resolution large-eddy simulations of flow in a steep Alpine valley. Part I: Methodology, verification, and sensitivity studies”. *Journal of Applied Meteorology and Climatology*, 45, 63–86. DOI: [10.1175/JAM2322.1](https://doi.org/10.1175/JAM2322.1) (cited on p. 9).
- Chu, X., L. Xue, B. Geerts, R. Rasmussen, and D. Breed (2014). “A Case Study of Radar Observations and WRF LES Simulations of the Impact of Ground-Based Glaciogenic Seeding on Orographic Clouds and Precipitation. Part I: Observations and Model Validations”. *Journal of Applied Meteorology and Climatology*, 53, 2264–2286. DOI: [10.1175/JAMC-D-14-0017.1](https://doi.org/10.1175/JAMC-D-14-0017.1) (cited on p. 9).
- Colle, B. (2004). “Sensitivity of orographic precipitation to changing ambient conditions and terrain geometries: An idealized modelling perspective”. *Journal of Atmospheric Sciences*, 61, 588–606. DOI: [10.1175/1520-0469\(2004\)061<0588:SOOPTC>2.0.CO;2](https://doi.org/10.1175/1520-0469(2004)061<0588:SOOPTC>2.0.CO;2) (cited on pp. 3, 16, 37).
- Colle, B. A., J. B. Wolfe, W. J. Steenburgh, D. E. Kingsmill, J. A. W. Cox, and J. C. Shafer (2005). “High-resolution simulations and microphysical validation of an orographic precipitation event over the Wasatch Mountains during IPEX IOP3”. *Monthly Weather Review*, 133, 2947–2971. DOI: [10.1175/MWR3017.1](https://doi.org/10.1175/MWR3017.1) (cited on p. 3).
- Colle, B. A. and Y. Zeng (2004). “Bulk microphysical sensitivities and pathways within the MM5 for orographic precipitation. Part II: Impact of barrier width and freezing level”. *Monthly Weather Review*, 132, 2802–2815. DOI: [10.1175/MWR2822.1](https://doi.org/10.1175/MWR2822.1) (cited on p. 3).
- Comola, F., M. Giometto, S. T. Salesky, M. B. Parlange, and M. Lehning (2018). “Scale analysis of snowfall deposition over Gaussian hills using large eddy simulation and Lagrangian stochastic particle-tracking”. *Journal of Fluid Mechanics*, in review (cited on pp. 6, 10, 59, 70, 74, 80).
- Cooper, S. J., N. B. Wood, and T. S. L’Ecuyer (2017). “A variational technique to estimate snowfall rate from coincident radar, snowflake, and fall-speed observations”. *Atmospheric Measurement Techniques*, 10, 2557–2571. DOI: [10.5194/amt-10-2557-2017](https://doi.org/10.5194/amt-10-2557-2017) (cited on p. 49).
- Croci-Maspoli, M. and H. C. Davies (2009). “Key Dynamical Features of the 2005/06 European Winter”. *Monthly Weather Review*, 137, 664–678. DOI: [10.1175/2008MWR2533.1](https://doi.org/10.1175/2008MWR2533.1) (cited on p. 2).
- Dadic, R., R. Mott, M. Lehning, and P. Burlando (2010a). “Parameterization for wind-induced preferential deposition of snow”. *Hydrological Processes*, 24, 1994–2006. DOI: [10.1002/hyp.7776](https://doi.org/10.1002/hyp.7776) (cited on p. 16).
- (2010b). “Wind influence on snow depth distribution and accumulation over glaciers”. *Journal of Geophysical Research*, 115, F01012. DOI: [10.1029/2009JF001261](https://doi.org/10.1029/2009JF001261) (cited on pp. 4, 16, 37).
- Daniels, M. H., K. A. Lundquist, J. D. Mirocha, D. J. Wiersema, and F. K. Chow (2016). “A New Vertical Grid Nesting Capability in the Weather Research and Forecasting (WRF) Model”. *Monthly Weather Review*, 144, 3725–3747. DOI: [10.1175/MWR-D-16-0049.1](https://doi.org/10.1175/MWR-D-16-0049.1) (cited on pp. 9, 38, 111).
- De Michele, C., F. Avanzi, D. Passoni, R. Barzaghi, L. Pinto, P. Dosso, A. Ghezzi, R. Gianatti, and G. Della Vedona (2016). “Using a fixed-wing UAS to map snow depth distribution: an evaluation at peak accumulation”. *The Cryosphere*, 10, 511–522. DOI: [10.5194/tc-10-511-2016](https://doi.org/10.5194/tc-10-511-2016) (cited on p. 13).
- De Wekker, S. F. J. (2002). “Structure and morphology of the convective boundary layer in mountainous terrain”. PhD thesis. University of Brithish Colombia, Department of Earth and Ocean Sciences, Vancouver, Canada. DOI: [10.14288/1.0052567](https://doi.org/10.14288/1.0052567) (cited on pp. 8, 60).

- Deardorff, J. W. (1970). “A numerical study of three-dimensional turbulent channel flow at large Reynolds numbers”. *Journal of Fluid Mechanics*, 41, 453–480. DOI: [10.1017/S0022112070000691](https://doi.org/10.1017/S0022112070000691) (cited on p. 8).
- (1980). “Stratocumulus-capped mixed layers derived from a 3-dimensional model”. *Boundary-Layer Meteorology*, 18, 495–527. DOI: [10.1007/BF00119502](https://doi.org/10.1007/BF00119502) (cited on p. 8).
- Deems, J. S., S. R. Fassnacht, and K. J. Elder (2006). “Fractal Distribution of Snow Depth from Lidar Data”. *Journal of Hydrometeorology*, 7, 285–297. DOI: [10.1175/JHM487.1](https://doi.org/10.1175/JHM487.1) (cited on pp. 36, 42, 52).
- (2008). “Interannual Consistency in Fractal Snow Depth Patterns at Two Colorado Mountain Sites”. *Journal of Hydrometeorology*, 9, 977–988. DOI: [10.1175/2008JHM901.1](https://doi.org/10.1175/2008JHM901.1) (cited on pp. 36, 37).
- Deems, J. S., T. H. Painter, and D. C. Finnegan (2013). “Lidar measurements of snow depth: a review”. *Journal of Glaciology*, 59, 467–479. DOI: [10.3189/2013JoG12J154](https://doi.org/10.3189/2013JoG12J154) (cited on pp. 5, 20).
- Doorschot, J. J. J., M. Lehning, and A. Vrouwe (2004). “Field measurements of snow-drift threshold and mass fluxes, and related model simulations”. *Boundary-Layer Meteorology*, 113, 347–368. DOI: [10.1007/s10546-004-8659-z](https://doi.org/10.1007/s10546-004-8659-z) (cited on pp. 5, 11).
- Doorschot, J. J. J. and M. Lehning (2002). “Equilibrium Saltation: Mass Fluxes, Aerodynamic Entrainment, and Dependence on Grain Properties”. *Boundary-Layer Meteorology*, 104, 111–130. DOI: [10.1023/A:1015516420286](https://doi.org/10.1023/A:1015516420286) (cited on p. 22).
- Dore, A. J., T. W. Choularton, D. Fowler, and A. Crossely (1992). “Orographic enhancement of snowfall”. *Environ. Pollut.*, 75, 175–179. DOI: [10.1016/0269-7491\(92\)90037-B](https://doi.org/10.1016/0269-7491(92)90037-B) (cited on pp. 4, 16, 36).
- Doyle, J. D. (1997). “The influence of mesoscale orography on a coastal jet and rainband”. *Monthly Weather Review*, 125, 1465–1488. DOI: [10.1175/1520-0493\(1997\)125<1465:TIOMOO>2.0.CO;2](https://doi.org/10.1175/1520-0493(1997)125<1465:TIOMOO>2.0.CO;2) (cited on p. 3).
- Doyle, J. D., C. C. Epifanio, A. Persson, P. A. Reinecke, and G. Zängl (2013). “Mountain Weather Research and Forecasting: Recent Progress and Current Challenges”. Ed. by K. F. Chow, F. S. De Wekker, and J. B. Snyder. Springer Netherlands. Chap. Mesoscale Modeling over Complex Terrain: Numerical and Predictability Perspectives, 531–589. DOI: [10.1007/978-94-007-4098-3\\_9](https://doi.org/10.1007/978-94-007-4098-3_9) (cited on pp. 8, 108).
- Dudhia, J. (2012). *Overview of WRF physics*. accessed: 22 December 2017. URL: [http://www2.mmm.ucar.edu/wrf/users/tutorial/201207/Physics\\_full.pdf](http://www2.mmm.ucar.edu/wrf/users/tutorial/201207/Physics_full.pdf) (cited on p. 112).
- Dyer, A. J. and B. B. Hicks (1970). “Flux-gradient relationships in the constant flux layer”. *Quarterly Journal of the Royal Meteorological Society*, 96, 715–721. DOI: [10.1002/qj.49709641012](https://doi.org/10.1002/qj.49709641012) (cited on pp. 38, 60).
- European Environmental Agency (2006). *CORINE Land Cover (CLC) 2006 raster data, Version 13* (cited on pp. 38, 105).
- Farinotti, D., J. Magnusson, M. Huss, and A. Bauder (2010). “Snow accumulation distribution inferred from time-lapse photography and simple modelling”. *Hydrological Processes*, 24, 2087–2097. DOI: [10.1002/hyp.7629](https://doi.org/10.1002/hyp.7629) (cited on p. 16).
- Faure, F. (2008). “Microscale Airflow Simulations over Complex Alpine Terrain”. PhD thesis. École Polytechnique Fédérale de Lausanne, Lausanne, Switzerland, Nr. 4071. DOI: [10.5075/epfl-thesis-4071](https://doi.org/10.5075/epfl-thesis-4071) (cited on pp. 9, 79).
- Field, P. R., R. J. Hogan, P. R. A. Brown, A. J. Illingworth, T. W. Choularton, and R. J. Cotton (2005). “Parameterization of ice-particle size distributions for mid-latitude stratiform cloud”. *Quarterly Journal of the Royal Meteorological Society*, 131, 1997–2017. DOI: [10.1256/qj.04.134](https://doi.org/10.1256/qj.04.134) (cited on p. 7).
- Frei, P., S. Kotlarski, M. A. Liniger, and C. Schär (2018). “Snowfall in the Alps: Evaluation and projections based on the EURO-CORDEX regional climate models”. *The Cryosphere*, 12, 1–24. DOI: [10.5194/tc-12-1-2018](https://doi.org/10.5194/tc-12-1-2018) (cited on p. 2).

- Freudiger, D., I. Kohn, K. Stahl, and M. Weiler (2014). “Large-scale analysis of changing frequencies of rain-on-snow events with flood-generation potential”. *Hydrology and Earth System Sciences*, 18, 2695–2709. DOI: [10.5194/hess-18-2695-2014](https://doi.org/10.5194/hess-18-2695-2014) (cited on p. 2).
- Gabella, M., P. Speirs, U. Hamann, U. Germann, and A. Berne (2017). “Measurement of Precipitation in the Alps Using Dual-Polarization C-Band Ground-Based Radars, the GPM Spaceborne Ku-Band Radar, and Rain Gauges”. *Remote Sensing*, 9. DOI: [10.3390/rs9111147](https://doi.org/10.3390/rs9111147) (cited on p. 41).
- Galperin, B., S. Sukoriansky, and P. S. Anderson (2007). “On the critical Richardson number in stably stratified turbulence”. *Atmospheric Science Letters*, 8, 65–69. DOI: [10.1002/asl.153](https://doi.org/10.1002/asl.153) (cited on p. 96).
- Garvelmann, J., S. Pohl, and M. Weiler (2015). “Spatio-temporal controls of snowmelt and runoff generation during rain-on-snow events in a mid-latitude mountain catchment”. *Hydrological Processes*, 29, 3649–3664. DOI: [10.1002/hyp.10460](https://doi.org/10.1002/hyp.10460) (cited on p. 2).
- Gauer, P. (2001). “Numerical modeling of blowing and drifting snow in Alpine terrain”. *Journal of Glaciology*, 47, 97–110. DOI: [10.3189/172756501781832476](https://doi.org/10.3189/172756501781832476) (cited on p. 9).
- Gerber, F., N. Besic, V. Sharma, R. Mott, M. Daniels, M. Gabella, A. Berne, U. Germann, and M. Lehning (2018). “Spatial variability of snow precipitation and accumulation in COSMO-WRF simulations and radar estimations over complex terrain”. *The Cryosphere Discussions*, in review. DOI: [10.5194/tc-2018-50](https://doi.org/10.5194/tc-2018-50) (cited on pp. 59–61, 65, 69, 71, 76, 78, 79, 81, 99, 103, 104, 108, 111–113).
- Gerber, F., M. Lehning, S. W. Hoch, and R. Mott (2017a). “A close-ridge small-scale atmospheric flow field and its influence on snow accumulation”. *Journal of Geophysical Research – Atmospheres*, 122, 7737–7754. DOI: [10.1002/2016JD026258](https://doi.org/10.1002/2016JD026258) (cited on pp. 37, 41, 59, 61, 65, 76, 78, 79, 81).
- Gerber, F., R. Mott, S. W. Hoch, M. Bavay, and M. Lehning (2017b). *DISCHMEX - Observations and simulations of the close-ridge small-scale atmospheric flow field and snow accumulation at Sattelhorn, Dischma valley, Davos, Switzerland*. Laboratory of Cryospheric Sciences, School of Architecture and Civil Engineering, École Polytechnique Fédérale de Lausanne, Lausanne, Switzerland. DOI: [10.16904/19](https://doi.org/10.16904/19) (cited on p. 33).
- Gerber, F., R. Mott, and M. Lehning (in review). “The importance near-surface winter precipitation processes in complex alpine terrain”. *Journal of Hydrometeorology*, (cited on pp. 77, 78, 81).
- Gerber, F., J. Sedlacek, and R. Knutti (2014). “Influence of the western North Atlantic and the Barents Sea on European winter climate”. *Geophysical Research Letters*, 41, 561–567. DOI: [10.1002/2013GL058778](https://doi.org/10.1002/2013GL058778) (cited on p. 2).
- Gerber, F. and V. Sharma (2018). *Running COSMO-WRF on very high resolution over complex terrain*. Laboratory of Cryospheric Sciences, École Polytechnique Fédérale de Lausanne, Lausanne, Switzerland. DOI: [10.16904/envidat.35](https://doi.org/10.16904/envidat.35) (cited on pp. 39, 44, 61).
- Germann, U., M. Boscacci, M. Gabella, and M. Sartori (2015). “Peak performance: Radar design for prediction in the Swiss Alps”. *Meteorological Technology International*, 42–45 (cited on pp. 11–13, 37, 41).
- Germann, U., G. Galli, M. Boscacci, and M. Bolliger (2006). “Radar precipitation measurement in a mountainous region”. *Quarterly Journal of the Royal Meteorological Society*, 132, 1669–1692. DOI: [10.1256/qj.05.190](https://doi.org/10.1256/qj.05.190) (cited on pp. 12, 41).
- Gill, D. (2015). *Real – Description of General Functions*. accessed: 21 December 2017. URL: [http://www2.mmm.ucar.edu/wrf/users/tutorial/china\\_2015/real.pdf](http://www2.mmm.ucar.edu/wrf/users/tutorial/china_2015/real.pdf) (cited on p. 111).
- Gill, D. and M. Pyle (2010). *Nesting in WRF*. accessed: 21 December 2017. URL: [http://222.195.136.24/lecture/study\\_wrfv3/tutorial/201007/WRFNesting.pdf](http://222.195.136.24/lecture/study_wrfv3/tutorial/201007/WRFNesting.pdf) (cited on p. 109).
- Gobiet, A., S. Kotlarski, M. Beniston, G. Heinrich, J. Rajczak, and M. Stoffel (2014). “21st century climate change in the European Alps - A Review”. *Science of The Total Environment*, 493, 1138–1151. DOI: [10.1016/j.scitotenv.2013.07.050](https://doi.org/10.1016/j.scitotenv.2013.07.050) (cited on p. 2).

- Gómez-Navarro, J. J., C. C. Raible, and S. Dierer (2015). “Sensitivity of the WRF model to PBL parametrisations and nesting techniques: evaluation of wind storms over complex terrain”. *Geoscientific Model Development*, 8, 3349–3363. DOI: [10.5194/gmd-8-3349-2015](https://doi.org/10.5194/gmd-8-3349-2015) (cited on pp. 38, 45, 112).
- Graf, P., U. Germann, M. Boscacci, L. Clementi, and H. Wernli (2013). *The use of polarimetric weather radar in the Alps: Identification and statistical analysis of radar target and hydrometeor types with 83m radial resolution*. Scientific Report MeteoSwiss No. 96, 104 pp. Federal Office of Meteorology and Climatology MeteoSwiss (cited on p. 11).
- Grazioli, J., G. Lloyd, L. Panziera, C. R. Hoyle, P. J. Connolly, J. Henneberger, and A. Berne (2015). “Polarimetric radar and in situ observations of riming and snowfall microphysics during CLACE 2014”. *Atmospheric Chemistry and Physics*, 15, 13787–13802. DOI: [10.5194/acp-15-13787-2015](https://doi.org/10.5194/acp-15-13787-2015) (cited on pp. 5, 6, 58, 67, 69, 81).
- Groot Zwaaftink, C. D., H. Löwe, R. Mott, M. Bavay, and M. Lehning (2011). “Drifting snow sublimation: A high-resolution 3-D model with temperature and moisture feedbacks”. *Journal of Geophysical Research: Atmospheres*, 116, D16107. DOI: [10.1029/2011JD015754](https://doi.org/10.1029/2011JD015754) (cited on p. 22).
- Groot Zwaaftink, C. D., R. Mott, and M. Lehning (2013). “Seasonal simulation of drifting snow sublimation in Alpine terrain”. *Water Resources Research*, 49, 1581–1590. DOI: [10.1002/wrcr.20137](https://doi.org/10.1002/wrcr.20137) (cited on p. 5).
- Grünewald, T., Y. Bühler, and M. Lehning (2014). “Elevation dependency of mountain snow depth”. *The Cryosphere*, 8, 2381–2394. DOI: [10.5194/tc-8-2381-2014](https://doi.org/10.5194/tc-8-2381-2014) (cited on p. 71).
- Grünewald, T., D. S., R. Cattin, P. Steiner, W. Steinkogler, F. Fundel, and M. Lehning (2012). “Mapping frequencies of icing on structures in Switzerland”. *Journal of Engineering and Industrial Aerodynamics*, 107–108, 76–82. DOI: [10.1016/j.jweia.2012.03.022](https://doi.org/10.1016/j.jweia.2012.03.022) (cited on pp. 41, 45).
- Grünewald, T., M. Schirmer, R. Mott, and M. Lehning (2010). “Spatial and temporal variability of snow depth and ablation rates in a small mountain catchment”. *The Cryosphere*, 4, 215–225. DOI: [10.5194/tc-4-215-2010](https://doi.org/10.5194/tc-4-215-2010) (cited on pp. 13, 20, 36).
- Grünewald, T., J. Stötter, J. W. Pomeroy, R. Dadic, I. Moreno Baños, J. Muarturià, M. Spross, C. Hopkinson, P. Burlando, and M. Lehning (2013). “Statistical modelling of the snow depth distribution in open alpine terrain”. *Hydrology and Earth System Sciences*, 17, 3005–3021. DOI: [10.5194/hess-17-3005-2013](https://doi.org/10.5194/hess-17-3005-2013) (cited on p. 71).
- Grünewald, T. and M. Lehning (2011). “Altitudinal dependency of snow amounts in two small Alpine catchments: Can catchment-wide snow amounts be estimated via single snow or precipitation stations?” *Annals of Glaciology*, 52, 153–158. DOI: [10.3189/172756411797252248](https://doi.org/10.3189/172756411797252248) (cited on p. 16).
- Grünewald, T. and M. Lehning (2015). “Are flat-field snow depth measurements representative? A comparison of selected index sites with areal snow depth measurements at the small catchment scale”. *Hydrological Processes*, 29, 1717–1728. DOI: [10.1002/hyp.10295](https://doi.org/10.1002/hyp.10295) (cited on p. 13).
- Gunn, K. L. S. and J. S. Marshall (1958). “The distribution with size of aggregate snowflakes”. *Journal of Meteorology*, 15, 452–461. DOI: [10.1175/1520-0469\(1958\)015<0452:TDWSOA>2.0.CO;2](https://doi.org/10.1175/1520-0469(1958)015<0452:TDWSOA>2.0.CO;2) (cited on p. 7).
- Gutmann, E., I. Barstad, M. Clark, J. Arnold, and R. Rasmussen (2016). “The Intermediate Complexity Atmospheric Research Model (ICAR)”. *Journal of Hydrometeorology*, 17, 957–973. DOI: [10.1175/JHM-D-15-0155.1](https://doi.org/10.1175/JHM-D-15-0155.1) (cited on p. 7).
- Haberkorn, A., M. Phillips, R. Kenner, H. Rhyner, M. Bavay, S. P. Galos, and M. Hoelzle (2015). “Thermal Regime of Rock and its Relation to Snow Cover in Steep Alpine Rock Walls: Gemsstock, Central Swiss Alps”. *Geografiska Annaler: Series A, Physical Geography*, 97, 579–597. DOI: [10.1111/geoa.12101](https://doi.org/10.1111/geoa.12101) (cited on pp. 1, 2).

- Hahn, R. S. and C. F. Mass (2009). “The impact of positive-definite moisture advection and low-level moisture flux bias over orography”. *Monthly Weather Review*, 137, 3055–3071. DOI: [10.1175/2009MWR2873.1](https://doi.org/10.1175/2009MWR2873.1) (cited on p. 7).
- Hallet, J. and S. C. Mossop (1974). “Production of secondary ice particles during the riming process”. *Nature*, 249, 26–28. DOI: [10.1038/249026a0](https://doi.org/10.1038/249026a0) (cited on p. 3).
- Hartmann, D., A. Klein Tank, M. Rusticucci, L. Alexander, S. Brönnimann, Y. Charabi, F. Dentener, E. Dlugokencky, D. Easterling, A. Kaplan, B. Soden, P. Thorne, M. Wild, and P. Zhai (2013). “Observations: Atmosphere and Surface”. *Climate Change 2013: The Physical Science Basis. Contribution of Working Group I to the Fifth Assessment Report of the Intergovernmental Panel on Climate Change*. Ed. by T. Stocker, D. Qin, G.-K. Plattner, M. Tignor, S. Allen, J. Boschung, A. Nauels, Y. Xia, V. Bex, and P. Midgley. Cambridge, United Kingdom and New York, NY, USA: Cambridge University Press. Chap. 2, 159–254. DOI: [10.1017/CBO9781107415324.008](https://doi.org/10.1017/CBO9781107415324.008) (cited on p. 2).
- Hill, F. F., K. A. Browning, and M. J. Bader (1981). “Radar and raingauge observations of orographic rain over south Wales”. *Quarterly Journal of the Royal Meteorological Society*, 107, 643–670. DOI: [10.1002/qj.49710745312](https://doi.org/10.1002/qj.49710745312) (cited on p. 4).
- Hill, M., R. Calhoun, H. J. S. Fernando, A. Wieser, A. Dörnbrack, M. Weissmann, G. Mayr, and R. Newsom (2010). “Coplanar Doppler Lidar Retrieval of Rotors from T-REX”. *Journal of the Atmospheric Sciences*, 67, 713–729. DOI: [10.1175/2009JAS3016.1](https://doi.org/10.1175/2009JAS3016.1). eprint: <https://doi.org/10.1175/2009JAS3016.1> (cited on p. 11).
- Hobbs, P. V. and A. J. Alkezweeny (1968). “The fragmentation of freezing water droplets in free fall”. *Journal of Atmospheric Sciences*, 25, 881–888. DOI: [10.1175/1520-0469\(1968\)025<0881:TFOFDW>2.0.CO;2](https://doi.org/10.1175/1520-0469(1968)025<0881:TFOFDW>2.0.CO;2) (cited on p. 3).
- Hogan, R. J., P. R. Field, A. J. Illingworth, R. J. Cotton, and T. W. Choullarton (2002). “Properties of embedded convection in warm-frontal mixed-phase cloud from aircraft and polarimetric radar”. *Quarterly Journal of the Royal Meteorological Society*, 128, 451–476. DOI: [10.1256/003590002321042054](https://doi.org/10.1256/003590002321042054) (cited on p. 69).
- Hong, S.-Y., Y. Noh, and J. Dudhia (2006). “A New Diffusion Package with an Explicit Treatment of Entrainment Processes”. *Monthly Weather Review*, 134, 2318–2341. DOI: [10.1175/MWR3199.1](https://doi.org/10.1175/MWR3199.1) (cited on pp. 38, 60, 112).
- Houze Jr., R. A. (2012). “Orographic effects on precipitating clouds”. *Reviews of Geophysics*, 50, RG1001. DOI: [10.1029/2011RG000365](https://doi.org/10.1029/2011RG000365) (cited on pp. 4, 6, 16, 36, 46).
- Houze Jr., R. A., C. N. James, and S. Medina (2001). “Radar observations of precipitation and airflow on the Mediterranean side of the Alps: Autumn 1998 and 1999”. *Quarterly Journal of the Royal Meteorological Society*, 127, 2537–2558. DOI: [10.1002/qj.49712757804](https://doi.org/10.1002/qj.49712757804) (cited on p. 3).
- Hug, C., F. Faure, M. Lehning, S. Mobbs, N. Raderschall, and J.-A. Hertig (2005). “Small scale wind field simulations for the steep Gaudergrat ridge using CFX-4 and ARPS; Influence of the boundary conditions and comparison with measurements”. *Online proceedings, ICAM/MAP 2005*, O3.4, 46–49 (cited on pp. 26, 27, 32).
- Huwald, H., C. W. Higgins, M.-O. Boldi, E. Bou-Zeid, M. Lehning, and M. B. Parlange (2009). “Albedo effect on radiative errors in air temperature measurements”. *Water Resources Research*, 45, W08431. DOI: [10.1029/2008WR007600](https://doi.org/10.1029/2008WR007600) (cited on pp. 41, 43).
- Iriza, A., R. C. Dumitrache, A. Lupascu, and S. Stefan (2016). “Studies regarding the quality of numerical weather forecasts of the WRF model integrated at high-resolutions for the Romanian territory”. *Atmósfera*, 29, 11–21. DOI: [10.20937/ATM.2016.29.01.02](https://doi.org/10.20937/ATM.2016.29.01.02) (cited on p. 101).
- Jankov, I., P. J. Schultz, C. J. Anderson, and S. E. Koch (2007). “The impact of different physical parameterizations and their interactions on cold season QPF in the American River basin”. *Journal of Hydrometeorology*, 8, 1141–1151. DOI: [10.1175/JHM630.1](https://doi.org/10.1175/JHM630.1) (cited on p. 7).



- Jiménez, P. A. and J. Dudhia (2012). “Improving the Representation of Resolved and Unresolved Topographic Effects on Surface Wind in the WRF Model”. *Journal of Applied Meteorology and Climatology*, 51, 300–316. DOI: [10.1175/JAMC-D-11-084.1](https://doi.org/10.1175/JAMC-D-11-084.1) (cited on pp. 38, 44, 45, 79, 112).
- Joss, J. and A. Waldvogel (1990). “Radar in Meteorology: Battan Memorial and 40th Anniversary Radar Meteorology Conference”. Ed. by D. Atlas. American Meteorological Society, Boston, USA. Chap. Precipitation measurement and hydrology, 577–597. DOI: [10.1007/978-1-935704-15-7\\_39](https://doi.org/10.1007/978-1-935704-15-7_39) (cited on p. 12).
- Jost, G., M. Weiler, D.R. Gluns, and Y. Alila (2007). “The influence of forest and topography on snow accumulation and melt at the watershed-scale”. *Journal of Hydrology*, 347, 101–115. DOI: [10.1016/j.jhydrol.2007.09.006](https://doi.org/10.1016/j.jhydrol.2007.09.006) (cited on p. 16).
- Kerr, T., M. Clark, J. Hendrikx, and B. Anderson (2013). “Snow distribution in a steep mid-latitude alpine catchment”. *Advances in Water Resources*, 55, 17–24. DOI: [10.1016/j.advwatres.2012.12.010](https://doi.org/10.1016/j.advwatres.2012.12.010) (cited on p. 16).
- Kinar, N. J. and J. W. Pomeroy (2015). “Measurement of the physical properties of the snowpack”. *Reviews of Geophysics*, 53, 481–544. DOI: [10.1002/2015RG000481](https://doi.org/10.1002/2015RG000481) (cited on p. 13).
- Kirchner, P. B., R. C. Bales, N. P. Molotch, J. Flanagan, and Q. Guo (2014). “LiDAR measurement of seasonal snow accumulation along an elevation gradient in the southern Sierra Nevada, California”. *Hydrology and Earth System Sciences*, 18, 4261–4275. DOI: [10.5194/hess-18-4261-2014](https://doi.org/10.5194/hess-18-4261-2014) (cited on p. 71).
- Klemp, J. B., W. C. Skamarock, and O. Fuhrer (2003). “Numerical consistency of metric terms in terrain-following coordinates”. *Monthly Weather Review*, 131, 1229–1239. DOI: [10.1175/1520-0493\(2003\)131<1229:NCOMTI>2.0.CO;2](https://doi.org/10.1175/1520-0493(2003)131<1229:NCOMTI>2.0.CO;2) (cited on p. 8).
- Korolev, A. (2007). “Limitations of the Wegener-Bergeron-Findeisen mechanism in the evolution of mixed-phase clouds”. *Journal of Atmospheric Sciences*, 64, 3372–3375. DOI: [10.1175/JAS4035.1](https://doi.org/10.1175/JAS4035.1) (cited on p. 3).
- Kosović, B. (1997). “Subgrid-scale modelling for the large-eddy simulation of high-Reynolds-number boundary layers”. *Journal of Fluid Mechanics*, 336, 151–182. DOI: [10.1017/S0022112096004697](https://doi.org/10.1017/S0022112096004697) (cited on p. 8).
- Lafore, J. P., J. Stein, N. Asencio, P. Bougeault, V. Ducrocq, J. Duron, C. Fischer, P. Héreil, P. Mascart, V. Masson, J. P. Pinty, J. L. Redelsperger, E. Richard, and J. Vilà-Guerau de Arellano (1998). “The Meso-NH Atmospheric Simulation System. Part I: adiabatic formulation and control simulations”. *Annales Geophysicae*, 16, 90–109. DOI: [10.1007/s00585-997-0090-6](https://doi.org/10.1007/s00585-997-0090-6) (cited on p. 6).
- Lee, J., H. H. Shin, S.-Y. Hong, P. A. Jiménez, J. Dudhia, and J. Hong (2015). “Impacts of subgrid-scale orography parameterization on simulated surface layer wind and monsoonal precipitation in the high-resolution WRF model”. *Journal of Geophysical Research – Atmospheres*, 120, 644–653. DOI: [10.1002/2014JD022747](https://doi.org/10.1002/2014JD022747) (cited on pp. 79, 112).
- Lehning, M., P. Bartelt, B. Brown, T. Russi, U. Stöckli, and M. Zimmerli (1999). “SNOWPACK model calculations for avalanche warning based upon a new network of weather and snow stations”. *Cold Regions Science and Technology*, 30, 145–157. DOI: [10.1016/S0165-232x\(99\)00022-1](https://doi.org/10.1016/S0165-232x(99)00022-1) (cited on p. 9).
- Lehning, M. and C. Fierz (2008). “Assessment of snow transport in avalanche terrain”. *Cold Regions Science and Technology*, 51, 240–252. DOI: [10.1016/j.coldregions.2007.05.012](https://doi.org/10.1016/j.coldregions.2007.05.012) (cited on pp. 13, 16, 37).
- Lehning, M., T. Grünwald, and M. Schirmer (2011). “Mountain snow distribution governed by an altitudinal gradient and terrain roughness”. *Geophysical Research Letters*, 38, L19504. DOI: [10.1029/2011GL048927](https://doi.org/10.1029/2011GL048927) (cited on p. 5).

- Lehning, M., H. Löwe, M. Ryser, and N. Raderschall (2008). “Inhomogeneous precipitation distribution and snow transport in steep terrain”. *Water Resources Research*, 44, W07404. DOI: [10.1029/2007WR006545](https://doi.org/10.1029/2007WR006545) (cited on pp. 4, 5, 9, 10, 13, 16, 17, 21, 31, 37, 52, 56, 58, 65, 66, 70, 71, 74, 80).
- Lehning, M. and R. Mott (2016). “Bodennahe atmosphärische Prozesse und ihre Wirkung auf die hochalpine Schneedecke”. *promet Heft, Deutscher Wetterdienst*, 98, 59–67 (cited on pp. 4, 33, 58).
- Lehning, M., I. Völksch, D. Gustafsson, T. A. Nguyen, M. Stähli, and M. Zappa (2006). “ALPINE3D: a detailed model of mountain surface processes and its application to snow hydrology”. *Hydrological Processes*, 20, 2111–2128. DOI: [10.1002/hyp.6204](https://doi.org/10.1002/hyp.6204) (cited on pp. 9, 80).
- Leung, L. R. and Y. Qian (2003). “The sensitivity of precipitation and snowpack simulations to model resolution via nesting in regions of complex terrain”. *Journal of Hydrometeorology*, 4, 1025–1043. DOI: [10.1175/1525-7541\(2003\)004<1025:TSOPAS>2.0.CO;2](https://doi.org/10.1175/1525-7541(2003)004<1025:TSOPAS>2.0.CO;2) (cited on p. 49).
- Lichti, D. D. and S. Jamsch (2006). “Angular resolution of terrestrial laser scanners”. *The Photogrammetric Record*, 21, 141–160. DOI: [10.1111/j.1477-9730.2006.00367.x](https://doi.org/10.1111/j.1477-9730.2006.00367.x) (cited on p. 13).
- Lilly, D. K. (1962). “On the numerical simulation of buoyant convection”. *Tellus A*, 14, 148–172. DOI: [10.1111/j.2153-3490.1962.tb00128.x](https://doi.org/10.1111/j.2153-3490.1962.tb00128.x) (cited on p. 8).
- Liston, G., R. Haehnel, M. Sturm, C. Hiemstra, S. Berezovskaya, and R. Tabler (2007). “Simulating complex snow distributions in windy environments using SnowTran-3D”. *Journal of Glaciology*, 53, 241–256. DOI: [10.3189/172756507782202865](https://doi.org/10.3189/172756507782202865) (cited on p. 9).
- Liu, C., K. Ikeda, G. Thompson, R. Rasmussen, and J. Dudhia (2011). “High-Resolution Simulations of Wintertime Precipitation in the Colorado Headwaters Region: Sensitivity to Physics Parameterizations”. *Monthly Weather Review*, 139, 3533–3553. DOI: [10.1175/MWR-D-11-00009.1](https://doi.org/10.1175/MWR-D-11-00009.1) (cited on pp. 39, 80, 114).
- López-Moreno, J. I. and J. M. García-Ruiz (2004). “Influence of snow accumulation and snowmelt on streamflow in the central Spanish Pyrenees”. *Hydrological Sciences*, 49, 787–802. DOI: [10.1623/hysj.49.5.787.55135](https://doi.org/10.1623/hysj.49.5.787.55135) (cited on p. 2).
- Lundquist, J. K. and S. T. Chan (2007). “Consequences of urban stability conditions for computational fluid dynamics simulations of urban dispersion”. *Journal of Applied Meteorology and Climatology*, 46, 1080–1097. DOI: [10.1175/JAM2514.1](https://doi.org/10.1175/JAM2514.1) (cited on p. 8).
- Lundquist, K. A., F. K. Chow, and J. K. Lundquist (2010). “An immersed boundary method for the Weather Research and Forecasting model”. *Monthly Weather Review*, 138, 796–817. DOI: [10.1175/2009MWR2990.1](https://doi.org/10.1175/2009MWR2990.1) (cited on pp. 8, 9, 54).
- (2012). “An Immersed Boundary Method Enabling Large-Eddy Simulations of Flow over Complex Terrain in the WRF Model”. *Monthly Weather Review*, 140, 3936–3955. DOI: [10.1175/MWR-D-11-00311.1](https://doi.org/10.1175/MWR-D-11-00311.1) (cited on pp. 9, 54).
- Ma, Y. and H. Liu (2017). “Large-Eddy Simulations of Atmospheric Flows Over Complex Terrain Using the Immersed-Boundary Method in the Weather Research and Forecasting Model”. *Boundary-Layer Meteorology*, 165, 421–445. DOI: [10.1007/s10546-017-0283-9](https://doi.org/10.1007/s10546-017-0283-9) (cited on pp. 9, 54).
- MacDonald, M. K., J. W. Pomeroy, and A. Pietroniro (2010). “On the importance of sublimation to an alpine snow mass balance in the Canadian Rocky Mountains”. *Hydrology and Earth System Sciences*, 14, 1401–1415. DOI: [10.5194/hess-14-1401-2010](https://doi.org/10.5194/hess-14-1401-2010) (cited on p. 5).
- Marty, C. and J. Blanchet (2012). “Long-term changes in annual maximum snow depth and snowfall in Switzerland based on extreme value statistics”. *Climatic Change*, 111, 705–721. DOI: [10.1007/s10584-011-0159-9](https://doi.org/10.1007/s10584-011-0159-9) (cited on p. 16).
- Mason, P. J. and D. J. Thompson (1992). “Stochastic backscatter in large-eddy simulations of boundary layers”. *Journal of Fluid Mechanics*, 242, 51–78. DOI: [10.1017/S0022112092002271](https://doi.org/10.1017/S0022112092002271) (cited on p. 8).



- Mass, C., D. Ovens, K. Westrick, and B. A. Colle (2002). “Does increasing horizontal resolution produce more skillful forecasts?” *Bulletin of the American Meteorological Society*, 83, 407–430. DOI: [10.1175/1520-0477\(2002\)083<0407:DIHRPM>2.3.CO;2](https://doi.org/10.1175/1520-0477(2002)083<0407:DIHRPM>2.3.CO;2) (cited on p. 49).
- Maurer, E. P., H. G. Hidalgo, T. Das, M. D. Dettinger, and D. R. Cayan (2010). “The utility of daily large-scale climate data in the assessment of climate change impacts on daily streamflow in California”. *Hydrology and Earth System Sciences*, 14, 1125–1138. DOI: [10.5194/hess-14-1125-2010](https://doi.org/10.5194/hess-14-1125-2010) (cited on p. 7).
- Mazzaro, L. J., D. Muñoz-Esparza, J. K. Lundquist, and R. R. Linn (2017). “Nested mesoscale-to-LES modeling of the atmospheric boundary layer in the presence of under-resolved convective structures”. *Journal of Advances in Modeling Earth Systems*, 9, 1795–1810. DOI: [10.1002/2017MS000912](https://doi.org/10.1002/2017MS000912) (cited on pp. 9, 79).
- McCabe, G. J., M. P. Clark, and L. E. Hay (2007). “Rain-on-Snow Events in the Western United States”. *Bulletin of the American Meteorological Society*, 88, 319–328. DOI: [10.1175/BAMS-88-3-319](https://doi.org/10.1175/BAMS-88-3-319). eprint: <https://doi.org/10.1175/BAMS-88-3-319> (cited on p. 2).
- MeteoSchweiz (2015). *Klimabulletin Oktober 2015*. Zürich (cited on p. 17).
- METI/NASA (2009). 2009, *ASTER Global Digital Elevation Model V002, NASA EOSDIS Land Processes DAAC, USGS Earth Resources Observation and Science (EROS) Center, Sioux Falls, South Dakota* (<https://lpdaac.usgs.gov>), accessed 01 24, 2018, at <http://dx.doi.org/10.5067/ASTER/ASTGTM.002>. *Aster GDEM is a product of NASA and METI*. (Cited on pp. 39, 102, 103).
- Michlmayr, G., M. Lehning, G. Koboltschnig, H. Holzmann, M. Zappa, R. Mott, and W. Schöner (2008). “Application of the Alpine3D model for glacier mass balance and glacier runoff studies at Goldbergkees, Austria”. *Hydrological Processes*, 22, 2941–3949. DOI: [10.1002/hyp.7102](https://doi.org/10.1002/hyp.7102) (cited on p. 84).
- Mirocha, J. D., J. K. Lundquist, and B. Kosović (2010). “Implementation of a Nonlinear Subfilter Turbulence Stress Model for Large-Eddy Simulation in the Advanced Research WRF Model”. *Monthly Weather Review*, 138, 4212–4228. DOI: [10.1175/2010MWR3286.1](https://doi.org/10.1175/2010MWR3286.1) (cited on pp. 8, 9, 44, 79).
- Mirocha, J., B. Kosović, and G. Kirkil (2014). “Resolved Turbulence Characteristics in Large-Eddy Simulations Nested within Mesoscale Simulations Using the Weather Research and Forecasting Model”. *Monthly Weather Review*, 142, 806–831. DOI: [10.1175/MWR-D-13-00064.1](https://doi.org/10.1175/MWR-D-13-00064.1) (cited on pp. 9, 44, 79).
- Mitchell, D. L. (1996). “Use of mass-and area-dimesional power laws for determining precipitation particle terminal velocities”. *Journal of Atmospheric Sciences*, 53, 1710–1723. DOI: [10.1175/1520-0469\(1996\)053<1710:UOMAAD>2.0.CO;2](https://doi.org/10.1175/1520-0469(1996)053<1710:UOMAAD>2.0.CO;2) (cited on p. 7).
- Moeng, C.-H. (1984). “A large-eddy-simulation model for the study of planetary boundary-layer turbulence”. *Journal of Atmospheric Sciences*, 41, 2052–2062. DOI: [10.1175/1520-0469\(1984\)041<2052:ALESMF>2.0.CO;2](https://doi.org/10.1175/1520-0469(1984)041<2052:ALESMF>2.0.CO;2) (cited on p. 8).
- Morrison, H., J. A. Curry, and V. I. Khvorostyanov (2005). “A New Double-Moment Microphysics Parameterization for Application in Cloud and Climate Models. Part I: Description”. *Journal of Atmospheric Sciences*, 62, 1665–1677. DOI: [10.1175/JAS3446.1](https://doi.org/10.1175/JAS3446.1) (cited on pp. 39, 46, 60, 68, 69, 91, 114).
- Morrison, H., G. Thompson, and V. Tatarskii (2009). “Impact of Cloud Microphysics on the Development of Trailing Stratiform Precipitation in a Simulated Squall Line: Comparison of One- and Two-Moment Schemes”. *Monthly Weather Review*, 137, 991–1007. DOI: [10.1175/2008MWR2556.1](https://doi.org/10.1175/2008MWR2556.1) (cited on pp. 39, 60, 114).
- Mott, R., M. Daniels, and M. Lehning (2015). “Atmospheric Flow Development and Associated Changes in Turbulent Sensible Heat Flux over Patchy Mountain Snow Cover”. *Journal of Hydrometeorology*, 16, 1315–1340. DOI: [10.1175/JHM-D-14-0036.1](https://doi.org/10.1175/JHM-D-14-0036.1) (cited on pp. 20, 40).

- Mott, R., M. Schirmer, M. Bavay, T. Grünewald, and M. Lehning (2010). “Understanding snow-transport processes shaping the mountain snow-cover”. *The Cryosphere*, 4, 545–559. DOI: [10.5194/tc-4-545-2010](https://doi.org/10.5194/tc-4-545-2010) (cited on pp. 4–6, 9, 10, 13, 16, 17, 32, 37, 45, 58, 59).
- Mott, R., M. Schirmer, and M. Lehning (2011). “Scaling properties of wind and snow depth distribution in an Alpine catchment”. *Journal of Geophysical Research*, 116, D06106. DOI: [10.1029/2010JD014886](https://doi.org/10.1029/2010JD014886) (cited on pp. 4, 36, 37).
- Mott, R., S. Schlögl, L. Dirks, and M. Lehning (2017). “Impact of Extreme Land Surface Heterogeneity on Micrometeorology over Spring Snow Cover”. *Journal of Hydrometeorology*, 18, 2705–2722. DOI: [10.1175/JHM-D-17-0074.1](https://doi.org/10.1175/JHM-D-17-0074.1) (cited on pp. 41, 61, 81).
- Mott, R., D. Scipión, M. Schneebeli, N. Dawes, A. Berne, and M. Lehning (2014). “Orographic effects on snow deposition patterns in mountainous terrain”. *Journal of Geophysical Research – Atmospheres*, 119, 1419–1439. DOI: [10.1002/2013JD019880](https://doi.org/10.1002/2013JD019880) (cited on pp. 4–6, 9, 10, 12, 16, 17, 20, 22, 36, 37, 58, 59, 62, 65, 66, 69, 72–74, 80).
- Mott, R. and M. Lehning (2010). “Meteorological Modeling of Very High-Resolution Wind Fields and Snow Deposition for Mountains”. *Journal of Hydrometeorology*, 11, 934–949. DOI: [10.1175/2010JHM1216.1](https://doi.org/10.1175/2010JHM1216.1) (cited on pp. 4, 5, 10, 20, 22, 29, 31, 32, 37, 58, 59, 65, 81, 86).
- Muñoz-Esparza, D., J. K. Lundquist, J. A. Sauer, B. Kosovic, and R. R. Linn (2017). “Coupled mesoscale-LES modeling of a diurnal cycle during the CWEX-13 field campaign: From weather to boundary-layer eddies”. *Journal of Advances in Modeling Earth Systems*, 9, 1572–1594. DOI: [10.1002/2017MS000960](https://doi.org/10.1002/2017MS000960) (cited on pp. 9, 79).
- Nemoto, M. and K. Nishimura (2004). “Numerical simulation of snow saltation and suspension in a turbulent boundary layer”. *Journal of Geophysical Research: Atmospheres*, 109, D18206. DOI: [10.1029/2004JD004657](https://doi.org/10.1029/2004JD004657). eprint: <https://agupubs.onlinelibrary.wiley.com/doi/pdf/10.1029/2004JD004657> (cited on p. 9).
- Niu, G.-Y., Z.-L. Yang, K. E. Mitchell, F. Chen, M. B. Ek, M. Barlage, A. Kumar, K. Manning, D. Niyogi, E. Rosero, M. Tewari, and Y. Xia (2011). “The community Noah land surface model with multiparameterization options (Noah-MP): 1. Model description and evaluation with local-scale measurements”. *Journal of Geophysical Research*, 116, D12109. DOI: [10.1029/2010JD015139](https://doi.org/10.1029/2010JD015139) (cited on pp. 38, 60, 113).
- Nohara, D., A. Kitoh, M. Hosaka, and T. Oki (2006). “Impact of Climate Change on River Discharge Projected by Multimodel Ensemble”. *Journal of Hydrometeorology*, 7, 1076–1089. DOI: [10.1175/JHM531.1](https://doi.org/10.1175/JHM531.1) (cited on p. 2).
- Obukhov, A. M. (1971). “Turbulence in an atmosphere with a non-uniform temperature”. *Boundary-Layer Meteorology*, 2, 7–29 (cited on p. 39).
- Panziera, L., C. N. James, and U. Germann (2015). “Mesoscale organization and structure of orographic precipitation producing flash floods in the Lago Maggiore region”. *Quarterly Journal of the Royal Meteorological Society*, 141, 224–248. DOI: [10.1002/qj.2351](https://doi.org/10.1002/qj.2351) (cited on p. 37).
- Paulson, C. A. (1970). “The mathematical representation of wind speed and temperature profiles in the unstable atmospheric surface layer”. *Journal of Applied Meteorology*, 9, 857–861. DOI: [10.1175/1520-0450\(1970\)009<0857:TMROWS>2.0.CO;2](https://doi.org/10.1175/1520-0450(1970)009<0857:TMROWS>2.0.CO;2) (cited on pp. 38, 60).
- Peskin, C. S. (1972). “Flow patterns around heart valves: A numerical method”. *Journal of Computational Physics*, 10, 252–271. DOI: [10.1016/0021-9991\(72\)90065-4](https://doi.org/10.1016/0021-9991(72)90065-4) (cited on p. 9).
- Peterson, T. C., L. O. Grant, W. R. Cotton, and D. C. Rogers (1991). “The effect of decoupled low-level flow on winter orographic clouds and precipitation in the Yampa River valley”. *Journal of Applied Meteorology*, 30, 368–386. DOI: [10.1175/1520-0450\(1991\)030<0368:TEODLL>2.0.CO;2](https://doi.org/10.1175/1520-0450(1991)030<0368:TEODLL>2.0.CO;2) (cited on p. 3).

- Petoukhov, V. and V. A. Semenov (2010). “A link between reduced Barents-Kara sea ice and cold winter extremes over northern continents”. *Journal of Geophysical Research – Atmospheres*, 115, D21111. DOI: [10.1029/2009JD013568](https://doi.org/10.1029/2009JD013568) (cited on p. 2).
- Pineda, N., O. Jorba, J. Jorge, and J. M. Baldasano (2004). “Using NOAA AVHRR and SPOT VGT data to estimate surface parameters: application to a mesoscale meteorological model”. *International Journal of Remote Sensing*, 25, 129–143. DOI: [10.1080/0143116031000115201](https://doi.org/10.1080/0143116031000115201) (cited on pp. 38, 105).
- Pohl, B. (2011). “Testing WRF capability in simulating the atmospheric water cycle over Equatorial East Africa”. *Climate Dynamics*, 37, 1375–1379. DOI: [10.1007/s00382-011-1024-2](https://doi.org/10.1007/s00382-011-1024-2) (cited on p. 49).
- Pontoppidan, M., J. Reuder, S. Mayer, and E. W. Kolstad (2017). “Downscaling an intense precipitation event in complex terrain: the importance of high grid resolution”. *Tellus A: Dynamic Meteorology and Oceanography*, 69, 1271561. DOI: [10.1080/16000870.2016.1271561](https://doi.org/10.1080/16000870.2016.1271561) (cited on pp. 58, 81).
- Prokop, A. (2008). “Assessing the applicability of terrestrial laser scanning for spatial snow depth measurements”. *Cold Regions Science and Technology*, 54, 155–163. DOI: [10.1016/j.coldregions.2008.07.002](https://doi.org/10.1016/j.coldregions.2008.07.002) (cited on pp. 13, 36).
- Purdy, J. C., G. L. Austin, S. A. W., and I. D. Cluckie (2005). “Radar evidence of orographic enhancement due to the seeder feeder mechanism”. *Meteorological Applications*, 12, 199–206. DOI: [10.1017/S1350482705001672](https://doi.org/10.1017/S1350482705001672) (cited on pp. 3, 37, 52).
- Raderschall, N., M. Lehning, and C. Schär (2008). “Fine-scale modeling of the boundary layer wind field over steep topography”. *Water Resources Research*, 44, W09425. DOI: [10.1029/2007WR006544](https://doi.org/10.1029/2007WR006544) (cited on pp. 9, 10, 20, 80).
- Rai, R. K., L. K. Berg, B. Kosović, J. D. Mirocha, M. S. Pekour, and W. J. Shaw (2017). “Comparison of Measured and Numerically Simulated Turbulence Statistics in a Convective Boundary Layer Over Complex Terrain”. *Boundary-Layer Meteorology*, 163, 69–89. DOI: [10.1007/s10546-016-0217-y](https://doi.org/10.1007/s10546-016-0217-y) (cited on p. 112).
- Rasmussen, R., C. Liu, K. Ikeda, D. Gochis, D. Yates, F. Chen, M. Tewari, M. Barlage, J. Dudhia, W. Yu, K. Miller, K. Arsenault, V. Grubišić, G. Thompson, and E. Gutmann (2011). “High-Resolution Coupled Climate Runoff Simulations of Seasonal Snowfall over Colorado: A Process Study of Current and Warmer Climate”. *Journal of Climate*, 24, 3015–3048. DOI: [10.1175/2010JCLI3985.1](https://doi.org/10.1175/2010JCLI3985.1) (cited on pp. 58, 81).
- Reinking, R. F. (1975). “Formation of graupel”. *Journal of Applied Meteorology*, 14, 745–754. DOI: [10.1175/1520-0450\(1975\)014<0745:FOG>2.0.CO;2](https://doi.org/10.1175/1520-0450(1975)014<0745:FOG>2.0.CO;2) (cited on p. 3).
- Reisner, J., R. M. Rasmussen, and R. T. Bruintjes (1998). “Explicit forecasting of supercooled liquid water in winter storms using the MM5 mesoscale model”. *Quarterly Journal of the Royal Meteorological Society*, 124, 1071–1107. DOI: [10.1002/qj.49712454804](https://doi.org/10.1002/qj.49712454804) (cited on pp. 69, 91).
- Richard, E., A. Buzzi, and G. Zängl (2007). “Quantitative precipitation forecasting in the Alps: The advances achieved by the Mesoscale Alpine Programme”. *Quarterly Journal of the Royal Meteorological Society*, 133, 831–846. DOI: [10.1002/qj.65](https://doi.org/10.1002/qj.65) (cited on pp. 58, 81).
- Riegl (Jan. 2015). *Datasheet Riegl VZ-6000*. Tech. rep. Riegl Laser Measurement Systems GmbH, Austria (cited on p. 20).
- Roe, G. H. and M. Baker (2006). “Microphysical and geometrical controls on the pattern of orographic precipitation”. *Journal of Atmospheric Sciences*, 63, 861–880. DOI: [10.1175/JAS3619.1](https://doi.org/10.1175/JAS3619.1) (cited on p. 3).
- Roth, A., R. Hock, T. V. Schuler, P. A. Bieniek, M. Pelto, and A. Aschwanden (2018). “Modeling winter precipitation over the Juneau Icefield, Alaska, using a linear model of orographic precipitation”. *Frontiers in Earth Science - Cryospheric Sciences*, 6:20. DOI: [10.3389/feart.2018.00020](https://doi.org/10.3389/feart.2018.00020) (cited on pp. 7, 58).

- Rutledge, S. A. and P. V. Hobbs (1984). “The mesoscale and microscale structure of organization of clouds and precipitation in midlatitude cyclones. XII: A diagnostic modeling study of precipitation development in narrow cold-frontal rainbands”. *Journal of Atmospheric Sciences*, 41, 2949–2972. DOI: [10.1175/1520-0469\(1984\)041<2949:TMAMSA>2.0.CO;2](https://doi.org/10.1175/1520-0469(1984)041<2949:TMAMSA>2.0.CO;2) (cited on p. 91).
- Saltikoff, E., P. Lopez, A. Taskinen, and S. Pulkkinen (2015). “Comparison of quantitative snowfall estimates from weather radar, rain gauges and a numerical weather prediction model”. *Boreal environment research*, 20, 667–678 (cited on p. 41).
- Schirmer, M. and M. Lehning (2011). “Persistence in intra-annual snow depth distribution: 2. Fractal analysis of snow depth development”. *Water Resources Research*, 47, W09517. DOI: [10.1029/2010WR009429](https://doi.org/10.1029/2010WR009429) (cited on pp. 36, 37, 81).
- Schirmer, M., J. Schweizer, and M. Lehning (2010). “Statistical evaluation of local to regional snowpack stability using simulated snow-cover data”. *Cold Regions Science and Technology*, 64, 110–118. DOI: [10.1016/j.coldregions.2010.04.012](https://doi.org/10.1016/j.coldregions.2010.04.012) (cited on p. 16).
- Schirmer, M., V. Wirz, A. Clifton, and M. Lehning (2011). “Persistence in intra-annual snow depth distribution: 1. Measurements and topographic control”. *Water Resources Research*, 47, W09516. DOI: [10.1029/2010WR009426](https://doi.org/10.1029/2010WR009426) (cited on pp. 5, 6, 36, 42, 64, 74, 81).
- Schlögl, S., M. Lehning, K. Nishimura, H. Huwald, N. J. Cullen, and R. Mott (2017). “How do stability corrections perform in the stable boundary layer over snow?” *Boundary-Layer Meteorology*, 165, 161–180. DOI: [10.1007/s10546-017-0262-1](https://doi.org/10.1007/s10546-017-0262-1) (cited on p. 11).
- Schlögl, S., M. Lehning, and R. Mott (in review). “Representation of horizontal transport processes in snowmelt modelling by applying a footprint approach”. *Frontiers in Earth Science*, (cited on pp. 41, 61, 81).
- Schmucki, E., C. Marty, C. Fierz, R. Weingartner, and Le (2017). “Impact of climate change in Switzerland on socioeconomic snow indices”. *Theoretical and Applied Climatology*, 127, 875–889. DOI: [10.1007/s00704-015-1676-7](https://doi.org/10.1007/s00704-015-1676-7) (cited on pp. 1, 36).
- Schneiderbauer, S. and A. Prokop (2011). “The atmospheric snow-transport model: SnowDrift3D”. *Journal of Glaciology*, 57, 526–542. DOI: [10.3189/002214311796905677](https://doi.org/10.3189/002214311796905677) (cited on p. 9).
- Schweizer, J., J. Bruce Jamieson, and M. Schneebeli (2003). “Snow avalanche formation”. *Reviews of Geophysics*, 41, 1016, 1016. DOI: [10.1029/2002RG000123](https://doi.org/10.1029/2002RG000123) (cited on p. 2).
- Scipión, D. E., R. Mott, M. Lehning, M. Schneebeli, and A. Berne (2013). “Seasonal small-scale spatial variability in alpine snowfall and snow accumulation”. *Water Resources Research*, 49, 1446–1457. DOI: [10.1002/wrcr.20135](https://doi.org/10.1002/wrcr.20135) (cited on pp. 5, 36, 37, 81).
- Silverman, N. L., M. P. Maneta, S.-H. Chen, and J. T. Harper (2013). “Dynamically downscaled winter precipitation over complex terrain of the Central Rockies of Western Montana, USA”. *Water Resources Research*, 49, 458–470. DOI: [10.1029/2012WR012874](https://doi.org/10.1029/2012WR012874) (cited on pp. 49, 55).
- Sinclair, M. R., D. S. Wratt, R. D. Henderson, and W. R. Gray (1997). “Factors affecting the distribution and spillover of precipitation in the Southern Alps of New Zealand - A case study”. *Journal of Applied Meteorology*, 36, 428–442. DOI: [10.1175/1520-0450\(1997\)036<0428:FATDAS>2.0.CO;2](https://doi.org/10.1175/1520-0450(1997)036<0428:FATDAS>2.0.CO;2) (cited on p. 3).
- Skamarock, W. C., J. B. Klemp, J. Dudhia, D. O. Gill, D. M. Barker, M. G. Duda, X.-Y. Huang, W. Wang, and J. G. Powers (2008). *A Description of the Advanced Research WRF Version 3*. Tech. rep. Boulder, Colorado, USA: Mesoscale and Microscale Meteorological Division, National Center for Atmospheric Research (cited on pp. 6, 38, 59, 60, 99, 109).
- Smagorinsky, J. (1963). “General circulation experiments with the primitive equations”. *Monthly Weather Review*, 91, 99–152. DOI: [10.1175/1520-0493\(1963\)091<0099:GCEWTP>2.3.CO;2](https://doi.org/10.1175/1520-0493(1963)091<0099:GCEWTP>2.3.CO;2) (cited on p. 8).

- Smith, R. B. (1979). “The influence of mountains on the atmosphere”. *Advances in Geophysics*, 21, 87–233. DOI: [10.1016/S0065-2687\(08\)60262-9](https://doi.org/10.1016/S0065-2687(08)60262-9) (cited on p. 3).
- Smith, R. and I. Barstad (2004). “A Linear Theory of Orographic Precipitation”. *Journal of Atmospheric Sciences*, 61, 1377–1391. DOI: [10.1175/1520-0469\(2004\)061<1377:ALTOOP>2.0.CO;2](https://doi.org/10.1175/1520-0469(2004)061<1377:ALTOOP>2.0.CO;2) (cited on pp. 7, 58).
- Sommer, C. G., M. Lehning, and R. Mott (2015). “Snow in a Very Steep Rock Face: Accumulation and Redistribution During and After a Snowfall Event”. *Frontiers in Earth Science*, 3:73. DOI: [10.3389/feart.2015.00073](https://doi.org/10.3389/feart.2015.00073) (cited on pp. 13, 16, 20, 31–33, 58, 71, 84).
- Stappeler, J., G. Doms, U. Schättler, H. W. Bitzer, A. Gassmann, U. Damrath, and G. Gregoric (2003). “Meso-gamma scale forecasts using the nonhydrostatic model LM”. *Meteorology and Atmospheric Physics*, 82, 75–96. DOI: [10.1007/s00703-001-0592-9](https://doi.org/10.1007/s00703-001-0592-9) (cited on p. 6).
- Stoelinga, M. T., R. E. Stewart, G. Thompson, and J. M. Thériault (2013). “Mountain Weather Research and Forecasting: Recent Progress and Current Challenges”. Ed. by K. F. Chow, F. S. De Wekker, and J. B. Snyder. Springer Netherlands. Chap. Microphysical Processes Within Winter Orographic Cloud and Precipitation Systems, 345–408. DOI: [10.1007/978-94-007-4098-3\\_7](https://doi.org/10.1007/978-94-007-4098-3_7) (cited on pp. 3, 4, 6, 7, 16, 36, 46, 52, 55, 58, 67).
- Stoner, A. M., K. Hayhoe, X. Yang, and D. J. Wuebbles (2012). “An asynchronous regional regression model for statistical downscaling of daily climate variables”. *International Journal of Climatology*, 33, 2473–2494. DOI: [10.1002/joc.3603](https://doi.org/10.1002/joc.3603) (cited on p. 7).
- Sturm, M. and C. Benson (2004). “Scales of spatial heterogeneity for perennial and seasonal snow layers”. *Annals of Glaciology*, 38, 253–260. DOI: [10.3189/172756404781815112](https://doi.org/10.3189/172756404781815112) (cited on p. 5).
- Talbot, C., E. Bou-Zeid, and J. Smith (2012). “Nested Mesoscale Large-Eddy Simulations with WRF: Performance in Real Test Cases”. *Journal of Hydrometeorology*, 13, 1421–1441. DOI: [10.1175/JHM-D-11-048.1](https://doi.org/10.1175/JHM-D-11-048.1) (cited on pp. 9, 38, 79).
- Tedesche, M. E., S. R. Fassnacht, and P. J. Meiman (2017). “Scales of snow depth variability in high elevation rangeland sagebrush”. *Frontiers of Earth Sciences*, 11, 469–481. DOI: [10.1007/s11707-017-0662-z](https://doi.org/10.1007/s11707-017-0662-z) (cited on p. 36).
- Tewari, M., F. Chen, W. Wang, J. Dudhia, M. A. LeMone, K. Mitchell, M. Ek, G. Gayno, J. Wegiel, and R. H. Cuenca (2004). “Implementation and verification of the unified Noah land surface model in the WRF model”. *20th conference on weather analysis and forecasting/16th conference on numerical weather prediction*, 11–15 (cited on p. 113).
- Trujillo, E., N. P. Molotch, M. L. Goulden, A. E. Kelly, and R. C. Bales (2012). “Elevation-dependent influence of snow accumulation on forest greening”. *Nature Geoscience*, 5, 705–709. DOI: [10.1038/ngeo1571](https://doi.org/10.1038/ngeo1571) (cited on p. 36).
- Vaughan, D., J. Comiso, I. Allison, J. Carrasco, G. Kaser, R. Kwok, P. Mote, T. Murray, F. Paul, J. Ren, E. Rignot, O. Solomina, K. Steffen, and T. Zhang (2013). “Observations: Cryosphere”. *Climate Change 2013: The Physical Science Basis. Contribution of Working Group I to the Fifth Assessment Report of the Intergovernmental Panel on Climate Change*. Ed. by T. Stocker, D. Qin, G.-K. Plattner, M. Tignor, S. Allen, J. Boschung, A. Nauels, Y. Xia, V. Bex, and P. Midgley. Cambridge, United Kingdom and New York, NY, USA: Cambridge University Press. Chap. 4, 317–382. DOI: [10.1017/CBO9781107415324.012](https://doi.org/10.1017/CBO9781107415324.012) (cited on p. 2).
- Vetterli, M. and J. Kovačević (1995). *Wavelets and Subband Coding*. Prentice-Hall: Upper Saddle River, NJ, USA (cited on p. 79).
- Vionnet, V., E. Brun, S. Morin, A. Boone, S. Faroux, P. Le Moigne, E. Martin, and J.-M. Willemet (2012). “The detailed snowpack scheme Crocus and its implementation in SURFEX v7.2”. *Geoscientific Model Development*, 5, 773–791. DOI: [10.5194/gmd-5-773-2012](https://doi.org/10.5194/gmd-5-773-2012) (cited on p. 9).



- Vionnet, V., E. Martin, V. Masson, G. Guyomarc'h, F. Naaim Bouvet, A. Prokop, Y. Durand, and C. Lac (2014). "Simulation of wind-induced snow transport and sublimation in alpine terrain using a fully coupled snowpack/atmosphere model". *The Cryosphere*, 8, 395–415. DOI: [10.5194/tc-8-395-2014](https://doi.org/10.5194/tc-8-395-2014) (cited on pp. 5, 9, 10, 80).
- Vionnet, V., E. Martin, V. Masson, C. Lac, F. Naaim Bouvet, and G. Guyomarc'h (2017). "High-resolution large eddy simulation of snow accumulation in alpine terrain". *Journal of Geophysical Research – Atmospheres*, 122, 11, 005–11, 021. DOI: [10.1002/2017JD026947](https://doi.org/10.1002/2017JD026947) (cited on pp. 5, 6, 9, 10, 36, 37, 58, 59, 73, 80).
- Vögeli, C., M. Lehning, N. Wever, and M. Bavay (2016). "Scaling Precipitation Input to Spatially Distributed Hydrological Models by Measured Snow Distribution". *Frontiers in Earth Science – Cryospheric Sciences*, 4:108. DOI: [10.3389/feart.2016.00108](https://doi.org/10.3389/feart.2016.00108) (cited on p. 80).
- Voigt, M. and V. Wirth (2013). "Mechanisms of Banner Cloud Formation". *Journal of Atmospheric Sciences*, 70, 3631–3640. DOI: [10.1175/JAS-D-12-0353.1](https://doi.org/10.1175/JAS-D-12-0353.1) (cited on pp. 26, 32).
- Wang, W. (2015). *Considerations for Designing an Numerical Experiment*. accessed: 22 December 2017. URL: [http://www2.mmm.ucar.edu/wrf/users/tutorial/201501/BEST\\_PRACTICES.pdf](http://www2.mmm.ucar.edu/wrf/users/tutorial/201501/BEST_PRACTICES.pdf) (cited on p. 114).
- Wang, W., C. Bruyère, M. Duda, J. Dudhia, D. Gill, M. Kavulich, K. Keene, H.-C. Lin, J. Michalakes, S. Rizvi, X. Zhang, J. Berner, and K. Fossell (2016). *Weather Research & Forecasting ARW Version 3 Modeling System User's Guide*. Tech. rep. Mesoscale and Microscale Meteorology Division, National Center for Atmospheric Research (cited on pp. 108, 109, 113).
- Wang, Z. and N. Huang (2017). "Numerical simulation of the falling snow deposition over complex terrain". *Journal of Geophysical Research - Atmospheres*, 122, 980–1000. DOI: [10.1002/2016JD025316](https://doi.org/10.1002/2016JD025316) (cited on pp. 5, 10, 16, 29, 31–33, 59, 78).
- Warscher, M., U. Strasser, G. Kraller, T. Marke, H. Franz, and H. Kunstmann (2013). "Performance of complex snow cover descriptions in a distributed hydrological model system: A case study for the high Alpine terrain of Berchtesgaden Alps". *Water Resources Research*, 49, 2619–2637. DOI: [10.1002/wrcr.20219](https://doi.org/10.1002/wrcr.20219) (cited on p. 29).
- Wastl, C. and G. Zängl (2008). "Analysis of mountain-valley precipitation differences in the Alps". *Meteorologische Zeitschrift*, 17, 311–321. DOI: [10.1127/0941-2948/2008/0291](https://doi.org/10.1127/0941-2948/2008/0291) (cited on p. 16).
- Webb, E. K. (1970). "Profile relationships: The log-linear range, and extension to strong stability". *Quarterly Journal of the Royal Meteorological Society*, 96, 67–90. DOI: [10.1002/qj.49709640708](https://doi.org/10.1002/qj.49709640708) (cited on pp. 38, 60).
- Wehra, A. and U. Lohrb (1999). "Airborne laser scanning – an introduction and overview". *Journal of Photogrammetry and Remote Sensing*, 54, 68–82. DOI: [10.1016/S0924-2716\(99\)00011-8](https://doi.org/10.1016/S0924-2716(99)00011-8) (cited on p. 13).
- Weigel, A. P., F. K. Chow, M. W. Rotach, R. L. Street, and M. Xue (2006). "High-resolution large-eddy simulations of flow in a steep Alpine valley. Part II: Flow Structure and Heat Budgets". *Journal of Applied Meteorology and Climatology*, 45, 87–107. DOI: [10.1175/JAM2323.1](https://doi.org/10.1175/JAM2323.1) (cited on p. 9).
- Weigel, A. P. and M. W. Rotach (2004). "Flow structure and turbulence characteristics of the daytime atmosphere in a steep and narrow Alpine valley". *Quarterly Journal of the Royal Meteorological Society*, 130, 2605–2628. DOI: [10.1256/qj.03.214](https://doi.org/10.1256/qj.03.214) (cited on p. 8).
- Werner, C. (2005). "Lidar". Ed. by W. C. Springer, New York, NY. Chap. Doppler Wind Lidar, 325–354. DOI: [10.1007/0-387-25101-4\\_12](https://doi.org/10.1007/0-387-25101-4_12) (cited on p. 11).
- Whiteman, C. (2000). *Mountain Meteorology: Fundamentals and Applications*. Oxford University Press, 376 (cited on p. 26).



- Winstral, A. and D. Marks (2002). “Simulating wind fields and snow redistribution using terrain-based parameters to model snow accumulation and melt over a semi-arid mountain catchment”. *Hydrological Processes*, 16, 3585–3603. DOI: [10.1002/hyp.1238](https://doi.org/10.1002/hyp.1238) (cited on p. 5).
- Winstral, A., D. Marks, and R. Gurney (2013). “Simulating wind-affected snow accumulations at catchment to basin scales”. *Advances in Water Resources*, 55, 64–79. DOI: [10.1016/j.advwatres.2012.08.011](https://doi.org/10.1016/j.advwatres.2012.08.011) (cited on p. 16).
- Wipf, S., V. Stoeckli, and P. Bebi (2009). “Winter climate change in alpine tundra: plant responses to changes in snow depth and snowmelt timing”. *Climatic Change*, 94, 105–121. DOI: [10.1007/s10584-009-9546-x](https://doi.org/10.1007/s10584-009-9546-x) (cited on pp. 1, 16).
- Wirz, V., M. Schirmer, S. Gruber, and M. Lehning (2011). “Spatio-temporal measurements and analysis of snow depth in a rock face”. *The Cryosphere*, 5, 893–905. DOI: [10.5194/tc-5-893-2011](https://doi.org/10.5194/tc-5-893-2011) (cited on pp. 13, 16, 20, 26, 29, 32).
- WSL Institute for Snow and Avalanche Research SLF (2015). *Meteorological and snowpack measurements from Weissfluhjoch, Davos, Switzerland*. WSL Institute for Snow and Avalanche Research SLF. DOI: [10.16904/1](https://doi.org/10.16904/1) (cited on p. 17).
- Wyngaard, J. C. (2004). “Toward Numerical Modeling in the “Terra Incognita””. *Journal of Atmospheric Sciences*, 61, 1816–1826. DOI: [10.1175/1520-0469\(2004\)061<1816:TNMITT>2.0.CO;2](https://doi.org/10.1175/1520-0469(2004)061<1816:TNMITT>2.0.CO;2) (cited on pp. 8, 38, 112).
- Xue, L., X. Chu, R. Rasmussen, D. Breed, B. Boe, and B. Geerts (2013). “The Dispersion of Silver Iodide Particles from Ground-Based Generators over Complex Terrain”. *Journal of Applied Meteorology and Climatology*, 53, 1342–1361. DOI: [10.1175/JAMC-D-13-0241.1](https://doi.org/10.1175/JAMC-D-13-0241.1) (cited on p. 9).
- Xue, M., K. K. Droegemeier, V. Wong, A. Shapiro, K. Brewster, F. Carr, D. Weber, Y. Liu, and D. Wang (2001). “The Advanced Regional Prediction System (ARPS) – A multi-scale nonhydrostatic atmospheric simulation and prediction tool. Part II: Model physics and applications”. *Meteorology and Atmospheric Physics*, 76, 143–165. DOI: [10.1007/s007030170027](https://doi.org/10.1007/s007030170027) (cited on pp. 6, 20).
- Yang, Z.-L., G.-Y. Niu, K. E. Mitchell, F. Chen, M. B. Ek, M. Barlage, L. Longuevergne, K. Manning, D. Niyogi, M. Tewari, and Y. Xia (2011). “The community Noah land surface model with multiparameterization options (Noah-MP): 2. Evaluation over global river basins”. *Journal of Geophysical Research*, 116, D12110. DOI: [10.1029/2010JD015140](https://doi.org/10.1029/2010JD015140) (cited on pp. 38, 60, 113).
- Zängl, G. (2007). “Small-scale variability of orographic precipitation in the Alps: Case studies and semi-idealized numerical simulations”. *Quarterly Journal of the Royal Meteorological Society*, 133, 1701–1716. DOI: [10.1002/qj.163](https://doi.org/10.1002/qj.163) (cited on pp. 58, 70).
- (2008). “The temperature dependence of small-scale orographic precipitation enhancement”. *Quarterly Journal of the Royal Meteorological Society*, 134, 1167–1181. DOI: [10.1002/qj.267](https://doi.org/10.1002/qj.267) (cited on pp. 4, 16, 36, 37).
- Zängl, G., D. Aulehner, C. Wastl, and A. Pfeiffer (2008). “Small-scale precipitation variability in the Alps: Climatology in comparison with semi-idealized numerical simulations”. *Quarterly Journal of the Royal Meteorological Society*, 134, 1865–1880. DOI: [10.1002/qj.311](https://doi.org/10.1002/qj.311) (cited on pp. 16, 36).
- Zhang, D.-L. and R. A. Anthes (1982). “A High-Resolution Model of the Planetary Boundary Layer – Sensitivity Tests and Comparisons with SESAME-79 Data”. *Journal of Applied Meteorology*, 21, 1594–1609. DOI: [10.1175/1520-0450\(1982\)021<1594:AHRMOT>2.0.CO;2](https://doi.org/10.1175/1520-0450(1982)021<1594:AHRMOT>2.0.CO;2) (cited on pp. 39, 60).
- Zhong, S. and F. K. Chow (2013). “Mountain Weather Research and Forecasting: Recent Progress and Current Challenges”. Ed. by K. F. Chow, F. S. De Wekker, and J. B. Snyder. Springer Netherlands. Chap. Meso- and Fine-Scale Modeling over Complex Terrain: Parameterizations and Applications, 591–653. DOI: [10.1007/978-94-007-4098-3\\_10](https://doi.org/10.1007/978-94-007-4098-3_10) (cited on p. 8).

# Glossary

## A

**Advanced Regional Prediction System, ARPS:** An atmospheric model.

**Airborne laser scanning, ALS:** Distance measurements performed with a laser scanner, which is mounted on an airplane, resulting in a point cloud describing the surface of the scanned area.

**Alpine3D:** An alpine surface processes model.

## B

**Bergeron-Findeisen process:** Ice/snow-particle growth on the expense of liquid rain drops or cloud droplets due to the difference in the saturation level over liquid and solid water. Also known as *Wegener-Bergeron-Findeisen process*.

## C

**Consortium for Small-Scale Modeling, COSMO:** An atmospheric model.

**CROCUS:** A snowpack model.

## D

**Direct numerical simulations, DNS:** Simulations which resolve the full spectrum of length scales.

## G

**Gray zone:** In numerical simulations - zone between scales at which all boundary layer processes need to be parameterized and scales at which the large energy-containing eddies are resolved. Also known as *terra incognita*.

## I

**Intermediate Complexity Atmospheric Research Model, ICAR:** An atmospheric model based on mountain wave theory.

**Immersed boundary method, IBM:** Method to define the atmosphere on a Cartesian grid to avoid coordinate transformations.

## L

**Large-eddy simulations, LES:** Simulations which resolve the large energy-containing eddies.

**Light Detection And Ranging, Lidar:** A remote sensing instrument to measure to small-scale flow field.

## M

**Meso-NH:** An atmospheric model.

## O

**Orographic precipitation enhancement:** Precipitation production due to topographically induce lifting condensation.

**P**

**Particle-flow interactions:** The influence of the local flow field on the pathways or precipitation particles and the particle distribution in the air.

**Plane position indicator, PPI:** Lidar and radar scans of horizontal cones.

**Planetary boundary layer, PBL:** The lowest layer of the atmosphere which is strongly affected by the surface.

**Pre-depositional precipitation processes:** All precipitation processes shaping the precipitation distribution before reaching the ground for the first time.

**Preferential deposition:** The snow distribution resulting from particle-flow interactions.

**Post-depositional processes:** Processes leading to a redistribution of snow, which was already deposited on the ground.

**R**

**Radio Detection and Ranging, Radar:** A remote sensing instrument to measure precipitation.

**Range height indicator, RHI:** Lidar and radar scans of vertical slices.

**Reynolds-Averaged Navier-Stokes equations, RANS:** Simulations where all turbulent motions are averaged out.

**S**

**Scale analysis:** Geostatistical analysis to determine dominant processes at different distance scales.

**Scale break:** Lag distances of the intersections of the model which is fitted to the variogram.

**Seeder-feeder mechanism:** Growth of precipitation due to snow or ice particles, which are falling from a high-level (seeder) cloud through a low-level (feeder) cloud, where they grow on the expense of cloud droplets.

**SNOWPACK:** A snowpack model.

**T**

**Terra incognita:** see *Gray zone*.

**Terrain-flow-precipitation interactions:** The effect of terrain-induced flow field variations on the precipitation formation and distribution.

**Terrestrial laser scan, TLS:** Distance measurements performed with a terrestrial laser scanner resulting in a point cloud describing the surface of the scanned area.

**Terrestrial laser scanner:** A remote sensing device to measure distances of a surface, producing a point cloud describing the surface of the scanned area.

**V**

**Variogram:** Geostatistical tool to determine the variance of a field of values depending on their locations.

**Velocity azimuth display, VAD:** Scans in the vertical above the lidar to retrieve the three-dimensional wind vectors.

**W**

**Weather Research and Forecasting model, WRF:** An atmospheric model.

**Wegener-Bergeron-Findeisen process:** see *Bergeron-Findeisen process*.

# Franziska Gerber

## Curriculum vitae

Flüelastrasse 11  
7260 Davos Dorf  
✉ gerberf@slf.ch  
\* 10.03.1988

### Education

- 2014–2018 **PhD Student**, *Laboratory of Cryospheric Sciences*, EPFL, Lausanne and WSL Institute for Snow and Avalanche Research SLF, Davos, supervised by Prof. Dr. M. Lehning.
- 2016 **ACE Maritime University**, *Swiss Polar Institute*.
- 2015 **Summer school**, *Innsbruck Summer School of Alpine Research*, Innsbruck.
- Aug 2013 **Master of Science ETH in Atmospheric and Climate Science**, *with distinction*.
- 2012 **Autumn course**, *University Center in Svalbard*, Longyearbyen, Norway.  
Course in air-ice-sea interactions
- 2011 **Exchange Semester**, *University Centre in Svalbard*, Longyearbyen, Norway.  
Courses in Arctic Geophysics
- 2010–2013 **Master**, *ETH*, Zürich.  
Master in Atmospheric and Climate Sciences
- Oct 2011 **Bachelor of Science ETH in Earth Sciences**.
- 2007–2010 **Bachelor**, *ETH*, Zürich.  
Bachelor in Earth Sciences; Major in Climate and Water

### PhD thesis

- title *From the clouds to the ground – The effect of flow-precipitation interactions on snow distribution in complex alpine terrain*
- supervisors Prof. Dr. Michael Lehning, Dr. Rebecca Mott-Grünwald

### Master thesis

- title *Influence of the western North Atlantic and the Barents Sea on European winter climate*
- supervisors Prof. Dr. Reto Knutti, Dr. Jan Sedlacek

### Experience

#### Vocational

- 2013–2014 **Scientific Internship**, *WSL Institute for Snow and Avalanche Research SLF*, Davos.
- 2013 **Scientific Assistant**, *Institute for Atmospheric and Climate Science, Climate Physics Group*, ETH Zürich.

## Tutoring

- 2011–2018 **Trainer Badminton**, *Academic Sports Association Zürich*, Zürich.  
2009 **Teaching Assistant**, *ETH*, Zürich, Geology for civil engineers.

---

## Skills

### Languages

- German Mother Tongue  
English Fluent  
French Good

### Computer skills

- very good NCL, R  
good Matlab, Python, LaTeX, MS Office, ArcGIS

### Field experience

- good terrestrial laser scanning  
experience installing and servicing meteorological stations, drone flights, various sea ice measurements, ship-based oceanographic and atmospheric measurements

---

## Publications

### Peer reviewed

- 2017 **Gerber, F.**, M. Lehning, S. W. Hoch, and R. Mott (2017). "A close-ridge small-scale atmospheric flow field and its influence on snow accumulation". *Journal of Geophysical Research - Atmospheres*, 122, pp. 7737–7754. DOI: 10.1002/2016JD026258.
- 2014 **Gerber, F.**, J. Sedlacek, and R. Knutti (2014). "Influence of the western North Atlantic and the Barents Sea on European winter climate". *Geophysical Research Letters*, 41, pp. 561–567. DOI: 10.1002/2013GL058778.

### In review/Submitted/Non-peer reviewed

- 2018 **Gerber, F.**, N. Besic, V. Sharma, R. Mott, M. Daniels, M. Gabella, A. Berne, U. Germann, and M. Lehning (2018). "Spatial variability of snow precipitation and accumulation in COSMO-WRF simulations and radar estimations over complex terrain". *The Cryosphere Discussions*, in review. DOI: 10.5194/tc-2018-50.

**Gerber, F.**, R. Mott, and M. Lehning (2018). "The importance near-surface winter precipitation processes in complex alpine terrain". *Journal of Hydrometeorology*, in review.

**Gerber, F.** and V. Sharma (2018). *Running COSMO-WRF on very high resolution over complex terrain*. Laboratory of Cryospheric Sciences, École Polytechnique Fédérale de Lausanne, Lausanne, Switzerland. DOI: 10.16904/envidat.35.